

Novel PVA/PLA-Graphene Three-
Dimensional Printed Nanocomposites for Gas
Sensing, Adsorption-Desorption Cooling and
Electrochromic Coatings

A thesis submitted for the degree of Doctor of Philosophy

by

Samuel Derek Rust

Wolfson Centre for Materials Processing, Brunel University London

Submitted September 2018

Abstract

Novel PVA hydrogel nanocomposites, symmetric three-dimension (3D) printed poly(vinyl) alcohol (PVA) hydrogels and asymmetric 3D printed PVA/poly(lactic) acid (PLA)-graphene (G) nanocomposites have been prepared and characterised in detail using Fourier transform IR (FTIR), scanning electron microscopy (SEM), thermogravimetric analysis (TGA), differential scanning calorimetry (DSC) and Raman spectroscopy. The aim was to produce new nanomaterials in part by fused deposition modelling (FDM) and to evaluate them as:

- (i) Personal sensors for sensing of (a) pollutants (e.g. NO/NO₂, SO₂, VOCs/PAHs and particulates) in the atmosphere that might adversely affect human health. With improved response time, sensitivity, selectivity, recovery time and stability and an improved low cost spatial and temporal resolution (b) oil that pollutes water and soil.
- (ii) Localised sensors for CO₂ that could be fine-tuned by water and monoethanolamine (MEA) incorporation to provide feedback on process efficiency affecting global warming and breathing efficiency.
- (iii) Coatings for improved adsorption-cooling of Al-clad building surfaces, lowering power consumption for air conditioning.
- (iv) Coatings for improved electrochromic displays.

Practical applications of such materials are remote patient monitoring through real-time breath analysis, synthetic sweating surfaces for residential and industrial buildings, wearable sensors connected to the IoT and solar reactive glass.

0.045mmol of CO₂ produced a conductance change in a hydrogel in 4s for a 3D printed PVA hydrogel with on-board H₂O; 1-1.5s slower than a quadrupole mass spectrometer (RGA). It could be that hydrogel sensors form an inexpensive method for breathing analysis and remote patient monitoring; tailoring for SO₂ or NO₂ detection remains to be seen. 3D printed PLA/G is unlikely to compete with vapour-deposited metal electrodes for detection of oil-in-water.

Infra-red thermography (IRT) showed that novel hydrogel coatings exhibited a larger cooling effect (-13K when H₂O swollen, -10K when MEA swollen and -11.8K when H₂O swollen asymmetric sample) than previously (SPIE) for over 4000s on a construction-type Al substrate and even a 2.6K cooling with PVA hydrogel/Al substrate over a 25h period.

“Real-world” IRT was also conducted with PVA-M_xO_y nanocomposite hydrogels and revealed that the species of M_xO_y affects the thermal signature of the gel differently when viewed against a background. More importantly, reversible electrochromic responses in novel WO₃/PVA hydrogels (with and without additional salt) seen in <1s, open the possibility of colour switchable cool coatings for buildings. Addition of various salts enabled initial tuning of colour to be achieved.

1. Introduction.....	1
1.1 Aims and Objectives	1
1.2 Context	1
1.3 Current Gas Sensor Technologies	5
1.3.1 Background.....	5
1.3.2 Electrochemical Sensors with Liquid Electrolytes	6
1.3.3 Thermal Conductivity Sensors	7
1.3.3.1 Wheatstone Bridge.....	8
1.3.4 Catalytic Combustion Sensor (Pellistor)	9
1.3.5 Nondispersive Infrared Absorption Sensors.....	9
1.3.6 Solid Electrolyte Sensor	10
1.3.7 Semiconductor Metal Oxide Sensor	12
1.3.8 Paramagnetic Sensors	14
1.3.9 Particulate Matter Sensing.....	15
1.3.10 Summary of Sensor Types.....	16
1.4 Infrared and Optical Coatings for Buildings	17
1.4.1 Background.....	17
1.4.2 Smart Windows	19
1.4.3 Electrochromic Coatings	20
1.4.4 Hydrogels	22
1.4.4.1 Background	22
1.4.4.2 Physically Crosslinked Hydrogels	24
1.4.4.3 Chemical Crosslinked Hydrogels	25
1.4.5 Summary.....	27
1.5 Three-Dimensional Printing Technologies	28
1.5.1 Background.....	28

1.5.2 Material Extrusion	29
1.5.2.1 Fused Deposition Modelling	30
1.5.3 Material Jetting	31
1.5.4 Binder Jetting.....	32
1.5.5 Directed Energy Deposition	33
1.5.6 Powder Bed Fusion.....	34
1.5.6.1 Electron Beam Melting	35
1.5.6.2 Direct Metal Laser Sintering and Selective Laser Sintering.....	35
1.5.6.3 Selective Heat Sintering.....	36
1.5.7 Vat Polymerisation	36
1.5.8 Sheet Lamination.....	37
1.5.9 Summary of Technologies.....	38
1.6 Materials of Interest	39
1.6.1 Polyvinyl Alcohol.....	40
1.6.2 Poly Lactic Acid.....	41
1.6.3 Graphene.....	42
1.6.4 Carbon Nanotubes (CNT).....	44
1.6.5 Tungsten Trioxide	46
1.7 Alternative Applications of Gas Detection	46
1.8 Oil Spill Detection.....	47
1.8.1 Background of Oil Composition	47
1.8.2 Oil Toxicity and Detection of Spillages	48
2 Methods.....	50
2.1 Instrumentation.....	51
2.1.1 Three-dimensional Printing	51
2.1.1.1 Material Extrusion	51

2.1.2 Scanning Electron Microscopy.....	56
2.1.3 Energy-Dispersive X-ray analysis.....	59
2.1.4 Thermogravimetric Analysis.....	61
2.1.5 Differential Scanning Calorimetry.....	62
2.1.6 Infrared Thermography.....	64
2.1.7 Raman Spectroscopy.....	67
2.1.8 Fourier Transform Infrared Spectroscopy.....	70
2.1.8.1 Attenuated Total Reflectance.....	72
2.1.9 Four Point Electrical Conductivity.....	73
2.1.10 Residual Gas Analysis.....	75
2.1.11 Dynamic Light Scattering.....	77
2.2 General Gas Testing Equipment.....	79
2.3 General Hydrogel Production.....	81
2.3.1 Background.....	81
2.3.2 Chemically Crosslinked Hydrogels.....	82
2.3.3 Physically Crosslinked Hydrogels.....	83
2.3.3.1 Conventional Freezer Method.....	83
2.3.3.2 Liquid Nitrogen Method.....	83
2.3.4 Hydrogels Incorporating Functional Micro and Nanoparticles.....	84
2.3.4.1 Synthesis of Tungsten Trioxide Nanoparticles.....	84
2.3.4.2 PVA Metal Oxide Slurry Method.....	84
2.3.4.3 In-situ PVA Metal Oxide Dispersion Method - Chemical Crosslinking.....	84
2.3.4.4 In-situ PVA Metal Oxide Dispersion Method - Physical Crosslinking.....	85
2.3.4.5 Electrochromic Testing.....	85
2.4 Breathing Experiments.....	86
2.5 Microconductivity.....	86

2.6 Summary of Techniques.....	87
3 Drying Characteristics and Hydrolysis of Polyvinyl Acetate.....	90
3.1 Introduction	90
3.2 Aims and Objectives	91
3.3 Results	91
3.3.1 PVAc Drying Times with Organic Solvents	91
3.3.2 Scanning Electron Microscopy of PVAc Films in Various Organic Solvents	91
3.3.3 Fourier Transform Infrared Spectroscopy	93
3.3.4 Infrared Thermography of Organic Solvents.....	97
3.3.5 Infrared Thermography of Organic Solvents with 5wt.% PVAc	98
3.3.6 Fourier Transform Infrared Spectroscopy of Controlled PVAc Hydrolysis	99
3.4 Summary	101
4 Production of Polyvinyl Alcohol Hydrogels and Thin Films Incorporating Functional Nanoparticles	103
4.1 Introduction	103
4.2 Aims and Objectives	104
4.3 Results	104
4.3.1 Production of PVA hydrogels.....	104
4.3.2 Visual Observations.....	106
4.3.3 Characterisation of Hydrogels	111
4.3.3.1 Fourier Transform Infrared Spectroscopy	111
4.3.3.2 Thermogravimetric Analysis	112
4.3.4 Infrared Thermography of PVA Hydrogels.....	113
4.3.5 Viscometry	118
4.3.6 Inclusion of Metal Oxide Nanoparticles in PVA Hydrogels and Films	118
4.3.6.1 Characterisation of PVA-M _x O _y hydrogels.....	119

4.3.6.2	Scanning Electron Microscopy of PVA/M _x O _y Slurry Method in Hydrogels .	119
4.3.6.3	Energy Dispersive X-ray of PVA/M _x O _y Slurry Method in Films	120
4.3.7	Synthesis of Tungsten Trioxide NPs	122
4.3.7.1	Thermogravimetric Analysis	122
4.3.8	Scanning Electron Microscopy of In-situ PVA Metal Oxide Dispersion Method	123
4.3.9	Synthesis of Gold NPs for Inclusion in PVA Hydrogel Matrix	125
4.3.10	Infrared Thermography of PVA-M _x O _y Hydrogels	125
4.4	Hydrogel Electrochromism	126
4.5	Summary	128
5	3-Dimensional Printed PVA-PLA Materials for Gas/Breathing Sensing Applications .	130
5.1	Introduction	130
5.2	Aims and Objectives	130
5.3	Results	131
5.3.1	1 st Initial Exploratory Sensor Designs	131
5.3.1.1	Water Uptake Testing	133
5.3.1.2	Fourier Transform Infrared	134
5.3.1.3	Summary	135
5.3.2	2 nd Phase Designs	135
5.3.2.1	Scanning Electron Microscopy	137
5.3.2.2	Fourier Transform Infrared	140
5.3.2.2	Micro Fourier Transform Infrared	141
5.3.2.3	Raman Spectroscopy	142
5.3.2.4	Thermogravimetric Analysis	144
5.3.2.5	Differential Scanning Calorimetry	146
5.3.2.6	PVA Water Uptake Investigations	148
5.3.2.7	Monoethanolamine Inclusion.....	150

5.3.3 Gas Testing	153
5.3.3.1 Printed PVA Hydrogel Gas Testing.....	157
5.3.3.2 Printed PVA Swollen with MEA Gas Testing.....	161
5.4 Atmospheric Breathing of Adult Males	165
5.5 Microconductivity	169
5.6 Summary	170
6 Cooling Performance of 3D Printed Hydrogels and Composites.....	172
6.1 Introduction	172
6.2 Aims and Objectives	172
6.3 Results	173
6.3.1 3D Printed Hydrogel Preparation	173
6.3.2 Infrared Thermography of 3D Printed Samples	173
6.3.3 Infrared Thermography of Conventionally Prepared PVA Hydrogel	179
6.4 Summary	182
7 Conclusions	183
7.1 Achievement of Aims.....	183
7.2 PVA-M _x O _y Nanocomposite Films and Hydrogels	183
7.3 Electrochromic Hydrogels.....	185
7.4 3D Printed Gas Sensors.....	186
7.5 Future Work	187
8 Appendix Items	189
8.1 FTIR Peak identification tables.....	189
8.2 List of Conferences Attended.....	200
8.3 List of Presentations Given	201
8.3 Miscellaneous Honours	201
8.4 Teaching	201

9	References	202
---	------------------	-----

Acknowledgements

I would like to extend my deepest and heartfelt thanks to my supervisor Professor Paul Sermon, who has guided me throughout this project. He has also shown continued support both professionally and personally and I cannot thank him enough for all he has done for me. Also to Mandy Sermon, for her support, proof-reading skills and general grammatical suggestions.

I am also grateful to Professor Jack Silver as Executive Director of the Wolfson Centre and my second supervisor.

I also wish to thank my family for the support they have afforded me financially, and for the encouragement they gave me to complete this work.

I am also indebted to Dr Myles Worsley for his seemingly endless notes on instrumentation new and old, and for his astonishing ability to decipher Prof. Sermon's handwriting when no other living mortal could!

An extra special thank you must go to Dr Inmaculada Andres, whose continued support as a friend and colleague lifted my spirits when things got a little too much.

I would like to thank Mr Abdul Ghani for the knowledge he has imparted to me through useful discussions related to aspects of TGA and DSC. Also Dr Lesley Hanna for all the administrative problems she has helped me to solve over the years, through her encyclopaedic knowledge of processes to follow and people to contact to get things done! I would also like to give an honourable mention Dr Terry Ireland, Dr Paul Marsh, Mr Steve Ferris, and Mr Maxwell Evans for assisting with ordering of chemicals and for allowing me to beg, borrow and steal equipment when I did not have or couldn't find what I needed.

Thanks must also go to PhD students present and past: Ahmed, Alex, Anil, Arjang, Ed, Fathullah, Iman, Rob, Virginia and to anyone I have missed. A special mention must go to Uche, for tolerating being my desk-neighbour and for her unwavering assistance in helping me to find data I thought I had lost forever.

Finally, I wish to thank members of ETC for maintaining first class characterisation facilities and for the training and guidance they give to users.

Dedication

I dedicate this thesis to the memory of my Grandmother Jill Marion Pullen (1945 – 2017).

She introduced me to the outdoors and encouraged me to explore the natural world.

She also taught me the value of perseverance.

List of Figures

<i>Figure 1 – Schematic diagram of a three-electrode electrochemical sensor, showing working, reference and counter electrodes [57].</i>	6
<i>Figure 2 – Schematic diagram of a thermal conductivity sensor, also referred to as a katharometer [64].</i>	7
<i>Figure 3 – Circuit diagram of a Wheatstone bridge, where R_u is an unknown resistance, R_2 and R_3 are equal value resistors and R_v is a variable resistor. V_i is a voltage applied and V_0 a measured null point voltage [71].</i>	8
<i>Figure 4 – Schematic diagram of a catalytic combustion sensor, also referred to as a pellistor [57].</i>	9
<i>Figure 5 – Schematic diagram of a typical NDIR gas sensor including a reference cell. The part marked “chopper” is an optical device to improve the signal to noise ratio of the device [79].</i>	10
<i>Figure 6 – Schematic diagram of a Nernst-type solid electrolyte detector [89].</i>	11
<i>Figure 7 – Adsorption of oxygen to form an EDL in (a) n-type and a HAL in (b) p-type oxide semiconductors resulting in electrical core-shell layers [109].</i>	12
<i>Figure 8 – (a) mechanism of gas sensing in an n-type SMO and (b) the equivalent circuit [109].</i>	13
<i>Figure 9 – Schematic diagram of a typical paramagnetic oxygen sensor [111].</i>	14
<i>Figure 10 – Visual representation of an ideal smart window; on warm days IR radiation is reflected, but visible light allowed through and on cool days both IR and visible light may pass into the room [136].</i>	19
<i>Figure 11 – Crystal structure of tungsten oxide showing the corner sharing characteristics of the oxygen and edge sharing of unit cells. Reproduced from [139].</i>	20
<i>Figure 12 – Example of an asymmetric electrochromic cell; electrochromic layers on each side are formed of different metal oxides. Reproduced and adapted from [151].</i>	21
<i>Figure 13 – Classification of hydrogels according to various features. Reproduced and adapted from [164].</i>	23
<i>Figure 14 – Acid catalysed crosslinking of PVA with GA [184].</i>	25
<i>Figure 15 – Functional groups able to readily undertake crosslinking with GA [185].</i>	26
<i>Figure 16 – (a) decomposition of an initiator to give two free radicals, (b) free radicals bond to monomer units [186].</i>	26
<i>Figure 17 – Three types of plastic presented structurally (a) thermoplastic, (b) elastomer and (c) thermoset [202].</i>	29
<i>Figure 18 – Generalised schematic diagram of a simple fused deposition modelling 3D printer [204].</i>	30

<i>Figure 19 – 3D printed model of a cervical spine based on CT images, made from ABS and produce via FDM [208].</i>	31
<i>Figure 20 – MJ model of an aorta from MR angiography images [210].</i>	31
<i>Figure 21 – Generalised schematic diagram of a binder jetting 3D printer. Adapted from [211].</i>	32
<i>Figure 22 – Model of an ankle produced using BJ [214].</i>	33
<i>Figure 23 – Schematic diagram of the directed energy deposition method [215].</i>	33
<i>Figure 24 – DED produced seat ring (a) original part, (b) new part produced by DED (c) new part after further processing and improvement [217].</i>	34
<i>Figure 25 – Generalised schematic diagram of the powder bed fusion method; specifically, selective light sintering [218].</i>	34
<i>Figure 26 – a selection of items produced by EBM [219].</i>	35
<i>Figure 27 – S-shaped aluminium tube made by DMLS [220].</i>	35
<i>Figure 28 – Schematic diagram of a vat polymerisation 3d printer; specifically using the stereolithography method [221].</i>	36
<i>Figure 29 – SLA produced model of conjoined twins showing blood vessels. This type of model is particularly good for surgical reconstruction and diagnosis [222].</i>	37
<i>Figure 30 – Schematic diagram of a sheet lamination process; specifically, laminated object manufacturing [223].</i>	38
<i>Figure 31 – Structure of (a) 100% hydrolysed PVA (b) partially hydrolysed PVA [224].</i>	41
<i>Figure 32 – Reaction schematic of hydrolysis of PVAc to PVA [225].</i>	41
<i>Figure 33 – Possible synthesis routes to producing high molecular weight PLA [227].</i>	42
<i>Figure 34 - Visual representation of single-layer (SL), few-layer (FL) and multi-layer (ML) arrangements of graphene shown on the atomic scale (approximately 100nm).</i>	43
<i>Figure 35 - Common modifications of planar graphene [230].</i>	43
<i>Figure 36 - Different chiral arrangements of SWCNTs (a) armchair (b) zigzag (c) chiral [235].</i>	45
<i>Figure 37 - Illustration of a single walled carbon nanotube and a multi walled carbon nanotube; the latter can comprise of many layers of tubes within tubes [236].</i>	45
<i>Figure 38 – Crystal structure of WO₃ (a) ideal cubic structure (b) WO₆ octahedra [248].</i>	46
<i>Figure 39 - A generalised schematic diagram of a material extrusion 3D printer [291].</i>	52
<i>Figure 40 - CAD model of a cylindrical sample to be printed, before conversion to STL file type.</i>	53
<i>Figure 41 – CAD model of a cylindrical sample after being converted to STL file type.</i>	53
<i>Figure 42 - Cylindrical sample viewed in Cura, a slicing software package.</i>	54
<i>Figure 43 - Ultimaker 3 three-dimensional printer.</i>	56

<i>Figure 44 - Schematic diagram of a scanning electron microscope; with emission, focusing, sample, detection and display parts shown [297].</i>	57
<i>Figure 45 – Sample preparation stages prior to analysis by SEM. (a) Affixing a sample onto an aluminium sample stub, (b) gold coating by placing the sample stub into a sputter coater and (c) securing the sample stubs to a multi-stub holder to be placed into the SEM chamber.</i>	58
<i>Figure 46 – Digital photograph of using a Polaron Emitech SC7640 High Resolution Sputter Coater.</i>	58
<i>Figure 47 - Optical photograph of a Zeiss Supra 35VP scanning electron microscope and associated analysis probes.</i>	59
<i>Figure 48 – Interaction volume of primary beam electrons [299].</i>	60
<i>Figure 49 - A schematic diagram of a typical TGA instrument; alternative designs can incorporate a top loading mechanism [300].</i>	61
<i>Figure 50 – (a) TA Instruments TGA Q600 TGA and (b) close-up of the sample pan arms which were connected to a microbalance.</i>	62
<i>Figure 51 - Diagram of the heat flux DSC showing the furnace cell [301].</i>	63
<i>Figure 52 – (a) TA instruments DSC Q2000 and (b) close-up of the reference and sample cells on raised platforms within a single furnace.</i>	64
<i>Figure 53 – Spectral emissive power of a blackbody versus wavelength.</i>	65
<i>Figure 54 – (a) FLIR ThermoCAM PM695 thermal imaging system and (b) the view seen by the operator.</i>	67
<i>Figure 55 - Visual representation of the differences between IR, Rayleigh, Raman (Stokes and anti-Stokes) and fluorescence electron energy levels [302].</i>	68
<i>Figure 56 – Raman spectra of pristine different number layered graphene compared to pristine graphite [308].</i>	69
<i>Figure 57 - (a) Renishaw Invia Raman microscope and (b) close-up of the microscope chamber.</i>	70
<i>Figure 58 - Schematic diagram of a Michelson interferometer [310].</i>	71
<i>Figure 59 - Shimadzu IRAffinity-1 Fourier transform infrared spectrophotometer.</i>	72
<i>Figure 60 - Schematic of a typical Attenuated Total Reflectance cell. [311].</i>	72
<i>Figure 61 – (a) Specac Quest ATR accessory and (b) close-up of the diamond ATR crystal.</i>	73
<i>Figure 62 - (a) Jandel RM2 control unit and (b) Jandel four-point conductivity probe.</i>	74
<i>Figure 63 – Schematic diagram of the principle components of an RGA [322].</i>	76
<i>Figure 64 – Schematic diagram of (a) linear channel electron multiplier and (b) curved channel electron multiplier [325].</i>	77

<i>Figure 65 – (a) full RGA setup including a laptop computer for real time monitoring and recording and (b) close-up of RGA unit showing the capillary inlet attached to the gas test rig.....</i>	<i>77</i>
<i>Figure 66 – Schematic drawing of a typical DLS setup [330].</i>	<i>78</i>
<i>Figure 67 – Diagram of a custom-built test rig designed to measure the response of hydrogel samples to injected samples of gas. (1.) gas supply, (2.) zeolite filter, (3.) gas flow meter, (4.) gas injection point, (5.) relative humidity bubbler, (6.) tube furnace, (7.) optional catalysis sample, (8.) glass reactor, (9.) residual gas analyser, (10.) laptop computer, (11.) Jandel RM2 control unit, (12.) Jandel four-point conductivity probe, (13.) sample of interest, (14.) gas tight test cell, (15.) Crowcon T3 multi gas sensor, (16.) particle size analyser, (17.) water bubbler, (18.) gas exit stream.</i>	<i>81</i>
<i>Figure 68 – Reaction mechanism of PVA crosslinking via a chemical method using glutaraldehyde [337].</i>	<i>82</i>
<i>Figure 69 – Formation of PVA hydrogels based on the creation of nodes/knots which promote hydrogen bonding between polymer chains [338].</i>	<i>83</i>
<i>Figure 70 – FTIR-ATR spectra of 5, 8 and 10wt.% PVAc dissolved in methyl formate.....</i>	<i>93</i>
<i>Figure 71 – FTIR-ATR spectra of 5, 8 and 10wt.% PVAc dissolved in dichloromethane.....</i>	<i>94</i>
<i>Figure 72 – FTIR-ATR spectra of 5, 8 and 10wt.% PVAc dissolved in methyl acetate.</i>	<i>95</i>
<i>Figure 73 – FTIR-ATR spectra of 5, 8 and 10wt.% PVAc dissolved in ethyl acetate.</i>	<i>95</i>
<i>Figure 74 – FTIR-ATR spectra of 5, 8 and 10wt.% PVAc dissolved in methyl ethyl ketone..</i>	<i>96</i>
<i>Figure 75 – Thermal images of (a) MF (b) MA (c) EA and (d) MEK showing the different evaporation characteristics from a 1ml drop of solvent onto a bench surface over time.</i>	<i>97</i>
<i>Figure 76– Thermal images of (a) MF (b) DCM (c) MA (d) EA and (e) MEK with 5wt.% dissolved PVAc showing the different evaporation characteristics from a 1ml drop of each solvent mixture onto a bench surface over time.....</i>	<i>98</i>
<i>Figure 77 – FTIR-ATR spectra of NaCl catalysed hydrolysis of 8wt.% PVAc dissolved in MF</i>	<i>99</i>
<i>Figure 78 – FTIR-ATR spectra of MgCl₂ catalysed hydrolysis of 8wt.% PVAc dissolved in MF.....</i>	<i>100</i>
<i>Figure 79 – FTIR-ATR spectra of Mg(NO₃)₂ catalysed hydrolysis of 8wt.% PVAc dissolved in MF.....</i>	<i>100</i>
<i>Figure 80 – Thermal image of a self-supporting PVA film positioned in front of a human hand.....</i>	<i>103</i>
<i>Figure 81 - PVA hydrogels from (a) physical crosslinking from freeze-thawing, and (b) chemical crosslinking using glutaraldehyde (GA). The PVA solutions used were 10 wt. %.</i>	<i>105</i>
<i>Figure 82 - PVA hydrogels from (a) 5 wt. % and (b) 10 wt. % PVA aqueous solutions.</i>	<i>105</i>
<i>Figure 83 – FTIR-ATR transmission spectra of PVA powder, 8wt.% PVA film and 8wt.% PVA hydrogel.</i>	<i>111</i>

<i>Figure 84 – TGA plot of 99+% hydrolysed PVA powder and physically crosslinked PVA hydrogels in air and N₂.</i>	112
<i>Figure 85 - Temperature variation of a physically crosslinked (freezer method) PVA hydrogel, of a physically crosslinked (N₂) PVA hydrogel and chemically crosslinked (GA) PVA hydrogel compared to local atmospheric and Al uncoated substrate temperature.</i>	114
<i>Figure 86 – Average differences in temperature of a physically crosslinked (freezer method), PVA hydrogel, of a physically crosslinked (N₂) and PVA hydrogel and chemically crosslinked (GA) PVA hydrogel compared to Al substrate.</i>	115
<i>Figure 87- Thermal images of (a) physically crosslinked (freezer method) (b) PVA hydrogel, of a physically crosslinked (N₂) (c) PVA hydrogel and chemically crosslinked (GA) PVA hydrogel (0-420mins).</i>	116
<i>Figure 88 - Thermal images of (a) physically crosslinked (freezer method) (b) PVA hydrogel, of a physically crosslinked (N₂) (c) PVA hydrogel and chemically crosslinked (GA) PVA hydrogel (480-1500mins).</i>	117
<i>Figure 89 - Temperature between a chemically-crosslinked (GA) PVA hydrogel and its immediate surroundings as a function of time after its preparation. Reproduced from [352].</i>	118
<i>Figure 90 – SEM micrographs of (a, b) 8wt.% PVA+ 4wt% SiO₂, (c, d) 8wt.% PVA + 4wt.% AC films and (e) 8wt.% PVA + 4wt.% WO₃.</i>	120
<i>Figure 91 – SEM-EDX of WO₃ in a PVA hydrogel matrix produced via the method described in 2.3.4.3.</i>	121
<i>Figure 92 – SEM micrographs of WO₃ NPs synthesised from the method outlined in 2.3.4.1.</i>	122
<i>Figure 93 – TGA plot of WO₃ NPs pre- and post- calcination at 773K.</i>	123
<i>Figure 94 – SEM-EDX micrographs of a dried PVA hydrogel with incorporated WO₃ NPs synthesised via the method described in 2.3.4.4.</i>	124
<i>Figure 95 - SEM-EDX micrograph and generated report of PVA-WO₃ nanocomposite film.</i>	124
<i>Figure 96 - Thermal images of (a) PVA-Au (b) PVA-WO₃ (c)PVA-AC hydrogels.</i>	125
<i>Figure 97 - Optical images of the colour change of a PVA-WO₃ (10 wt. %) hydrogel with no added salt.</i>	126
<i>Figure 98 - Optical images of the colour change of a PVA-WO₃ (1 wt.%) hydrogel with no added salt.</i>	127
<i>Figure 99 - Optical images of the colour change of PVA-WO₃ (5 wt.%) hydrogels with varying amounts of perchlorate salts and different cations.</i>	128
<i>Figure 100 – 3D printed PVA cuboid shapes delaminating into separate layers with increasing water uptake. (a) single layer of printed PVA hydrated with H₂O buckling and twisting evident (b) a different single layer from the same sample of printed PVA hydrated with H₂O showing fused layers coming apart.</i>	133

<i>Figure 101 – FTIR-ATR evidence of H₂O uptake in a 3D printed hydrated PVA sample compared to PVA powder.</i>	134
<i>Figure 102 – Digital photographs of a range of 3D printed asymmetrically layered PVA-PLA/graphene designs.</i>	136
<i>Figure 103 – SEM micrographs of unprocessed PLA/G filament.</i>	138
<i>Figure 104 – SEM micrographs of faces, edges and interfaces of PVA-PLA/G composites.</i>	139
<i>Figure 105 – FTIR-ATR transmission spectra of printed PLA/graphene and PVA.</i>	140
<i>Figure 106 - μFTIR chemical maps of the interface between PVA-PLA/G.</i>	141
<i>Figure 107 - μFTIR spectra of the interface between PVA-PLA/G.</i>	142
<i>Figure 108 – Raman spectra of PLA/graphene filament and PLA/graphene printed.</i>	143
<i>Figure 109 – Raman spectra of PVA filament and PVA printed.</i>	144
<i>Figure 110 – TGA of printed PLA/graphene and unprocessed PLA/graphene in N₂ and air.</i>	145
<i>Figure 111 – TGA of printed PVA and unprocessed PVA in N₂ and air.</i>	146
<i>Figure 112 – DSC curve of freezing and thawing of H₂O held in a printed PVA hydrogel.</i>	147
<i>Figure 113 – Weight % increase of printed PVA samples due to H₂O uptake on exposure to different relative humidity's.</i>	148
<i>Figure 114 – FTIR-ATR transmission spectra of dried printed PVA, monoethanolamine and printed PVA swollen with MEA.</i>	150
<i>Figure 115 – FTIR-ATR transmission spectra of dried printed PVA, printed PVA swollen with deionised water and printed PVA swollen with MEA.</i>	151
<i>Figure 116 - FTIR-ATR transmission spectra of printed PVA swollen with different ratios of MEA:H₂O.</i>	153
<i>Figure 117 – Images of (a) printed PVA swollen with MEA (b) simple PVA hydrogel swollen with H₂O.</i>	153
<i>Figure 118 – Response of a printed PVA hydrogel exposed to different volumes of injected CO₂.</i>	154
<i>Figure 119 - Response of printed PVA swollen with MEA exposed to different volumes of injected CO₂.</i>	156
<i>Figure 120 – RGA response to individual pulses of injected CO₂.</i>	156
<i>Figure 121 – RGA and printed PVA hydrogel response to 0.045mmol injected CO₂.</i>	157
<i>Figure 122 – RGA and printed PVA hydrogel response to 0.089mmol injected CO₂.</i>	158
<i>Figure 123 – RGA and printed PVA hydrogel response to 0.134mmol injected CO₂.</i>	158
<i>Figure 124 – RGA and printed PVA hydrogel response to 0.179mmol injected CO₂.</i>	159
<i>Figure 125 – RGA and printed PVA hydrogel response to 0.223mmol injected CO₂.</i>	159
<i>Figure 126 –RGA and printed PVA hydrogel response to 0.268mmol injected CO₂.</i>	160

<i>Figure 127 –RGA and printed PVA swollen with MEA response to 0.045mmol injected CO₂.</i>	161
<i>Figure 128 –RGA and printed PVA swollen with MEA response to 0.089mmol injected CO₂.</i>	161
<i>Figure 129 – RGA and printed PVA swollen with MEA response to 0.134mmol injected CO₂.</i>	162
<i>Figure 130 –RGA and printed PVA swollen with MEA response to 0.179mmol injected CO₂.</i>	162
<i>Figure 131 – RGA and printed PVA swollen with MEA response to 0.223mmol injected CO₂.</i>	163
<i>Figure 132 – RGA and printed PVA swollen with MEA response to 0.268mmol injected CO₂.</i>	164
<i>Figure 133 – %CO₂ detected from repeat exhaling from (a) 73yo male (b) 24yo male and (c) 28yo male.</i>	166
<i>Figure 134 - %O₂ detected from repeat exhaling from (a) 73yo male (b) 24yo male and (c) 28yo male.</i>	167
<i>Figure 135 – UFP concentration from repeat exhaling from (a) 73yo male (b) 24yo male and (c) 28yo male.</i>	168
<i>Figure 136 - Preliminary conductivity-time-depth profiles (blue=water and red=oil). The surface is at 0cm depth.</i>	169
<i>Figure 137 – Plot of seawater (SW) minus deionised water (DW) conductivity (μS) vs time for a Cu wire and PLA/G electrode.</i>	170
<i>Figure 138 – Temperature variation of a printed PVA hydrogel H₂O-swollen, PVA swollen with MEA and dual layered asymmetric PVA hydrogel-PLA/graphene compared to local atmospheric and Al uncoated substrate temperature.</i>	174
<i>Figure 139 – Temperature variation of printed PVA hydrogel swollen with H₂O compared to atmospheric and Al uncoated substrate temperature.</i>	175
<i>Figure 140 – Temperature variation of printed PVA swollen with MEA compared to atmospheric and Al uncoated substrate temperature.</i>	176
<i>Figure 141 – Temperature variation of a dual asymmetric printed PVA hydrogel-PLA/G (non-swollen) compared to atmospheric and Al uncoated substrate temperature.</i>	177
<i>Figure 142 – Thermal images of (a) printed PVA hydrogel (b) printed PVA swollen with MEA (c) dual asymmetric layers printed PVA hydrogel and PLA/graphene.</i>	178
<i>Figure 143 - Temperature variation of a conventionally produced PVA hydrogel compared to atmospheric and Al uncoated substrate temperature.</i>	180
<i>Figure 144 – Thermal images of (a) conventionally prepared physically crosslinked PVA hydrogel with on-board H₂O.</i>	181

List of Tables

<i>Table 1 – WHO guidelines on safe exposure levels to a range of atmospheric pollutants hourly, daily or annually. PM is composed of numerous compounds and exact ppb levels cannot be given as one sample may differ from another, therefore a mean value is given [43].</i>	3
<i>Table 2 - Generalised summary of gas sensor types, rated by performance.</i>	17
<i>Table 3 – Current technologies which may be retrofitted to a building in order to improve its efficiency and lower energy usage. Reproduced from [129].</i>	18
<i>Table 4 - Standard terminology for additive manufacturing technologies, reproduced from [201].</i>	39
<i>Table 5 – Work of adhesion between oil and water phases.</i>	48
<i>Table 6 – Phase characteristics of three known hydrocarbons.</i>	48
<i>Table 7 – Interfacial tensions of aromatic compounds.</i>	48
<i>Table 8 – Key properties of a range of common FDM materials *Nylon 6, one form of nylon, commonly used [296].</i>	55
<i>Table 9 - Summary of analytical techniques used and reasons for selecting.</i>	87
<i>Table 10 – Solvents used in PVAc drying time experiments.</i>	91
<i>Table 11 – Observations noted about the appearance, strength and speed of formation of hydrogels produced via physical crosslinking in a conventional freezer (298-248-298K). Highlighted in green are the conditions which produced hydrogels with the most desirable properties.</i>	106
<i>Table 12 - Observations noted about the appearance, strength and speed of formation of hydrogels produced via physical crosslinking using liquid nitrogen to crash cool the solution (298-77-298K).</i>	107
<i>Table 13 - Observations noted about the appearance, strength and speed of formation of hydrogels produced via chemical crosslinking with GA. Highlighted in green are the conditions which produced hydrogels with the most desirable properties.</i>	109
<i>Table 14 - Sample list of PVA hydrogel with amount of MO NP's included and their relevant emissivity's (ϵ) *Activated Carbon.</i>	119
<i>Table 15 - 3D printed PVA initial designs used here.</i>	132
<i>Table 16 – Peak identification of PLA/graphene filament before and after printing.</i>	143
<i>Table 17 – Peak identification of PVA filament before and after printing.</i>	144
<i>Table 18 – Mass change and weight % change of printed PVA exposed to various different saturated salt solutions.</i>	149
<i>Table 19 – Volume of water taken up by the printed PVA matrix</i>	149
<i>Table 20 - Summary table of aims/objectives and the amount (as a %) the author believes has been achieved.</i>	183

<i>Table 21 - FTIR-ATR peak identifications of methyl formate with 5, 8 and 10wt.% of dissolved PVAc.....</i>	<i>189</i>
<i>Table 22 - FTIR-ATR peak identifications of dichloromethane with 5, 8 and 10wt.% of dissolved PVAc.....</i>	<i>190</i>
<i>Table 23 - FTIR-ATR peak identifications of methyl acetate with 5, 8 and 10wt.% of dissolved PVAc.</i>	<i>190</i>
<i>Table 24- FTIR-ATR peak identifications of ethyl acetate with 5, 8 and 10wt.% of dissolved PVAc.</i>	<i>191</i>
<i>Table 25 - FTIR-ATR peak identifications of methyl ethyl ketone with 5, 8 and 10wt.% of dissolved PVAc.....</i>	<i>192</i>
<i>Table 26 - FTIR-ATR peak identifications of PVA and catalysed (NaCl) hydrolysis products of PVAc.</i>	<i>193</i>
<i>Table 27 - FTIR-ATR peak identifications of PVA and catalysed (MgCl₂) hydrolysis products of PVAc.</i>	<i>194</i>
<i>Table 28 - FTIR-ATR peak identifications of PVA and catalysed Mg(NO₃)₂ hydrolysis products of PVAc.</i>	<i>194</i>
<i>Table 29 – FTIR-ATR peak identifications of PVA powder 99+% hydrolysed.</i>	<i>195</i>
<i>Table 30 – FTIR-ATR peak identifications of PVA film cast from 8wt.% aqueous PVA solution.....</i>	<i>195</i>
<i>Table 31 – FTIR-ATR peak identifications of a physically crosslinked hydrogel cast from 8wt.% aqueous PVA solution.....</i>	<i>195</i>
<i>Table 32 – Identification of peaks in FTIR spectra of PVA powder.....</i>	<i>196</i>
<i>Table 33 – Identification of peaks in FTIR spectra of printed PVA hydrogel.</i>	<i>196</i>
<i>Table 34 – FTIR-ATR peak identifications for printed PLA/graphene.....</i>	<i>196</i>
<i>Table 35 – FTIR-ATR peak identifications for printed PVA.....</i>	<i>196</i>
<i>Table 36 - FTIR-ATR peak identifications for printed PVA.</i>	<i>197</i>
<i>Table 37 - FTIR-ATR peak identifications for monoethanolamine.</i>	<i>197</i>
<i>Table 38 - FTIR-ATR peak identifications for printed PVA swollen with monoethanolamine.</i>	<i>197</i>
<i>Table 39 - FTIR-ATR peak identifications for printed PVA.</i>	<i>197</i>
<i>Table 40 - FTIR-ATR peak identifications for printed PVA swollen with water.</i>	<i>198</i>
<i>Table 41 - FTIR-ATR peak identifications for printed PVA swollen with monoethanolamine.</i>	<i>198</i>
<i>Table 42 - FTIR-ATR peak identifications for printed PVA swollen in neat MEA.....</i>	<i>198</i>
<i>Table 43- FTIR-ATR peak identifications for printed PVA swollen with 90% MEA 10% H₂O.</i>	<i>199</i>

<i>Table 44 - FTIR-ATR peak identifications for printed PVA swollen with 70% MEA 30% H₂O.</i>	199
<i>Table 45- FTIR-ATR peak identifications for printed PVA swollen in 100% H₂O.</i>	199

List of Equations

<i>Equation 1 – Relationship between R_v, R_u, R_2 and R_3.</i>	8
<i>Equation 2 – Rearrangement of Equation 1 to make R_u the subject.</i>	8
<i>Equation 3 – Beer-Lambert law.</i>	10
<i>Equation 4 – Nernst equation, used to calculate the equilibrium voltage of an electrolyte cell.</i>	11
<i>Equation 5 – relationship of gas sensing response between p-type and n-type SMO gas sensors.</i>	14
<i>Equation 6 – Calculation of enthalpy of transition.</i>	64
<i>Equation 7 - Relationship between spectral absorptance, transmittance and reflectance of infrared energy striking an object.</i>	65
<i>Equation 8 - Planck's law of blackbody radiation.</i>	65
<i>Equation 9 - Wien's displacement law defines the wavelength at which maximum emission occurs from a blackbody.</i>	66
<i>Equation 10 - Ohm's law.</i>	74
<i>Equation 11 - Calculation of resistivity from length, area and resistance.</i>	74
<i>Equation 12 – Calculation of conductivity from resistivity.</i>	74
<i>Equation 13 - Calculation to determine which geometric factor should be included when undertaking sheet resistance measurements.</i>	75
<i>Equation 14 – Calculation of the scattering vector (q), where n is the solvent refractive index, λ_0 is the vacuum wavelength of the laser and θ is the scattering angle (nominally 90 degrees).</i>	78
<i>Equation 15 – Stokes-Einstein equation used to calculate hydrodynamic diameter. k_B is the Boltzmann constant, T is temperature and η dispersant viscosity [332].</i>	79
<i>Equation 16 - Synthesis of WO_3 from sodium tungstate [340].</i>	85
<i>Equation 17 – Method to calculate the number of individually printed layers.</i>	136
<i>Equation 18 – Reynolds number (Re) equation, where V is velocity (m/s), D is diameter (m) and ν is kinematic velocity (m^2/s).</i>	155

List of Abbreviations/Acronyms

Abbreviation	Term
μP	Microparticle
3D	Three-dimensional
ABS	Acrylonitrile butadiene styrene
AM	Additive manufacturing
ATR	Attenuated total reflectance
BJ	Binder jetting
BSE	Back-scattered electron detection
CAD	Computer aided design
CNT	Carbon nanotube
DED	Direct energy deposition
DI	Deionised
DLP	Digital light processing
DLS	Dynamic light scattering
DMLS	Direct metal laser sintering
DSC	Differential scanning calorimetry
EBM	Electron beam melting
EBSD	Electron back-scattered diffraction
EDX	Energy-dispersive x-ray analysis
FDM	Fused deposition modelling
FTIR	Fourier transform infrared spectroscopy
GA	Glutaraldehyde
IAQ	Indoor air quality
IoT	Internet of things
IR	Infrared
IRT	Infrared thermography
LMD	Laser metal deposition
LOM	Laminated object manufacturing
ME	Material extrusion
MEA	Monoethanolamine
MJ	Material jetting
MJM	Multi-jet modelling
MO	Metal oxide

MWCNT	Multiwall carbon nanotube
NDIR	Nondispersive infrared absorption
NP	Nanoparticle
PAH	Poly aromatic hydrocarbons
PBF	Powder bed fusion
PBIH	Powder bed and inkjet printing
PC	Polycarbonate
PLA	Polylactic acid
PM	Particulate matter
PP	Plaster-based 3D printing
PPB	Parts per billion
PPE	Personal protective equipment
PPM	Parts per million
PPT	Parts per trillion
PTA	Peroxopolytungstic acid
PVA	Polyvinyl alcohol
PVAc	Polyvinyl acetate
RGA	Residual gas analysis
RH	Relative humidity
SBS	Sick building syndrome
SEM	Scanning electron microscope
SHS	Selective heat sintering
SL	Sheet lamination
SLA/STL	Stereolithography
SLS	Selective laser sintering
SMO	Semiconductor metal oxide
SWCNT	Single walled carbon nanotube
TEM	Transmission electron microscope
TGA	Thermogravimetric analysis
UAM	Ultrasonic additive manufacturing
UV	Ultraviolet
VOC	Volatile organic compounds
VP	Vat polymerisation
WHO	World Health Organisation
YSZ	Yttria stabilised zirconia

1. Introduction

1.1 Aims and Objectives

The aims of this work were as follows:

- Develop PVA hydrogels through physical and chemical crosslinking methods, investigating the effects of swelling, degree of crosslinking and environmental conditions and characterising these using SEM, TGA, DSC, FTIR, IR thermography and gravimetry.
- Synthesise functional M_xO_y NPs (WO_3) and Au via sol-gel and microwave methods that could be incorporated into the hydrogel matrix where they could be characterised for dispersion and electrochromism.
- Produce PVA/PVAc hydrogels and thin films with various organic solvents and assess drying rates therein.
- Using a 3D printer, produce gas sensor substrates using PVA, PLA and PLA containing graphene including a mixture of these materials for asymmetric layered devices, that could be assessed for hydrogel forming tendencies, incorporation, and operation for gas sensing.
- Utilise the desirable structural properties of PVA to produce thin films and hydrogels incorporating different functional NPs which could tune the emissivity (ϵ) of a surface. Characterisation and testing of these materials in laboratory and real-world settings.

The author returns to consider the extent to which these aims were successfully achieved in section 7.

1.2 Context

Society is increasingly becoming concerned with how atmospheric pollutants affect human health and quality of life [1]. The negative effects of short [2] and long-term [3] exposure to indoor [4, 5] and outdoor pollutants [6] such as carbon monoxide (CO) [7], sulphur dioxide (SO_2) [8] and nitrogen dioxide (NO_2) [9] have been studied in depth. Additionally, more attention is now being given to volatile organic compounds (VOCs) [10, 11], polycyclic aromatic hydrocarbons (PAHs) [12], particulate matter (PM), and fine particulate matter ($PM_{2.5}$) where the aerodynamic diameter is less than $2.5\mu m$ [13] which is thought to have a detrimental effect on human health [14]. Health complaints from exposure include (but are not limited to) respiratory problems [15, 16] and disease [17], premature births [18], impaired

cognitive function [19, 20], increased stroke risk [21] and in some cases premature death [22]. The World Health Organisation (WHO) reported in 2014 that one in eight premature deaths are attributable to air pollution [23].

Air pollutants arise from a wide range of sources. Indoor pollutants can originate as a result of cooking, smoking, heating, and lighting and additionally household cleaning products [24-26]. Building and furnishing materials may also contribute to the quality of air [27]. It has even been reported that newly built dwellings contain a vast array of VOCs prior to being occupied [28]. This is particularly concerning, as it is estimated that people in developed countries spend up to 90% of their time indoors, either at home or at work [29].

Outdoor pollutants are primarily linked to the combustion of fossil fuels [30, 31] for transportation, power generation and industrial use. Pollutants are not only detrimental to human health but have the potential to cause an increase in the global temperature through the greenhouse effect. Greenhouse gases are: H₂O, CO₂, CH₄, N₂O, O₃, CFCs and HFCs. The mechanism and potential consequences of this temperature rise are extremely well documented [32], if not unequivocally accepted by some politicians [33].

Pollutants can be particularly problematic in built up areas such as cities where concentrations of these species accumulate. Areas of high pollutant concentration caused by poor street design and lack of air exchange have been termed pollutant or street canyons [34]. This phenomenon is perpetuated by high population density, the effect of building entrapment, automotive traffic, and lack of green spaces. This can lead to the phenomenon of sick building syndrome (SBS) [35, 36]. SBS was considered so important that NASA investigated ways to remove or reduce the problem, given that perhaps the ultimate example of an enclosed space is a spacecraft [37]. The approach taken by NASA was to investigate plants which are able to remove atmospheric pollutants. Other areas where SBS and pollutant levels, (specifically CO₂) is being realised is in the cabin of vehicles. This is particularly problematic when concentrations rise to levels which may impair cognitive function. Guidelines established by WHO, state that permissible levels of CO₂ in enclosed spaces should not exceed 1000ppm [38], although the American Conference of Governmental Industrial Hygienist (ACGIH) set the threshold limit value (TLV) at 5000ppm (in 1946). Regardless, some studies have revealed that when air is recirculated inside a car, CO₂ levels can reach 3000ppm [39], which could affect concentration levels of the driver.

Occupationally, CO₂ levels have also found to be hazardous, even fatal to human health. Scott, et al. cite numerous examples of where acute and chronic exposure, as well as CO₂ build-up in enclosed spaces have resulted in fatal outcomes [40]. Links have also been made with the quality of outdoor air and how it affects indoor air quality (IAQ) [41]. It has also been suggested that there may be a synergy between various atmospheric pollutants, further exacerbating the effects on human health [42]. Current limits on pollutant levels set by WHO are:

Table 1 – WHO guidelines on safe exposure levels to a range of atmospheric pollutants hourly, daily or annually. PM is composed of numerous compounds and exact ppb levels cannot be given as one sample may differ from another, therefore a mean value is given [43].

	Exposure levels (µm/m ³)		Exposure levels (ppb)	
	PM _{2.5}	10 (annual mean)	25 (24h mean)	n/a*
PM ₁₀	20 (annual mean)	50 (24h mean)	n/a*	n/a*
NO ₂	40 (annual mean)	200 (1h mean)	21.2 (annual mean)	106.4 (1h mean)
SO ₂	20 (24h mean)	500 (10min mean)	7.6 (24h mean)	191.1 (10min mean)
CO ₂	1000ppm			

**PM is made up of a variety of compounds, therefore calculating ppb levels accurately is not possible.*

PM is a general term applied to particles ranging in size. PM_{2.5} refers to the particles in a cubic metre of air with an average diameter less than or equal to 2.5µm; this is known as fine particulate matter. PM₁₀ refers to particles in a cubic metre of air with an average particle diameter of less than or equal to 10µm.

It is therefore clear that effective solutions must be implemented in order to reduce the risk to public health. The solution may be thought of as two-fold.

Firstly, effective detection and monitoring of pollutant species must be achieved through rapidly responding, highly sensitive gas sensing materials, enabling users to be quickly notified when concentrations rise above acceptable limits. Industrial quality wearable gas sensors exist, but these are cumbersome, power consuming, standalone devices primarily used by people expecting a certain level of exposure, linked to the environment they are working in. Wireless gas sensors are not yet the norm; however attitudes are changing in industry, with the benefits of wirelessly networked gas sensors becoming realised [44]. This change in attitude could encourage greater attention being given to the development of smaller, lower powered wireless devices which may be used by the general public.

Exciting developments are happening with the “Internet of Things” (IoT) with some estimating that up to 7 trillion devices may be connected by 2025 [45]. The IoT is a general term given to a range of devices (electronic and mechanical) connected via the internet. Advances are being made in the type and variety of devices which may be included, with sensors making up a significant percentage of connected devices [46]. Currently, advanced devices may give an indication on air quality; however, this is often comprised of data downloaded from the internet rather than live location-specific measurements.

Early attempts have been made to develop wireless, chemically sensing devices [47]. However, these are not combined with clothing or an aesthetically pleasing medium. It is therefore clear that there is a need for small, low powered, highly sensitive and rapidly responding gas sensors which may form part of the IoT and are aesthetically pleasing, in order that consumers will want to buy them.

Secondly, an overall reduction in the volume of pollutants produced from anthropogenic sources is necessary. Newer technology for building design should be embraced [48], reducing the heating and cooling demands of industrial and residential buildings [49], implementing more efficient uses of energy [50], non-fossil fuelled modes of transportation and making greater use of renewable energy sources [51].

When combined these two approaches give both short and long-term advantages to public health. Short term advantages would be better understanding of the dynamics of air pollutants and their effects by widespread, reliable data collection. This would enable spatial and temporal distribution of pollutants to be mapped, which would enable policymakers to take more informed action to tackle this problem [52]. This combined with notifications to the user of what type and concentrations of pollutants they have been exposed to could aid in diagnosing health complaints earlier, potentially making them more treatable. The general public are becoming more engaged with the health effects of pollutants and there is a genuine demand for more detail to be obtained. Longer term advantages would be improved building and transportation design linked with better urban planning and a more widespread ability to reduce harmful atmospheric pollutants.

1.3 Current Gas Sensor Technologies

1.3.1 Background

Gas sensors with different properties and applications have been developed over many years. Current sensors technologies are based upon: electrochemical, thermal conductivity, catalytic combustion, infrared absorption, solid electrolyte, metal oxide semiconductor and paramagnetic changes [53]. These technologies may be divided into two categories: sensing via variation in electrical properties and sensing based on variation of other measurable properties [54].

Sensors may be graded on their effectiveness based on various performance criteria [55]:

- Response time – the time taken for a signal to be generated above background level by the sensor once the concentration of gas has reached the minimum sensitivity level.
- Selectivity – the ability of the sensor to detect a specific gas or mixture.
- Sensitivity – the minimum concentration of gas that a sensor can detect, this can be stated as parts per million (ppm) or parts per billion (ppb). It may also be given as a ratio of change in resistances: R_a/R_g for reducing gases and R_g/R_a for oxidising gases where R_a is the resistance of the gas sensor in a reference gas (normally air) and R_g the resistance sensor in the target gas. Sensitivity (S) is calculated as $(R_a - R_g)/R_a \times 100$.
- Recovery time – the time taken for the sensor to return to its original baseline state once the gas concentration has returned to pre-exposure levels.
- Stability – this property is two-fold. Firstly, stability is the ability of the sensor to produce reliable results for a fixed period of time. Secondly, the ability of the sensor to produce reliable results when exposed to a variety of different environments: temperature, humidity, shock, acidic/alkaline environments.

A further consideration is the susceptibility of a sensor to “cross-sensitivity”. This is where a gas different to that of the target species is present and can interfere or inhibit the function of the sensor. Three types of interference are possible:

1. Positive - the sensor responds to the target gas and the foreign species. This may indicate to the user that the target gas is present when in fact it is not or that it is present in greater quantities than is true.
2. Negative – the sensor does not respond accurately to the target gas, instead indicating that there is none present, or that it is present in smaller quantities than is true.

3. Inhibition – the sensor does not respond at all, as the foreign species blocks/inhibits the sensor which can take hours/days to recover to baseline levels, if at all.

Based on these criteria, the ideal sensor would be one which has a rapid response time, is highly selective, exceptionally sensitive down to ppb or ppt level, has a fast recovery time and has a long service life (exceedingly stable). By using nano-engineering, it is envisioned that smaller size and lower power consumption devices can be produced which encompass all of the performance criteria listed.

1.3.2 Electrochemical Sensors with Liquid Electrolytes

Electrochemical gas sensors are a mature technology with the first being developed in the latter half of the 20th century [56]. This type of sensor measures electrical current at an electrode where the target gas is oxidised or reduced. From this, the concentration of the gas may be calculated as *the signal generated is proportional to the concentration of gas present*.

Electrochemical gas sensors can comprise of two, three and occasionally four electrodes sealed in an electrolyte solution (commonly an aqueous solution of strong acids or bases). Electrochemical reactions take place at the working electrode with subsequent reactions occurring at the counter electrode to balance the system, resulting in an overall redox reaction. A signal is generated between the two electrodes, proportional to the concentration of species present. The reference electrode is kept at a constant voltage in order to maintain a fixed voltage on the working electrode.

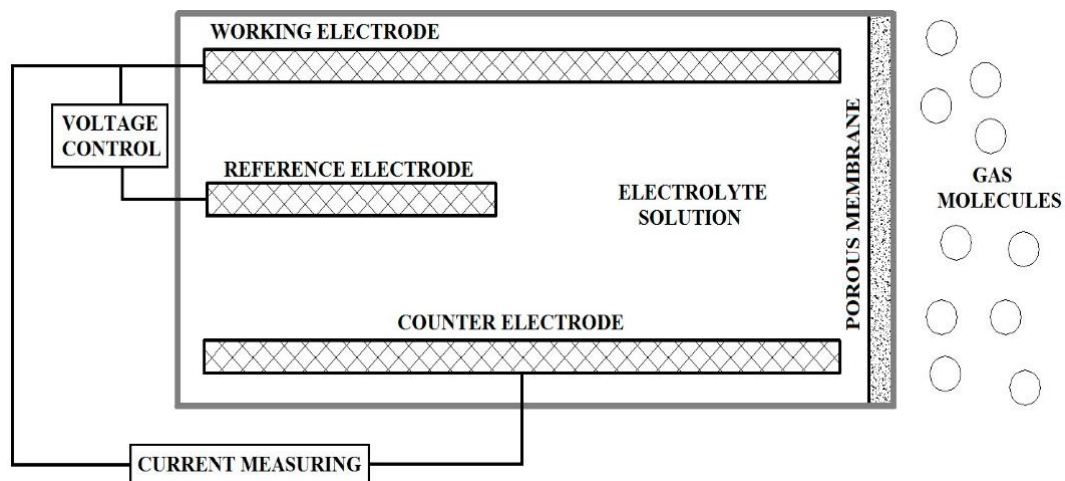


Figure 1 – Schematic diagram of a three-electrode electrochemical sensor, showing working, reference and counter electrodes [57].

Electrochemical gas sensors are commonly used in air quality monitoring, where they may detect: CO, NO₂, SO₂, ozone (O₃) and nitrogen monoxide/nitric oxide (NO) [58]. Hydrogen

(H₂) is also detectable using this type of sensor [59]. Environmental analysis may be performed using electrochemical sensors. Recent work on 2D nanomaterial-based sensors have yielded promising results for detecting heavy metal ions, organic compounds, pesticides, bacteria and antibiotics [60]. More specific uses for this type of sensor are for drug detection. Diclofenac can be detected using Au-Pt bimetallic NPs and multi-walled carbon nanotubes (MWCNTs) [61]. Sensitive detection of acetaminophen has also been reported using a phosphorus-doped graphene-based electrode [62]. Although an established technology, there is still much interest in this type of sensor, owing to the potential developments of nanocomposite electrodes and the advantages in performance this could bring [63].

1.3.3 Thermal Conductivity Sensors

Thermal conductivity sensors work by sensing changes in the thermal conductivity of a gas stream by use of a reference gas. Two resistively heated wires are situated in separate chambers and exposed to a thermally conductive stream of gas giving a stable, known resistance value. When the target gas species enters the stream, it is able to diffuse into one chamber causing the temperature of the wire to change. This is due to the reference gas being unable to maintain the temperature of the wire due to a change in thermal conductivity of the mixture. This also causes a resistance change which may be measured with respect to a reference chamber via a Wheatstone bridge.

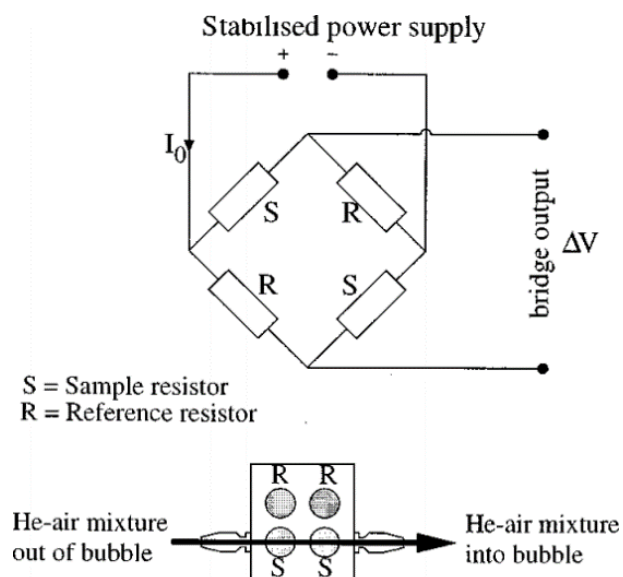


Figure 2 – Schematic diagram of a thermal conductivity sensor, also referred to as a katharometer [64].

This type of sensor has been in existence for a century [65] and has been shown to respond to a range of gases, including: CO₂, H₂, nitrogen (N₂), helium (He) and argon (Ar) [66]. Widely

used in gas chromatography [67], hydrogen safety [68], natural gas analysis may also be conducted with thermal conductivity sensors [69]. Other sectors which have benefited from this technology include automotive [70].

1.3.3.1 Wheatstone Bridge

Many sensors and analytical devices utilise a Wheatstone bridge. This is an electrical circuit designed to measure an unknown resistance extremely accurately. It utilises two legs of a bridge circuit, one with known resistances and a second with an unknown aspect.

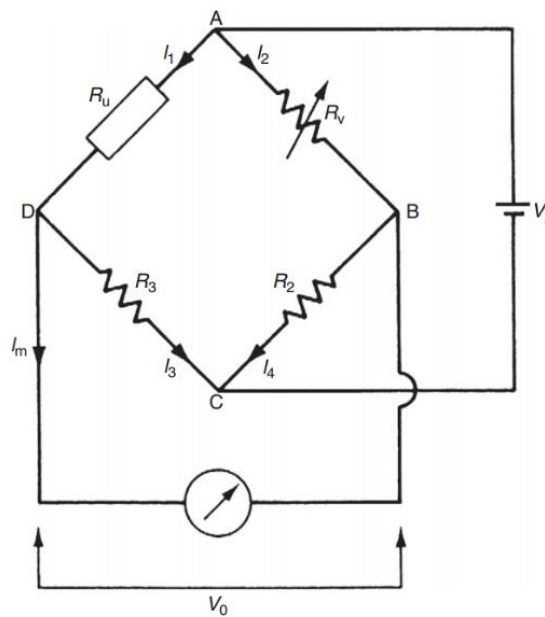


Figure 3 – Circuit diagram of a Wheatstone bridge, where R_u is an unknown resistance, R_2 and R_3 are equal value resistors and R_v is a variable resistor. V_i is a voltage applied and V_0 a measured null point voltage [71].

The variable resistor R_v is adjusted until the circuit is balanced, i.e. $V_0 = 0$. When this is true, resistances follow the relationship in Equation 1.

$$\frac{R_3}{R_u} = \frac{R_2}{R_v}$$

Equation 1 – Relationship between R_v , R_u , R_2 and R_3 .

Equation 1 may be rearranged so that R_u becomes the subject, shown in Equation 2.

$$R_u = \frac{R_3 R_v}{R_2}$$

Equation 2 – Rearrangement of Equation 1 to make R_u the subject.

This type of arrangement is common in analytical devices which rely on resistance measurements to determine the concentration of a species. Wheatstone bridges may be found

in: piezoresistive sensors [72], pressure sensors [73] and thermal flow sensors [74] to give some examples.

1.3.4 Catalytic Combustion Sensor (Pellistor)

This type of sensor consists of two elements joined by a Wheatstone bridge circuit and variable resistor. One element is inactive and referred to as the compensator (reference) element. The second element is known as the detector element. The detector element contains a catalyst bead (often rhodium) which promotes gas combustion in the presence of oxygen causing a rise in temperature above a baseline T at which the catalyst (e.g. $\text{Pt}/\text{Al}_2\text{O}_3$) is active. This increase changes the resistance of the circuit and therefore produces an imbalance, which is output as a voltage signal. The signal is then proportional to the concentration of gas present.

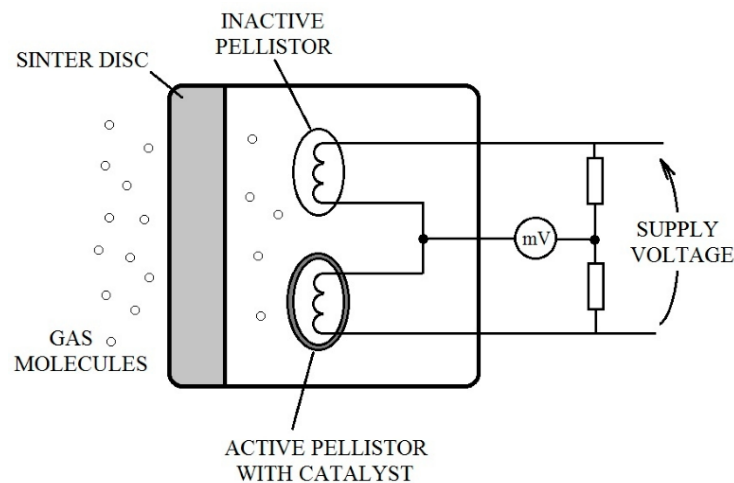


Figure 4 – Schematic diagram of a catalytic combustion sensor, also referred to as a pellistor [57].

This type of sensor requires oxygen to be present in order that combustion may occur. Gases which may be detected using this sensor include: H_2 , hydrocarbons and a range of VOCs [75, 76], which may be relevant to the problem of sick building syndrome [77]. Reliable detection of methane is also achieved via this method [78]. An example of a commercially available pellistor based sensor is Crowcon T4 portable multigas detector.

1.3.5 Nondispersive Infrared Absorption Sensors

Nondispersive infrared absorption sensors (NDIR) work on the principle that VOCs undergo characteristic absorption in the IR band of the electromagnetic spectrum. An IR source of light located at one end of a sensor cell is aimed linearly at a detector located at the opposite end. In a perfect vacuum all IR light would reach the detector. However, when target gases enter the cell they absorb radiation at wavelengths specific to their composition, thus satisfying the Beer-

Lambert law (Equation 3), where I is the beam intensity at the detector, I_0 is the initial beam intensity, k is the absorption coefficient, C the gas concentration and L the optical path length (sample cell length). This reduces the amount of light able to reach the detector. This difference may be output as an electrical signal. The decrease in IR light intensity is proportional to the concentration of gases present. An optical filter controls the selectivity of the sensor by only allowing light of certain wavelengths to pass to the detector.

$$I = I_0 \times \exp(-kCL)$$

Equation 3 – Beer-Lambert law

It is possible to include a reference cell to this type of sensor. A non-absorbent gas, commonly nitrogen fills a second cell and IR light passes through as in the first. The signal measured is the difference between the measurement and reference cells.

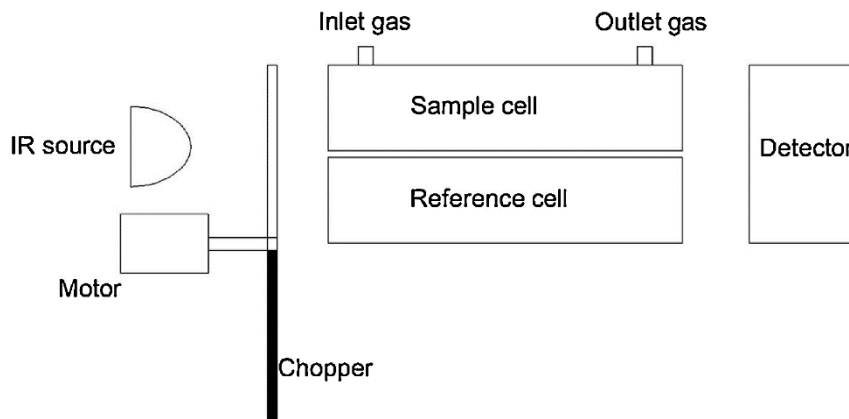


Figure 5 – Schematic diagram of a typical NDIR gas sensor including a reference cell. The part marked “chopper” is an optical device to improve the signal to noise ratio of the device [79].

This type of sensor may be used to detect CO_2 [80], which is particularly useful in breath analysis [81, 82]. Other detectable species are: ethanol [83], ethylene [84], hydrocarbon analysis [85] and additionally CH_4 and CO [86].

1.3.6 Solid Electrolyte Sensor

This type of detector has been around for many years, with commercialisation starting in the 1970’s [87]. However, this is still an active area of research, fuelled by the ever-present demand for more sensitive, better selective and faster responding gas sensors.

A solid electrolyte detector employs a material with ionic conducting properties. These properties can be classified to include amperometric, potentiometric or conductometric measurements. These types of detectors work on a similar principle, which is that the material

is sensitive to the presence of gases. One of the earliest sensors of this type is yttria-stabilised zirconia (YSZ) which has been used in car lambda (λ) or air/fuel (A/F) sensors for decades [88].

In an YSZ sensor zirconium ions may be replaced with yttrium ions which have a lower valency. This enables oxide ion vacancies (\square) to be generated. As temperature rises, it is possible for oxide ions (O^{2-}) to be transported through the structure, thus increasing the ionic (electrical) conductivity which may increase exponentially with temperature. The YSZ component is situated between two platinum electrodes with oxygen moving through the electrolyte structure in ionic form to the side with the lowest partial pressure. In doing so, up to four electrons may be transported from the platinum electrode. This is a cathodic process. The reverse may happen on the other side of the sensor: an anodic process.

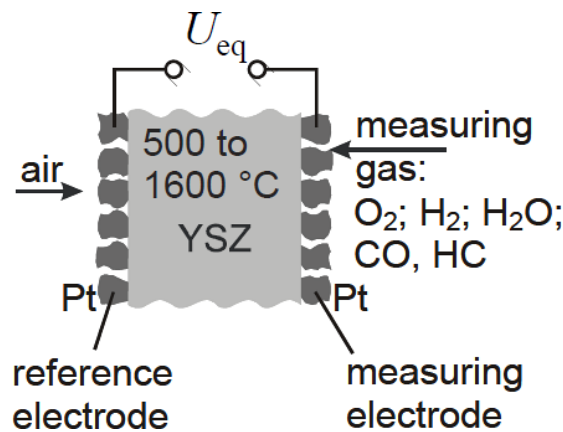


Figure 6 – Schematic diagram of a Nernst-type solid electrolyte detector [89].

The equilibrium voltage may be calculated by the Nernst equation (Equation 4), where E is the equilibrium voltage of the cell, E^o the standard electrode potential, R the molar gas constant, T the temperature, z the number of moles of electrons transferred (per mole of reaction) and F the Faraday constant. Values in the square brackets are concentrations of ions:

$$E = E^o - \frac{RT}{zF} \ln \frac{[\text{reduced form}]}{[\text{oxidised form}]}$$

Equation 4 – Nernst equation, used to calculate the equilibrium voltage of an electrolyte cell.

This type of detector is therefore known as a Nernst-type oxygen sensor. Other forms of solid electrolyte detectors work in a similar manner. Gases which are commonly detected using this method are NO_x [90], O_2 [91] which may be based on materials such as $La_{0.8}Sr_{0.2}Ga_{0.8}Mg_{0.2}O_{3-\delta}$, [92] and NH_3 which can be based on a variety of materials, including: $(Al_{0.2}Zr_{0.8})_{4/3.8}NbP_3O_{12}$ [93], $Ce_{0.8}Gd_{0.2}O_{1.9}$ [94] and even polymeric materials such as polyaniline (PANI) [95]. H_2

sensors have also been reported based on composite electrolytes [96]. Trace gas analysis has been achieved from coulometric solid electrolyte sensors [97].

1.3.7 Semiconductor Metal Oxide Sensor

Semiconductor Metal Oxide (SMO) Sensors are arguably the most studied of all gas sensor types due to their low cost and flexibility [98]. The gas sensing characteristics of semiconductors was first discovered in 1931 by P. Brauer when it was noticed that adsorption of water vapour affected the resistance of Cu_2O . Early SMO sensors were based on ZnO and SnO_2 thin films [99]. The performance of SMO sensors is largely dependent on the structure of the metal oxide and thus nanostructured materials bring exciting new prospects to this area [100].

SMO sensors may be split into two categories: n-type metal oxides and p-type metal oxides. Examples of n-type are: SnO_2 [101], ZnO [102], WO_3 [103], and TiO_2 [104] and p-type examples are: NiO [105], CuO [106], Cr_2O_3 [107] and Co_3O_4 [108]. Both types of sensor are chemiresistive; with changes in electrical resistance being observed when a target analyte is introduced. Research on n-type semiconductor gas sensors is by far the dominant area.

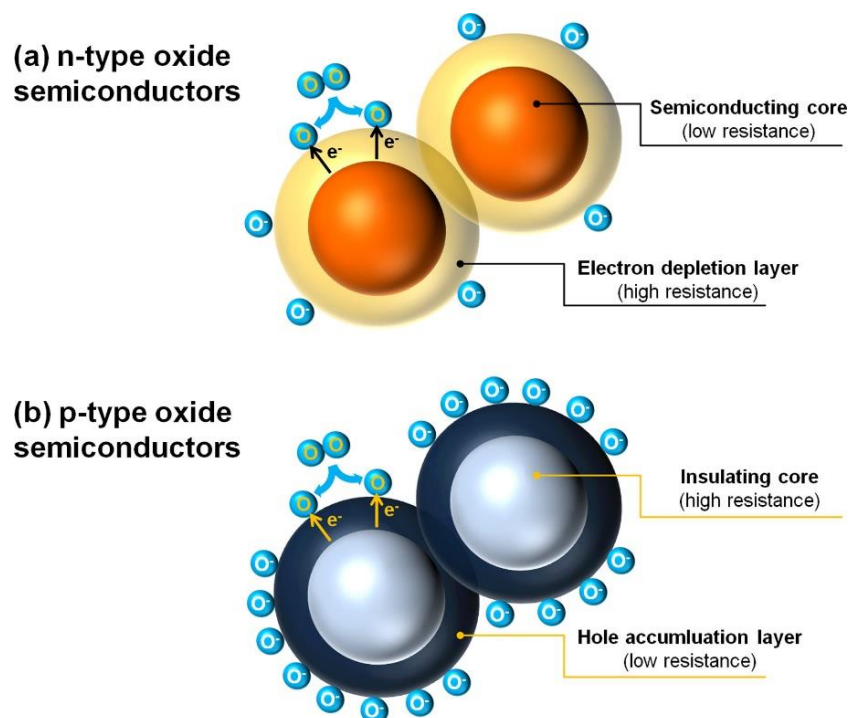


Figure 7 – Adsorption of oxygen to form an EDL in (a) n-type and a HAL in (b) p-type oxide semiconductors resulting in electrical core-shell layers [109].

The mechanism for sensing begins with adsorption of oxygen onto the surface of the oxide semiconductor in order that an electrical core-shell layer may be formed. In n-type examples this oxygen is ionised (dependent on temperature) to form O_2^- , O^{2-} and O^- as a result of electrons being taken near the surface of the semiconductor. Formation of a resistive electron depletion layer (EDL) and an n-type semiconducting region can then occur. In a p-type oxide, oxygen anions are adsorbed which results in a hole accumulation layer (HAL) forming near the material surface (Figure 7).

The mechanism by which each type of semiconductor conducts is different. In n-type oxides the resistive shell to shell contacts determine the resistance. When a reducing gas is introduced to the oxide, oxygen anions oxidise the gas. Electrons which are left over are injected back into the semiconducting core resulting in a decrease in resistance proportional to the concentration of gas present.

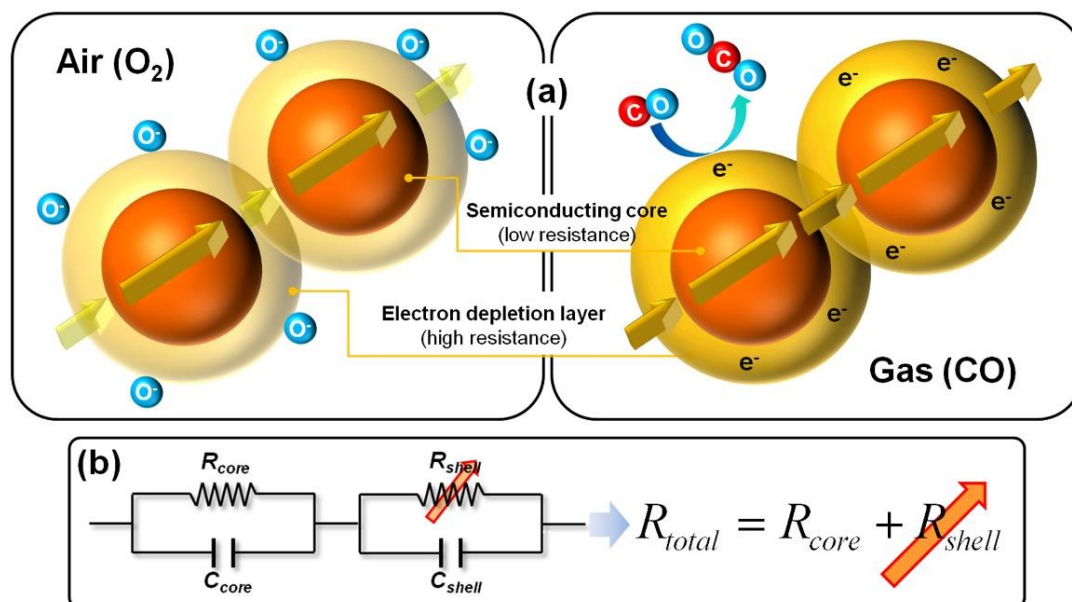


Figure 8 – (a) mechanism of gas sensing in an n-type SMO and (b) the equivalent circuit [109].

In p-type systems, parallel paths exist across the resistive core and along the semiconducting shell. There is competition between these two routes. When a reducing gas is oxidised, electrons are injected back into the material resulting in a reduction in the concentration of holes in the shell layer causing resistance to increase. There is also a consideration that if the oxide semiconductor particles are bigger than double the HAL thickness, the change in concentration of holes won't significantly alter the resistivity between particles contacts. It has been suggested by [110] that owing to the similar morphologies and that most conduction in p-

type oxides occurs along the semiconducting shells, the response of p-type semiconductor gas sensors (S_p) is equal to the square root of n-type semiconductor gas sensors (S_n):

$$S_p = \sqrt{S_n}$$

Equation 5 – relationship of gas sensing response between p-type and n-type SMO gas sensors.

Because of this relationship, development of highly sensitive p-type SMO gas sensors is challenging, perhaps partially explaining why n-type have received greater attention.

1.3.8 Paramagnetic Sensors

This type of sensor relies on the magnetic effects of oxygen, and thus is used for O_2 detection. O_2 is one of very few paramagnetic gases, meaning that it is attracted to a magnetic field, as opposed to most gases which show diamagnetic properties, i.e. they are repelled from a magnetic field. Paramagnetism is a temperature-dependent process and may repel O_2 at high temperatures.

In a typical sensor, the displacement body is arranged asymmetrically in a magnetic field generated by the field concentrators. When oxygen is introduced, it is attracted to and concentrates in the magnetic field, exerting a force on the displacement body. This results in the displacement body rotating, which may be detected using a light source, mirror and photodetector. A current is applied to the compensation coil to return the displacement body to its original position. The current required to do this is proportional to the oxygen concentration present. The main components of this type of sensor are shown in Figure 9.

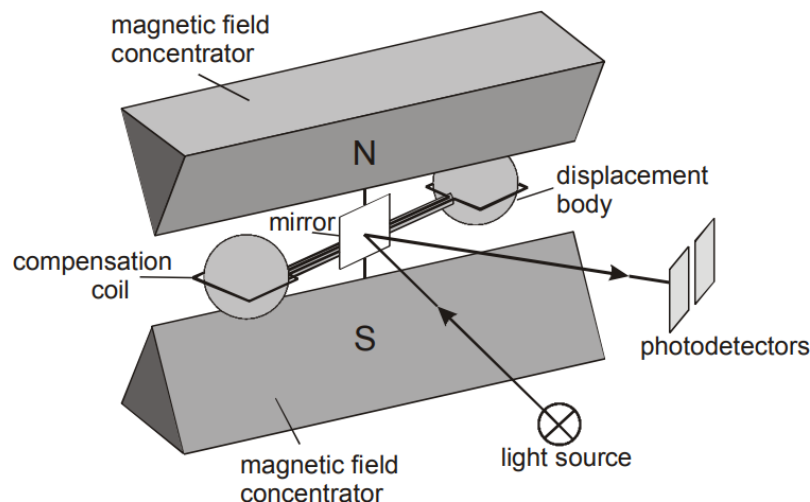


Figure 9 – Schematic diagram of a typical paramagnetic oxygen sensor [111].

Sensors of this type are normally used in industrial applications due to their reliability and maintenance free operation. Once constructed, no further calibration is required due to the absence of a chemical reaction.

Oxygen is the predominant gas detected using this technology; however there are differences in the design of sensors used [112, 113]. The Servomex OxyDetect is an example of a commercially available paramagnetic oxygen sensor.

1.3.9 Particulate Matter Sensing

With PM being recognised as a significant health concern, effective and reliable monitoring of concentration levels is essential. Various methods exist to achieve this, with perhaps the most simplistic being to collect particles via a filter, then use gravimetry to calculate weight differences. This is a type of direct measurement although more elegant and accurate solutions exist.

A tapered element oscillating microbalance (TEOM) is an internationally accepted method for measuring PM₁₀ and PM_{2.5} [114]. This device consists of an inlet of specific size drawing in particles via a vacuum pump. The particles travel to a flow splitter where the PM enters a filter connected to a vibrating glass tube. As PM is deposited on the tube the mass change causes the frequency of vibration to decrease. The frequency change is proportional to the mass of PM in the tube. Limitations of this method are susceptible to large temperature changes and mechanical noise.

Other methods used for monitoring particulate concentrations approved by the department for environment, food and rural affairs (DEFRA) are: β -attenuation analysers and optical analysers [115].

β -attenuation analysers (BAM) are widely used for detection of PM₁₀ and PM_{2.5}. β -rays from a radioactive source (typically ¹⁴C or ⁸⁵Kr) are directed at a detector which gives a baseline reading. Positioned between the source and detector is a filter onto which the PM is deposited. Particles on the filter attenuate the β -rays by absorbing some of the energy passing through. The change in energy reaching the detector is proportional to the mass of particles on the filter.

Optical analysers are based on the interaction between light (laser, IR or visible) and airborne PM. Light of known luminescence is shone at a detector. The intensity loss between the source and detector is attributable to particles scattering or absorbing the beam prior to detection. This is a type of indirect particle detector.

Overall, detection of PM₁₀ and PM_{2.5} with current technology requires either the physical collection of material or a stabilised light source and sensitive detector. A method which differs from the above and is not used by DEFRA is electrostatic precipitation which involves charging the particles then measuring the current they carry. Because of the way PM is monitored, it is unlikely the materials used in this work will be suitable for PM detection.

1.3.10 Summary of Sensor Types

A range of previous and current gas sensor technologies has been reviewed. It is evident that some areas, although well established, will continue to benefit from further research, particularly with materials in the nanoscale: notably, sensors relying on solid state structures: catalytic combustion sensors, solid electrolyte sensors and semiconductor metal oxide sensors. These types of sensors have in the past employed bulk materials; however the tide is now turning with the majority of new publications listing materials in the nano- scale due to their superior performance. These may either be nanoparticles [116], nanowires [117], nanotubes [118], nanorods [119], nanobelts [120], nanoflowers [121], nanocombs [122] or quantum dots [123]. Combinations of these types have also been reported [124].

With the vast amount of possibilities for gas sensor materials present, now is an exciting time to be involved with this area. This work will look at semiconductor metal oxide type gas sensors coupled with 3D printed substrates as it is believed that this is an area which is yet to be exploited. Some work has been conducted on the humidity and CO₂ gas sensing properties of double-layer graphene [125].

The advantages of employing 3D printed substrates are the speed of production and the tuneability of sensor size. Incorporation of functional components can be achieved; either pre-printing in the filament [126] or post printing via solvent uptake and hydrogel formation.

Disadvantages are the lack of literature surrounding how incorporation of different functional components in the filament affects the print quality. Adjustments may also need to be made to flow rate, temperature and build plate temperature to ensure successful prints.

Table 2 - Generalised summary of gas sensor types, rated by performance.

Technology	Detectable gases	Accuracy	Sensitivity	Response time
Electrochemical Sensors with Liquid Electrolytes	Electrochemically active gases (approx. 20)	±0.5ppb	0 - 10ppb	<50s
Thermal Conductivity Sensors	H ₂ , CH ₄ , CO ₂ , He	±2%	0.1%	<20s
Catalytic Combustion Sensor (Pellistor)	Combustible gases (VOC's)	±1%	1-2% Vol. CH ₄	<15s
Nondispersive Infrared Absorption Sensors	Hydrocarbon gases, CO ₂	±30ppm	20-50ppm	<20s
Solid Electrolyte Sensor	Approx. 150 different	±5ppb	10+ ppb	20-90s
Semiconductor Metal Oxide Sensor	NH ₃ , NO ₂ , CO, H ₂ , CH ₄ , O ₂ (primarily)	±0.2ppb	<1ppb	<20s
Paramagnetic Sensors	O ₂ (primarily)	±1%	±0.02%	<15s

1.4 Infrared and Optical Coatings for Buildings

The purpose of such coatings are twofold. Firstly when referring to coatings visible in the infrared region it is envisioned that these may take the form of an easy, quick drying spray. Once applied this could aid emergency services to easily identify a target building from the air or ground, especially at night. This would be particularly useful in an urban environment where navigation could be difficult. Coatings which exhibit properties in the optical region would be useful for temperature and lighting control within a building. A reflective coating could be used as a passive cooling technique in summer months, thus reducing the need for active techniques, such as air conditioning, which is highly power consuming.

1.4.1 Background

When describing the context for this project, it was stated that a holistic approach was the most favoured way to look at the issue of improving air quality; both through effective monitoring and reduction in the anthropogenic sources of air pollution. One method which is particularly attractive, is the reduction in demand for energy, which in turn would facilitate a reduction in

power generation and therefore harmful emissions. It is true to say that the infrastructure for power generation from 100% renewable sources is many decades away. The UK government has a current target to reduce harmful emissions by 80% by 2050 (from 1990 levels) [127]. This can only be achieved through a combination of renewable power generation and the adoption of more efficient uses of power.

Currently, it is estimated that buildings in Europe account for 40% of total final energy use and 36% of CO₂ emissions [128]. Much of this is through the need to heat, cool and light both industrial and residential buildings. Building construction began to address some of these heating demands by designing more airtight buildings; however this has led to the phenomenon of “sick building syndrome”.

Table 3 provides a range of technologies which may be fitted to a building in order to reduce energy demands.

Table 3 – Current technologies which may be retrofitted to a building in order to improve its efficiency and lower energy usage. Reproduced from [129].

Building retrofit technologies

Heating and cooling demand reduction	Energy efficient equipment & low energy technologies
<ul style="list-style-type: none"> • Air tightness • Building fabrication insulation • Window retrofits (i.e. multiple glazing, low energy coatings, shading systems, etc.) • Cool roof and cool coatings 	<ul style="list-style-type: none"> • Control upgrade • Natural ventilation • Lighting upgrade • Thermal storage • Energy efficient equipment and appliances • Heat recovery
Human factors	Renewable energy technologies & electrical retrofits
<ul style="list-style-type: none"> • Comfort requirements • Occupancy regimes • Management and maintenance • Occupancy activities • Access to controls, etc. 	<ul style="list-style-type: none"> • Solar thermal systems • Wind power systems • Biomass systems • Geothermal power systems • Electric system retrofits, etc.

Innovative ideas to address the temperature needs of a building are required if the energy usage is to reduce. A potential area to explore, linked to gas sensing materials is the use of functional coatings which may be applied to a surface to change the reflective characteristics. This technology is also relevant to cool roof and cool coatings.

1.4.2 Smart Windows

Smart windows are comprised of glass which has been treated with an optical coating able to dynamically change to light and temperature differences. This improves the efficiency of the window by allowing it to respond to changes in the outdoor environment. This can potentially reduce the need for artificial lighting and heating and thus reduce energy usage [130].

Many different technologies provide a route to smart windows. Some examples are, but not limited to: electrochromic [131], thermochromic [132], photochromic [133], organic light emitting diode (OLED) [134] and photovoltaic [135].



Figure 10 – Visual representation of an ideal smart window; on warm days IR radiation is reflected, but visible light allowed through and on cool days both IR and visible light may pass into the room [136].

This work is concerned predominantly with electrochromic devices which often utilise the properties of metal oxide nanoparticles. This area draws parallels with another arm of this work; SMO gas sensors. Many materials and preparations are closely linked [137]. Further crossovers exist with respect to functionalised carbon nanotubes, which have been demonstrated to exhibit electrochromism when based on polydiacetylene [138]. It is owing to these reasons' attention has also been paid to the properties of electrochromic devices.

1.4.3 Electrochromic Coatings

Electrochromism is the reversible change of the optical properties of a material when exposed to a current or electric field.

The most studied and arguably best-known electrochromic material is tungsten oxide. Tungsten oxide is comprised of octahedrally shaped repeat units, which undertake corner sharing of oxygen atoms giving an overall chemical formula of WO_3 . The crystal structure of WO_3 is shown in Figure 11.

Owing to the nature of edge sharing amongst unit cells, oxides which exhibit electrochromism are oxygen deficient. Also apparent is the presence of voids in the structure (as depicted with the blue arrow in Figure 11). These voids are of a size large enough to accommodate ions from an electric field. When a cation is inserted into the structure, electrons originating from the electrodes are also present to act as charge balancers. This influx of electrons is able to alter the valency of the metal atom centre. A photon which interacts with the tungsten oxide layer is able to drive an electron from one tungsten atom to another, meaning that optical absorption occurs. The density of inserted electrons is proportional to the number of inserted ions which controls the intensity of the absorption.

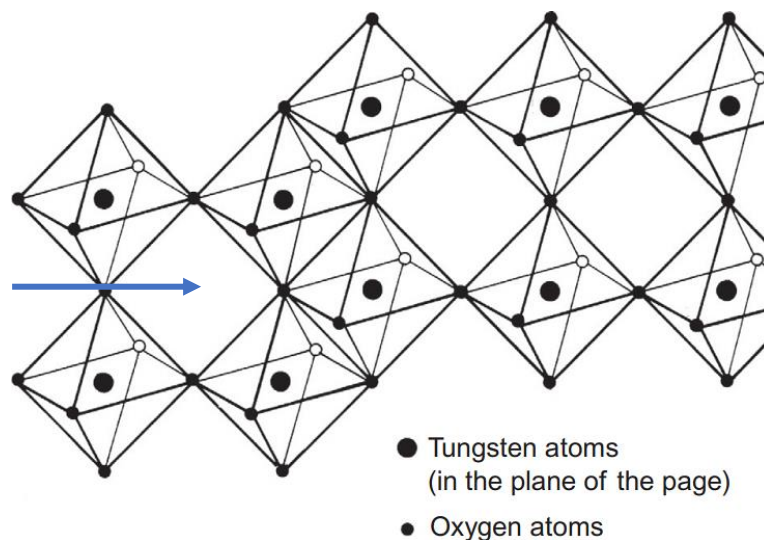


Figure 11 – Crystal structure of tungsten oxide showing the corner sharing characteristics of the oxygen and edge sharing of unit cells. Reproduced from [139].

Two types of metal oxides exist in terms of electrochromism. Firstly, metal oxides which experience charge insertion become optically absorbing (lighter). On the contrary, metal oxides which undergo charge extraction become optically reflecting (darker). A high-performance electrochromic device typically has oxides of both types as the colour change will be the same.

One will expel a charge whilst the other simultaneously accepts. An example of this is given in Figure 12.

The electrochromic properties of metal oxides may be driven by the nature of electrolyte combined with type and level of dopant. When doped with a metal, tungsten oxide may be referred to as a tungsten bronze, owing to the colour it exhibits. A tungsten bronze has the generalised formula M_xWO_3 [140], where M is an alkali metal, often sodium (Na) or potassium (K) and the value of x is $0 < x < 1$. This type of structure is an example of a non-stoichiometric compound. A prominent feature of these materials is their superconducting ability [141]. Tungsten bronzes have also been noted for their catalytic activity, with routes for low temperature synthesis having been previously studied [142]. Common synthesis routes for electrochromically active metal oxide nanoparticles are: sol-gel [143], microwave assisted synthesis [144], chemical vapour deposition [145], hydrothermal treatment [146], spray pyrolysis [147], electrodeposition [148] and thermal evaporation [149]. New routes such as annealing [150] are being investigated for large scale production with a view to supplying technology for the emerging smart window market.

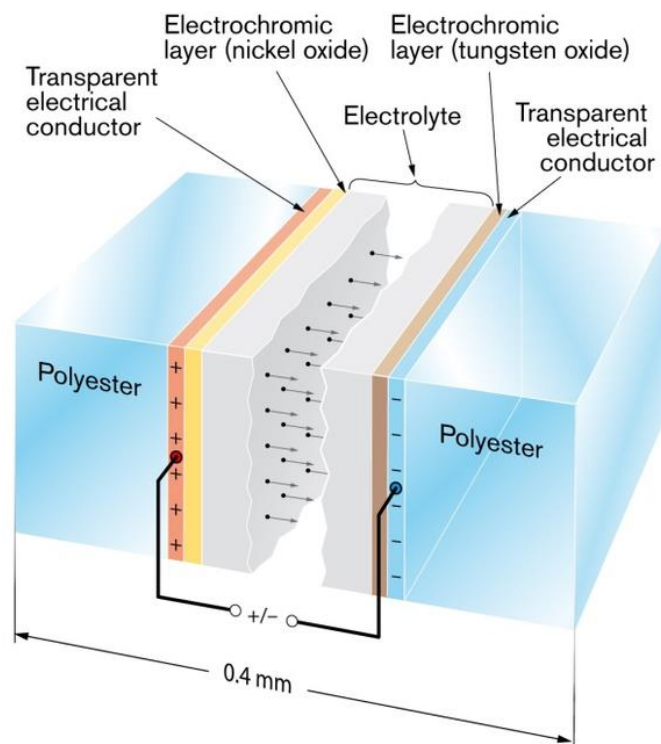


Figure 12 – Example of an asymmetric electrochromic cell; electrochromic layers on each side are formed of different metal oxides. Reproduced and adapted from [151].

Inorganic metal oxides are not the only type of materials which exhibit electrochromism. Organic electrochromics and combinations of organic and inorganic materials do exist [152].

Of particular interest are conjugated polymers due to the ease of synthesis, ability to adjust colouration and their low cost [153]. Examples of this type of electrochromic material are: poly(3,4-ethylene-dioxythiophene) (PEDOT) [154], polypyrrole (PPy) [155], polythiophene [156] and polyaniline (PANI) [157] and even combinations of these materials [158, 159].

Although there is literature on organic electrochromics, for the purpose of this work inorganic metal oxides are the preferred route to electrochromism. This is due to the many different properties this group of materials exhibits, namely gas sensing and electrochromism.

1.4.4 Hydrogels

1.4.4.1 Background

A hydrogel is a three-dimensional network of polymer chains crosslinked either chemically or physically with water dispersed uniformly throughout. The hydrophilic nature of this species is related to the functional groups present on the polymer chain. Dependent on the degree of crosslinking, hydrogels may be swollen significantly by water, but are also able to resist dissolution in water.

This is not a new area of research, with the first reference to a hydrogel being published in the 1890s [160, 161]. However, modern attention to this class of materials first began to emerge around 60 years ago with the emergence of synthetic hydrogels [162], which prompted wide interest in this highly adaptable material [163].

Hydrogels serve a wide range of functions and may be classified in different ways, with modification of a single or multiple aspect(s) resulting in the display of different, often improved properties. Mahinroosta, et al. (Figure 13) classified hydrogels by: physical structure, ionic charge, synthesis route, size, type of bond and mechanical and structural properties.

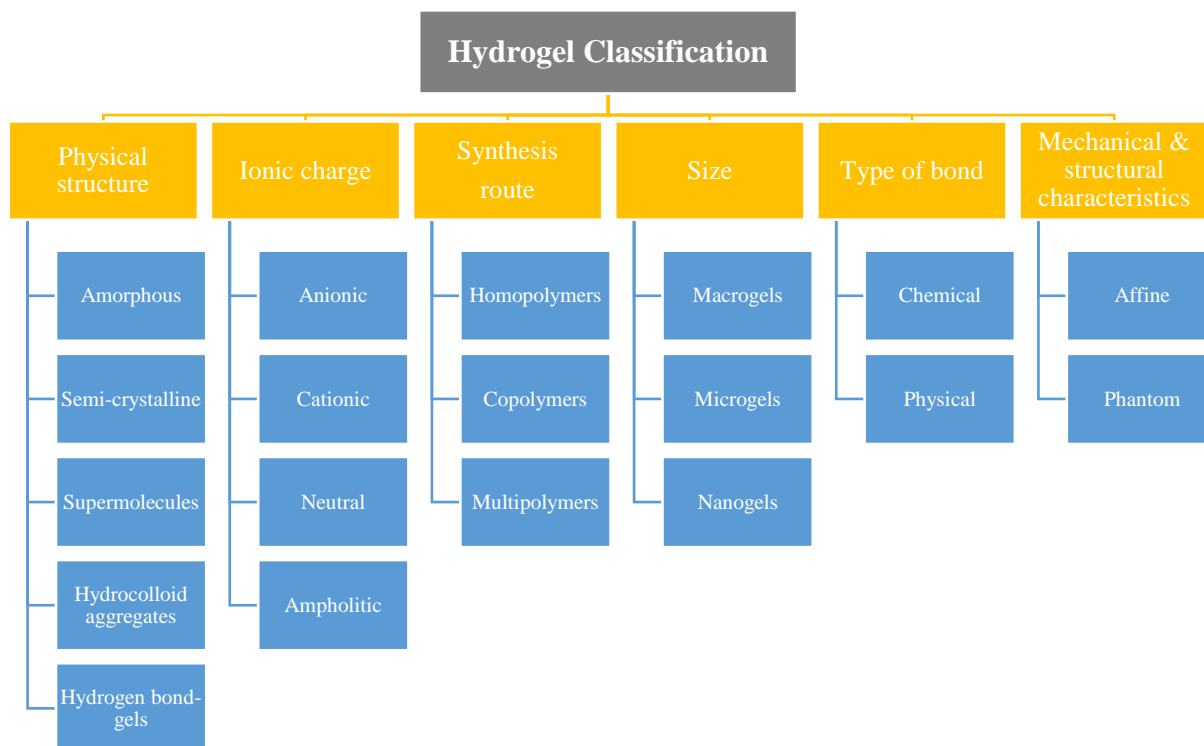


Figure 13 – Classification of hydrogels according to various features. Reproduced and adapted from [164].

Hydrogels have found uses in a wide range of applications. Owing to the biocompatibility of some hydrogels, the medical sector has been quick to utilise hydrogels in a range of applications [165], including: drug delivery [166], tissue engineering [167], regenerative medicine [168], wound dressing [169] and ophthalmic medicine [170] to name just some. Hydrogels have also proved useful in a range of sensor applications: pH sensors [171], photonic sensors [172], nitrite sensing [173] and humidity sensors [174]. Other uses include as a method to cool buildings [175], through sweating surfaces [176], wastewater treatment [177], agricultural [178] and reduction in marine biofouling [179].

It is clear that hydrogels are important in many areas, with wide-ranging applications. In this work the author was particularly interested in hydrogels for sensors and building cooling. This links with the prime motivation for his work, namely cleaner air through better pollutant sensing, combined with a reduction in energy use.

In order that the most appropriate hydrogel type and material is selected for this work, synthesis methods and materials should be considered. This is perhaps best done by looking at the two forms of crosslinking.

1.4.4.2 Physically Crosslinked Hydrogels

Physically crosslinked hydrogels are so called because they require no separate chemical species to act as a crosslinker. Instead a gel is formed using the intermolecular forces which exist between polymer chains. There are several methods used to promote interactions of this type.

Freeze-thawing is probably the simplest of all physical methods as it requires no specialist equipment. Solutions of the polymer are exposed to temperatures below the freezing point of the solvent, resulting in the formation of microcrystals as a result of hydrogen bonding. Upon thawing, these crystal structures survive in the polymer matrix holding polymer chains together around trapped solvent molecules. Depending on the degree of crosslinking desired, multiple freeze-thaw cycles may be required. The temperature range of this method is also reported to have an effect on the properties of the final gel [180].

Ionic interaction is another method of crosslinking polymers and relies on the inclusion of ions with di- or tri- valency. This method requires that the polymer chain is ionically active i.e. a polyelectrolyte. Polyelectrolytes are electrolytes containing polymers which when dissolved in an aqueous solution result in dissociation of the electrolytes, leaving a charged polymer. The oppositely charged ion, which is included, forms ionic bonds between the polymer chains, resulting in crosslinking. This method can result in hydrogels with excellent mechanical properties [181].

Complex coacervation is an additional physical crosslinking method often used to form more complicated hydrogels. This route relies on the interactions between anions and cations based on the theory that opposite charges are attracted to one another. A polyanion solution and polycation solution are mixed and dependent on pH and concentration, are able to form soluble or insoluble complexes. Hydrogels formed via this method have been used in the controlled release of drugs [182].

These methods are the most widely recognised types of physical crosslinking. Other methods, such as stereocomplexation [183] do exist, but are still reliant on the same principles of charge interaction or intermolecular forces.

1.4.4.3 Chemical Crosslinked Hydrogels

Unlike physical crosslinking which relies on interactions between polymer chains, chemical crosslinking is the result of an included crosslinker or bonding of polymer chains via other means. This type of crosslinking uses covalent bonding to join polymer chains. Advantages of this method are the ability to fine tune the level of crosslinking, by only including a finite amount of crosslinker. This method is also fast compared to the freeze-thawing method described in 1.3.4.2 and can result in gels with high mechanical strength. Disadvantages are the need for cross-linkers, which may present toxicity or biocompatibility issues.

Although “chemical crosslinking” is the generic name given to this type of bonding, chemical crosslinking is also a specific process. A cross-linker (e.g. glutaraldehyde or epichlorohydrin) and catalyst (e.g. hydrochloric acid or sulphuric acid) are reacted with the polymer chain under specific conditions, forming a covalently bonded chemical bridge between functional groups on the polymer chains. An example of this is the acid catalysed crosslinking of PVA with glutaraldehyde (GA). Hydroxy groups on the PVA chain react with the carbonyl groups on the GA molecule resulting in the formation of polar covalent carbon-oxygen bonds between the PVA and GA with the loss of water.

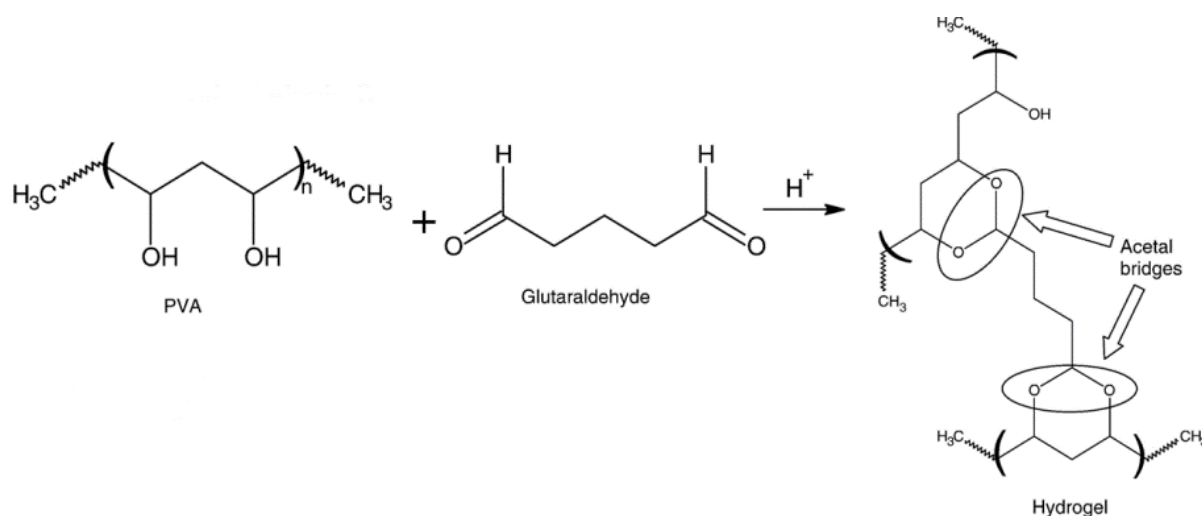


Figure 14 – Acid catalysed crosslinking of PVA with GA [184].

Other examples of functional groups which readily undertake this type of crosslinking with aldehydes are amine and carboxylic acid groups. This type of bonding is highly dependent on stoichiometry of the reactants which can result in highly tuneable crosslinking and hydrogels with different properties.

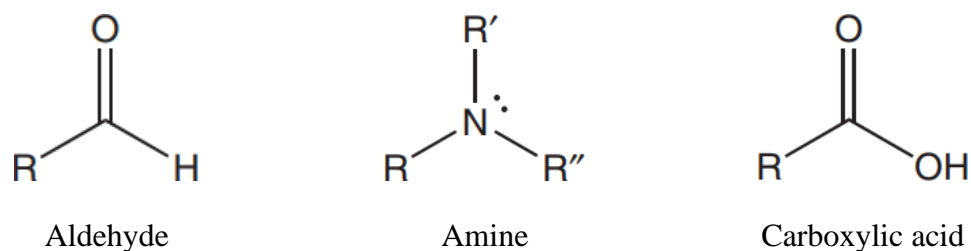
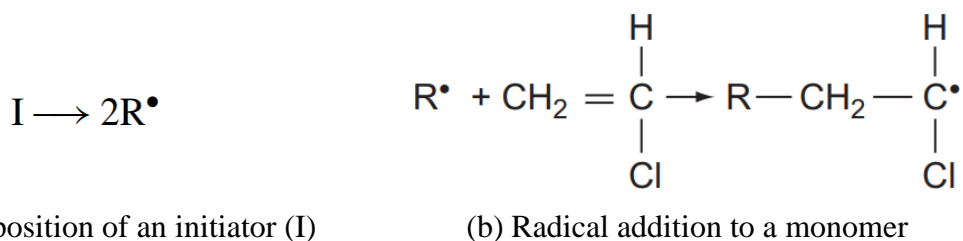


Figure 15 – Functional groups able to readily undertake crosslinking with GA [185].

One of the most common forms of chemical crosslinking is radical polymerisation. This method uses free radicals from a decomposed initiator (cross-linker) and small monomer units to construct a polymer network (Figure 16). Once a desired number of monomers have bonded to form a polymer network the reaction is terminated via the annihilation of two radicals.



(a) Decomposition of an initiator (I)

(b) Radical addition to a monomer

Figure 16 – (a) decomposition of an initiator to give two free radicals, (b) free radicals bond to monomer units [186].

Grafting is an example of chemical crosslinking which can be achieved through inclusion of a chemical reagent (chemical grafting) or through the use of an electron beam to initiate free radical polymerisation (radiation grafting). Grafting in polymer chemistry can refer to three types: grafting to, grafting from and grafting through.

Grafting to, uses a reactive polymer backbone to which pre-formed functional side chains are grafted. Grafting from, is a copolymerisation process where monomers are grafted onto a macroinitiator polymer backbone. Grafting through, is the polymerisation of monomers using an initiator. The chemical crosslinking of polymer chains to form hydrogels can be achieved using any of these processes.

Radiation grafting uses a focused beam of energy to initiate free radicals which leads to bonding of successive monomer units. By using this method, control of chain length growth and degree of crosslinking may be achieved.

Other crosslinking processes such as enzymatic reactions [187], condensation reactions and degradation exist [188], but these methods are beyond the scope of this work.

1.4.5 Summary

There is much that can be done in order to improve the thermal efficiency of buildings. This may be achieved through smart glass, which employs a range of technologies. For this work we are principally interested in exploring electrochromic coatings owing to the number of shared materials between this technology and SMO gas sensors. Electrochromic coatings can be applied to windows or other surfaces in order to control the IR and optical radiation striking it.

Secondly, passive cooling systems, such as “cool roof and cool coatings” (Table 3) may be achieved through hydrogel coatings. Many different hydrogels exist, with a range of chemical and physical methods to facilitate crosslinking, stability and controlled dehydration. Regeneration and therefore, cycling of hydrogels are also achievable. When bound in a polymer matrix, water is in the liquid state, but evaporates to vapour upon dehydration.

It is important to emphasise the coating aspect of this work and how this will be achieved with respect to the surfaces found on a building. Two types of coating are envisioned, firstly 3D printed PVA hydrogels. These will be custom made using FDM to fit on the cladding which is typically aluminium derived. Secondly electrochromically active coatings which will also be 3D printer derived. These will help tune the IR and optical light striking the hydrogels, improving the evaporation rate of guest solvent. Both aspects of work aim to passively cool the building thus reducing the need for active technologies, such as air conditioning, in turn lowering the power consumption of industrial and residential buildings.

Gas sensing is also a pillar of this work and hydrogels have been shown to be adaptable as various types of sensors. This is also true of some metal oxides which exhibit both electrochromism and gas sensing characteristics. This work will therefore focus on functional hydrogels which may incorporate metal oxide nanoparticles. From this it is hoped that a hydrogel may be tuneable to show electrochromism, gas sensing properties and work as a passive cooling device.

Finally, consideration must be given to the method of production for this type of material. It is clear that a polymeric material must be employed for a hydrogel to be formed and that this will be swollen by a solvent. It is also conceivable that this solvent may act as an electrolyte in an electrochromic cell. Three-dimensional (3D) printing has been suggested as a method to produce hydrogels [189]. Therefore, it is possible that IR and optical coatings may be produced

on-demand via a 3D printing technology. 3D printing will be pursued as a fundamental technology for the fabrication of hydrogel and gas sensor substrates for the first time.

1.5 Three-Dimensional Printing Technologies

1.5.1 Background

Three-dimensional (3D) printing is now more popular than ever, with the availability, practicality and diversity of printers ever increasing. 3D printing is based on the concept of additive manufacturing (AM) which works on the principle of creating a structure by adding material from nothing. Traditional manufacturing methods use subtractive manufacturing and create an object by removing material from a solid starting piece. 3D printing is feasible where one or more dimensions of the required structure is not less than the resolution of the printer. An example of this would be a sheet of polymer with a required thickness of 0.05mm. Often the lowest possible layer height of a FDM printer is 0.1mm, therefore this would not be a feasible item to print with this technology.

Examples of AM can be found almost anywhere, from the home hobbyist, designing items for fun to professional users printing functional parts on an industrial scale. 3D printing is widely used in the medical sector [190] with applications such as transdermal drug delivery [191], orthognathic surgery [192], cardiology [193], general surgery [194] and regenerative dentistry [195].

Other sectors have also benefitted from the maturation of 3D printing technology, notably the engineering sector. Applications of 3D printing can be found in the automotive [196], aerospace [197] and construction sectors. Use in construction is two-fold: both for functional prototypes and for manufacture of the final components [198]. Finally, and slightly closer to home, 3D printing is finding a niche within the laboratory for everyday science, particularly in analytical and separation sciences. The ability to print complex geometries with ease is improving ways of preparing and supporting samples for analysis [199].

All AM processes can be divided into seven distinct categories; however, each category may contain several different technologies [200]. Each method has advantages and disadvantages; however, most users will choose a printer type based on precision of printed models, size of model required, speed at which the model can be printed, the material(s) the model is required to be printed in (for strength, heat resistance, electrical conductivity, etc.) and the cost of the

materials involved. It is important that each technology is reviewed and the appropriate one selected for use in this work.

1.5.2 Material Extrusion

Material extrusion (ME) is the general name given to a process where a solid thermoplastic filament is heated to a semi-liquid state before being fed through specific diameter aperture at a controllable rate. A combination of movements in the X, Y and Z planes coupled with the cooling properties of the filament enables an item to be constructed layer by layer. Fused deposition modelling (FDM) is the main technology associated with ME.

Figure 17 shows the structure of three different types of plastic. Plastics used in ME are based on thermoplastic materials, with no crosslinking and only weak intermolecular forces holding chains together. Because of this property they are able to be melted and reformed making them ideal for use in ME.

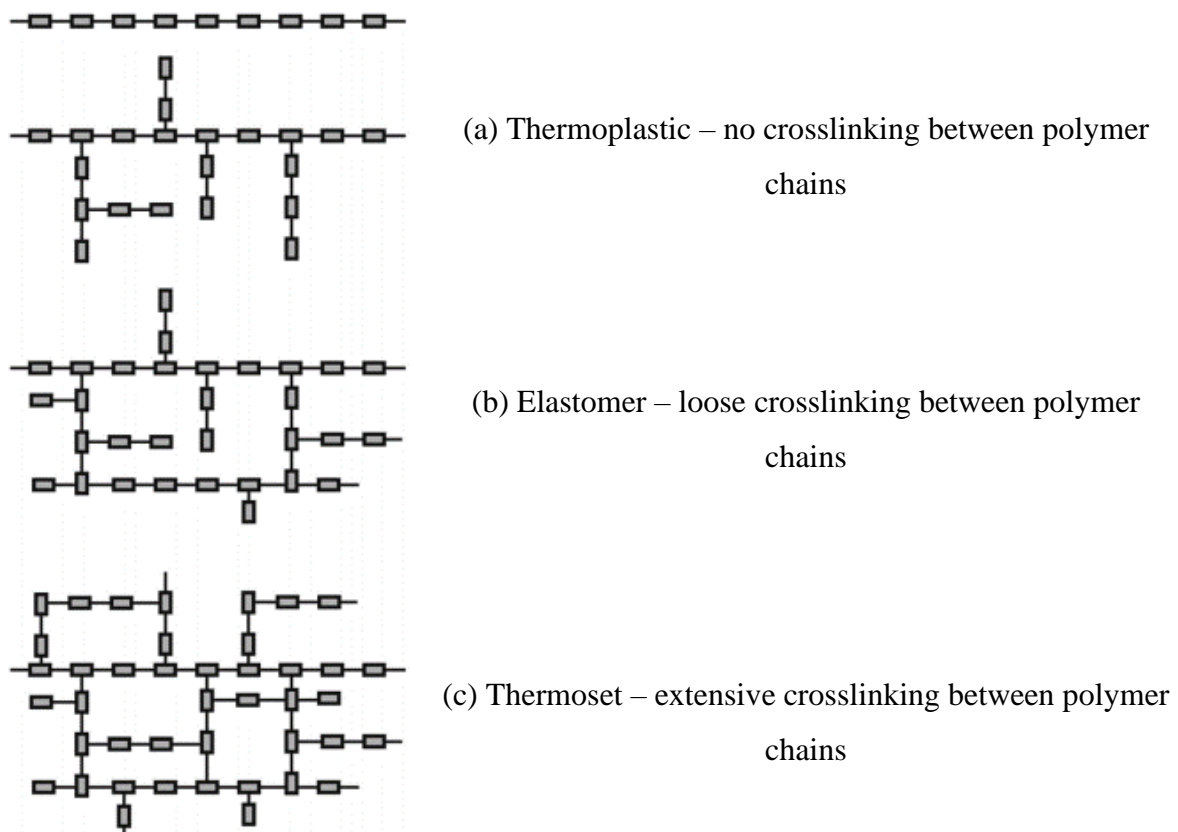


Figure 17 – Three types of plastic presented structurally (a) thermoplastic, (b) elastomer and (c) thermoset [202].

Figure 17 shows the structure of three different types of plastic. Plastics used in ME are based on thermoplastic materials, with no crosslinking and only weak intermolecular forces holding chains together. Because of this property they are able to be melted and reformed making them ideal for use in ME.

1.5.2.1 Fused Deposition Modelling

Fused deposition modelling (FDM) is a commonly used ME technique which was originally developed by Stratasys Inc. [203]. Predominantly used for functional prototypes and low quantity production, it is one of the earliest types of AM yet remains one of the most popular. This is largely due to its low cost combined with safety and efficiency; FDM is capable of processing production grade thermoplastics within a well-ventilated home or office setting.

FDM works by “fusing” streams of semi-liquid thermoplastic filament together when deposited on build plate. This is achieved by allowing each stream contact with the previously deposited one. Whilst still in a semi-liquid state the thermoplastic properties of the polymer stream allow mixing, so that once cooled they form a single continuous layer of material.

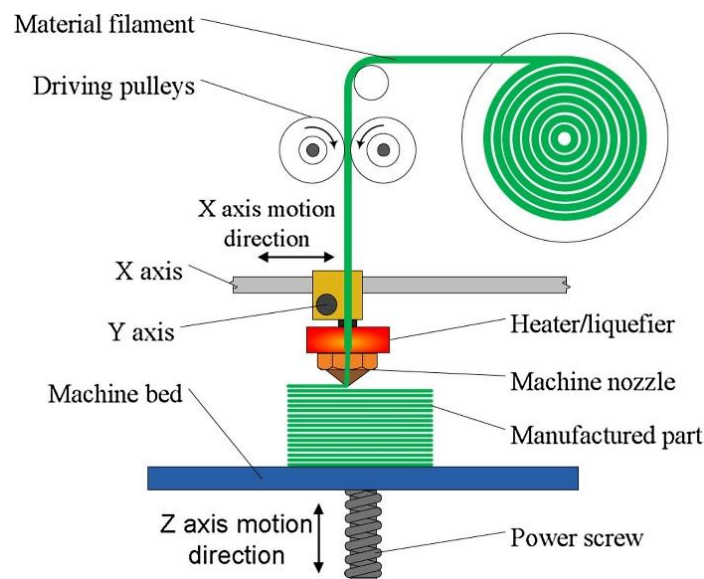


Figure 18 – Generalised schematic diagram of a simple fused deposition modelling 3D printer [204].

Advantages of FDM include the diversity of objects which may be made [205] combined with the simplicity, speed and low cost of this technology. Drawbacks include, visible layers on the finished item, weak mechanical properties and the limited number of materials available to print with [206, 207].

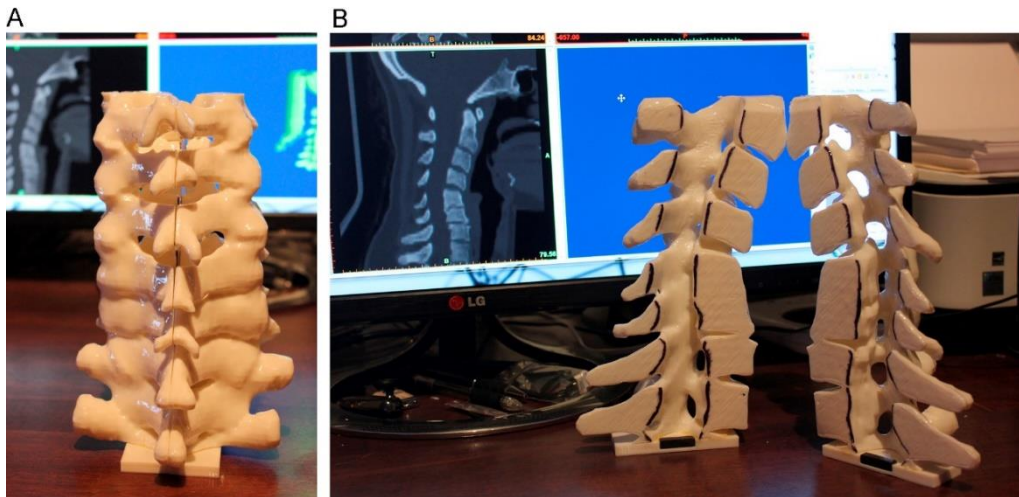


Figure 19 – 3D printed model of a cervical spine based on CT images, made from ABS and produce via FDM [208].

1.5.3 Material Jetting

Material jetting (MJ) works in a similar fashion to a traditional inkjet printer. The build material is in a liquid state and is deposited from a print head by jetting onto a build plate. The print head moves in the X and Y planes to deposit a layer, which once complete is either allowed to solidify, or cured using UV light. The build plate then moves in the Z plane in order that the next layer may be deposited. Build materials are commonly based on polymers and plastics, such as: polypropylene, high-density polyethylene and high impact polystyrene. However, other print materials, notably an aqueous ink incorporating zirconium oxide (ZrO_2) have been reported [209] for printing of ceramics.

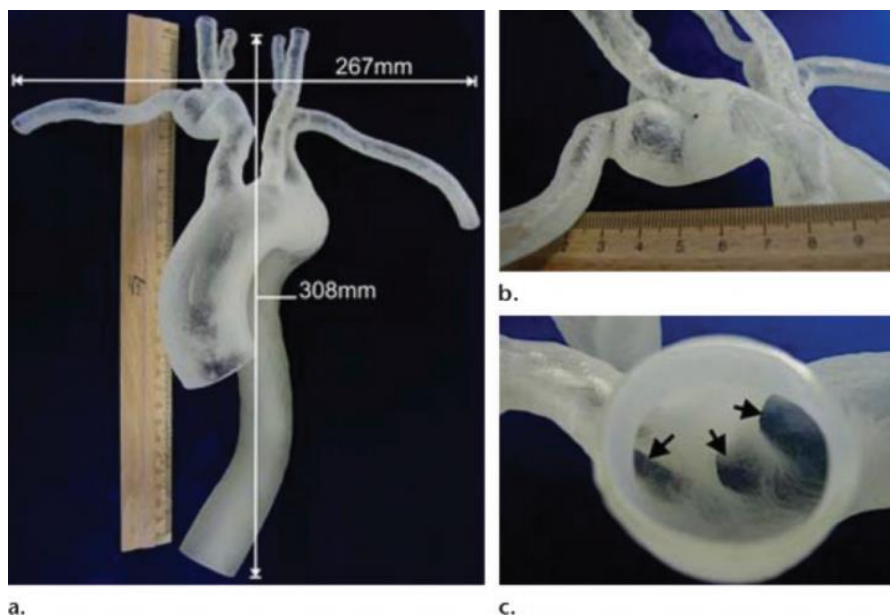


Figure 20 – MJ model of an aorta from MR angiography images [210].

Advantages of this technique are that it may be used to print complex structures; it is fast and efficient with minimal waste material. When fitted with a multi-jet head this process is known as multi-jet modelling (MJM) and may simultaneously deposit materials in a variety of colours. Disadvantages of this technique are the extensive need for support materials to be used which go to waste once the print is finished. High resolution printing may be achieved but is limited by the number of materials available [200].

1.5.4 Binder Jetting

Binder jetting (BJ) is the collective name for two different technologies: powder bed and inkjet 3D printing (PBIH) and plaster-based 3D printing (PP). Although named differently, the process behind how a model is created is the same.

BJ is the combination of two materials: a powder-based material which the final model is created from and a binder. Examples of the materials which may be used are stainless steel, glass and acrylonitrile butadiene styrene (ABS). In a BJ printer a layer of powder is spread onto the build plate, where required, an adhesive binder is deposited by a print head on top of the powder, binding the material. The build plate is then moved in the z plane and another layer of powder is diffused on top of the binder. This process repeats until the model is finished. Unbound powder is retained around the model and can be re-used.

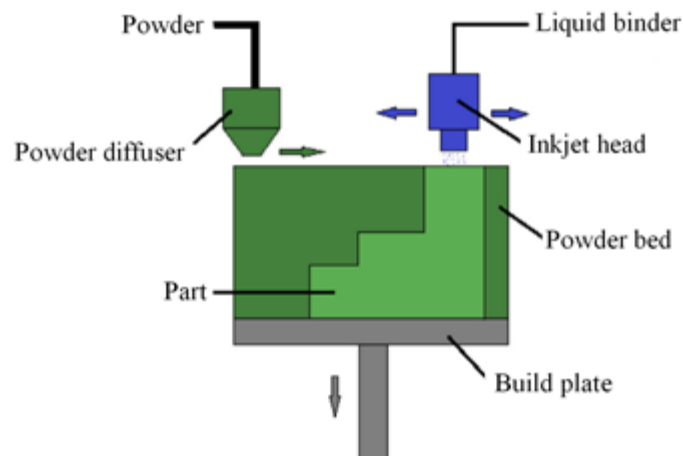


Figure 21 – Generalised schematic diagram of a binder jetting 3D printer. Adapted from [211].

Advantages of this method are the wide range of materials available and the possible mixtures of binder and powder. This method is quick but has a poor to moderate quality of finish. Disadvantages are the overall mechanical strength of the model, which due to the use of binder

can make this method unsuitable for structural parts [212]. Depending on the binder used, a long period of post print setting may be required [213].

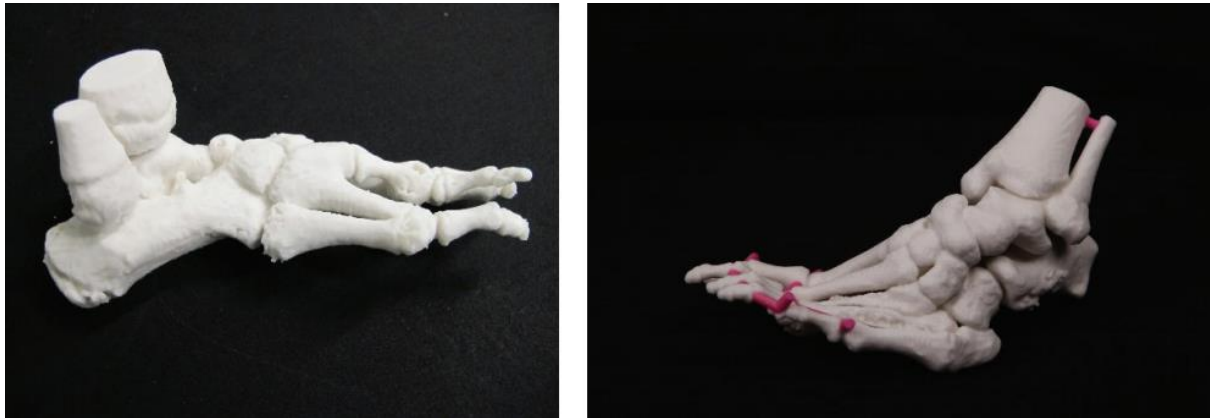


Figure 22 – Model of an ankle produced using BJ [214].

1.5.5 Directed Energy Deposition

Directed energy deposition (DED) is a 3D printing technique commonly used to include additional material or to make repairs to an existing object. This technique commonly, but not exclusively uses metallic powders to create objects. Other materials which can be used are polymers and ceramics.

DED works by feeding a substrate to the build plate where it is melted by a laser or electron beam. The laser is not confined to the X and Y planes as in other techniques and may move upon 4 or even 5 axes. Models are created layer by layer as the material solidifies.

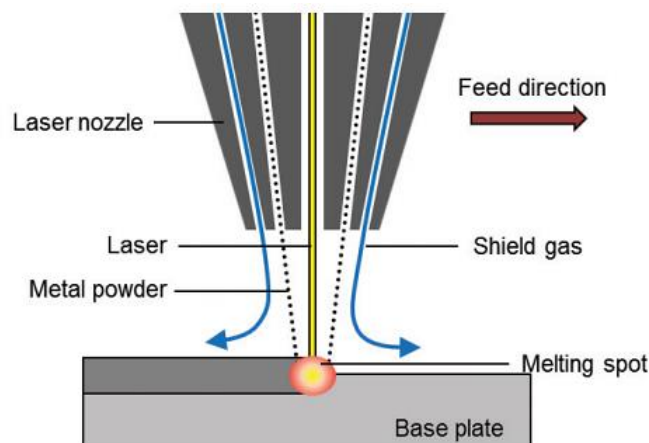


Figure 23 – Schematic diagram of the directed energy deposition method [215].

Advantages of this method are the ability to make repairs to an existing object and to create mechanically functional parts. Other advantages include the ability to print metallic items with a high level of accuracy. Disadvantages include the need to undertake further processing of the

part after creation to improve the quality of the finish. This technique is also fairly specialised and has not yet advanced into mainstream use [216].

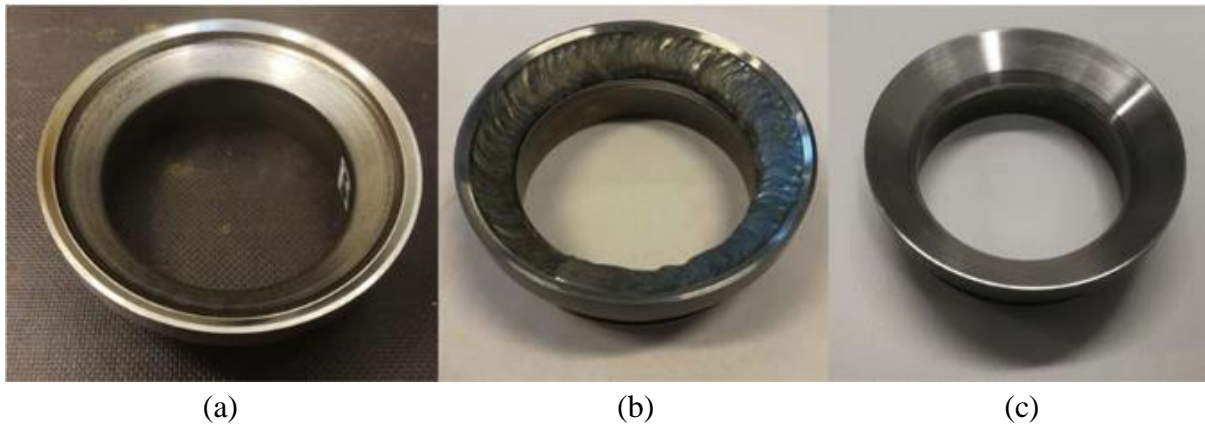


Figure 24 – DED produced seat ring (a) original part, (b) new part produced by DED (c) new part after further processing and improvement [217].

1.5.6 Powder Bed Fusion

Powder bed fusion (PBF) is a collective name given to a range of technologies which all utilise a similar mechanism. All of these processes use either a laser or electron beam to melt or fuse a powder together. Once one layer has been fused, a roller deposits the next layer of powder ready for melting. The differences in technologies relate to the powder material or the heating process.

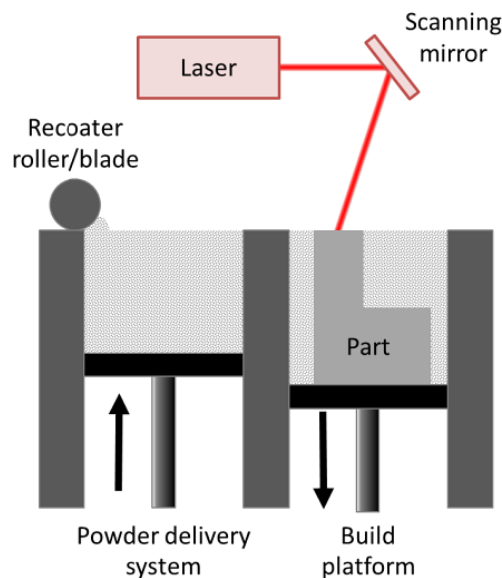


Figure 25 – Generalised schematic diagram of the powder bed fusion method; specifically, selective light sintering [218].

1.5.6.1 Electron Beam Melting

In electron beam melting (EBM) a vacuum is required so that the beam may be focused. EBM is predominantly employed to create functional parts using metals and alloys. Advantages of this method are that there are no voids within the final product. Therefore parts have full mechanical strength and this technique is also fast. Disadvantages are the high cost associated with the printer and materials, making it only suitable for industrial use.



Figure 26 – a selection of items produced by EBM [219].

1.5.6.2 Direct Metal Laser Sintering and Selective Laser Sintering

These techniques use the same sintering process, but different materials and these may be combined. Selective Laser Sintering (SLS) produces objects from plastics and polymers which originate in powder form. A laser selectively sinters parts of the powder joining it together molecularly. Direct Metal Laser Sintering (DMLS) uses exactly this technique, although employs higher temperatures to sinter metal powders rather than plastic ones. A third technique known as selective laser melting (SLM) goes further and actually melts the parts together removing voids.



Figure 27 – S-shaped aluminium tube made by DMLS [220].

Advantages of these techniques are relatively low cost combined with a wide range of suitable starting materials. Disadvantages are the lack of mechanical strength. The quality of the finish is also highly dependent on the powder grain size.

1.5.6.3 Selective Heat Sintering

Selective heat sintering (SHS) differs somewhat from the other three technologies in the sense that it does not use a laser to melt powder. Instead a heated print head travels across each layer of powder selectively melting areas to make up the model. As with the other techniques a roller deposits the next layer of powder and the build plate lowers in the Z plane. SHS can produce objects from thermoplastics, but not metal. Advantages of this technique are a much lower cost than SLS, DMLS and EMB. However, this technique is much slower than the other three and has limitation on the size of model which may be produced.

1.5.7 Vat Polymerisation

Vat polymerisation (VP) encompasses two technologies, which although follow the same principle, can result in different quality levels of finish. VP produces objects layer by layer and consists of a container filled with a liquid photopolymer resin and an UV light source. This light source is able to cure the photopolymer selectively as the build plate moves the model down ready for the next layer to be cured.

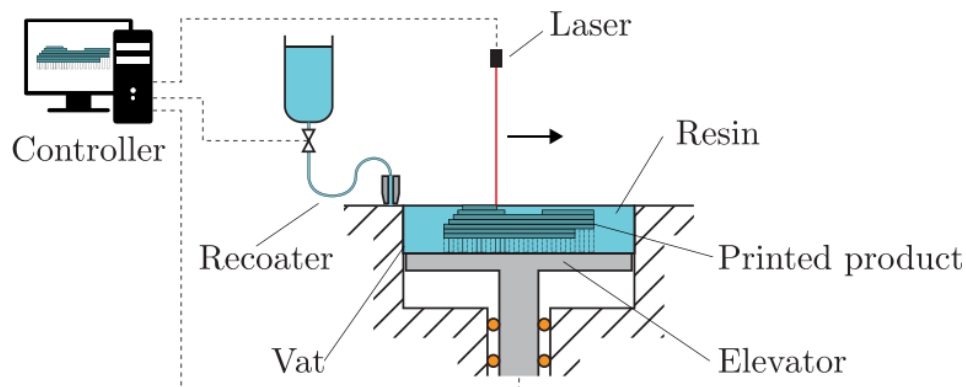


Figure 28 – Schematic diagram of a vat polymerisation 3d printer; specifically using the stereolithography method [221].

Two technologies are used in VP, firstly stereolithography (SLA) which uses a laser emitting UV light to cure the photopolymer selectively. An advantage of SLA is the ability to give a high level of accuracy combined with a good quality finish. However, this technique is expensive. The second technology is digital light processing (DLP) which uses a digital projector screen to flash the entire photopolymer layer at once with an image of the item being

printed. This method is cheaper than SLA and is more versatile, with a wide range of bulbs available with different intensities and wavelengths. However, the quality of the finished item is not as good as SLA.



Figure 29 – SLA produced model of conjoined twins showing blood vessels. This type of model is particularly good for surgical reconstruction and diagnosis [222].

Overall VP is able to produce large models quickly, with good quality finishes. Disadvantages include the limited types and cost of photopolymers available. Post-processing is also required to remove excess resin, potentially making this an untidy technique with additional health and safety concerns.

1.5.8 Sheet Lamination

Sheet lamination can be divided into two different processes: laminated object manufacturing (LOM) and ultrasonic additive manufacturing (UAM). This process works by combining consecutive layers of material through use of adhesive (LOM) or ultrasonic welding (UAM). Material is fed from a spool at one side of the build plate to one on the opposite side. A laser or cutter creates a shape, adhesive is applied, and the material is moved on ready for the next layer to be applied. This continues, layer by layer until the object is made. The need for a “cutting” step means that this method is a combination of additive and subtractive manufacturing, so not strictly 3D printing.

Models created in this way have very low mechanical strength and are only used for aesthetic items. LOM predominantly uses paper as a build material, whereas UAM can use a variety of metals, including copper, aluminium and titanium.

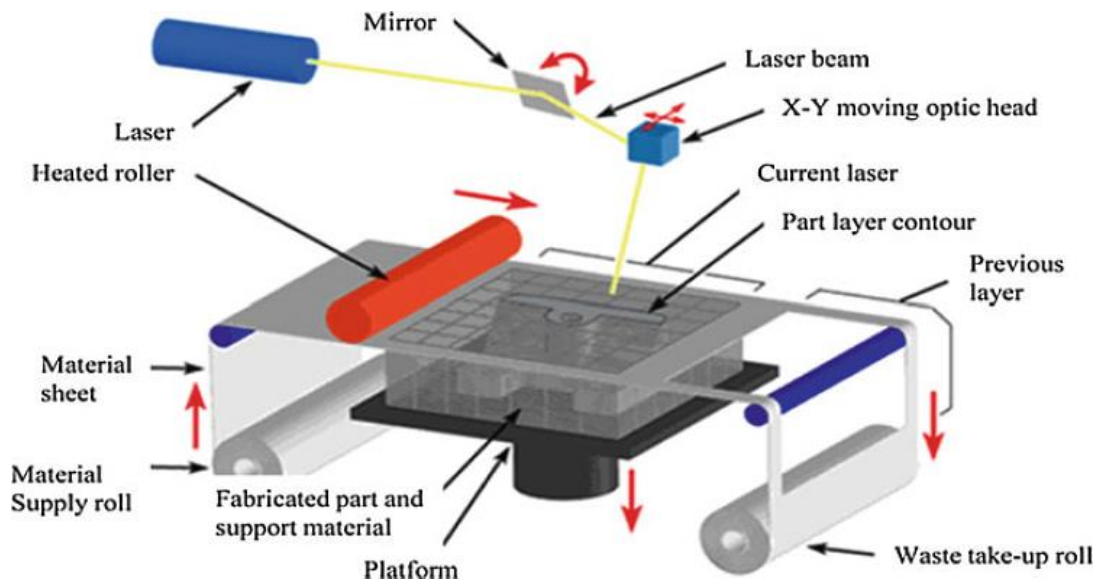


Figure 30 – Schematic diagram of a sheet lamination process; specifically, laminated object manufacturing [223].

Advantages of LOM are low cost and speed of manufacture attributable to the way the model is cut, i.e. only the outline of the shape not the entire plane. Disadvantages is the poor quality of the finish, which due to the accuracy of cutting may require significant post-processing to be of an acceptable standard.

1.5.9 Summary of Technologies

It is evident that 3D printing technologies are wide ranging, both in the number and type of methods available and the materials they are able to process. For this project preference must be given to technologies which have a proven record in producing models which are electrically conductive. Attention must also be given to the type and variety of materials which a technology can process. This work has little interest in methods which can only process metallic starting materials. Moreover, materials which can be used as substrates for further chemical processing, either pre, during or post printing are the most desirable.

Based on this assessment, FDM is the most appropriate technology to meet the needs of this project. Of particular interest are the materials polyvinyl alcohol (PVA) and polylactic acid (PLA), which may be easily processed by FDM. This technology is also financially viable for this work.

Further adaption of this method may be achieved by the inclusion of a paste extruder. This allows custom mixtures to be extruded from the existing print head and is a potential route to printing electronically conductive materials.

Table 4 - Standard terminology for additive manufacturing technologies, reproduced from [201].

Additive Manufacturing Categories	Additive Manufacturing Technologies
Material Extrusion (ME)	Fused Deposition Modelling (FDM)
Material Jetting (MJ)	Multi-jet Modelling (MJM)
Binder Jetting (BJ)	Powder Bed and Inkjet 3D Printing (PBIH) Plaster-based 3D Printing (PP)
Directed Energy Deposition (DED)	Laser Metal Deposition (LMD)
Powder Bed Fusion (PBF)	Electron Beam Melting (EBM) Selective Laser Sintering (SLS) Direct Metal Laser Sintering (DMLS) Selective Heat Sintering (SHS)
Vat Polymerisation (VP)	Stereolithography (SLA) Digital Light Processing (DLP)
Sheet Lamination (SL)	Laminated Object Manufacturing (LOM) Ultrasonic Additive Manufacturing (UAM)

1.6 Materials of Interest

The process of identifying suitable materials must consider a number of factors. Firstly, the project is to incorporate 3D printing for the gas sensor substrate. It is therefore sensible to consider 3D printing technologies and the materials they are able to use. Secondly, substrates will need to be chemically treated dependent on the target analyte being investigated. Materials will also need to be electrically or ionically conductive with good chemical stability. High surface area is also desirable as this is directly linked to gas sensor sensitivity; therefore materials in the nano-scale are considered. Coatings that are to be applied in the environment should be green and non-toxic or have low toxicity so that they may not affect wildlife or leach into the aquatic environment once dispensed with. Consideration must also be given to the method of application used for the coating and what personal protective equipment (PPE) users may or may not use. Overall, it is highly desirable for base materials to be chemically stable, non-toxic, environmentally friendly and biodegradable.

There are a number of other useful applications which share the same base materials as gas sensors; such as the development of infrared and optical coatings. Various coatings can be found which alter or tune the surface properties of a material. These can be particularly important in both civil and military applications. Civil uses may include medical, architectural and maritime, whilst military uses could include: surveillance, stealth or tagging. It is therefore clear that the materials being developed will be useful and will have greater performance capabilities than the present generation.

The materials chosen for use in this project all satisfy one or more of the strands of research. Polymeric materials PVA and PLA are both ubiquitous in 3D printing. PVA hydrogels are common and so it is feasible that 3D printed PVA could be adapted into hydrogel form. PLA has been incorporated with graphene previously and with the gas sensing properties of graphene well known, this opens up the possibility of a 3D printed PLA/G gas sensor. Furthermore PLA is a biodegradable polymer, thus contributing to the green credentials of this project. Both PVA and PLA are durable and tough polymers which is an ideal property when one considers the environment these materials will ultimately be exposed to; namely the outside of a building and the variety of weather conditions possible.

Graphene and CNTs have a vast amount of literature supporting their use as gas sensing materials, it is for this reason they are interesting. Also considered is the surface area of graphene and the importance this has on the sensitivity of gas sensors.

Finally tungsten trioxide is often hailed as the original electrochromic material and so there is logic in utilising this class of metal oxide. Literature exists to support the synthesis of nanoscale particles and so high performance electrochromic coatings are possible.

1.6.1 Polyvinyl Alcohol

Polyvinyl Alcohol (PVA) is a synthetic polymer commonly derived from polyvinyl acetate through partial or full hydroxylation. PVA was first prepared by W. O. Herrmann and W. Haehnel in 1924 via saponifying polyvinyl esters with stoichiometric amounts of caustic soda solution. Further work in 1932 by W. O. Herrmann, et. al. yielded the method still in use today.

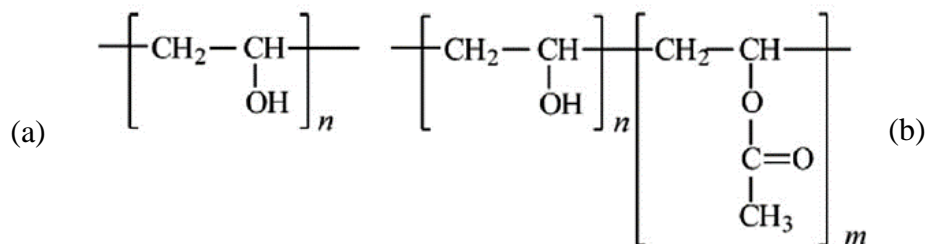


Figure 31 – Structure of (a) 100% hydrolysed PVA (b) partially hydrolysed PVA [224].

Unlike other polymers, PVA is not produced from its corresponding monomer. Vinyl acetate undergoes free radical polymerisation to form polyvinyl acetate (PVAc). PVAc is then treated with methanol (CH₃OH) and sodium hydroxide (NaOH) to remove acetate groups replacing with alcohol.

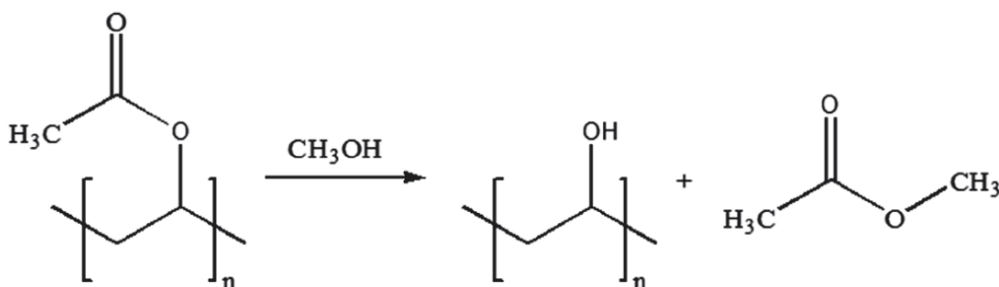


Figure 32 – Reaction schematic of hydrolysis of PVAc to PVA [225].

PVA is biocompatible, non-toxic and water soluble. It is also commonly used in 3D printing as a soluble support material. PVA hydrogels are common and have been used in a wide range of applications. It is for these reasons that PVA is an attractive material to this project.

1.6.2 Poly Lactic Acid

Poly lactic acid (PLA) is a biodegradable and renewable bioplastic which exhibits thermoplastic properties, commonly produced from corn-starch and sugar cane. PLA is an aliphatic polyester which requires further polymerisation of the *L* and *D* isomers for high molecular weight polymer chains to be produced.

PLA is commonly used as a 3D printing filament owing to the ease by which it may be used. FDM 3D printers in particular are able to process this material well. There is also literature to suggest that PLA/graphene hybrid materials may be produced [226], which would be an interesting route to produce 3D printed gas sensing materials due to what is already known about the gas sensing characteristics of graphene.

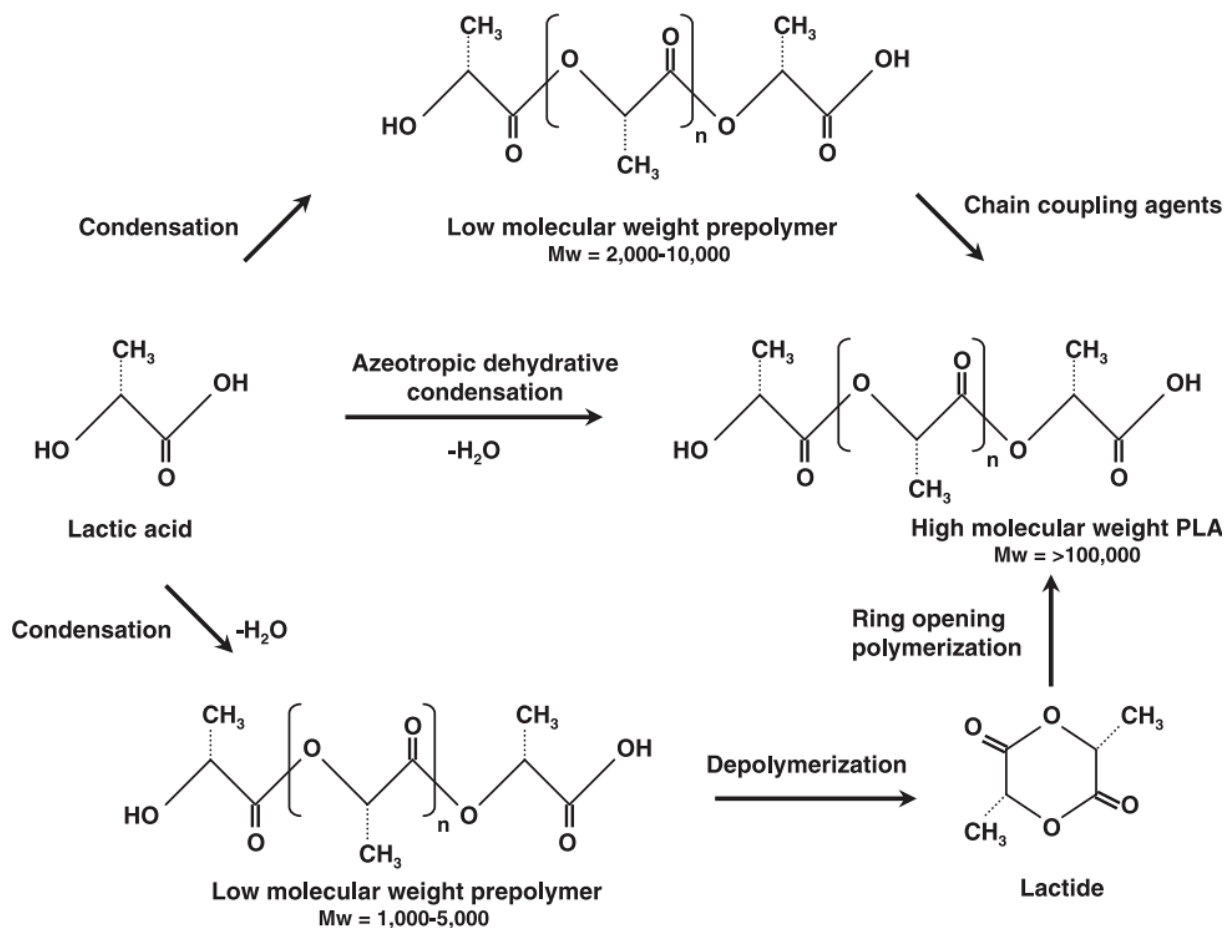


Figure 33 – Possible synthesis routes to producing high molecular weight PLA [227].

1.6.3 Graphene

Although theorised about and produced inadvertently for years, graphene is a material which has attracted colossal multidisciplinary attention for more than a decade since the first high-quality isolation by Novoselov and Geim in 2004 [228]. Structurally, graphene is comprised of two dimensional, hexagonally shaped patterns of sp² bonded carbon atoms. This arrangement gives an exceptionally high theoretical surface area of 2,630 m² g⁻¹. Graphene exhibits a thermal conductivity of 5,000 W m⁻¹ K⁻¹ and an electrical conductivity of 6.4 x 10⁶ S cm⁻¹. This combined with high physical and mechanical strength, a Young's modulus of approximately 1,100GPa makes it a highly desirable material [229].

Graphene can be produced in many forms depending on the desired application. Single-layer (SL), few-layer (FL) and multi-layer (ML) are common arrangements.

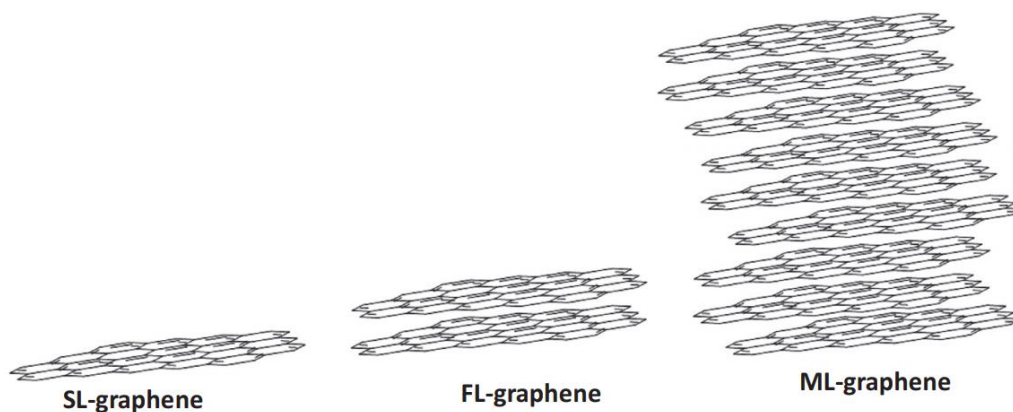


Figure 34 - Visual representation of single-layer (SL), few-layer (FL) and multi-layer (ML) arrangements of graphene shown on the atomic scale (approximately 100nm).

Single planar sheets of graphene may be manipulated to form other structures; commonly formed structures are carbon nanotubes (CNTs), graphite and spherical fullerenes (Buckyballs). Chemical modification of graphene can be undertaken to attach functional or reactive groups which may act as a link to biomolecules or other ligands. Complex modification is often required to retain the conductive nature of these unsaturated graphene sheets; however if done successfully, exploitation of the unique properties of graphene combined with enhanced functionalisation can be achieved.

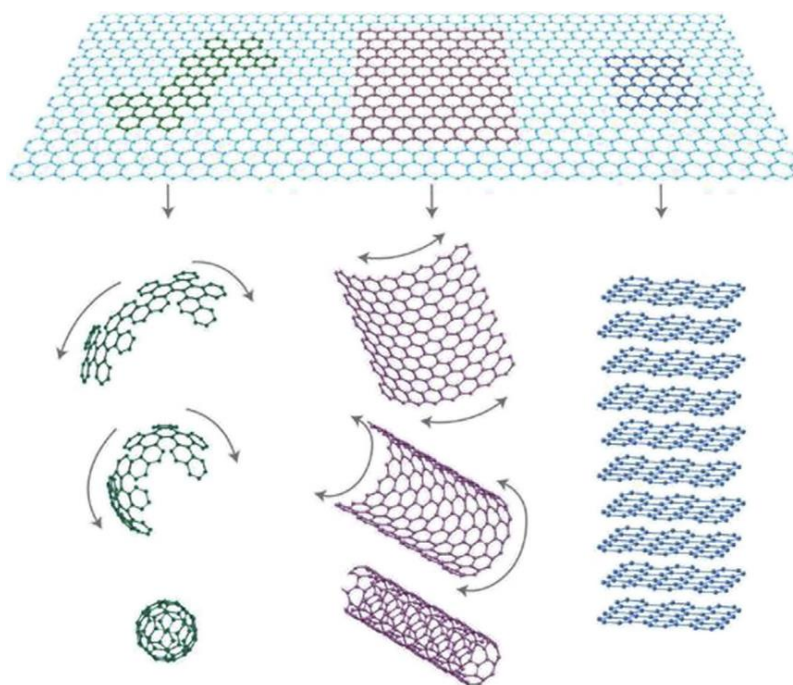


Figure 35 - Common modifications of planar graphene [230].

Graphene is of interest due to the properties listed above: its massive surface area makes it ideally suited to gas sensor applications, particularly for sensing single molecules. Traditional solid state, bulk sensors lack the fine sensitivity to detect very low concentrations or single

molecules and intrinsic noise is caused by fluctuations due to thermal motion of charges and defects. This noise is greater than the signal generated when a single molecule is adsorbed onto a traditional gas sensor surface. The result is that the signal gets lost within the noise and is undetectable [231]. This is a major limitation of traditional solid, bulk sensors making it impossible to reach very low resolutions. However, it has been reported that graphene does not suffer from similar levels of background noise. Molecules being adsorbed have a more pronounced effect on the electrical properties of graphene; this combined with very low levels of intrinsic signal disturbance, enables parts per billion (ppb) and parts per trillion (ppt) levels of detection to be reached, within the capabilities of single molecule detection [232].

Graphene has several advantages over traditional gas sensors, perhaps firstly the gas sensing mechanism it uses. A gas molecule undergoes absorption, adsorption or desorption at the surface; this causes the conductivity of graphene to be changed significantly. The gas molecules act as electron donors or acceptors interrupting the electrical conductivity which is easily detected using a four-probe measurement in the case of planar graphene. Four-point conductivity measurements are a huge advantage allowing for low contact resistance. Furthermore, graphene has very few crystal defects when compared to traditional gas sensors; this gives an exceptionally low level of excess noise enabling much lower and more accurate levels of detection. Finally, graphene is a two-dimensional structure giving it a massive surface to volume ratio. These advantages promote graphene as an ideal candidate for use as a gas sensor, particularly in applications requiring very low levels of detection and possibly able to detect single molecules. It is also possible to combine graphene with traditional 3D printer filaments [233, 234], which would enable utilisation of another new technology. For these reasons' graphene has been identified as a material of significant interest.

1.6.4 Carbon Nanotubes (CNT)

Graphene comes in many forms; planar sheets may be processed further for other forms to be constructed. A common form of graphene is carbon nanotubes (CNTs) which are widely used and now ubiquitous in the field of nanomaterials. A single sheet of planar graphene may be wrapped into a tubular shape to form a single wall carbon nanotube (SWCNT).

Conversely, multiwall carbon nanotubes (MWCNTs) may be formed by wrapping subsequent layers of graphene around the initial layer.

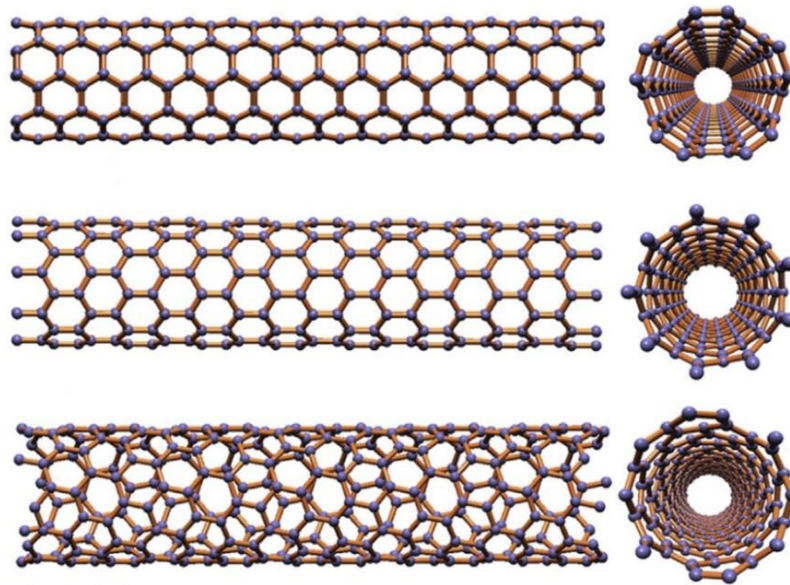


Figure 36 - Different chiral arrangements of SWCNTs (a) armchair (b) zigzag (c) chiral [235].

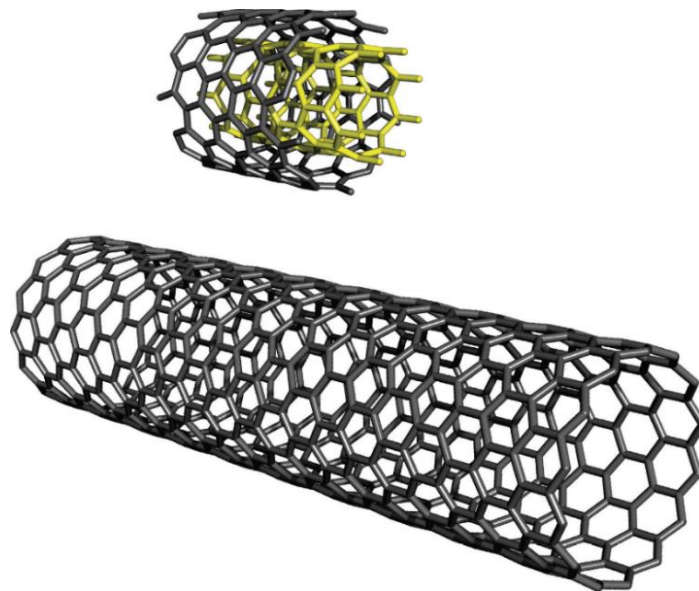


Figure 37 - Illustration of a single walled carbon nanotube and a multi walled carbon nanotube; the latter can comprise of many layers of tubes within tubes [236].

CNTs have an electrical conductivity of around 10^6 S cm^{-1} [237]; thermal conductivity is approximated at $5,800 \text{ W m}^{-1} \text{ K}^{-1}$ for SWCNT [238] and $10,000 \text{ W m}^{-1} \text{ K}^{-1}$ for MWCNT. The Young's modulus of CNTs is approximately 900GPa [239].

Although these properties are less than that of planar graphene, CNTs are worth considering as potential gas sensing materials when used in conjunction with graphene. There is literature to support enhanced gas sensing properties when CNTs and graphene are used together as a hybrid system [240, 241].

1.6.5 Tungsten Trioxide

Tungsten trioxide (WO_3) is a transition metal oxide, which exhibits electrochromic [242], gas sensing [243] and catalytic properties [244]. These properties make it an ideal candidate for a range of potential applications including: electrochromic (smart) windows [245], gas sensors [246], photocatalysts [247].

Structurally WO_3 consists of perovskite units (ABO_3) and is similar to MoO_3 . WO_3 possesses nonstoichiometric properties and is able to form tungsten bronzes. WO_3 crystals are formed through edge and corner sharing of WO_6 octahedra. Several phase transformations can be observed: monoclinic II ($\epsilon\text{-WO}_3$) (only stable at sub-zero temperature), triclinic ($\delta\text{-WO}_3$), monoclinic I ($\gamma\text{-WO}_3$), orthorhombic ($\beta\text{-WO}_3$), tetragonal ($\alpha\text{-WO}_3$) and cubic (rarely observed experimentally). These phase transformations can occur during heating and cooling.

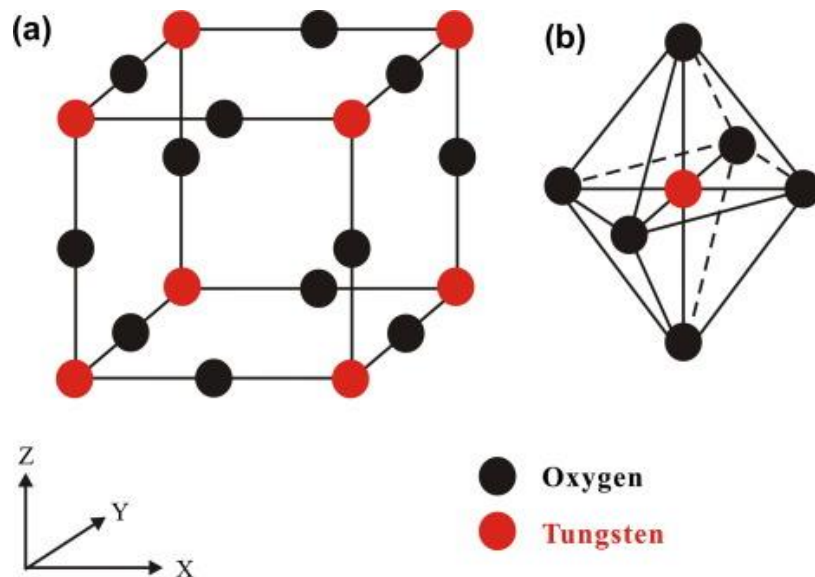


Figure 38 – Crystal structure of WO_3 (a) ideal cubic structure (b) WO_6 octahedra [248].

Electrical conductivity of a single crystal WO_3 is dependent on stoichiometry but is in the range of 10 to 10^{-4} Scm^{-1} [249]. The band gap of WO_3 is between $2.6 - 3.0 \text{ eV}$ which has been investigated extensively owing to the role it plays in the properties described [250].

1.7 Alternative Applications of Gas Detection

The benefits of small, low powered CO_2 sensing devices cannot be underestimated. Whilst obviously useful in areas of high pollutant concentration, other applications are also considered.

Analysis of exhaled breath has been investigated previously in medical diagnosis and health monitoring. Links have been made between aniline and o-toluidine and early detection of lung cancer [251]. 8-isoprostane, 3-nitrotyrosine and leukotriene B4 have been associated with COPD [252], Liver degeneration through detection of isoprene and CH₃OH [253], diagnosis of diabetes by determination of acetone [254], pentane and CS₂ for schizophrenia [255], pancreatitis by H₂S, NO and an m/z=66 species [256] and finally HCN (*Pseudomonas aeruginosa* infection in cystic fibrosis [257]). This non evasive approach is potentially quick and may be performed during general health screening. Some disadvantages of off-line PTR-MS suggested for large screening of exhaled air have been reported [258].

A sensor of this type may be useful to older members of the population who may live alone or in remote areas or see few visitors. It is envisioned that a 3D printed CO₂ sensor may act as an emergency device, by detecting changes in CO₂ concentration.

1.8 Oil Spill Detection

1.8.1 Background of Oil Composition

The materials proposed for this work have previously found uses as markers for oil spills in water and on land. The author believes that it is important to consider where alternative uses exist, so that comparison of material performance can be conducted.

Crude oil exhibits variations in chemical composition based upon the area of extraction and can be divided into: paraffinic (primarily paraffin based), naphthenic (cycloparaffin in heavy fractions) and aromatic. Owing to these differences, direct correlations cannot be reliably drawn between samples from alternate regions. It is important to consider that regardless of origin, crude oil is variable in composition, although generally, concentrations of aromatics and naphthalene's exceed that of alkane paraffins. Such phases have yet further different interfacial tensions (and work adhesions) with water.

Table 5 shows the work of adhesion for different hydrocarbons where the work of adhesion between the oil and water phases (W_{o-w}) equals the sum of the surface tensions of the pure phases in contact with their vapours minus the oil-water interfacial tension γ_{o-w} as in the Dupre equation ($W_{o-w} = \gamma_o - \gamma_w - \gamma_{o-w}$).

Table 5 – Work of adhesion between oil and water phases.

Hydrocarbon	W_{o-w} (mJ.m ⁻²)
Alkanes	36-48
Aromatic	63-67
Primary alcohols	92-97

Further examples of hydrocarbons with known characteristics are also considered in Table 6:

Table 6 – Phase characteristics of three known hydrocarbons.

Hydrocarbon	γ_o	γ_{o-w}	W_{o-w}
Cyclohexane	25.3	49.7	48.8
n-hexane	18.4	51.1	40.1
Benzene	28.9	35.0	66.7

$$\gamma_{\text{water}}=72.8\text{mN.m}^{-1}$$

Furthermore, it is interesting that aromatic hydrocarbons exhibit larger T dependencies for their interfacial tensions (Table 7):

Table 7 – Interfacial tensions of aromatic compounds.

Hydrocarbon	γ_o	γ_{o-w}	$\delta\gamma/dT$
Octane	21.69	51.68	-0.095
Dodecane	25.44	52.90	-0.088
Hexadecane	27.46	53.77	-0.085
Benzene	28.88	35.00	-0.130

where $d\gamma/dT$ for water is +0.160.

1.8.2 Oil Toxicity and Detection of Spillages

Environmental forensics can enable the source of spilled petroleum oil products to be detected using fluorescence spectroscopy [259]. The chemical composition (and equivalent alkane carbon number (EACN) [206, 261] increases and varies with the effects of weathering, owing to the formation of long-term recalcitrant polar compounds [262] (produced in water and soil), soluble naphthenic organic compounds (NOCs) and petroleum acids [263, 264]. This poses a large problem when oil enters marine, freshwater or soil environments. Commonly noted effects are; oil spilled into the marine environment has been shown to have enhanced bioactivity, bioavailability and toxicity [265-267] to biota [268]. Water-accommodated

fractions (WAF) of crude oil are toxic to zebrafish (*Danio rerio*) in early life stages [269]. Domestic heating oil (DHO) seeping into freshwater are toxic to molluscs [270].

Plants are affected by oil seeping to soil [271] and haemolytic anaemia in birds and mammals [272] including mice [273, 274] is thought to be caused by ingested petroleum.

The toxic effects of petroleum-based oil can be long-term if PAHs accumulate in sediments [275]. Continual weathering subsequently generates more WAF [276] and water-soluble fractions (WSF) [277] from the initial spill.

Treatment of toxic spilled oil can be chemical, physical or bio, with the latter requiring larger space requirements than chemical treatment [278]. However, the primary step must be to detect that a spill has occurred. It was considered that *micro* conductivity could provide a low-cost sensor. This, it was thought might be part of “oil production engineered nanometrically” (OPEN).

The objectives of this work were to develop novel micro-conductivity of water and hence land pollution by oil. Bench scale experiments [279, 280] and in-situ ¹³NMR and oxygen sensing [281, 282] may help understand the kinetics [283, 284] of remediation and structure-transport relationships [285-287].

2 Methods

The instrumentation and synthesis methods selected in this chapter have been chosen to enable the aims to be achieved. 3D printing has been selected for its ease of use and for the sheer flexibility of design it enables. With the end product likely to be used in construction, custom designs will be required, it is for this reason 3D printing is a core method in this work.

Analytical techniques that have been employed serve two purposes, firstly as a means to assess the performance of the synthesised gas sensing materials and secondly to probe the structure, stability and quality of the precursors and synthesised materials.

The RGA is a reliable and durable mass spectrometry method used to analyse species by mass/charge ratio. In this work it is used as a technique to confirm that injected gases have traversed the gas rig setup and passed over the sample being analysed. An RGA was chosen over a traditional mass spectrometer owing to its durability and ease of adaptation. This helps the gas sensing aims to be achieved by giving a reliable figure to compare the performance of the 3D printed samples to.

SEM-EDX, Raman, FTIR, DLS are all techniques which are used to probe the structure and chemistry of the samples. SEM-EDX in particular allows viewing of the interactions between the polymer matrix and inclusive metal oxides. FTIR allows differences in chemical structure to be investigated, this is important in this work as 3D printed materials may not possess the same purity as lab grade precursors. DLS enables particle size to be calculated, important when considering surface area of gas sensing or electrochromically active components.

Furthermore, techniques such as TGA and DSC allow the thermal stability of a sample to be tested, DSC is particularly important in determining levels and ratios of on board solvents.

Aims can therefore be achieved by only taking forward samples which have been subjected to an array of techniques.

The chemical synthesis methods chosen represent reliable, safe and cost effective means to synthesis samples for testing. This helps the commercialisation of the aims, by making the materials financially viable.

2.1 Instrumentation

2.1.1 Three-dimensional Printing

A three-dimensional (3D) printer enables the user to create a physical object, in a variety of materials, from a computer aided design (CAD) model. Different types of 3D printer exist, using a variety of additive manufacturing (AM) techniques. AM works on the principle of creating a structure by adding material. Conversely, subtractive manufacturing techniques remove material from a solid piece [288]. 3DAM enables complex models to be produced which would be unsuitable for subtractive manufacturing [289, 290]. In this work, fused deposition modelling (FDM), a form of material extrusion, was considered the most appropriate method. It is relatively cheap compared to other methods and a wide variety of materials can be used. Materials of particular interest are polyvinyl alcohol (PVA) and polylactic acid (PLA) including composites of these. Conductive forms of PLA can be procured as a base material, some of which contain graphene. This was attractive to this project as graphene is widely known to be useful as a gas sensing material.

2.1.1.1 Material Extrusion

Material extrusion is the general name given to a process where a solid thermoplastic filament is fed at constant pressure and rate into a heated print head. The filament is heated to a semi-liquid state before being extruded through a nozzle with specific diameter size (commonly 0.1 - 0.8 mm) onto a build plate. The print head moves in the X and Y planes to create a layer. Once on the build plate, the material cools rapidly returning to a hardened solid state. It would be possible to explore the LWIR thermography (IRT) to investigate accurate temperatures. The build plate then moves in the Z plane a set distance dependent on layer height and thus quality of the finished model, allowing the print head to deposit the next layer.

Figure 39 shows a generalised schematic of a dual extrusion FDM 3D printer. This type is capable of employing 2 filaments thus eliminating the need to change over material types and allowing the printing of dissolvable support parts such as PVA.

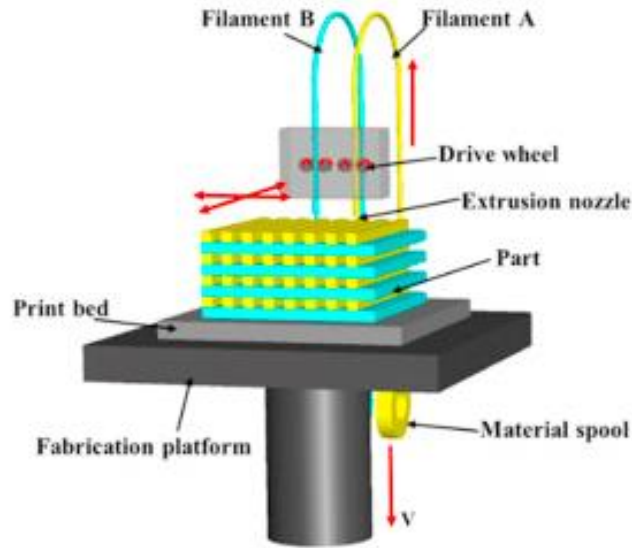


Figure 39 - A generalised schematic diagram of a material extrusion 3D printer [291].

Whilst nanotechnology has been expanding in most fields, 3D printing to produce nanostructured materials is still in its infancy. Some work has been conducted in the medical sector on nanostructured materials from 3D printing [292], although these methods focus on conventional inkjet printing rather than AM. Graphene has been incorporated in metallic 3D printing to produce nanocomposite materials with superior properties [293]. Other forms of AM using polymeric precursor materials have also been treated with graphene to improve mechanical and electrical properties [294]. Of particular relevance to this work is the inclusion of graphene in PLA for use in FDM [295].

Models which are to be produced via FDM predominantly originate from a variety of CAD software packages. The CAD package used in this project is “Autodesk fusion 360”. This was chosen as it is free to academic users, it is intuitive to use and utilises the cloud platform, allowing for easy sharing of designs.

Owing to the range of CAD packages and the different file types, designs can potentially be exported in; a universal file type must be adopted before a model can be printed. It first must be converted into a stereolithography (STL) file, which approximates the surface geometry of the model using triangles. Figure 40 shows how a cylindrical model appears after it has been designed in the Autodesk software package. Figure 41 shows the same sample after it has been converted to STL file type. In this instance the surface geometry has been approximated to 264 individual triangles. It is possible to increase the level of refinement, thus using a greater number of smaller triangles to better approximate the geometry of the model.

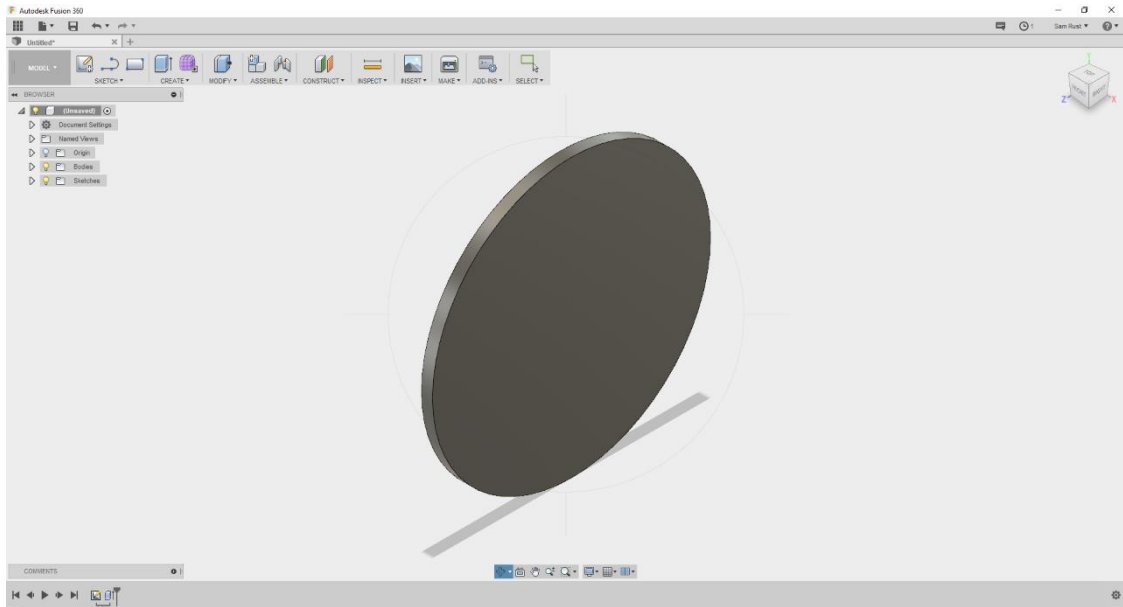


Figure 40 - CAD model of a cylindrical sample to be printed, before conversion to STL file type.

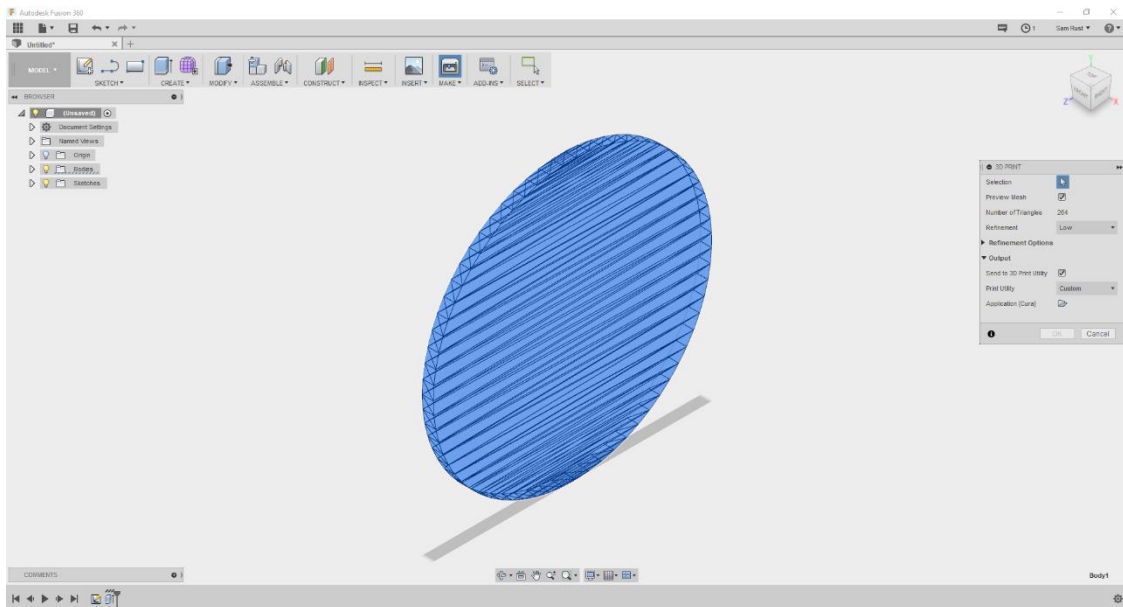


Figure 41 – CAD model of a cylindrical sample after being converted to STL file type.

Once a design has been produced in STL format, it must be imported for processing in an appropriate “slicing” or “cutting” software package. This software breaks down the model into individual horizontal layers (Z plane) and then calculates the path that the print head will take to create the model (X and Y planes). It also calculates where support material is required and the correct orientation of parts. Other parameters can also be decided such as the material the model is to be printed in, the height of each layer (determines the quality of finish on the model), printing temperature (must be appropriate for the material being used), temperature of the build plate (important for good adhesion of the model) and material flow rate. The software

also gives an indication to the user of how long the model will take to print and how much material will be used to create it.

The slicing software used in this project is called “Cura”. This was chosen as it was developed and recommended by the manufacturer of the printer being used. Figure 42 shows how the cylindrical model appears once it has been “sliced” in Cura. Printing options and parameters are shown on the right-hand panel.

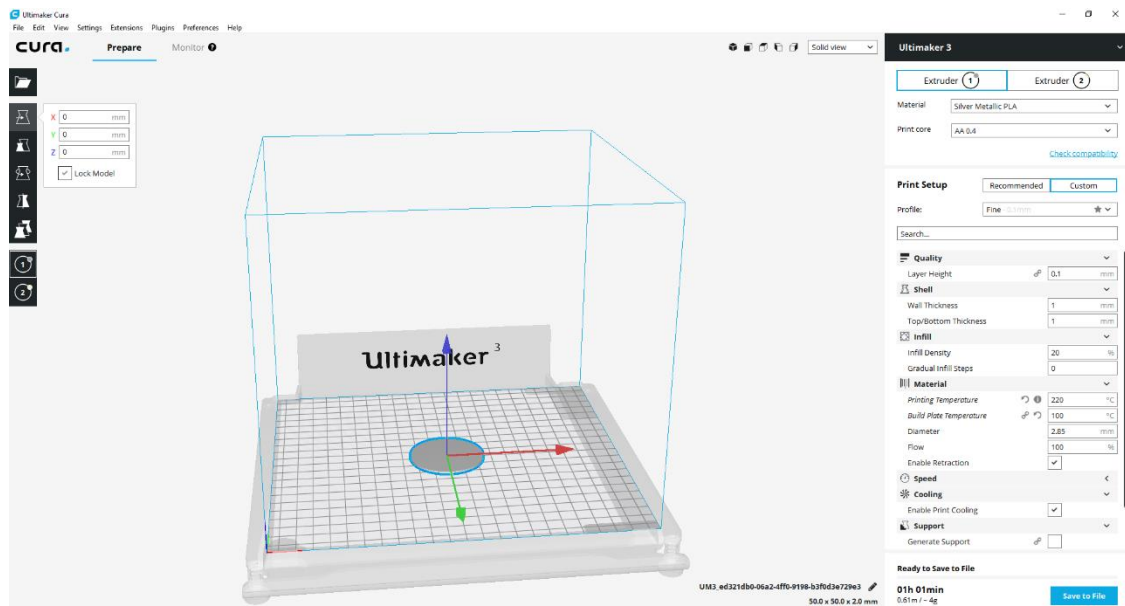


Figure 42 - Cylindrical sample viewed in Cura, a slicing software package.

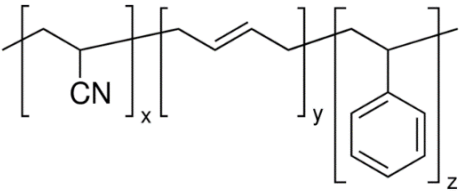
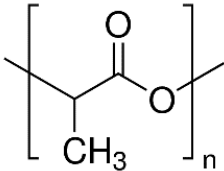
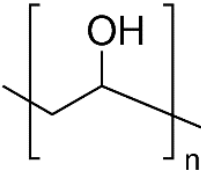
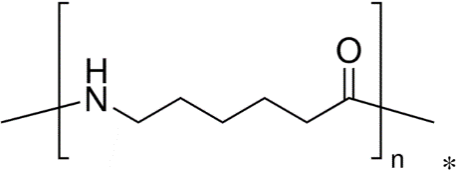
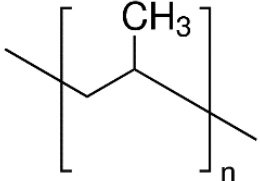
The final stage before printing is to export the sliced model as a “.gcode” file. This is a numerical control programming language, which gives instructions to the motors controlling the print head telling them when and how far to move and at what speed.

The 3D printer selected for this work was an Ultimaker 3 FDM (as shown in Figure 43). This printer is capable of dual extrusion including water soluble supports and can print models in a variety of materials, namely: acrylonitrile butadiene styrene (ABS), polylactic acid (PLA), polyvinyl alcohol (PVA), polyamide (nylon) and polypropylene (PP) are the most common. Table 8 shows the chemical structure of these materials and some key properties which were considered when selecting materials. Materials were purchased directly from the printer manufacturer (Ultimaker), except for the PLA/Graphene filament, which was purchased from Black Magic 3D, a company specialising in materials for R&D.

Specific purity values were hard to obtain from filament manufacturers, owing to the generally intended end use. Manufacturers do not generally anticipate end users to require analytical grade purity given the wide variation in melting temperatures. Purities of 95% would be

considered acceptable for general use and would not significantly affect the thermal or mechanical properties of an item.

Table 8 – Key properties of a range of common FDM materials *Nylon 6, one form of nylon, commonly used [296].

Material	Melting range (K)	Diameter (mm)	Key Features	Structure
ABS	498 - 518	2.85 ± 0.05	Mechanical properties, minimal warping	
PLA	318 - 433	2.85 ± 0.10	Tensile strength, high print speed, surface quality	
PVA	436	2.85 ± 0.10	Non-toxic, good thermal stability	
Nylon	458 - 468	2.85 ± 0.05	High strength to weight ratio, abrasive resistance	
PP	403	2.85 ± 0.10	Good heat resistance, high strength to weight ratio	
PLA-Graphene	443 - 513	1.75 ± 0.05	$0.6\Omega\text{cm}^{-1}$ volume resistivity, high strength	

The Ultimaker 3 printer is capable of printing at a build speed of $24\text{mm}^3\text{s}^{-1}$ at temperatures between 453 and 553K. The XYZ resolution of the printer is 12.5, 12.5, $2.5\mu\text{m}$ giving

exceptional accuracy. Layer resolutions of 60 - 150 μ M (0.25mm nozzle), 20 - 200 μ M (0.4mm nozzle) and 20 - 600 μ M (0.8mm nozzle) are achievable.

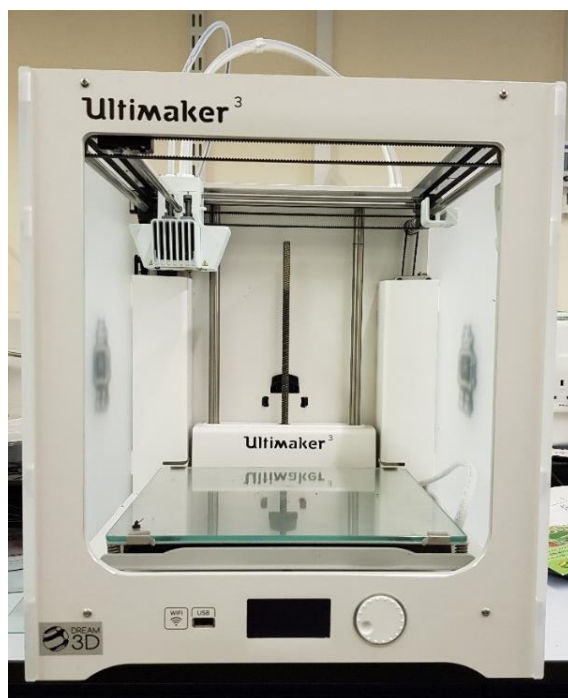


Figure 43 - Ultimaker 3 three-dimensional printer.

2.1.2 Scanning Electron Microscopy

It is often necessary in materials science to undertake characterisation using microscopy. Whilst optical microscopy can provide information on the properties of a sample to the sub-millimetre (<mm) to micrometre (μ m) scale, it requires an electron microscope to give images at high resolution on the nanometre (nm) scale. It was necessary to view samples on this scale to understand the homogeneity/heterogeneity and dispersion of the WO₃ nanoparticles (NPs) within the hydrogel matrix. For example, the geometry of the WO₃ NPs in-situ required investigation. Furthermore, information about the printed PLA/PVA interface and understanding of the surface morphology (roughness/smoothness) of printed samples needed gathering.

SEM uses a focused beam of electrons originating from an electron gun. The electron gun typically employs a tungsten filament, which is electrically heated until it emits electrons. This beam is then focused using magnetic lenses so that it scans over the sample in an evacuated chamber. Electrons interact with the sample causing multiple processes to occur, notably, elastic scattering of electrons, secondary electron emission and the emission of electromagnetic radiation. Multiple detectors can be inserted within the evacuated chamber to detect these

different species and collect information allowing an image to be produced. Routinely, secondary electrons are collected to produce the typically-displayed SEM image. Figure 44 shows a generalised schematic on an SEM.

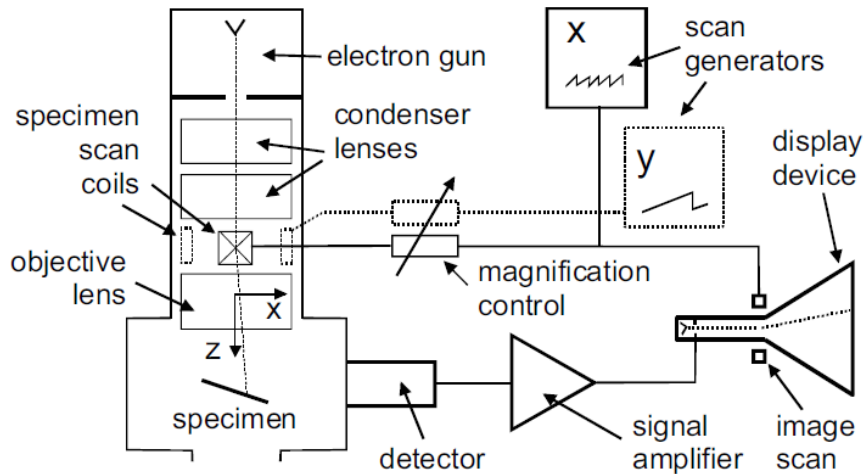


Figure 44 - Schematic diagram of a scanning electron microscope; with emission, focusing, sample, detection and display parts shown [297].

Samples to be analysed were first dehydrated (in the case of hydrogels) before being fixed onto a standard aluminium sample stub using double-sided carbon tape. Gold coating was required to achieve a good level of conductivity through the sample and stub. This was achieved using an argon source gold sputter with two applications of 1.5 nm gold coating. Sputter coating is a physical vapour deposition method used to deposit a thin film onto a substrate. A cathodic material, in this case gold, is bombarded with inert gas (e.g. argon) causing erosion of the target, referred to as “sputtering”. The sputtered gold atoms are attracted to the oppositely charged anode on which the substrates to be coated are placed, causing a thin film of gold atoms to be deposited on the substrate surface [298]. Once gold coated, sample stubs were secured onto a multi-stub holder enabling up to nine samples to be placed inside the SEM chamber in one session.

Gold coating was achieved using a Polaron Emitech SC7640 High Resolution Sputter Coater fitted with a gold target with argon as a carrier gas. Coating thicknesses which can be achieved with this instrument were in the range of 1 - 20nm. It was thought that a minimum advisable coating thickness was 2nm to eliminate sample charging in the SEM.

The depth at which samples in this work will be analysed is dependent on the information required. Penetration depths of 1-2 μ m are possible with a high energy electron beam. However, the information required about the structure of a samples will be typically in the

region of 100 – 500nm. The author is interested in the surface characteristics of the samples, the boundary layer of PLA/PVA samples and the interactions of inclusive MO_x NPs in hydrogel and thin film matrices.

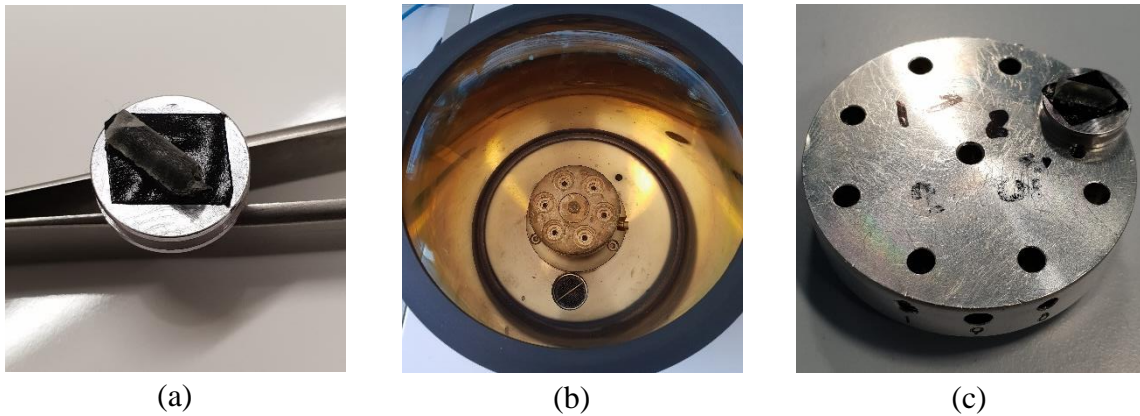


Figure 45 – Sample preparation stages prior to analysis by SEM. (a) Affixing a sample onto an aluminium sample stub, (b) gold coating by placing the sample stub into a sputter coater and (c) securing the sample stubs to a multi-stub holder to be placed into the SEM chamber.



Figure 46 – Digital photograph of using a Polaron Emitech SC7640 High Resolution Sputter Coater.

Where EDX analysis was to be undertaken, gold coating was where possible eliminated or reduced to enable the accurate collection of elemental data from the sample. In cases where gold was amongst the elements being analysed, carbon coating was a viable alternative to gold coating.

SEM images were collected using a Zeiss Supra 35VP Field Emission Gun Electron Microscope fitted with a range of analytical techniques including energy-dispersive x-ray

analysis (EDX), back-scattered electron detection (BSE) and electron back-scattered diffraction (EBSD).

An acceleration voltage of between 4 and 20 kV was used and the working distance from the sample was in the range of 8-10 mm to enable safe and reliable focusing on the sample without the risk of the sample stage making physical contact with the electron gun. In this instance SEM analysis should be considered a destructive technique due to the need to affix the samples to stubs with carbon tape and to gold coat them. As SEM operates under vacuum, it was also necessary to dehydrate the hydrogel samples for analysis to be conducted.



Figure 47 - Optical photograph of a Zeiss Supra 35VP scanning electron microscope and associated analysis probes.

2.1.3 Energy-Dispersive X-ray analysis

Energy-Dispersive X-ray analysis (EDX) commonly called EDAX or EDS is an analytical technique used to identify the elemental composition of a material. Commonly used in conjunction with SEM or TEM systems, EDX provides peaks corresponding to the elements within the sample under analysis. Depending on the application this makes EDX a quantitative, semi-quantitative and qualitative technique. The distribution of elements can also be mapped across the sample.

To obtain the elemental profile the sample is bombarded with a beam of focused electrons from the electron gun within the SEM/TEM. This causes inner shell lower energy electrons from atoms within the sample up to 1 -2 μm deep to be ejected (along with the incoming bombarding electron) causing a vacancy. The depth at which EDX can penetrate is related to the escape

depth of an X-ray, characterised by the interaction volume of primary beam electrons (Figure 48). A higher energy outer shell electron can fill the vacancy generated, with the energy difference being made up in the form of a characteristic X-ray. The energy of the X-ray is specific to the element from which it is emitted. Therefore, it is possible to detect the number of X-rays relative to the energy they carry.

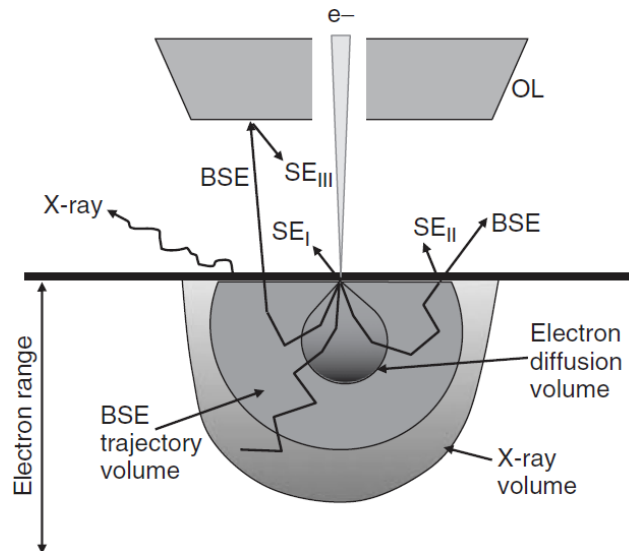


Figure 48 – Interaction volume of primary beam electrons [299].

Silicon drift detectors are often used to detect characteristic X-rays emanating from the surface of the sample. When an X-ray hits the detector a charge pulse is created equal to that of the X-ray, this charge pulse is then converted by a charge sensitive preamplifier to a voltage pulse still equal to the energy of the original X-ray. A multichannel analyser then determines which signal corresponds to which X-ray by voltage and the data is displayed to the user on screen. For an X-ray to be generated, there is a requirement for an outer shell electron to fill the void left when an inner shell electron is ejected. Therefore, EDX cannot be used on H or He owing to the absence of a K-shell. Elements from Li to Ne can be difficult to quantify owing to valence electrons being involved in characteristic X-ray generation. Typical detection limits of this technique are 0.1wt% with combined errors resulting in precision levels of $\pm 2\%$.

EDX analysis was undertaken using an Oxford Instruments Octane Elect EDS System capable of low energy sensitivity and low voltage microanalysis. Spot and line analysis were particularly useful features of this system as this enabled rapid analysis of samples and gave an indication of elemental changes present across a sample and at the PVA-PLA interfaces.

2.1.4 Thermogravimetric Analysis

Thermogravimetric analysis (TGA) investigates the physical and chemical changes a material undergoes when heated or cooled through a defined temperature range. A known mass of sample is heated through a set temperature range at a defined rate ($\beta = \delta T / \delta t$) in a controlled atmosphere. The system can hold at specific temperatures ($\beta = 0$) or increase/decrease ($\beta > 0$ or < 0) as desired. The atmosphere which the sample is heated can also be controlled. Air is used when standard conditions may need replicating, or an inert gas (N_2) can be used when combustion is undesirable. With the variability of conditions available TGA can give information on the properties of a material, such as changes in mass attributable to oxidation, or the temperature at which thermal decomposition occurs. This allows determination of the variety of components within a composite material by interpreting the mass changes at different temperatures.

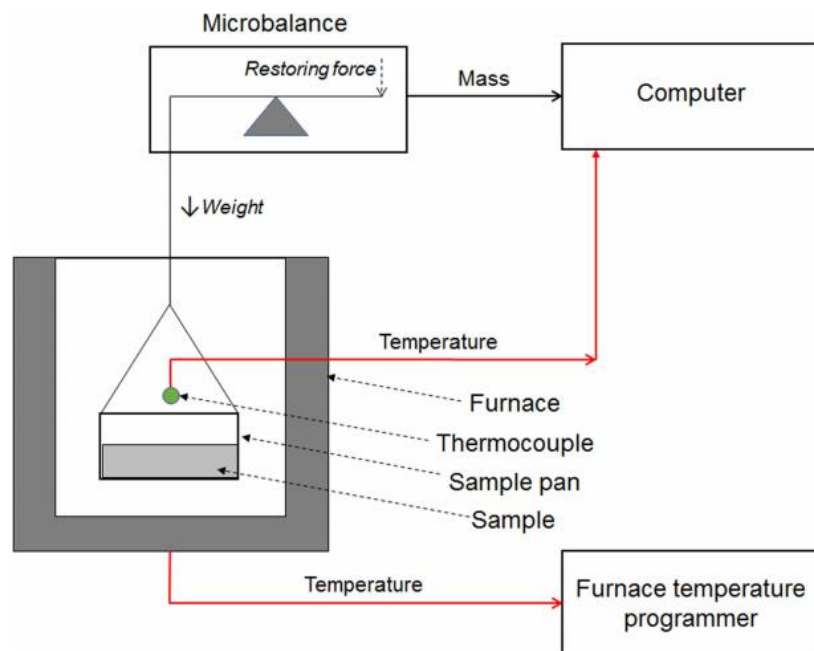


Figure 49 - A schematic diagram of a typical TGA instrument; alternative designs can incorporate a top loading mechanism [300].

Figure 49 shows a basic design of TGA which almost all modern instruments use. Gas flows into the furnace removing gases which may have evolved during the analysis run ensuring that they do not interfere with the microbalance, allowing for a controllable atmosphere. A null point precision microbalance ensures that the sample remains within the heated region in the furnace avoiding variations in temperature. This also forms part of a Wheatstone bridge and is marked as “restoring force” in Figure 49. When the microbalance arm moves (as sample mass changes) the bridge circuit restores the arm to its initial position. A computer logs all temperature and mass changes and outputs this graphically via an ascii file.

A TA Instruments TGA Q600 was used throughout this project. Typically, heating runs were conducted between 293K and 973-1073K (maximum performance of the instrument 1273K). A ramp rate of 10K min^{-1} was utilised and samples were nominally run in an atmosphere of air at a flow rate of $90\text{cm}^3/\text{min}$, followed by a subsequent run in N_2 . Prior to analysis, the sample was reduced to an appropriate size (approx. 4-5 mm) to fit into the sample pan; a maximum sample weight of 1g can be loaded into the instrument. Dependent on the upper temperature limit of the run, either a standard temperature platinum pan (up to 973K) or high temperature platinum pan (up to 1273K) was employed. The latter was used to prevent thermal welding of the pan to the sample stage at higher temperatures. The sample was added to the pan, mass zeroed and then loaded into the furnace to be heated. In cases where residue was left in the pan after the thermal cycle was completed, SEM-EDX was employed for elemental analysis. TGA was considered a destructive technique as samples were going to be thermally decomposed and unrecoverable.

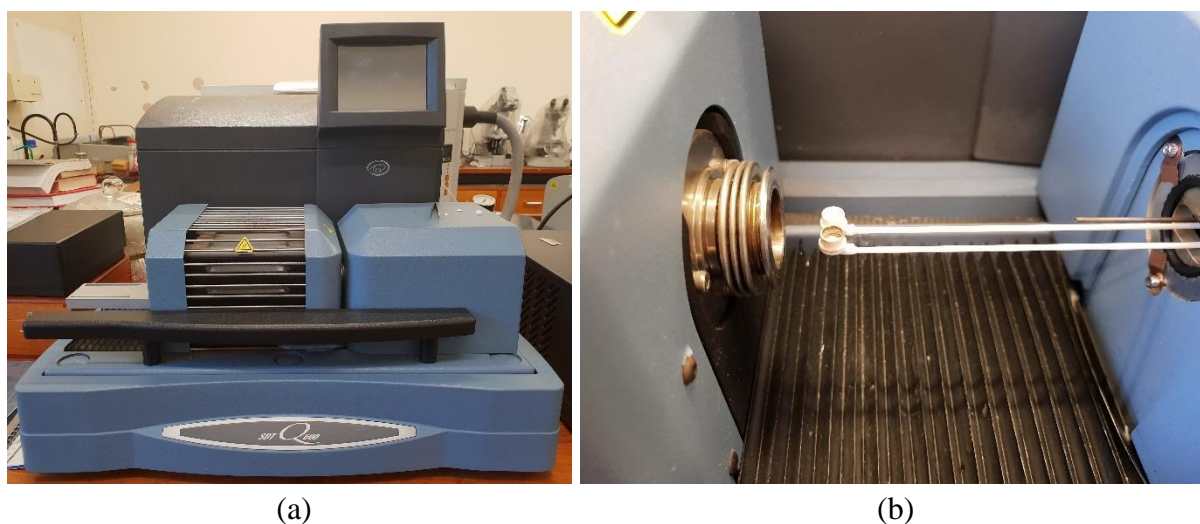


Figure 50 – (a) TA Instruments TGA Q600 TGA and (b) close-up of the sample pan arms which were connected to a microbalance.

2.1.5 Differential Scanning Calorimetry

Differential scanning calorimetry (DSC) is used to monitor the heat flow (HF; mW) to and from a sample. This is achieved by comparing the changes in heat flow within a sample of known mass against a reference material as it is heated or cooled. Endothermic processes such as the phase transition from solid to liquid will require a higher heat flow in the sample of interest with respect to the reference to maintain the same rate of temperature increase. Conversely, an exothermic process such as crystallisation will require a reduced heat flow within the sample of interest with respect to the reference material. Phase transitions, melting,

glass transitions and curing kinetics can all be detected by monitoring heat flow. The accuracy of temperature is $\pm 0.1\text{K}$ with a precision of $\pm 0.01\text{K}$ and a calorimetric precision of $\pm 0.05\%$. The instrument used had a sensitivity of $0.2\mu\text{W}$.

There are two types of DSC found commonly; heat flux DSC and power compensation DSC. Heat flux DSC as used in this work contains two raised platforms within a single furnace. A heat conduction path of known thermal resistance is used to exchange heat. The measurement taken is the temperature difference between a reference pan which has a well-defined heat capacity over a range of temperatures and a second pan containing the sample being analysed. This is achieved using individual thermocouples connected to the raised platforms. A third detector is used to measure temperature at the base of the sensor. The difference in temperature between the two pans results in heat flow between the two to maintain equal temperatures. The temperatures measured can then be used to calculate the heat flowing into the sample with respect to the reference pan. Figure 51 shows the general outline of a heat flux DSC.

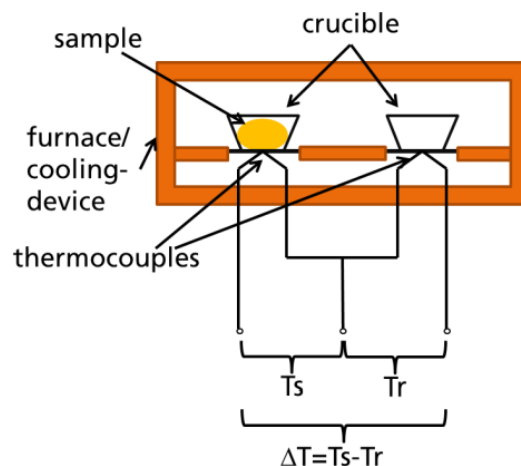


Figure 51 - Diagram of the heat flux DSC showing the furnace cell [301].

Power compensation DSC is comprised of two individual furnaces; one containing a sample pan and the second containing the reference pan. Each furnace also contains a detector. An electrical circuit inputs equal energy into both pans; where there is a temperature difference a second circuit compensates for any heat taken in or given off by the sample being analysed by increasing or reducing the heat supplied to the sample pan to bring it equal to the reference pan. This difference in energy is recorded and used to calculate the heat absorbed or liberated by the sample.

Data is output as a DSC curve which plots heat flow (mW) against temperature (K). Peaks which appear in the curve are indicative of a heat event and can be integrated using Equation

6 to give the enthalpy of transition (ΔH), where K represents the calometric constant and A the area under the curve.

$$\Delta H = KA$$

Equation 6 – Calculation of enthalpy of transition.

In this work there was particular interest in phase transitions and melting within the PVA hydrogel matrix, with DSC enabling investigation of this.

A TA instruments DSC Q2000 was used for this work. Typically, a DSC run involves multiple cycles to improve the reliability of the data with temperatures ranging from 193K to 353K and ramp rates between 0.5Kmin^{-1} to 10Kmin^{-1} . DSC was considered semi-destructive as some samples could be reused after analysis; however others underwent significant structural changes, making them unusable. The DSC produced ascii files that could be analysed on a variety of graphical software packages.

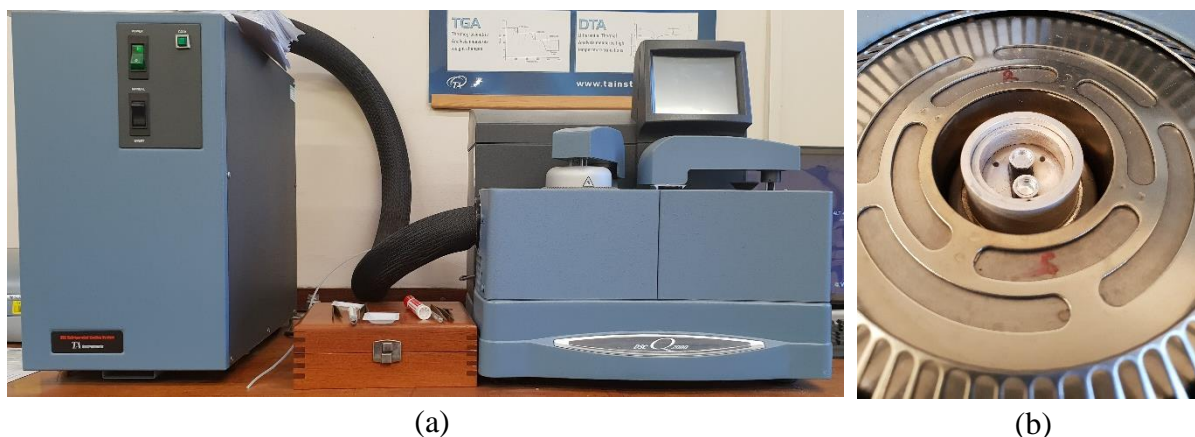


Figure 52 – (a) TA instruments DSC Q2000 and (b) close-up of the reference and sample cells on raised platforms within a single furnace.

2.1.6 Infrared Thermography

Infrared thermography (IRT) is a technique which produces visible images from light in the IR section ($700\text{nm} < \lambda < 1\text{mm}$) of the electromagnetic spectrum (as opposed to a conventional camera which uses visible light ($400 < \lambda < 700\text{nm}$)). All bodies with a temperature above absolute zero (0K) emit in the form of IR energy. Emitted radiation is a function of the temperature of the material; as an object increases in temperature it radiates a greater amount of IR energy. Once the emitted radiation encounters another object, it can be dissipated in three different ways:

1. Absorbance – the absorptivity of the body,
2. Transmission – the transmissivity of the body and
3. Reflection – the reflectivity of the body.

These types of energy dissipation can be described in Equation 7 where α_λ is the spectral absorptance (the ratio of the energy absorbed by the object), ρ_λ the spectral reflectance (the ratio of the energy reflected by the object) and τ_λ the spectral reflectance (the ratio of the energy transmitted by the object). All three parameters are wavelength dependent, the sum of which must equal one at any wavelength.

$$\alpha_\lambda + \rho_\lambda + \tau_\lambda = 1$$

Equation 7 - Relationship between spectral absorptance, transmittance and reflectance of infrared energy striking an object.

A hypothetical perfect material where the transmissivity and reflectivity are zero is referred to as blackbody, i.e. all energy striking this object is absorbed and radiation is emitted across all wavelengths. The spectral emissive power (E_λ) of a blackbody can be described by Planck's Law which is shown as Equation 8 where h is the Planck constant, c is the speed of light, k refers to the Boltzmann constant, T is the absolute temperature and λ refers to wavelength.

$$E_\lambda = \frac{8\pi hc}{\lambda^5 \left(e^{\left(\frac{hc}{\lambda k T} \right)} - 1 \right)}$$

Equation 8 - Planck's law of blackbody radiation.

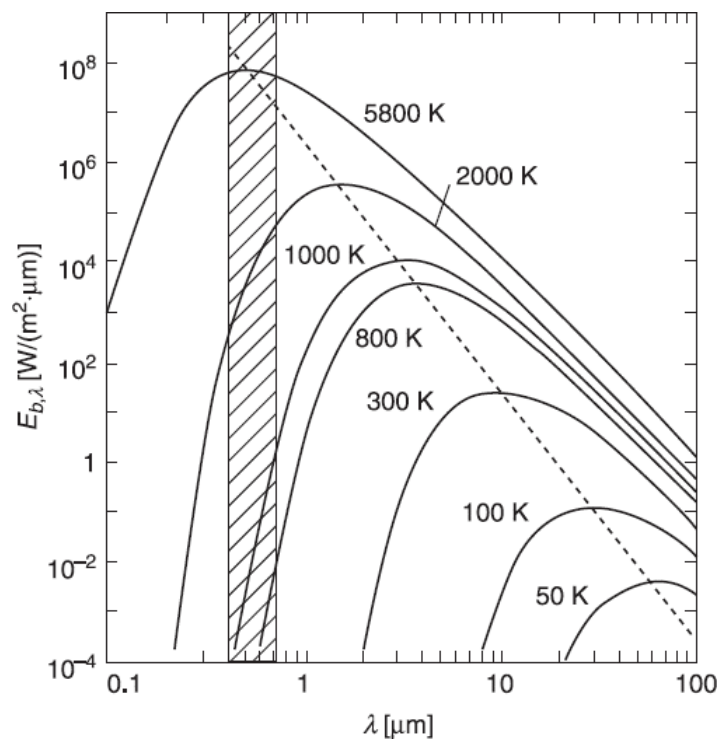


Figure 53 – Spectral emissive power of a blackbody versus wavelength.

Figure 53 is a graphical representation of Equation 8, with Planck distribution plotted on the y-axis against wavelength on the x-axis at constant temperature lines. What is apparent is that

with increasing temperature at a given wavelength, the spectral emission also increases. This emission then tends to a maximum at each temperature line. As wavelengths get longer the temperature decreases, wavelengths increase.

Equation 8 can be derived to calculate the wavelength at which the maximum emissive power occurs. Upon deriving the maximum emissive power, the value calculated is referred to as Wien's displacement law: this is given in Equation 9, where λ refers to wavelength and T is temperature.

$$\lambda_{\max}T = 2.898 \times 10^{-3} \mu\text{m.K}$$

Equation 9 - Wien's displacement law defines the wavelength at which maximum emission occurs from a blackbody.

Equation 9 indicates that as the temperature of a measured object decreases, its emission wavelength increases. Interestingly, if one plots a line at 5800K (which is the approximate radiation temperature of the Sun (an equivalent blackbody)) the area under the curve falls within the visible region on the electromagnetic spectrum (marked with the striped area in Figure 53). It is also worth noting that at a temperature of 300K, radiation is focussed within the infrared area of the electromagnetic spectrum.

It is therefore apparent that there is a definite correlation between the temperature of the surface of a body and the spectral composition and intensity of the radiation it emits. IRT relies on this relationship and by determining the intensity of radiation emitted by a body, the temperature of this body may also be determined.

Throughout this work a FLIR ThermaCAM PM695 thermal imaging system was used. The temperature range for this system was 233K to 393K or 273K to 773K dependant on the mode selected, with an accuracy of $\pm 2\text{K}$ and a thermal sensitivity of 0.08K at 303K. Images acquired had a resolution of 320 x 240 pixels. Spot and area measurements could be set up to simultaneously measure multiple samples. A minimal focal distance of 0.5m was required when using this instrument. Periodic saving of images was a feature of this system and enabled images to be acquired less than 1s apart.

Also used was a FLIR ThermaCAM SC3000 thermal imaging system. This instrument had an accuracy of $\pm 1\text{K}$ and thermal imaging range of 253K to 1773K. The thermal sensitivity of this system is 20mK at 303K. A minimal focal distance of 0.3m was required when using this instrument. Despite performance improvements over the PM695, the big advantage to this

system was the ability to connect to a PC or laptop computer, which when coupled with FLIR software enabled live analysis to be conducted.

In order that samples were accurately analysed, minimal sample preparation was required. Samples were placed onto a clean uniform base, within the focusing distance capabilities of the thermal imaging system (minimum 0.3m or 0.5m) and with no physical barrier in-between which could interfere with thermal sensing. Hydrogel samples would dehydrate during the time they were exposed to the atmosphere and in some cases could be regenerated after measurements were taken; however this was not always the case. This made IRT a semi-destructive technique.

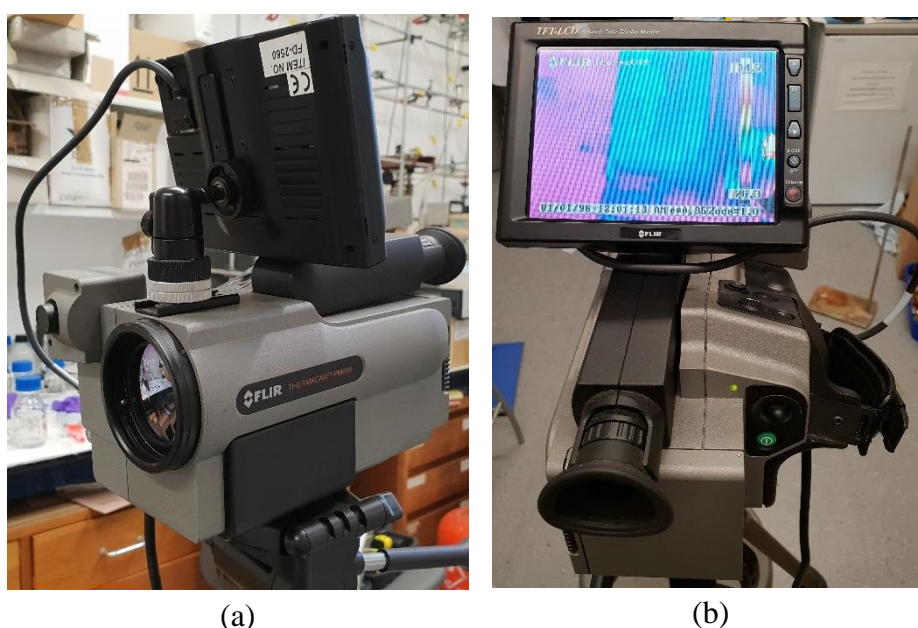


Figure 54 – (a) FLIR ThermoCAM PM695 thermal imaging system and (b) the view seen by the operator.

2.1.7 Raman Spectroscopy

Raman spectroscopy is a vibrational rotational spectroscopic technique able to give information about chemical bonds and therefore structural information about a sample. Laser light of a specific wavelength is directed at a sample, irradiating it. The light interacts with the sample in different ways. The predominant interaction is elastic scattering, known as Rayleigh scattering which occurs where the incident and emitted photons have the same energy. However, another type of scattering occurs when the irradiating photons interact with the molecule. A very small number of photons (approximately one in tens of millions) undergo a form of inelastic scattering, known as Raman scattering. This occurs when a photon is absorbed causing an electron to be temporarily promoted to a higher virtual energy state. The new energy level is unstable, and the electron immediately falls from this state to a different energy level than it

originally occupied and, in the process, emits a photon. Depending on whether energy was taken by, or given to the molecule, the difference in energy can be positive (anti-Stokes scattering) or negative (Stokes scattering). The newly emitted photon can then be detected by the instrument allowing a Raman spectrum to be generated. It is important to note that Rayleigh, Stokes, and anti-Stokes scattering differs to that of infrared or fluorescence, in the sense that the excited electron occupies a virtual state, rather than a specific vibrational or electronic excited state. This is represented in Figure 55.

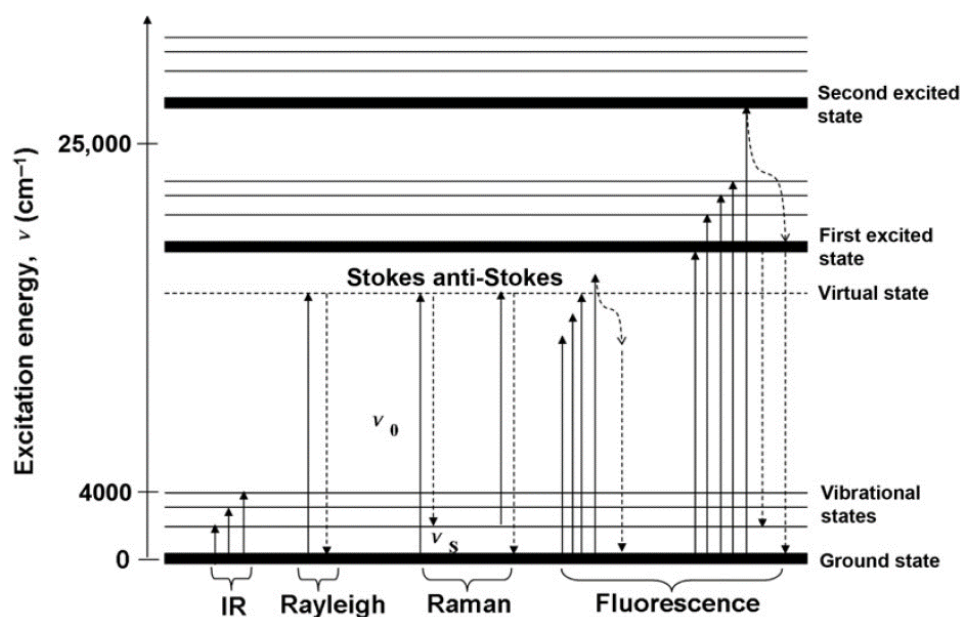


Figure 55 - Visual representation of the differences between IR, Rayleigh, Raman (Stokes and anti-Stokes) and fluorescence electron energy levels [302].

Raman spectroscopy is particularly useful for looking at small samples or areas as it often employs a microscope to focus the laser and to collect the scattered photons. This has been particularly useful in this work, as reliable asymmetric sample layer analysis could be achieved. The technique is also widely employed and has found uses in nanomaterials [303], particularly in graphene-based applications [304], owing to the multitude of properties graphene exhibits. Layer evaluation [305], doping [306] and investigation of impurities of graphene [307] are possible using Raman spectroscopy. Graphene can be considered the “building-block” of all sp^2 -bonded carbon allotropes. Therefore, the properties of graphene investigated by Raman can provide insight into all other dimensionalities of sp^2 -bonded carbon allotropes.

Figure 56 is the Raman spectra for pristine graphene with different number of layers. Looking at a single layer of pristine graphene a peak at approximately 1580cm^{-1} is apparent and arises from C-C in-plane vibrations (a stretching mode). This occurs in the G band and is also

apparent in other sp^2 carbon allotropes. A second peak at approximately 2700cm^{-1} is also evident and is referred to as a 2D band. This peak is not defect activated, unlike the D band at approximately 1350cm^{-1} which arises from the breathing modes of six-atom rings as a result of defects. The absolute positions of these peaks are variable and is related to the wavelength of laser used to excite the sample. Moreover, the 2D band reduces in intensity and becomes broader as a result of interactions between layers which cause changes in the electronic environment. It is therefore interesting to note that distinguishing between 5+ layers of graphene and graphite is not possible.

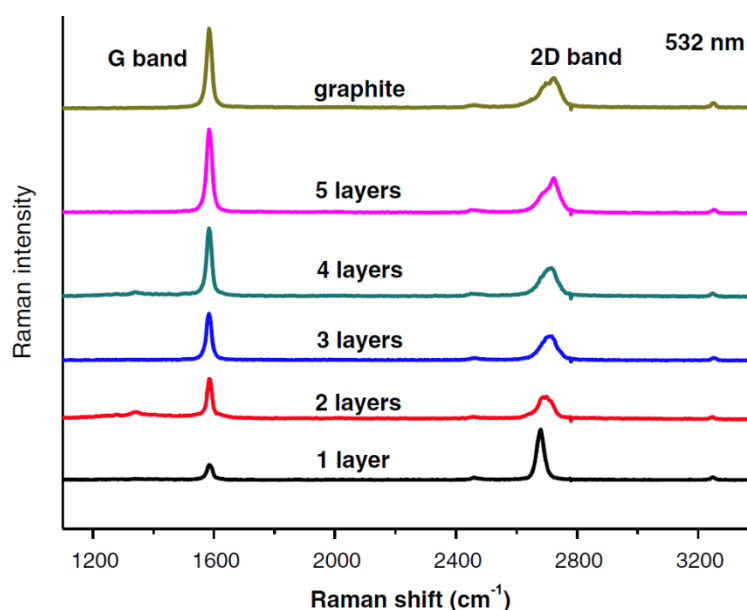


Figure 56 – Raman spectra of pristine different number layered graphene compared to pristine graphite [308].

Raman spectra of graphene becomes even more interesting with the presence of different defects, which greatly opens up the possible number of peaks present [309]. This, however, is far beyond the scope of which Raman was used in this work. This technique is fast (approximately 1 minute per point scan) and non-destructive allowing samples to be used again elsewhere.

In this work Raman spectroscopy has been used only to confirm the presence of graphene. A Renishaw Invia Micro Raman system fitted with a 514nm laser up to 50mW power was used with objectives of 20 x and 50 x employed. Laser power was adapted to the material being investigated to obtain the best spectra. No special sample preparation was required to undertake Raman spectroscopy.

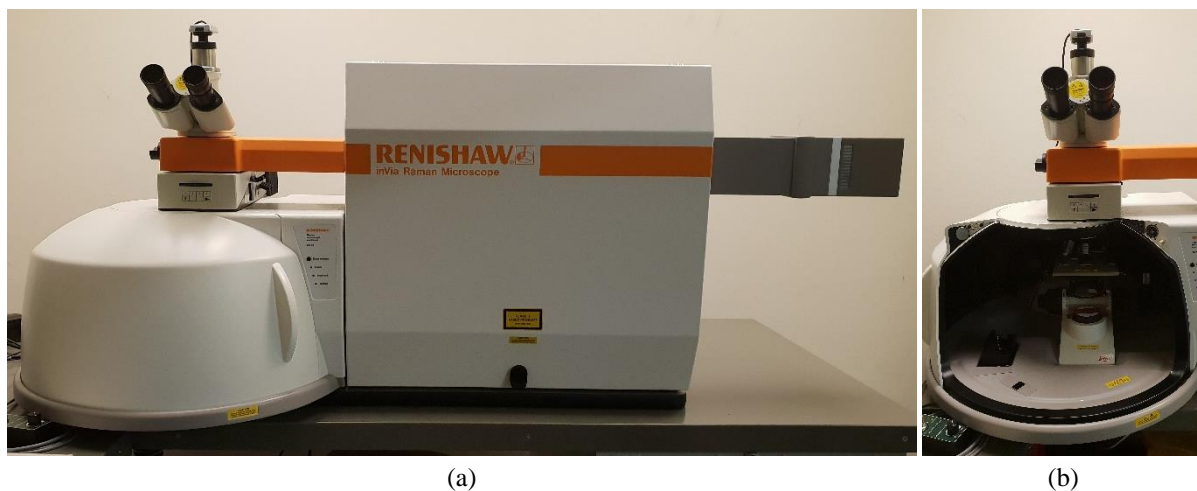


Figure 57 - (a) Renishaw InVia Raman microscope and (b) close-up of the microscope chamber.

2.1.8 Fourier Transform Infrared Spectroscopy

Fourier Transform Infrared Spectroscopy (FTIR) is an analytical technique able to identify functional groups present within a molecule based on the transition energies exhibited when the molecule is excited by IR radiation.

Unlike other spectroscopy techniques (e.g. ultraviolet-visible spectroscopy) which use a monochromatic light beam to determine how much energy is absorbed at each wavelength, FTIR shines light in the IR region of the electromagnetic spectrum at the sample simultaneously (typically at $600 - 4000\text{cm}^{-1}$ for a mid-IR instrument). This polychromatic light beam from a black body radiator interacts with a Michelson interferometer where it is split into two beams by a beam splitter. Half of the beam is transmitted and interacts with the fixed mirror; the other half is reflected, interacting with the moving mirror. Both beams are reflected and recombine at the beam splitter. Assuming the distance between the moving mirror and the beam splitter is the same as the distance between the fixed mirror and the beam splitter the beams can have wavelengths which interact constructively resulting in maximum intensity. Conversely, the distances can be different and destructive interference can occur causing a reduction in intensity and the peaks and troughs of the wave do not align. These differences produce what is referred to as an interferogram. Figure 58 shows the beam splitter within the Michelson interferometer.

The recombined beam then interacts with the sample being investigated, which can either absorb or transmit IR radiation at specific wavelengths depending on its structure. If the sample absorbs specific wavelengths, then these are subtracted from the interferogram. When striking the detector, time versus variation in energy for all wavelengths is reported. Time and

frequency are reciprocals which enables a mathematical function known as a Fourier transform to be undertaken allowing a spectrum of intensity versus frequency to be produced. Spectra are commonly plotted as % transmittance/absorbance versus wavelength/wavenumber.

Not all molecules can be detected using FTIR, selection rules exist which determine if a molecule exhibits IR active vibrations. These rules are based on molecular dipole moment changes which must occur if a molecule may be detectable using FTIR. Homonuclear diatomic molecules (e.g. N_2) do not have a dipole moment present and therefore cannot be vibrationally excited. Other types of molecules (e.g. CO_2) interact with the IR radiation inducing a dipole moment, owing to the displacement of the centre of charge.

These rules also extend to the degrees of freedom which a molecule exhibits. Non-linear molecules have three translational and three rotational degrees of freedom, as well as normal modes of vibration. Linear molecules have three translational and two rotational. It can be said that a molecule of n atoms has $3n$ degrees of freedom. Therefore, non-linear molecules have $3n - 6$ normal modes and linear molecules have $3n - 5$. To take CO_2 as an example, three atoms are present, the molecule is linear, therefore, $3 \times 3 - 5$ is equal to four. CO_2 has 4 normal modes (fundamental vibrations).

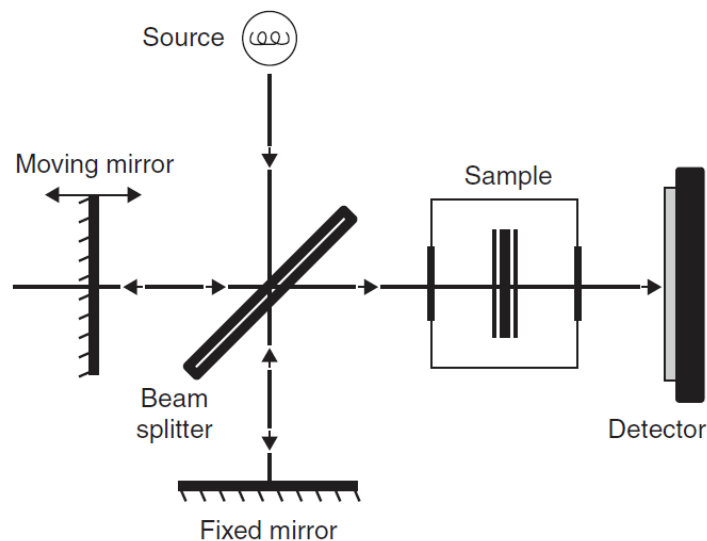


Figure 58 - Schematic diagram of a Michelson interferometer [310].

For this work a Shimadzu IRAffinity-1 Fourier transform infrared spectrophotometer as displayed in Figure 59 was used, with a typical run employing 45 scans with a resolution of 2cm^{-1} .



Figure 59 - Shimadzu IRAffinity-1 Fourier transform infrared spectrophotometer.

2.1.8.1 Attenuated Total Reflectance

Attenuated total reflectance (ATR) is an accessory which can be added to an FTIR reducing the sample preparation required and increasing the variety of samples which can be analysed. Compared to traditional FTIR which analyses properties in bulk and requires sample preparation, ATR collects surface information, up to a depth of approximately 1 to 2 μ m, requiring minimal sample preparation. This is particularly useful for thin film materials.

ATR works by measuring the changes which occur in an internally reflected beam of IR when contact with the sample is made. A beam of IR is directed at a high refractive index, optically dense crystal (typically zinc selenide or germanium) at a specific angle. The internal reflectance gives rise to an evanescent wave which extends beyond the surface of the crystal into the sample being analysed. At wavelengths where the beam is absorbed by the sample, energy is lost, and the beam is attenuated. The resultant radiation continues to the detector and is plotted as usual. Figure 60 shows a typical ATR setup.

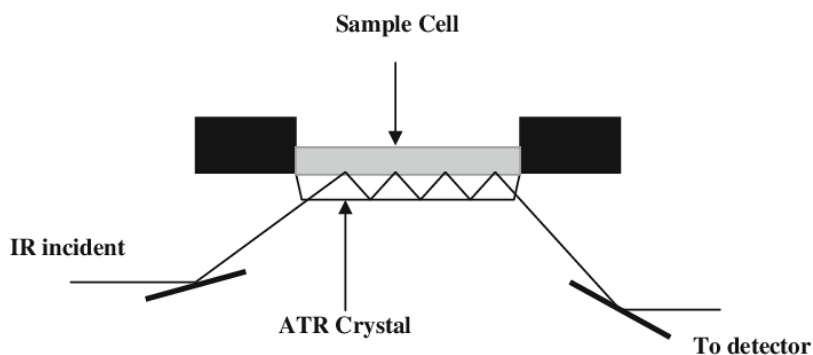


Figure 60 - Schematic of a typical Attenuated Total Reflectance cell. [311].

Throughout this work, FTIR measurements were obtained using a Specac Quest ATR accessory which contained a diamond ATR crystal (Figure 61).

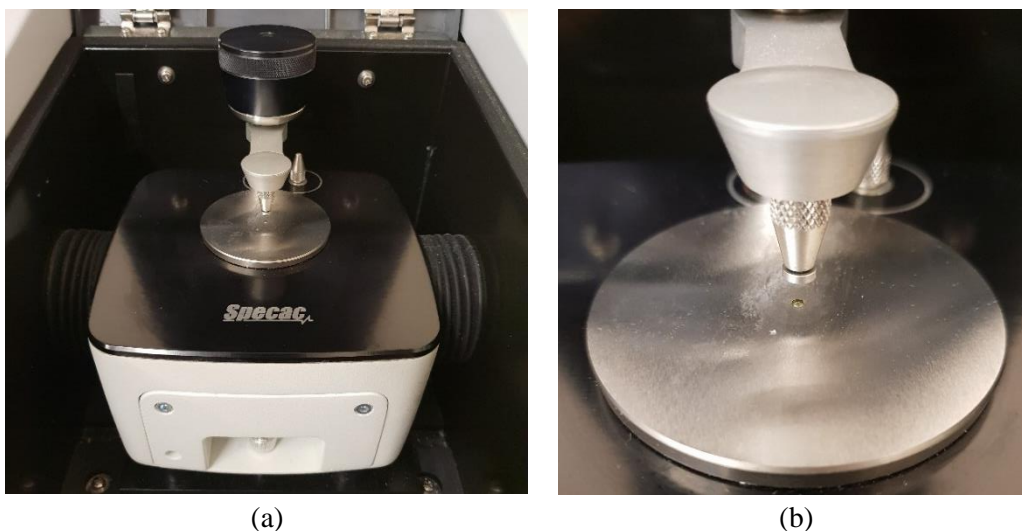


Figure 61 – (a) Specac Quest ATR accessory and (b) close-up of the diamond ATR crystal.

2.1.9 Four Point Electrical Conductivity

The gas sensors which were one aim of the present work can operate through changes in electrically conductivity. This is a pivotal property which is to be exploited when monitoring different gases. A conductivity change in a material can be indicative of a gas species being adsorbed and desorbed onto a material surface. This is well documented in the case of graphene [312-315]. There is also literature to support conductivity in PVA hydrogels as a substrate, albeit in medical applications [316, 317].

It was therefore essential that accurate and reliable conductivity (σ) measurements can be taken in order to correctly determine if and when a gas species has been adsorbed or desorbed onto a gas sensing surface. In order for this to be achieved a Jandel cylindrical four-point conductivity probe, coupled with a Jandel RM2 control unit were combined with a gas tight test cell. Hydrogel/PLA-graphene samples were placed onto the four contact needles and then sealed within the test cell. This enabled a controllable atmosphere whilst retaining the ability to take conductivity measurements.

A constant current (0.1 – 10 μ A) was applied to the outer two pins whilst the inner two pins measure the resultant voltage. The distance from one pin to the next was 0.635mm. The manufacturer recommended that for reliable and accurate measurements, the current was adjusted so that the voltage measured fell to a value lower than 200mV.



Figure 62 - (a) Jandel RM2 control unit and (b) Jandel four-point conductivity probe.

Known parameters are therefore, distance between pins, current applied and voltage induced. Additionally, diameter of the gel/sample being tested is known. From these values the resistance of a sample can be calculated using Equation 10, where R is resistance stated in ohms (Ω), V is voltage stated in volts (V) and I is current stated in amperes (A):

$$R = \frac{V}{I}$$

Equation 10 - Ohm's law.

Using the resistance value (R) from Equation 10 and taking into account the length (l) between points at which the voltage is measured in cm and the cross-sectional area (A) of the sample in cm^2 the resistivity of a sample could be calculated using Equation 11:

$$\rho = \frac{R \times A}{l}$$

Equation 11 - Calculation of resistivity from length, area and resistance.

It was possible to calculate conductivity (σ) stated in Siemens (S cm^{-1}) which is the inverse of resistivity:

$$\sigma = \frac{1}{\rho}$$

Equation 12 – Calculation of conductivity from resistivity.

It is also important to include a geometric factor when undertaking four-point conductivity measurements. The need for such a factor is the result of limitations in the number of current paths available due to the proximity of a boundary (edge of a sample). An ideal sample would extend infinite distance in all directions in plane from the point of measurement. However, this is a theoretical model and does not fully apply to real world examples. In every other case there will be one or more restrictions on the paths current could take due to the presence of a boundary. A good example would be a semi-infinite sample which extends infinitely in all directions, but which has a thickness less than infinity. This sample would therefore require a

correction based on its thickness. A distance measurement (diameter) is taken across the two closest points on the sample. In the samples used in this work this is typically the height or thickness of the cylinders as this was the current path limiting factor. Once obtained, this value is used to decide which geometric factor must be included when undertaking sheet resistance measurements from a simple calculation, where d is the diameter of the nearest points on the sample in the x , y or z planes and s is the spacing between each probe:

$$x = \frac{d}{s}$$

Equation 13 - Calculation to determine which geometric factor should be included when undertaking sheet resistance measurements.

Once the value for x is known, the correction value can be obtained from a list of values published by [318].

2.1.10 Residual Gas Analysis

A residual gas analyser (RGA) is a type of quadrupole % response mass spectrometer, although often far more durable than standard mass spectrometers which are generally static instruments. An RGA is often moveable and can be employed in a wide range of scenarios, commonly found as an ammonia detector [319]. An RGA can also be coupled with other techniques to monitor the quality of a vacuum in their system [320]. Other uses for RGAs have been found in the semi-conductor manufacturing sector, where it is a well-used technique employed to measure which species are out-gassed during the degas phase of semi-conductor production. When used in this capacity, an RGA is also able to detect when this process reaches an endpoint [321].

Typically, a complete RGA setup will consist of a vacuum pump, turbomolecular pump, ioniser, quadrupole mass filter, an ion detector and a computer. The system is under vacuum, this is achieved initially by a standard vacuum pump, then latterly with a turbomolecular pump which enables a stable pressure of $1e^{-4}$ Torr (13.33mPa) to be achieved. Gases which enter the chamber firstly interact with the ioniser consisting of two filaments producing electrons. These electrons are drawn to a central electrostatic wire mesh due to the applied potential difference between the two structures. Here, neutrally charged gas atoms or molecules collide with the electrons in a variety of ways: elastic collisions occur where there is no change in charge, conversely, inelastic collisions also occur. For a change in charge to occur (ionisation) the electron colliding with a species must possess the minimum energy that a molecule requires to ionise, referred to as the ionisation potential.

The variety of species then travel into an ion focusing section where electrostatic lenses accelerate and focus them into a beam before entering the quadrupole mass analyser (filter). The quadrupole consists of four cylindrical rods electrically biased which sorts (filters) the ions based on mass to charge ratio (m/z). Ions which are of interest as chosen by the operator pass through the quadrupole, whereas undesirable ions are deflected to the side and become neutralised and undetected.

The final stage is the ion detector which consists of a negatively charged piece of metal known as a Faraday cup. This attracts the positively charged ions and is measured using a sensitive ammeter. The signal measured is proportional to the component parts of the ions passed through the quadrupole. Furthermore, it is important to note that species which can be multiply ionised, for example a krypton (Kr) atom which has been multiply charged will give different sized peaks relative to the charge they carry. A Kr^{2+} ion will give a peak twice the size of a Kr^+ ion.

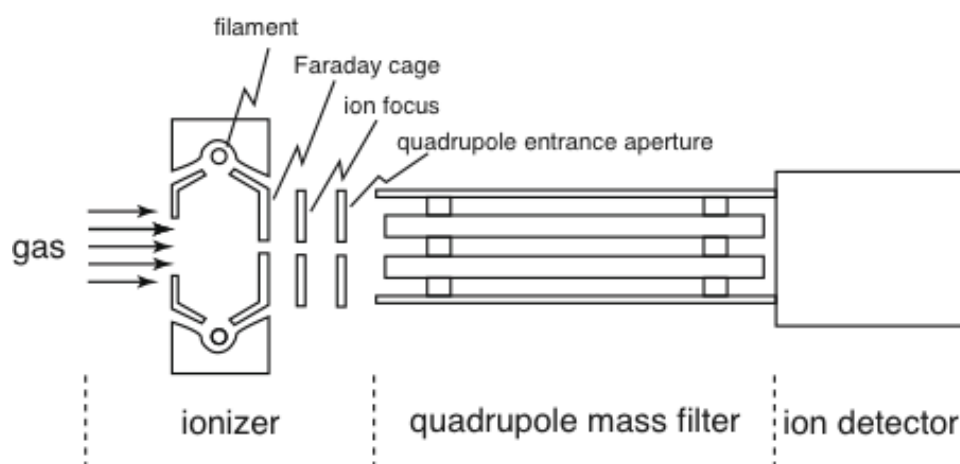


Figure 63 – Schematic diagram of the principle components of an RGA [322].

It is possible to increase the sensitivity of an RGA by including a secondary electron multiplier. Here a glass tube coated with a semiconducting material is included in the setup. When a single electron or ion bombards a secondary emissive metal plate it can induce the emission of between 1 to 3 further electrons, which if directed by the inclusion of a potential difference to another metal plate, can cause yet more electrons to be induced. By doing this the signal detected can be amplified up to 10^6 times, [323, 324] allowing for the detection of trace gases.

In this work a European Spectrometry Systems GeneSys EcoSys-P RGA was used. This instrument can measure any gas species up to 200 amu, with up to 64 sample species measured simultaneously, quantitatively or qualitatively. Sensitivities of up to ppb levels can be detected with a response time of 120m/s. No sample preparation was required as the instrument formed

part of a gas testing rig. The RGA was employed downstream of a sample being analysed and was present to confirm the presence of an injected gas which must first have passed over the sample at a known flow rate.

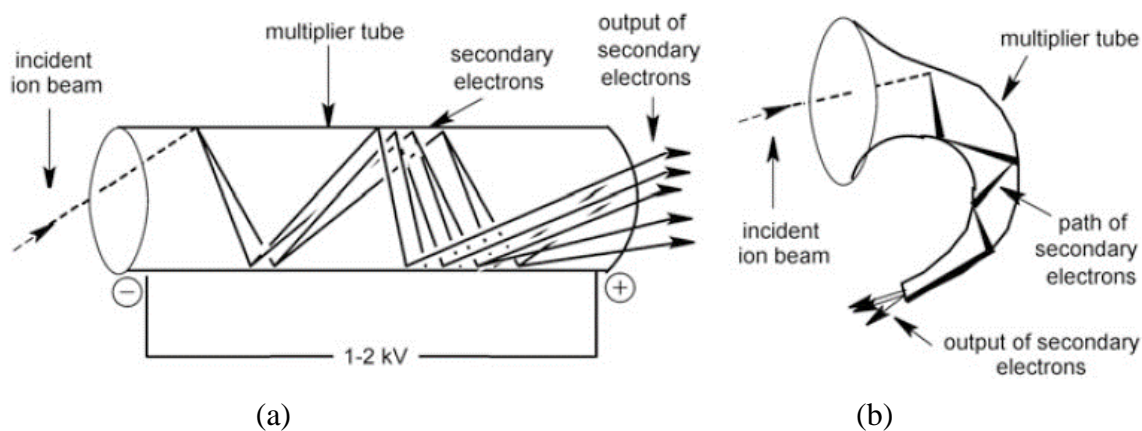


Figure 64 – Schematic diagram of (a) linear channel electron multiplier and (b) curved channel electron multiplier [325].

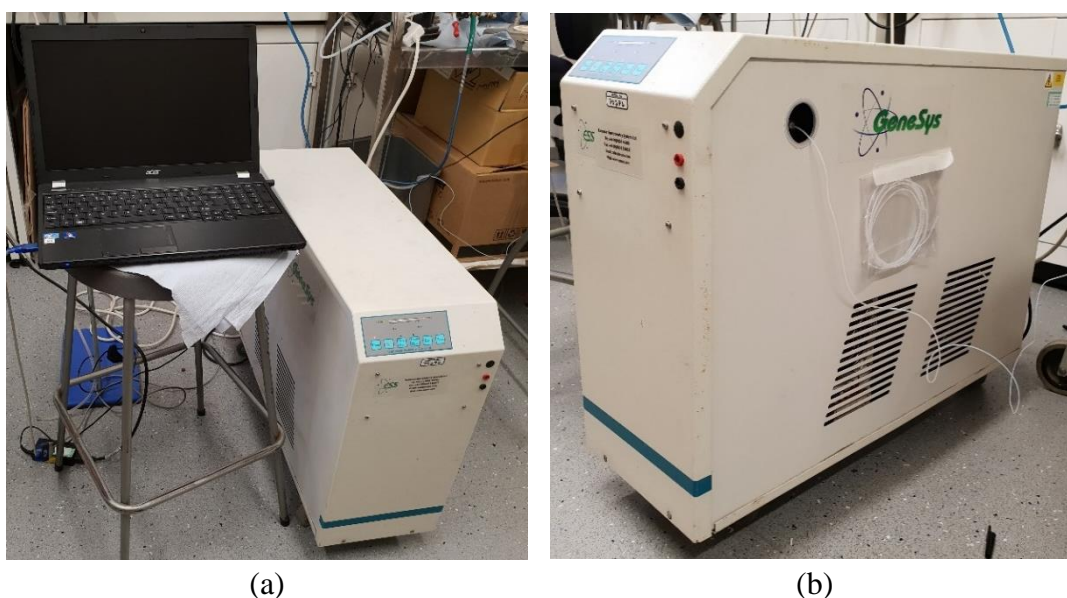


Figure 65 – (a) full RGA setup including a laptop computer for real time monitoring and recording and (b) close-up of RGA unit showing the capillary inlet attached to the gas test rig.

2.1.11 Dynamic Light Scattering

Dynamic light scattering (DLS) is a commonly used technique for measuring the size and distribution of particles in the nanometer and micrometer range; it may also be used to determine the shape of particles. DLS is widely used in many areas of nanotechnology [326-329]. There is also literature where DLS has been used in hydrogel analysis [329]. This makes DLS an ideal characterisation method of primary particle sizes for this project.

A monochromatic laser beam is directed at the suspension of particles causing Brownian motion to be excited. The wavelength of the light beam is altered upon hitting particles within the suspension, creating a Doppler shift: a difference in frequency between un-scattered and scattered light. Small particles (< 100nm) cause tiny differences in frequency resulting in quick fluctuations and a small Doppler shift, whereas for larger particles, fluctuations are longer resulting in a larger Doppler shift.

DLS is still considered an elastic scattering process where the energy of the primary beam is equal to the energy of the scattered radiation as the differences owing to Doppler shifts are minute. However, as there is a difference, DLS can be thought of as a quasielastic light scattering technique. [331].

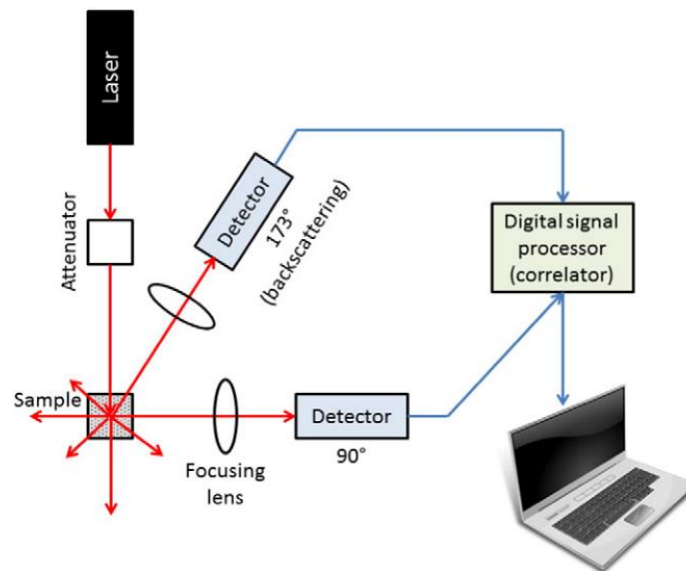


Figure 66 – Schematic drawing of a typical DLS setup [330].

For particle size to be calculated a description of the particle size distribution and its motion is obtained using the autocorrelation function and measuring the diffusion coefficient of the particle. The scattering vector (q) can be calculated using Equation 14.

$$q = \frac{4\pi n}{\lambda_0} \sin\left(\frac{\theta}{2}\right)$$

Equation 14 – Calculation of the scattering vector (q), where n is the solvent refractive index, λ_0 is the vacuum wavelength of the laser and θ is the scattering angle (nominally 90 degrees).

The translational diffusion coefficient (D) can now be calculated from the speed of the Brownian motion. Once D is known the hydrodynamic diameter (D_H) is calculable using the Stokes-Einstein equation.

$$D_H = \frac{k_B T}{3\pi\eta D}$$

Equation 15 – Stokes-Einstein equation used to calculate hydrodynamic diameter. k_B is the Boltzmann constant, T is temperature and η dispersant viscosity [332].

During this work a Malvern Instruments Zetasizer was used. This instrument is able to measure particle size diameters between 0.3nm to 10 μ m. It features a 633nm laser and can measure sample concentrations from 0.1ppm to 40% w/v. Samples to be analysed first had to be dispersed within a solvent and placed into a cuvette. In most cases the samples being analysed were nanoparticles produced via sol-gel methods and so could be readily dispersed in a solvent and recovered after analysis. This made DLS a non-destructive technique. Data can be exported as an ascii file for plotting in a suitable software package for graphical representation.

2.2 General Gas Testing Equipment

Samples which are thought to exhibit gas sensing properties were tested on a custom-built gas test rig, designed to measure responses to an injected gas. The rig included a range of different sensors aimed at improving the reliability of the data obtained, this ranged from a highly sensitive RGA to rugged commercially available handheld gas sensors as well as the samples produced. The system should be considered a closed one in the sense that detectors receive a direct gas stream. The only exception to this is the Crowcon T3 multi gas sensor (marked 15. in Figure 67) which did not have a direct coupling. In this instance a very fine stream of gas was directed at close range (>1cm) towards the instrument inlet using a glass Pasteur pipette connected to the gas stream. All other detectors had a closed connection.

The system enabled a number of variables to be included which increased the scope of the experiment. Firstly, the carrier gas (1) nominally used air, however other gases (N₂, Ar, etc.) could be coupled to the system instead of air. The volume of carrier gas travelling through the system could be accurately controlled; a rough increase/decrease in flow could be achieved using the gas regulator attached to the carrier gas cylinder (1). However, for a more accurate tuning of gas flow, a flow meter was included (3) which enabled adjustments to be made to cm³min⁻¹ tolerances. An injection point (4) which consisted of an enclosed rubber septum allowed gases and humidity of interest to be injected using a gas-tight syringe. Two syringes were available with volumes ranging from 0.1ml to 10ml. The gas initially selected in this work is CO₂. CO₂ is a linear molecule and a significant atmospheric pollutant known to contribute to the greenhouse effect. Dangerous in high concentrations is it of significant interest. Furthermore, CO₂ exhaled during a normal respiratory cycle may be analysed for remote

patient monitoring, which could prove useful in the medical field. MEA is a known CO₂ scrubber and hydrogels with on-board MEA have been synthesised, therefore this forms a logical analysis route. Future tests may involve NO₂ and SO₂ which are also linear molecules and may well form similar interactions with on board hydrogel solvents. Hydrogels were selected for their durability and ability to host large volumes of on-board solvents. They can be synthesised from non-toxic (bio)polymers and are easily adaptable in geometry. The relative humidity (%RH) of the system was also controllable from a gas bubbler (5). Saturated salt solutions were used to control the %RH. There is much literature on the use of saturated salt solutions in laboratory testing for relative humidity control [333-335]. A wide range of saturated salt solutions and therefore %RH were available [336]. The temperature of the gas(es) can be controlled using a tube furnace (6) in which a glass reactor (8) was inserted. There was also the option to include catalysis samples within the glass reactor (7) if desired. The sample under investigation (13) was placed on top of a Jandel four-point conductivity probe (12) which was fitted into a gas tight test cell (14) containing an inlet and outlet for the gas.

Static parts of the system include a zeolite filter (2) at the beginning of the system to remove any impurities which may arise from the gas supply. An RGA (9) and laptop computer (10) were included which represent the high sensitivity and reliability part of monitoring. Real-time monitoring of the system could be achieved using this instrument. The Jandel RM2 control unit (11) was adjustable in the sense that current could be changed. By adjusting the current, the voltage measured could be kept within the manufacturer's guidelines (under 200mV). A Crowcon T3 multi gas sensor (15) was included to confirm the presence of the sample gas post-test cell. Also included was a particle size analyser (16) to monitor the increase or decrease in gas concentration. Finally, a simple water bubbler (17) was included at the end of the system to confirm that gas had indeed progressed the whole system to the exit point (18).

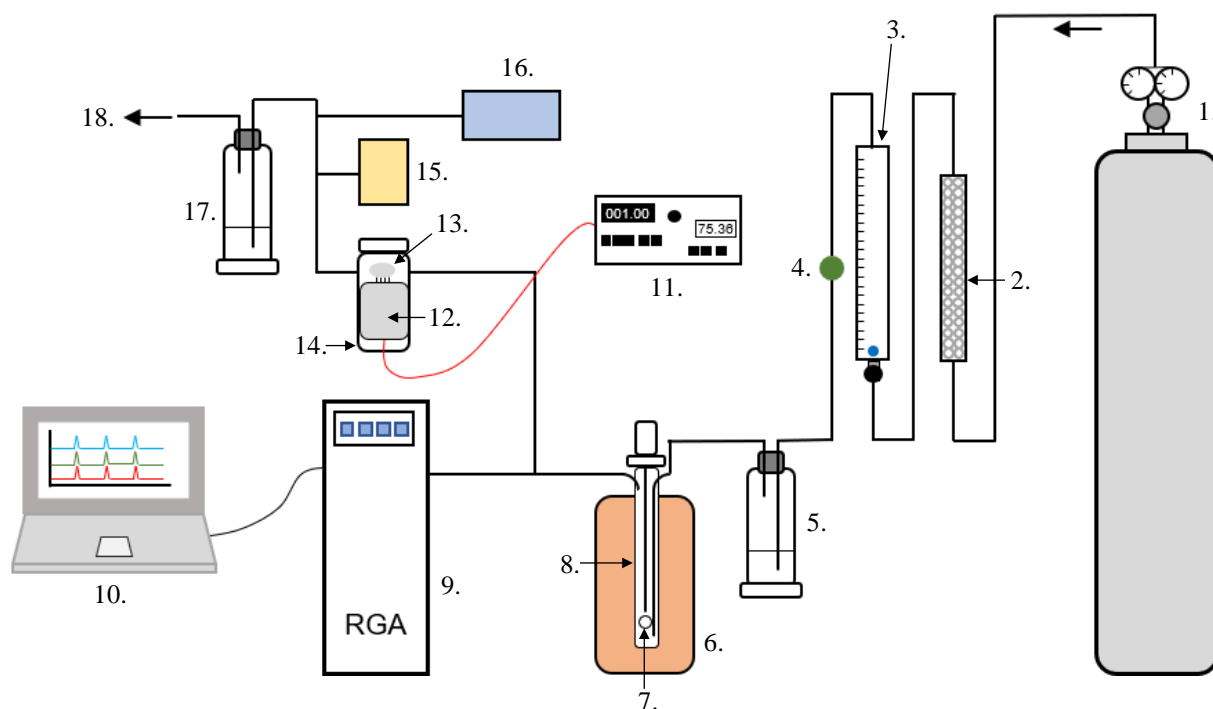


Figure 67 – Diagram of a custom-built test rig designed to measure the response of hydrogel samples to injected samples of gas. (1.) gas supply, (2.) zeolite filter, (3.) gas flow meter, (4.) gas injection point, (5.) relative humidity bubbler, (6.) tube furnace, (7.) optional catalysis sample, (8.) glass reactor, (9.) residual gas analyser, (10.) laptop computer, (11.) Jandel RM2 control unit, (12.) Jandel four-point conductivity probe, (13.) sample of interest, (14.) gas tight test cell, (15.) Crowcon T3 multi gas sensor, (16.) particle size analyser, (17.) water bubbler, (18.) gas exit stream.

The time taken for a test gas to travel through the system from injection to sensor response is important as it is indicative of the performance of samples under investigation. Typically the RGA indicates a response to an injected gas 2.5s from the moment of injection when flow rate of 250ml/min is used for the carrier gas. The accuracy of the flow meter used is $\pm 5\%$ of the maximum reading on the meter (in this case 1000ml/min). The RGA returns to baseline levels 4 to 5s from the moment of injection. This gives a reliable benchmark figure to work relate to.

The space time of the injected gas may be calculated by dividing the volumetric flow rate (250ml/min) by the volume of the sample (1cm^3).

2.3 General Hydrogel Production

2.3.1 Background

Hydrogels are three-dimensional crosslinked polymer networks that trap solvent molecules and that may be swollen by H_2O . There are two forms of crosslinking: a chemical one, based on the addition of functional molecules (crosslinker) bridging covalently the polymer's repeat

units together and a physical one, based on creating nodes/knots that are less soluble in water by freeze-thawing cycles.

Hydrogels were selected for this work owing to the adaptability and properties they exhibit. Their ability to be swollen with guest solvent(s) and to release this in a controlled manner make them highly desirable sweating surfaces. Furthermore the non-toxic and biodegradable nature of the polymer makes this class of material attractive for use in the natural environment and public domain. Lastly, hydrogels are highly tuneable, evaporation of guest solvent can be achieved through the degree of crosslinking, this property can also determine the durability and toughness of the material. The ability of a hydrogel polymer matrix to host metal oxide nanoparticles in a dispersed manner also makes them attractive electrochromic devices.

2.3.2 Chemically Crosslinked Hydrogels

Poly(vinyl alcohol) (PVA) powder was purchased from Sigma Aldrich (with M_w 89,000-98,000, 99+% hydrolysed) along with crosslinker glutaraldehyde (GA) 25% aqueous solution, ($\geq 98\%$ purity) and hydrochloric acid (HCl). These were used without further processing. Various weight percent aqueous solutions of PVA were produced (typically between 5-10%) by dissolving exact amounts of PVA powder in deionised (DI) water at 363K for 3 hours whilst stirring. From this an amount (typically 50cm^3) of PVA solution was added to a beaker and heated to 333K whilst stirring. A calculated amount of GA (depending on the level of crosslinking required) in acidic conditions (pH 4-5) controlled by the addition of HCl, was then added to the PVA solution, which was stirred before being cast into a plastic petri dish.

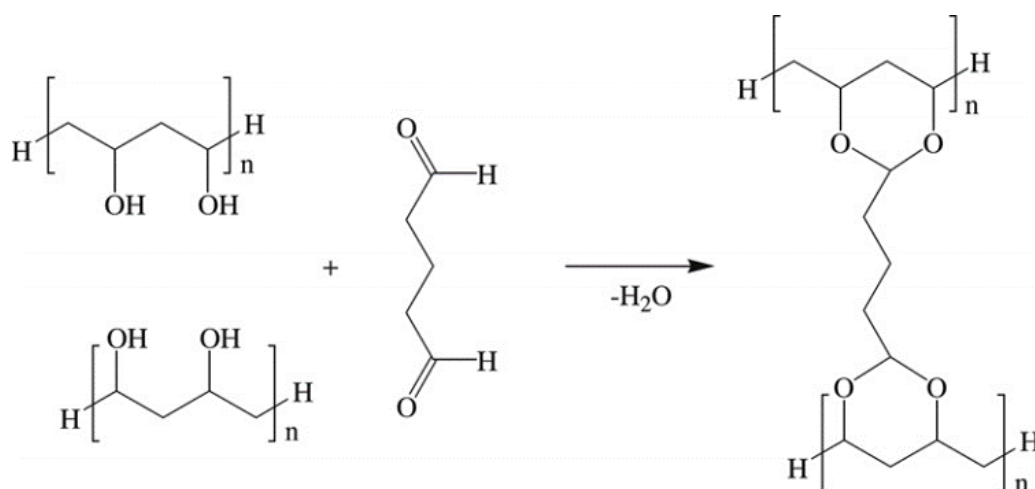


Figure 68 – Reaction mechanism of PVA crosslinking via a chemical method using glutaraldehyde [337].

Once the crosslinking reaction had occurred, the newly formed hydrogel was washed in acetone before being stored in a fridge at 276K to slow the rate of dehydration from the sample until it was ready for further use.

2.3.3 Physically Crosslinked Hydrogels

2.3.3.1 Conventional Freezer Method

Various weight percent aqueous solutions of PVA were produced with the GA step omitted as described in 2.3.2. From the stock solution, 50cm³ was added to a plastic petri dish covered with a lid. This was then subjected to several thermal cycles of freezing and thawing. A typical cycle involved freezing the solution to 248K overnight in a conventional freezer, before allowing it to thaw to room temperature (298K). This cycle was repeated 3 to 5 times depending on the degree of crosslinking required. Samples were kept covered by a lid at all times to reduce the risk of contamination and to minimise the evaporation rate of water from the PVA solution. Using this method multiple hydrogels could be produced simultaneously.

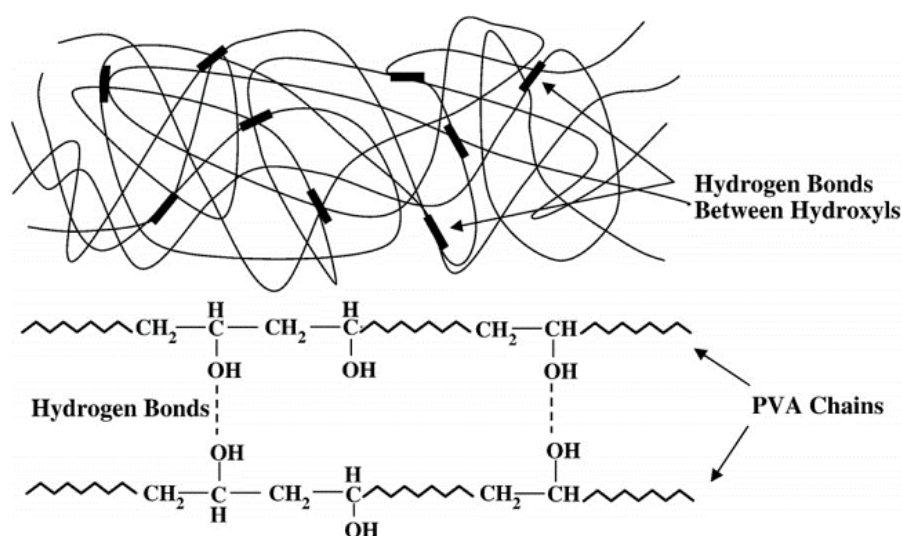


Figure 69 – Formation of PVA hydrogels based on the creation of nodes/knots which promote hydrogen bonding between polymer chains [338].

2.3.3.2 Liquid Nitrogen Method

A faster method following the same theory as described in 2.3.3.1 involved replacing the slow convention freezer step with a faster method based on the use of liquid nitrogen. As reported in 1.3.4.2 it is thought that the temperature range of freezing/thawing has an effect on the final properties of the gel and was the rationale behind use of this method. Here, liquid nitrogen (77K) was used to crash cool the PVA solution. This method allowed several thermal cycles to be completed in a few hours. However, the additional safety, cost, and controllability

implications of this method, made it less desirable for mass production. This method was however used on occasion.

2.3.4 Hydrogels Incorporating Functional Micro and Nanoparticles

Several methods have been used to incorporate functional microparticles (μP 's) and nanoparticles (NPs) within a PVA hydrogel matrix. Methods incorporated aspects of physical or chemical crosslinking which are a feature of hydrogel formation.

2.3.4.1 Synthesis of Tungsten Trioxide Nanoparticles

Tungsten trioxide (WO_3) NPs (approx. 50nm) were produced using a sol-gel route [339]. Tungsten powder was dissolved in hydrogen peroxide (H_2O_2) to form a peroxopolytungstic acid (PTA). To this was added an ethoxy-propoxy-ethoxylate (copolymer $\text{EO}_{20}\text{PO}_{70}\text{EO}_{20}$ – Pluronic-123) in ethanol (EtOH).

The mixture was refluxed at 353K for 2h at which point a colour change to dark blue occurred and a solid separated out. The solid is collected by standard filtration. It is then dried and calcined in a furnace at 773K for 5h to obtain WO_3 nanocrystals.

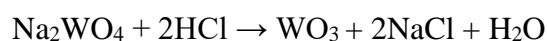
2.3.4.2 PVA Metal Oxide Slurry Method

Physically cross-linked 10 wt.% PVA hydrogels were loaded with a variety of metal oxide (M_xO_y) μP s and NPs to investigate the effect this would have on the emissivity (ϵ) of a surface when the sample was applied. The synthesis route for all of these consisted of producing a 10 wt.% aqueous solution of PVA. From this 50cm³ was taken for each sample. Between 1 to 20 wt.% of the desired M_xO_y was ground in an agate pestle and mortar with a small amount (typically 10ml) of PVA solution to create a PVA/ M_xO_y slurry. This step ensured a good level of particle dispersion within the sample. The slurry was then added to the remaining PVA solution and the 50cm³ sample was then stirred for 20min and cast in a petri dish. A cycle of freeze-thawing (298K to 248K to 298K) was then employed to create the physically-crosslinked sample.

2.3.4.3 In-situ PVA Metal Oxide Dispersion Method - Chemical Crosslinking

This approach involved synthesising WO_3 precursors within a PVA solution produced via the method described in 2.3.2. This method exploited a property of WO_3 , which is stability under acidic conditions. The method uses the acidic environment already created during hydrogel stabilisation. This second method had several advantages compared to the slurry method

described in 2.3.4.2. Firstly, the WO₃ precursors are more likely to be well dispersed and of nanometric size within the PVA matrix. This prevents coalescence and growth of bigger WO₃ crystallites. Furthermore, the preparation involved a ‘one-pot’ synthesis, with the reagents being measured by volume, rather than weight. Lastly in the case of the slurry, some μPs settled if not stirred. This was not the case with fully soluble reagents. WO₃ precursors were prepared from sodium tungstate as described in Equation 16.



Equation 16 - Synthesis of WO₃ from sodium tungstate [340].

Compared to the chemical crosslinking of PVA described in 2.3.2, Equation 16 is fast (for stoichiometric amounts of HCl). This posed the problem of segregation between rapidly formed (bigger) crystals of the precursors and the PVA crosslinked matrix. Ideally, Na₂WO₄-containing crosslinked PVA needed to form first, allowing Equation 16 to happen within the gel. Several techniques were explored with the most successful technique being used to make a solution of PVA, Na₂WO₄ and GA. Onto this diluted HCl was gently cascaded on top of the solution. This allowed the HCl to permeate slowly through the PVA solution, crosslinking it by activating GA and allowing Equation 16 to take place within a crosslinked matrix.

2.3.4.4 In-situ PVA Metal Oxide Dispersion Method - Physical Crosslinking

An alternative route allowing physical crosslinking (non-acidic) to be used with the method outlined in 2.3.4.3 has also been devised. Aqueous PVA was mixed with Na₂WO₄ and GA to form solution which then underwent the freeze-thawing cycles outlined in 2.3.3. The gel was then placed in a bath of diluted HCl to initiate the reaction shown in Equation 16. This method had limitations, the most apparent being how to ensure the reaction described in Equation 16 reached an endpoint. Another limitation was the degree of physical crosslinking required to ensure that PVA did not further dissolve in dilute HCl.

2.3.4.5 Electrochromic Testing

PVA-WO₃ nanocomposite hydrogels which were to be examined for electrochromic colour changes were cut to reduced sizes (typically 5mm³) before being sandwiched between fluorine doped tin oxide (FTO) or indium doped tin oxide (ITO) glass. This step enabled the colour change to be observed, whilst providing a conductive route. Electrodes from a power supply with controllable voltage/current were attached to the glass using copper tape, thus completing the circuit.

2.4 Breathing Experiments

Here the author has briefly explored real-time analysis [341] of CO₂ (m/z=44) and HCN (m/z=27) in exhaled air using an RGA (VG Sensorlab and ESS Genysis) a well-established technique for CO₂ detection [342]. Ultrafine Particle (UFP) concentrations were also detected in tandem with RGA measurements using a TSI P-Trak 8525 condensation particle number counter (the performance of this has been previously reviewed [343]) Repeated inhalation-exhalation by the author, his supervisor and a colleague while they were sedentary and inactive during tidal breathing in urban air was measured taken as a function of time.

The purpose of these experiments were to assess if the samples and materials used in this project may additionally form the basis of a low cost respiratory indicator that could enable remote patient monitoring of vulnerable or elderly people by a healthcare professional.

2.5 Microconductivity

It was thought that *micro*-conductivity may provide an automated HT scanner detecting oil in water drawing parallels with petroleum electrical resistivity tracking of oil-water interfaces. Electrical resistance tomography (ERT) is used to probe crystallisation reactors [344], steam injection [345, 346], groundwater/oil-wells [347], liquid interfaces [348, 349] and flow in pipelines.

Initial attempts were made to test a petroleum electrical resistivity tomographic tracker (PERTT) unit. This works with a lap-top powered electrode array from Industrial Tomography Systems plc (ITS). The PERTT probes can be 1cm to 3m in depth/length and can be submerged. They are powered at 0.1mA. Importantly, they can probe oil and water-in-oil as well as the easier oil-in-water and water phases.

Attempts were made to use low cost PLA/G 3D printed and Cu electrodes to measure oil and water conductivities. This was achieved by connecting identical length electrodes of PLA/G filament to a multimeter. Filaments were separated using an epoxy-resin (Araldite[®]) with equal lengths emerging from a watertight cap and with a known distance (2mm) between filaments. The enabled the filaments to be submerged in the water-oil being analysed. Lengths of Cu wire were cut to identical lengths and connected to a multimeter. These were kept separate by plastic insulator. Measurements were taken using a commercial multimeter at 30s intervals.

2.6 Summary of Techniques

When selecting analytical techniques for characterisation of materials, it is important to select methods which are appropriate. Methods must be able to tell the user about the sample reliably. Accuracy, which is the closeness of an obtained value to that of the true value and precision, the closeness of obtained values to one another, are highly important in chemical analysis. Values should also be reproducible, such that identical results may be obtained when repeating the experiment or technique.

It is therefore prudent to understand the margin of error which a technique may have. This may be stated as a $\pm\%$ value or as a specific value, i.e. $\pm 1\text{K}$. This means that the value obtained may be greater than or less than the true value by the margin given. Other types of error, such as systematic errors may occur when there is a fundamental design flaw, or incorrect set-up of parameters in an experiment. This type of error commonly results in the values obtained being inaccurate by the same amount. It is important to note that these values may be precise (i.e. closely resembling one another) but not accurate.

The advantages of the techniques chosen for this work are that they are established, commonly used techniques and so may be relied upon. The accuracy and precision of these techniques are typically $\pm 2\%$ at worst. Methods are generally fast, able to give results in minutes (FTIR, Raman, DLS, SEM-EDX, IRT, RGA) or hours (TGA, DSC). Sample preparation for analysis is also quick and simple and in some cases non-destructive.

Table 9 - Summary of analytical techniques used and reasons for selecting.

Technique	Purpose	Reason selected
3D printing	Creation of polymer substrates for further processing as gas sensors/electrochromic devices.	Highly tuneable, able to print complex geometries, fast, safe, can process materials attractive to this work.
SEM-EDX	Viewing of structural features within polymer matrix, particle size analysis, elemental composition.	Fast, reliable, able to view nanometer scale features and give elemental composition mapping, non-destructive.

TGA	To investigate the thermal stability and properties of a material within a controlled environment.	Standard, reliable technique used to determine the quality of 3D printed precursors and processed materials compared to their analytical grade counterparts. Also useful at elucidating thermally controlled side reactions of materials.
DSC	Determining the physical state of bound water in a hydrogel matrix.	Controllable cooling and heating rates of this technique enables the heat flow required to thaw or freeze on board water to be determined. This method also enables the physical state of water to be determined.
IRT	View the thermal characteristics of materials and surfaces in the IR waveband.	A primary technique in this work for determining the cooling effectiveness of the hydrogels/sweating surfaces when applied to a building surface. Spot, line and area measurements can be taken simultaneously enabling a vast amount of data to be collected.
Raman	To analyse the 3D printed PLA-Graphene samples and filament and to determine graphene content.	Highly regarded and primary technique for graphene determination. Filaments were purchased from a manufacture, with specific graphene content confidential. Used as a confirmatory technique to prove graphene was indeed present.
FTIR	Determination of organic compounds,	Useful in drying studies with a variety of solvents and for controlled hydrolysis experiments to determine if hydrolysis had indeed taken place. Finally useful at comparing analytical grade materials to 3D printer filaments.
Four point electrical conductivity	Accurate technique for measuring current/resistance changes across a surface.	Four point conductivity is more accurate than 2 point methods and with the geometric factor incorporated is a reliable technique to measure the surface resistance of a material.

RGA	Determination of gaseous compounds via mass/charge ratio	Robust and reliable mass spec which can be used indoors and outdoors, can be attached to a gas rig and gives rapid results which may be viewed in real time, particularly useful at determining is injected pulses of gas have traversed the gas rig system.
DLS	Used for particle size analysis	Minor used technique, but able to give particle size range and average size of metal oxide nanoparticles in a solvent. Particularly useful when used in conjunction with SEM-EDX to investigate agglomeration.

Synthesis techniques have been obtained from reliable peer reviewed journals and use techniques which do not require complex apparatus, or high temperatures and pressures. Because of this, the chemistry in this project may be considered “green chemistry”.

3 Drying Characteristics and Hydrolysis of Polyvinyl Acetate

The purpose of this chapter is twofold; firstly to determine how inclusion of a variety of organic solvents may affect the drying rate of a PVA-Metal Oxide or PVAc-Metal Oxide thin film. Secondly, to investigate if catalysed hydrolysis of PVAc to PVA is possible with a variety of on-board guest solvents.

The drying times of films are relevant to the electrochromic and IR coating aspects of this work. It is possible that a thin film may need to be applied to a surface rapidly, for instance by security services or search and rescue teams. Atmospheric and weather conditions may result in the film being washed off or damaged and so quick drying is essential. Furthermore, the rate of solvent evaporation may enable specific tuning of hydrogels which are to be used as sweating surfaces. This would mean that hydrogels may be preloaded or regenerated with a specific solvent to increase or decrease the cooling effect based on the dynamic conditions of the building and atmosphere.

Hydrolysis of PVAc to PVA is an interesting step in this work. PVA does not readily dissolve in many organic solvents, however PVAc does. PVAc is the precursor to PVA and therefore it is relevant to investigate if controlled catalysed hydrolysis is possible whilst retaining on-board solvent. This will be particularly useful for electrochromic thin films in which the electrochromic aspect (metal oxide) will be dispersed within the polymer matrix.

3.1 Introduction

PVA does not dissolve readily in organic solvents. Therefore attempts at tuning the rate of on-board solvent evolution by swelling the PVA polymer matrix with solvents other than H₂O proved difficult. However, as described in **1.5.1**, PVA is produced via hydrolysis of PVAc. Interestingly, PVAc is readily dissolved in a range of organic solvents. Therefore, the possibility of hydrolysing PVAc to PVA whilst dissolved in an organic solvent was investigated.

Drying rates of PVA are important in the application of PVA-M_xO_y nanocomposites to a surface. Commercial use of these materials, for example in stealth coatings, or night-vision taggants is envisioned. These materials may be sprayable onto a surface which may be detected by an IR camera. This would be very useful in emergency situations at night.

3.2 Aims and Objectives

The aim of this section of work was to tune the drying rates of PVA coatings via catalysed hydrolysis of PVAc dissolved in a range of organic solvents (MA, MF, EA, MEK and DCM). IRT was used to analyse solvent evaporation rates and FTIR to track the progress of hydrolysis.

3.3 Results

3.3.1 PVAc Drying Times with Organic Solvents

Firstly, drying times of various organic solvents with dissolved PVAc were investigated. The range of solvent selected typically had low boiling points and subsequently high vapour pressure compared to air at 293K. Importantly, PVAc readily dissolved into all solvents selected.

3.3.2 Scanning Electron Microscopy of PVAc Films in Various Organic Solvents

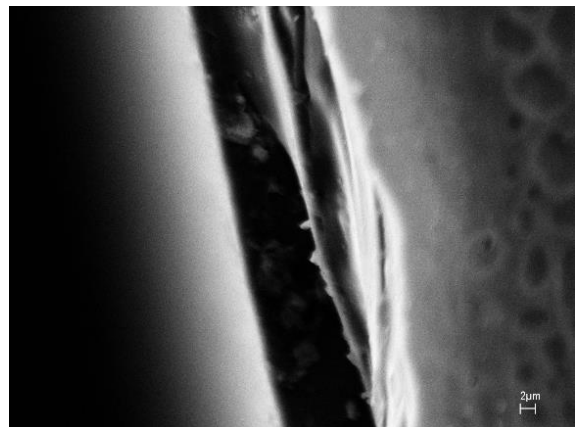
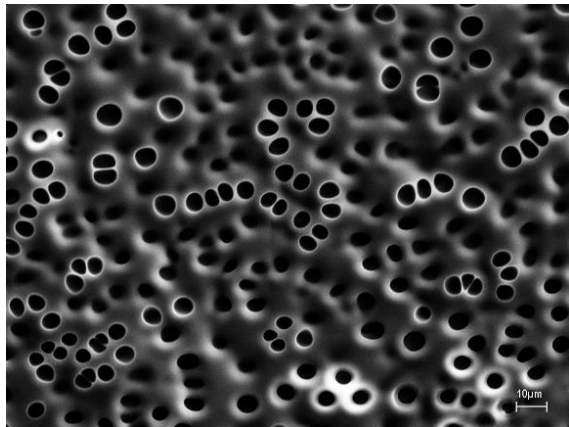
PVAc was dissolved into a variety of solvents with concentrations of 5, 8 and 10 wt.%. Table 10 outlines the properties of the solvents used. Samples were prepared at room temperature by dissolving the appropriate wt.% of PVAc into the selected solvent. The sample was covered (to prevent solvent evolution) and gently agitated for 1h, by which point all the PVAc had dissolved fully. All samples gave colourless solutions.

Table 10 – Solvents used in PVAc drying time experiments.

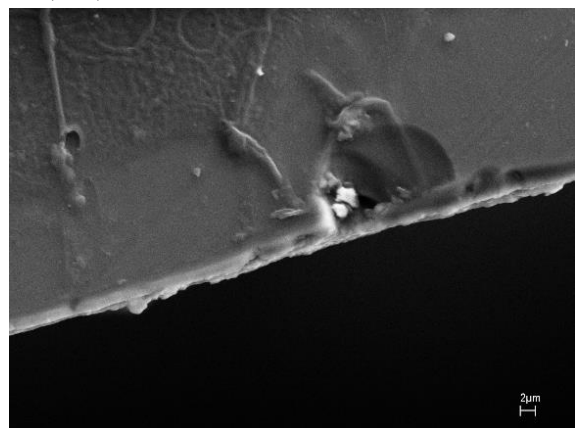
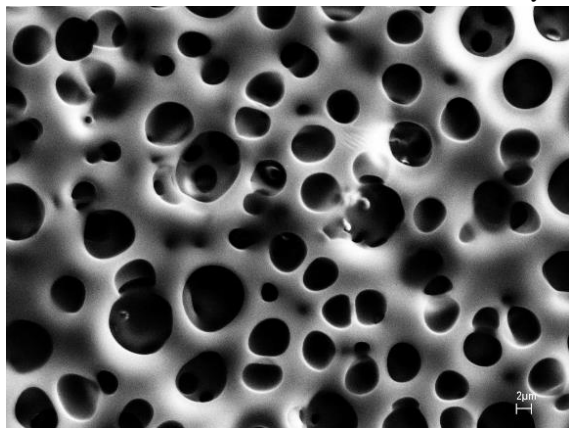
Solvent	Boiling point	Vapour density	Vapour Pressure*
Methyl Formate (MF)	306K	2.10	65.3 kPa (293K)
Dichloromethane (DCM)	313K	2.90	47.1 kPa (293K)
Methyl Acetate (MA)	330K	2.55	22.0 kPa (293K)
Ethyl Acetate (EA)	350K	3.00	9.7 kPa (293K)
Methyl Ethyl Ketone (MEK)	353K	2.49	9.5 kPa (293K)

*vs Air at 293K

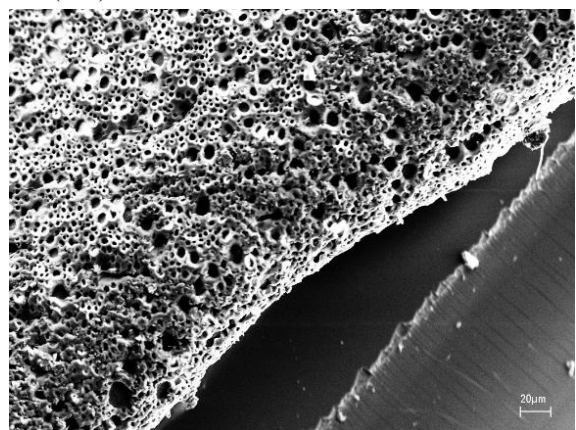
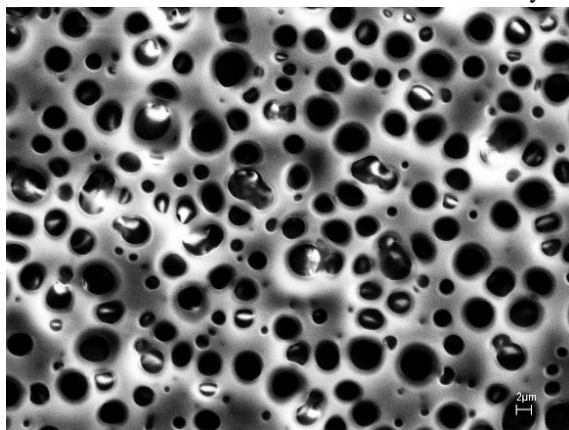
PVAc films were produced by dip coating a glass slide into solutions of PVAc/solvent. Once dried these were analysed by SEM. Film thickness for the samples analysed varies from 2-5 μ m. It appears that samples with a lower boiling point give thinner films, possibly related to the speed of drying. Hole diameters seem to vary from 2-10 μ m in size. The existence of holes in PVAc films is most likely due to the rapid evolution of solvent from the polymer matrix upon casting as a film. Boiling points for the samples used are low and therefore evaporation would be quick.



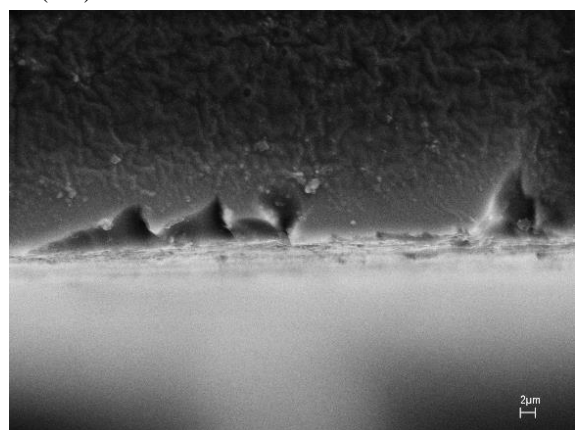
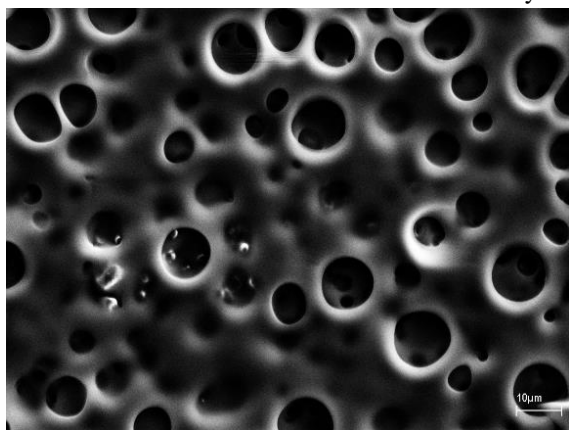
Methyl Acetate (MA)



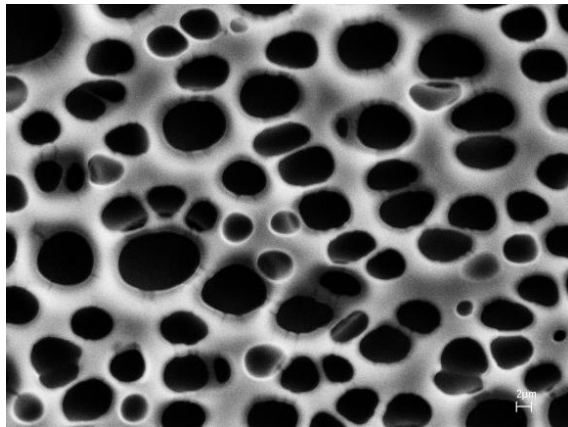
Methyl Formate (MF)



Ethyl Acetate (EA)



Methyl Ethyl Ketone (MEK)



Dichloromethane (DCM)

3.3.3 Fourier Transform Infrared Spectroscopy

Fourier transform infrared (FTIR) coupled with an ATR diamond crystal accessory was used in transmittance mode to characterise specific chemical groups and particularly to investigate the effect of PVAc concentration on the host solvent. A resolution of 2cm^{-1} and 45 repeat scans were selected to obtain accurate and reliable data.

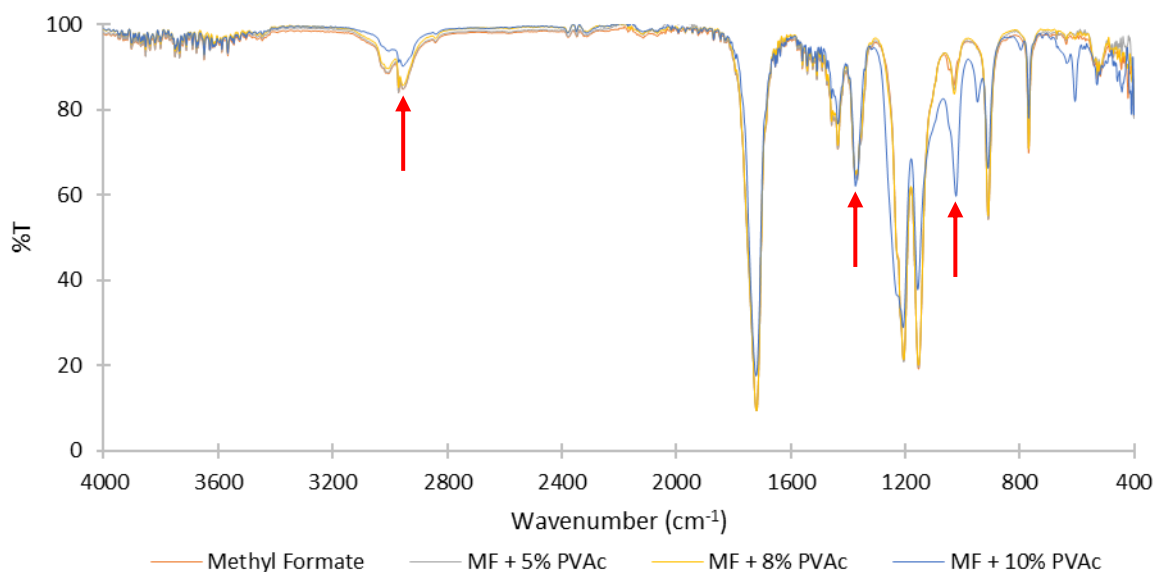


Figure 70 – FTIR-ATR spectra of 5, 8 and 10wt.% PVAc dissolved in methyl formate.

The spectra obtained shows many peaks and identification of the compound each bond originates from proved complex. Spectra obtained, mostly show good agreement between all samples analysed. Peaks identified by a red arrow (and highlighted in Table 21) show bonds which have either been shifted, distorted or show bonds in a different environment. The C-H stretch identified at 2954cm^{-1} , 90.2%T for sample MF + 10%PVAc is of higher transmittance and lower wavenumber than other samples in that region. It is thought that this specific bond

relates to PVAc instead of MF, unlike others in that region. Similarly at 1022cm^{-1} , 59.8%T the C-O stretch identified is likely to be from a different environment to other C-O stretches in this region.

The C-H bending identified at 1373cm^{-1} , 64.8%T & 62.1%T exists at a different wavenumber to the C-H bending identified for MF. In this case, it is thought that the MF has been distorted by the inclusive PVAc.

Overall, when overlaid, no single spectra is obviously different to others obtained, indicating in this case that PVAc and any new bonds associated with dissolution in MF is of too lower concentration to be detectable, or has been masked by the strong solvent spectra.

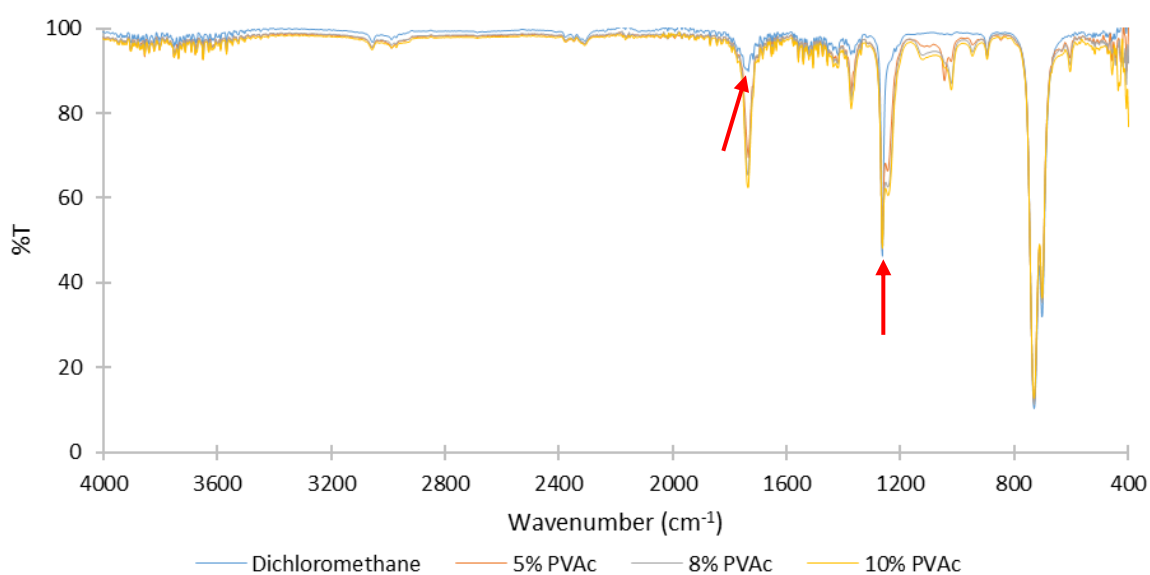


Figure 71 – FTIR-ATR spectra of 5, 8 and 10wt.% PVAc dissolved in dichloromethane.

The FTIR spectra for DCM is fairly simple, with only C-H, or C-Cl bonds present in the compound. The bond identified at 1734cm^{-1} , 89.9%T for the DCM sample is different to the C=O stretch at the same wavenumber for samples containing PVAc. In the case of DCM, this peak may be identified as a C-H aromatic overtone. The transmittance value is significantly higher than the transmittance values for PVAc containing samples (~65% T).

A peak which the author has had trouble identifying relates to the DCM spectra and is at 1263cm^{-1} , 46.4%T (highlighted in purple in Table 22). This peak also exists for PVAc containing samples where it has been identified as a C-O stretch. However, no such bond exists in DCM. The author therefore believes that this peak may correspond to a different aromatic overtone, or that the DCM sample has somehow become contaminated, possibly via ineffective cleaning of the ATR crystal between sample runs.

When overlaid, no single spectra (excluding DCM at 1734cm^{-1}) is obviously different to others obtained, indicating in this case that PVAc and any new bonds associated with dissolution in DCM is of too lower concentration to be detectable.

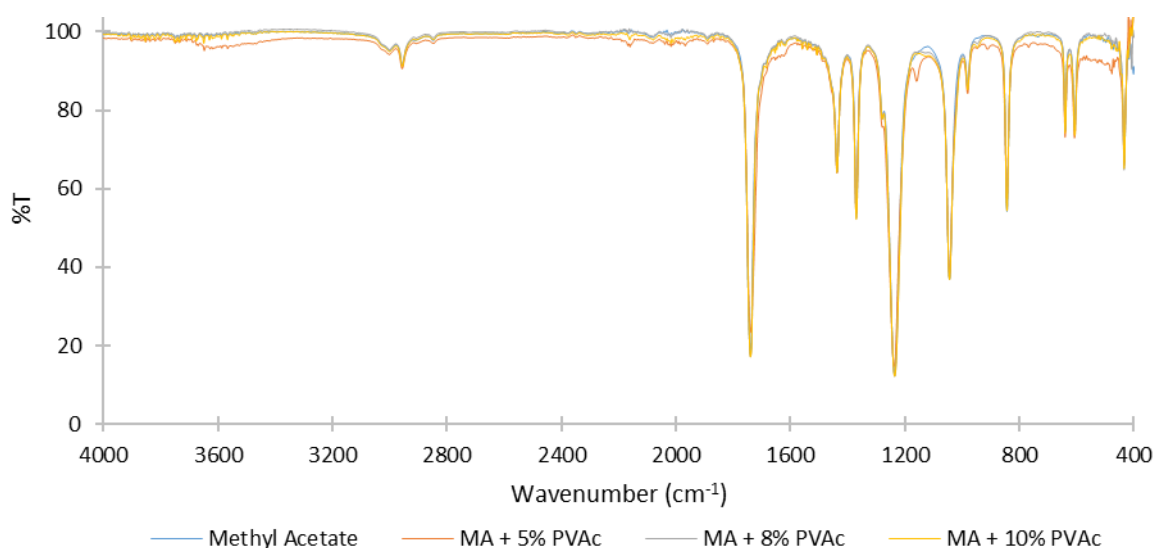


Figure 72 – FTIR-ATR spectra of 5, 8 and 10wt.% PVAc dissolved in methyl acetate.

The spectra shown in Figure 72 is simplistic compared to others investigated in this work. Bonds, associated wavenumbers and %T values are all close. Spectra of neat MA and MA containing PVAc when superimposed show near perfect alignment indicating that PVAc and any new bonds associated with dissolution in MA is of too lower concentration to be detectable or has been masked by the strong solvent spectra.

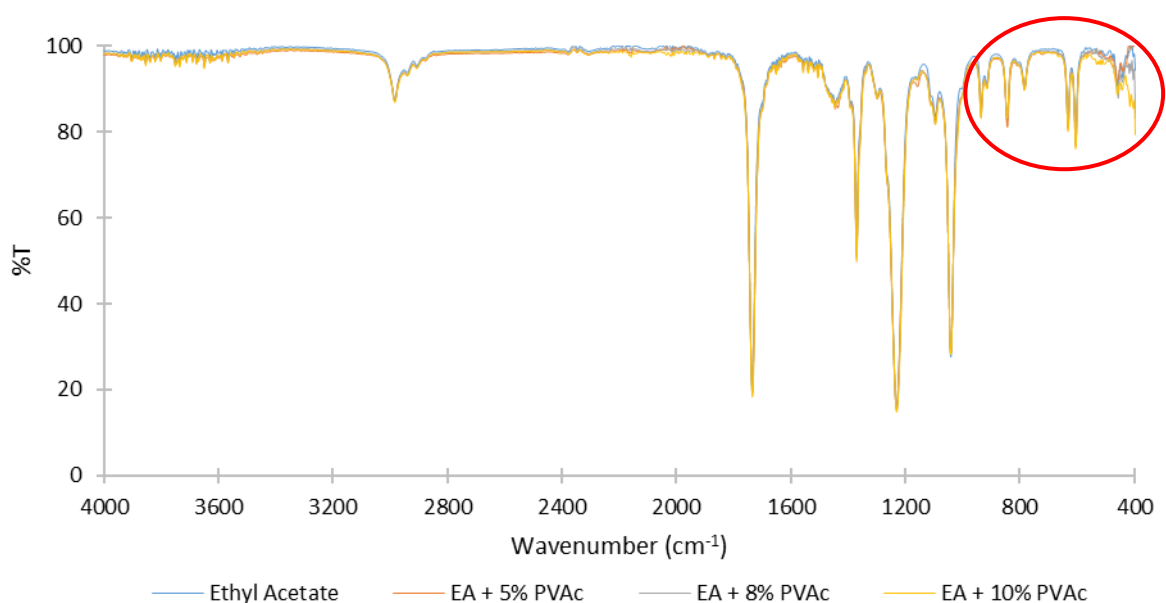


Figure 73 – FTIR-ATR spectra of 5, 8 and 10wt.% PVAc dissolved in ethyl acetate.

The spectra for EA and EA with dissolved PVAc shown in Figure 73, is nearly identical to the MA spectra shown in Figure 72. This is understandable given their near identical chemical

structure. Of note are the additional C-H bending peaks (circled) in the fingerprint region (from 1000-500 cm^{-1}) indicative of different C-H environments.

As with Figure 72, superimposing spectra, does not indicate any noticeable differences; with %T within 2-3% of each other indicating minimal distortion and wavenumber values the same throughout.

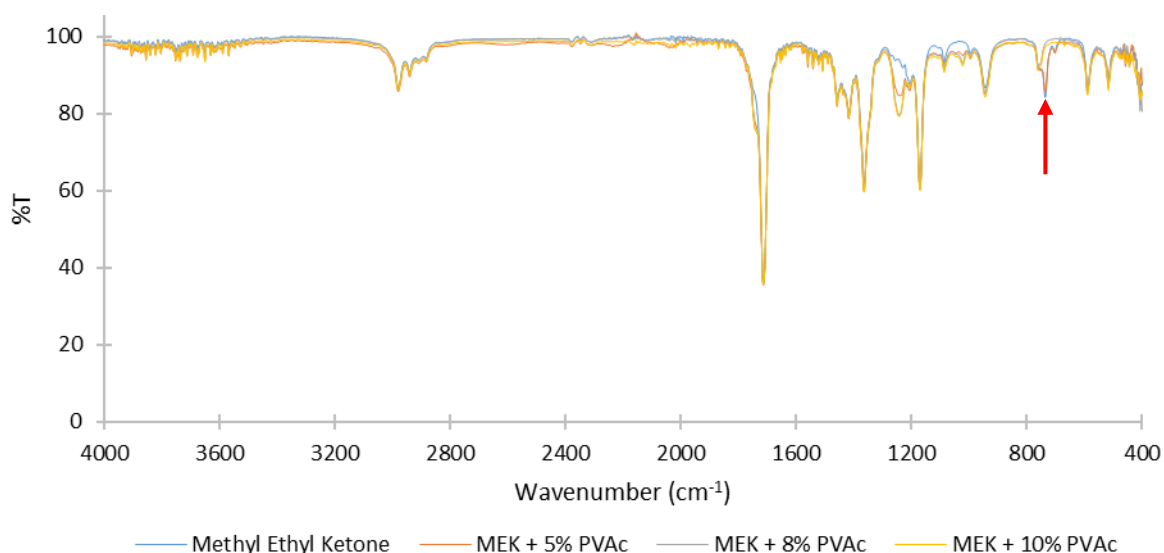


Figure 74 – FTIR-ATR spectra of 5, 8 and 10wt.% PVAc dissolved in methyl ethyl ketone.

The spectra for MEK and MEK with dissolved PVAc is shown in Figure 74. Broadly speaking all samples give near-identical spectra. However a C-H bend exists for neat MEK and MEK + 5% PVAc at 736 cm^{-1} , 84.3%T (highlighted in Table 25). This peak is not apparent for samples of MEK with 8 and 10% dissolved PVAc. This is interesting and suggests that an environment which existed before the inclusion of PVAc ceases to once the PVAc concentration passes a certain point (in this case between 5-8%). The author believes that this shows the initiation of a reaction, however it is difficult to conclude if this reached an end point and what the product(s) were as no new different bond exists in the MEK + 8/10% PVAc samples.

Overall, visual observations indicate that PVAc powder may be successfully dissolved in a range of organic solvents. FTIR generally confirms uniformity between different concentrations of dissolved PVAc. However, in some cases the different wavenumber and %T for the same bond, indicate that there is traces of undissolved polymer.

3.3.4 Infrared Thermography of Organic Solvents

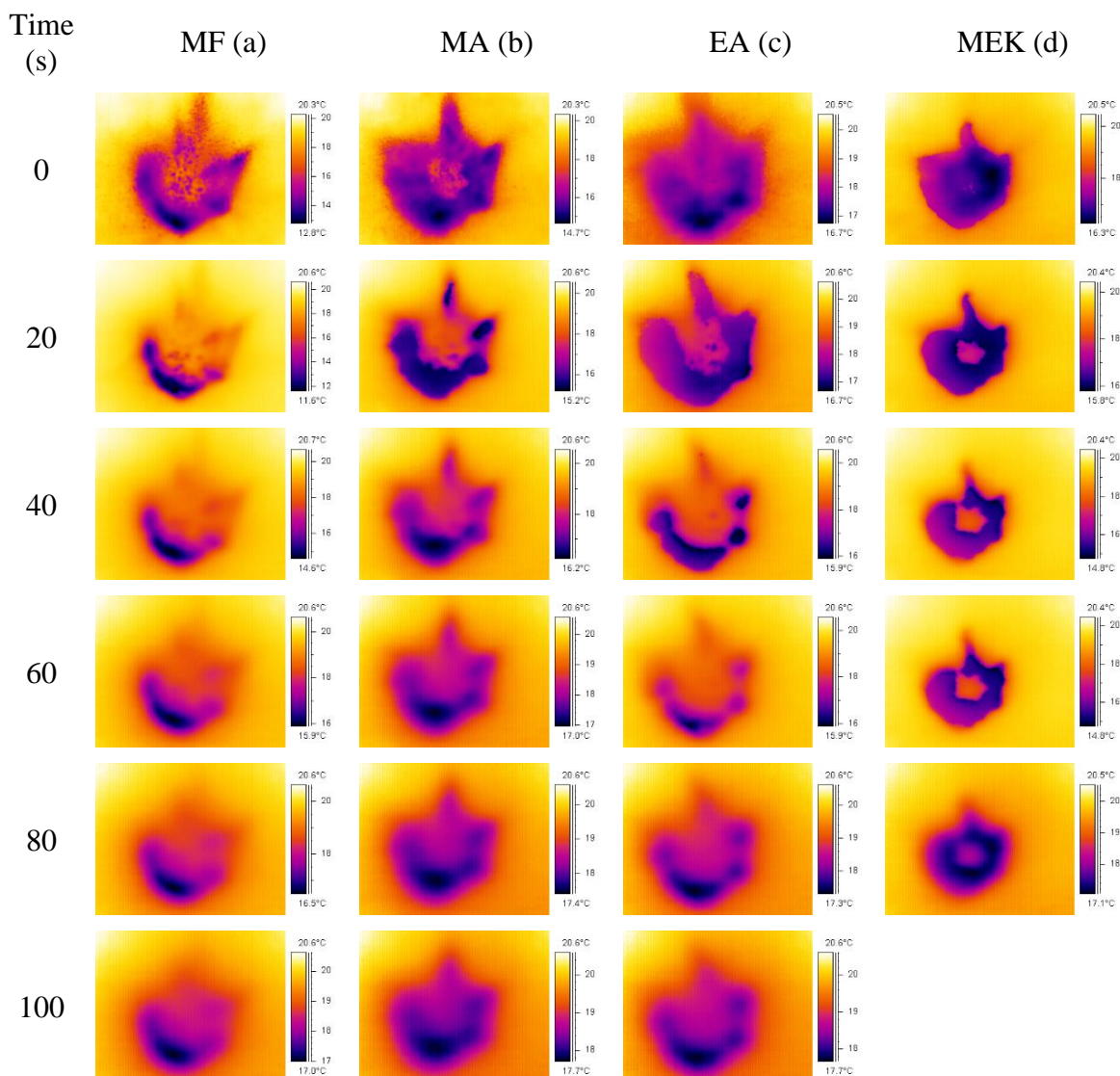


Figure 75 – Thermal images of (a) MF (b) MA (c) EA and (d) MEK showing the different evaporation characteristics from a 1ml drop of solvent onto a bench surface over time.

IRT was used to investigate how the solvents selected affected the surface applied to. Samples were used as received without further treatment. Applications to a cleaned whiteboard were made using a commercially bought spray bottle. Approximately 1ml of solvent was delivered in a single spray. Thermal images were obtained at 1s intervals for 2 minutes. All spraying experiments were conducted at 294K.

MF recorded the largest change in temperature with a minimum of 284.75K, 10K cooler than the surface applied to. IRT images also show MF to have the smallest cooled area (compared to the initial spray) after 100s. DCM images were unobtainable as the spray bottle was incompatible with DCM resulting in “clogging” of the spray bottle nozzle. The final MEK

image was also unreliable owing to the loss of focus by the IR camera when imaging this sample.

3.3.5 Infrared Thermography of Organic Solvents with 5wt.% PVAc

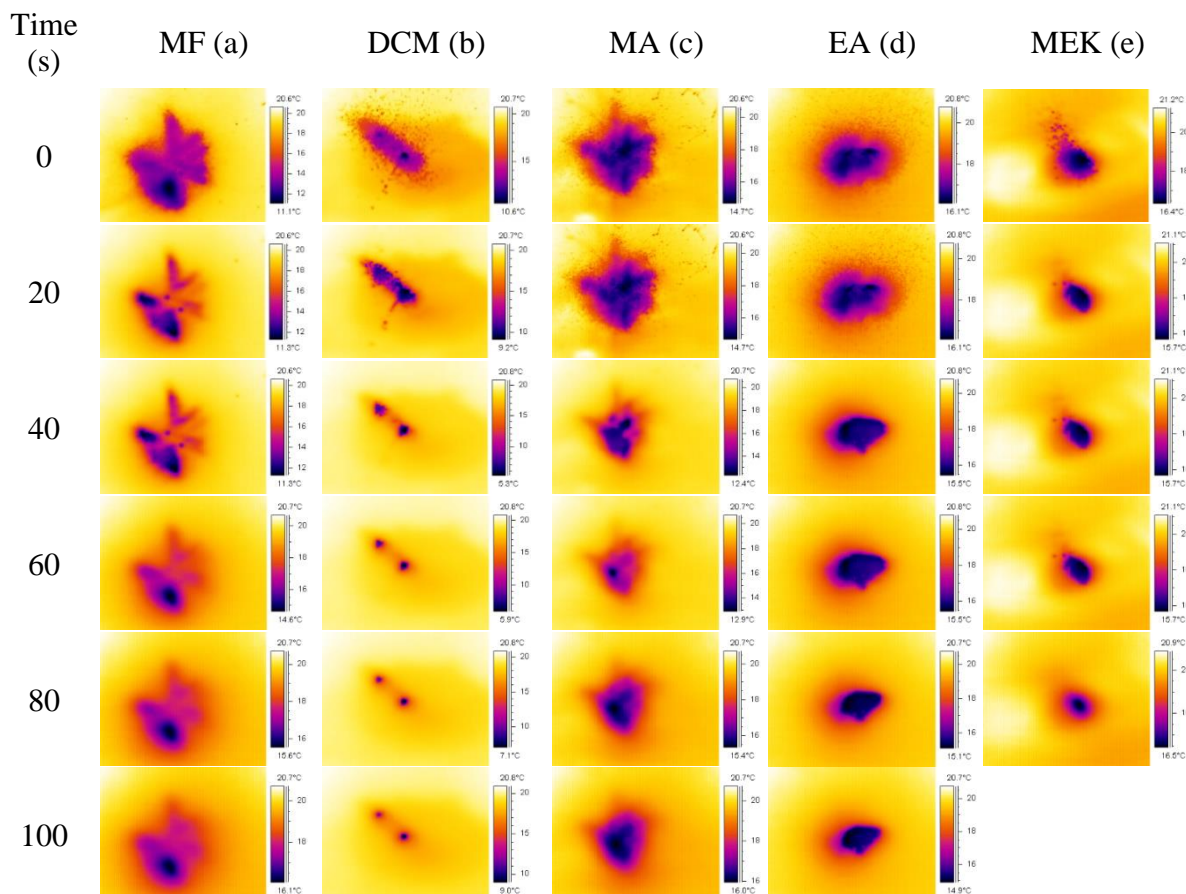


Figure 76– Thermal images of (a) MF (b) DCM (c) MA (d) EA and (e) MEK with 5wt.% dissolved PVAc showing the different evaporation characteristics from a 1ml drop of each solvent mixture onto a bench surface over time.

Continuing investigations from section 3.3.4, solvent evolution experiments were repeated, but with inclusive PVAc. 5wt.% of PVAc was dissolved in each solvent using the method described in 3.3.2. Samples were sprayed onto a cleaned whiteboard using a commercially bought spray bottle. Approximately 1ml of solvent was delivered in a single spray. Thermal images were obtained at 1s intervals for 2 minutes. All spraying experiments were conducted at 294K.

DCM was this time investigated, however a different method of delivery was used (glass pipette) which delivered the same volume of sample as the spray bottle but in a less disperse manner (2 drops can clearly be seen in Figure 76 (b)). MF again performed well with the majority of solvent evaporating by 100s with the exception of a non-disperse region. Other solvents investigated were still present in significant amounts after 100s.

Based on the investigations in 3.3.4 and 3.3.5 the author decided that MF was the most appropriate solvent to progress to hydrolysis investigations.

3.3.6 Fourier Transform Infrared Spectroscopy of Controlled PVAc Hydrolysis

Controlled hydrolysis of PVAc was conducted using three catalysts: NaCl, MgCl₂ and Mg(NO₃)₂ to evaluate the most effective method. The ionic strength is important here as it affects the solvation of reactants and intermediates in turn affecting the reaction rate. FTIR was selected to investigate new bond formation within the samples. 8wt.% PVAc was dissolved in MF and 8wt.% of catalyst added to the solution. Hydrolysis of PVAc is base catalysed and during the reaction CH₃COOH will be produced. The inclusion of NH₄OH neutralises CH₃COOH enabling the reaction to progress.

FTIR spectra were taken at regular intervals (21, 88 and 133hrs). The 21hr spectra has been omitted from the results as there was significant noise interference rendering it unreliable. A resolution of 2cm⁻¹ and 45 repeat scans were selected to obtain accurate and reliable data.

Figure 77 shows the spectra for unprocessed PVA and spectra taken at points from the initiation of the hydrolysis reaction. It is quite clear that hydrolysis has not taken place with no new bonds being formed (O-H would be expected). Possible reasons for this are acid rather than basic conditions existing in the reaction medium. This reaction was also undertaken at room temperature (298K) and even with the presence of a catalyst, may not be sufficient to overcome the activation energy barrier.

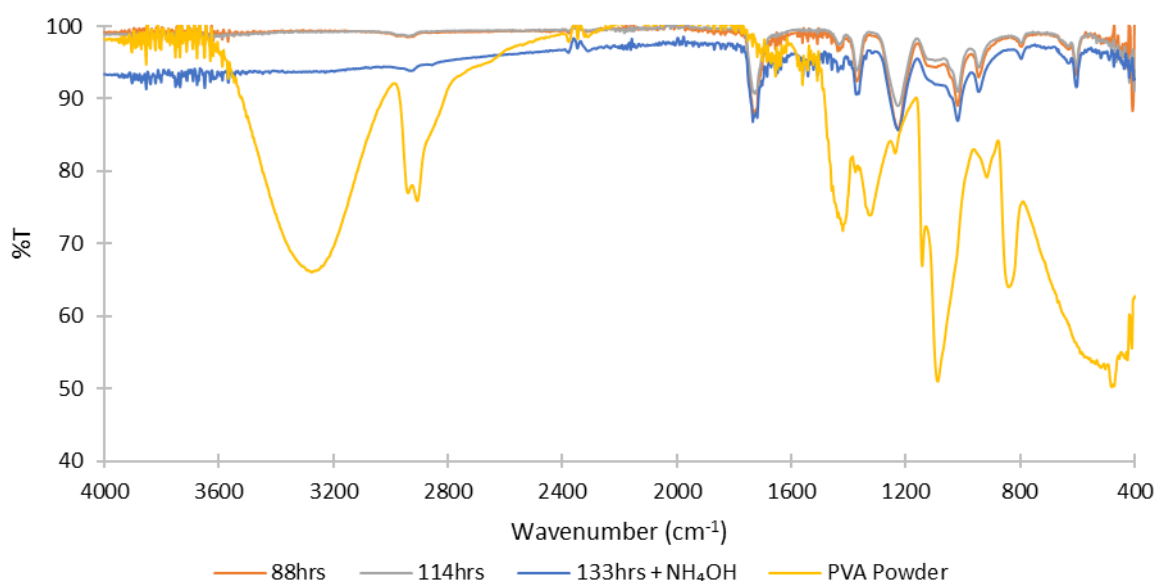


Figure 77 – FTIR-ATR spectra of NaCl catalysed hydrolysis of 8wt.% PVAc dissolved in MF .

Figure 78 shows $MgCl_2$ catalysed hydrolysis of PVAc in MF. Also shown is the spectra for unprocessed PVA. The purpose of using different catalysts was to investigate the effect this has on initiation hydrolysis. It is apparent that hydrolysis has not been initiated and that there has been no chemical changes within the PVAc-MF solution. As before possible reasons include insufficient catalyst and inappropriate temperature. It should be noted here that this reaction was conducted at room temperature owing to the low boiling point (306K) of MF. This is the primary reason for investigating different catalysts.

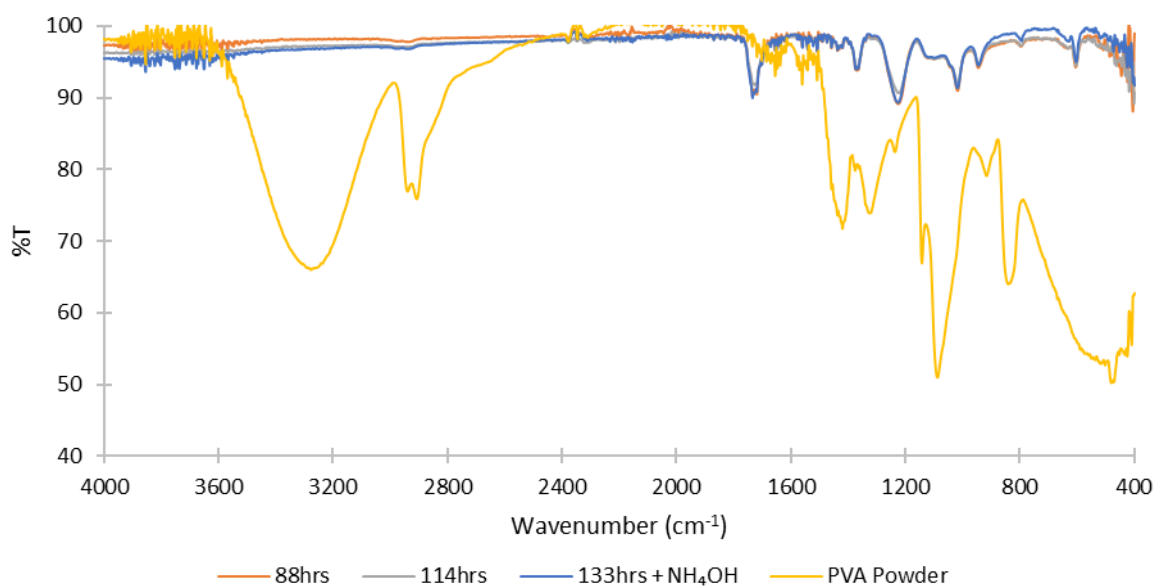


Figure 78 – FTIR-ATR spectra of $MgCl_2$ catalysed hydrolysis of 8wt.% PVAc dissolved in MF.

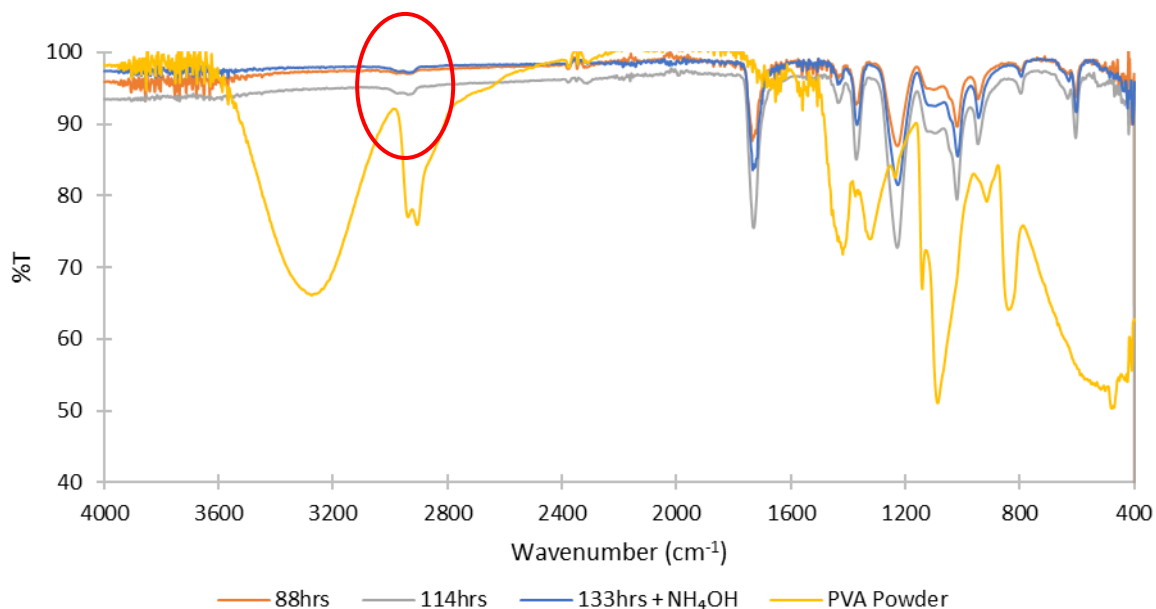


Figure 79 – FTIR-ATR spectra of $Mg(NO_3)_2$ catalysed hydrolysis of 8wt.% PVAc dissolved in MF.

Figure 79 shows the spectra for $\text{Mg}(\text{NO}_3)_2$ catalysed hydrolysis of 8wt.% PVAc. This is the most interesting of samples analysed as there is a hint that hydrolysis may have been initiated. The area circled red in Figure 79, although too small to be reliably identified, suggests that PVA may have been produced. Peaks in this region typically correspond to O-H or C-H groups and although this murmur exists in the other two spectra, here it has an intensity of perhaps 95%T. However, this tiny, unidentifiable peak is not enough evidence to draw any positive conclusions about the initiation of PVA hydrolysis.

Further investigation into reaction conditions and catalyst concentration are required. It may also be sensible to reconsider the solvent PVAc is dissolved in, by compromising drying time to facilitate successful hydrolysis.

3.4 Summary

Drying times of PVAc in a range of organic solvents has been conducted. SEM micrographs indicated a polymer matrix littered with holes thought to be the result of solvent evaporation, through a semi-dry PVAc film. FTIR of dissolved PVAc indicated little remaining solid. More troubling is the unidentified peak in Figure 71. It would be prudent to take repeat measurements to eradicate the possibility of contamination.

Evaporation characteristics of neat solvents with and without dissolved PVAc were investigated using IRT. MF proved to be the fastest at evolving from a surface. This was expected owing the boiling point of 306K (the lowest of all solvents explored). Emphasis must be place on the importance of film and hydrogel drying rates as this is the basis of cooling and IRT identification. This aspect of the chapter was successful and was taken forward to base hydrolysis studies.

Base hydrolysis of PVAc was studied in the solvent medium using a range of catalysts.

Ultimately this was unsuccessful, although the sample catalysed with $\text{Mg}(\text{NO}_3)_2$ gave a tantalising hint that hydrolysis may have been initiated, but evidence was weak and so it cannot be concluded with certainty that base hydrolysis had occurred. Figure 77 and Figure 78 show no clear indication hydrolysis has initiated as no O-H peaks can be seen on the spectra. This aspect of the work is frustrating, hydrolysing PVAc whilst in a solvent medium would have enabled a range of drying rates to be taken forward for further work enhancing the tunability of materials. It is likely that acid rather than basic conditions existing in the reaction medium.

This reaction was also undertaken at room temperature (298K) and even with the presence of a catalyst, may not be sufficient to overcome the activation energy barrier.

Overall, investigations into drying times are important, especially if a potential commercial use could be for night search and rescue using IR imaging. Further work is warranted in this area to decide conclusively if base hydrolysis of PVAc is possible whilst dissolved in organic solvent.

This aspect of the work will not be taken forward further in the project as time and resources would be better spent on refining PVA hydrogels and thin films incorporating functional nanoparticles. This will offer a different route to tuneability of IRT response.

4 Production of Polyvinyl Alcohol Hydrogels and Thin Films Incorporating Functional Nanoparticles

4.1 Introduction

PVA is a synthetic polymer derived from polyvinyl acetate (PVAc) through partial or full hydroxylation. PVA is commonly used in medical devices due to its low protein adsorption, biocompatibility, high water solubility and chemical resistance [350].

It is evident from the literature that use of green, non-toxic biocompatible PVA is useful. Its surface tension/viscosity (γ/η) values in aqueous solution allows it to form self-supporting films and coatings [351]. The emissivity of PVA films and coatings has not been previously investigated. It affects IR thermal imaging in a way that may be useful in IR stealth coatings. Interestingly, when a self-supporting PVA film was used above a bare human hand at 304K the thermal image of the latter was obscured.

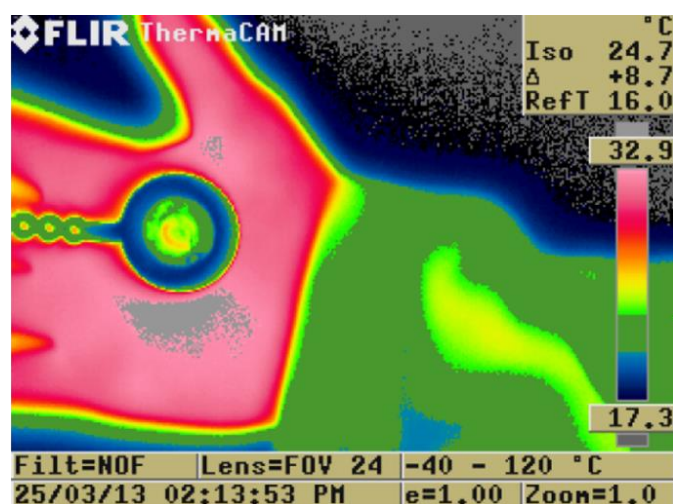


Figure 80 – Thermal image of a self-supporting PVA film positioned in front of a human hand.

It was hoped that stabilised PVA structures may be chemically treated to incorporate functional nanoparticles of known emissivity and reflective/antireflective properties. By loading the polymer matrix with such materials may increase the tuneability, such that surfaces may appear thermally different to their surroundings and potentially invisible to an IR camera. Secondary use of this type of material would be effective as a passive cooling system in buildings, potentially incorporating electrochromic materials for switchable systems to be applied.

Chapter 4 showed that PVA hydrogels are effective at reducing the temperature of a surface relative to its surroundings, based on the release of solvent from the polymer matrix. In this chapter this mechanism is taken further, by developing a nanocomposite material, able to

obscure the long wave infrared (LWIR) and short-wave infrared (SWIR) properties of a surface. Electrochromism has also been considered as a way of passively cooling buildings, by making surfaces either more reflective or absorbing. The author believes that electrochromism in hydrogels is a novel area of research.

4.2 Aims and Objectives

This chapter aimed to utilise the desirable structural properties of PVA to produce hydrogels and thin films incorporating different functional NPs which could tune the emissivity (ϵ) of a surface to one which is within a desired range. The desired range is dependent on which application the coating is to be used in. Military uses will be confidential, however passive cooling hydrogels for buildings will typically be close to zero (reflective) for warm days or close to 1 (absorbing/blackbody) on cooler days. The purpose of which is to reflect excess IR radiation or absorb it.

This required the production of PVA hydrogels using both chemical and physical crosslinking methods. PVA films were formed due to desirable surface tension/viscosity (γ/η) values, however further stabilisation is required once samples extend beyond certain dimensions.

Characterisation of materials and testing using appropriate IR camera equipment was also required to ensure they perform in laboratory and real-world settings. Drying times of PVA/PVAc structures containing different organic solvents was also considered.

4.3 Results

4.3.1 Production of PVA hydrogels

A range of simple PVA hydrogels with varying degrees of crosslinking and PVA concentrations were investigated. Both chemical and physical crosslinking methods were utilised to investigate any resultant differing physical and mechanical properties of the hydrogel.

Glutaraldehyde (GA) was selected as a chemical crosslinker and two methods of physical crosslinking were used: freezing at 248K in a conventional freezer and crash cooling at 77K using liquid nitrogen. In all cases 50cm³ of PVA solution was used as the basis for each hydrogel. Freeze-thaw cycles were conducted between 1 and 5 times on each concentration of PVA solution. Where chemical crosslinking was used, the same volume range of GA was used with each concentration of PVA solution.

Figure 81 shows a typical physically crosslinked and chemically crosslinked PVA hydrogel immediately after crosslinking. The physical freeze-thawing technique yielded hydrogels that were of a white opaque appearance, due to light scattering as a result of the dual amorphous/semi-crystalline network formed. The chemically crosslinked hydrogels were clear, translucent with no visible inclusions. Upon drying in ambient conditions, the hydrogels collapsed to a light, clear, hard material with no visible light scattering, indicating poor or no porosity.

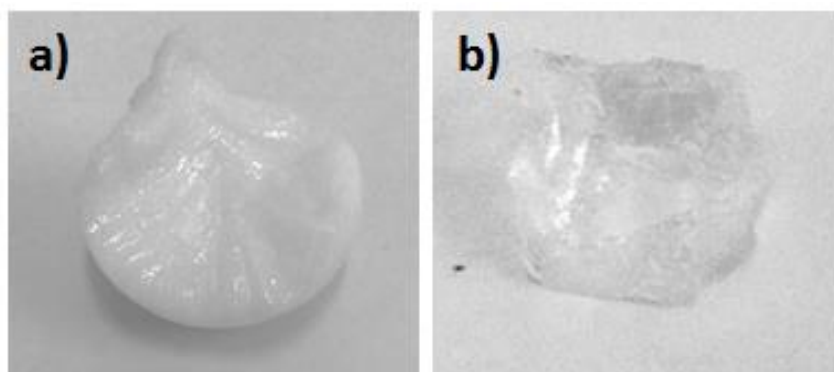


Figure 81 - PVA hydrogels from (a) physical crosslinking from freeze-thawing, and (b) chemical crosslinking using glutaraldehyde (GA). The PVA solutions used were 10 wt. %.

Figure 82 shows two hydrogels that have been dried in ambient conditions over a period of time. The size difference is due to the amount of PVA present in the sample. (Note that when hydrated, the two samples were of similar size).

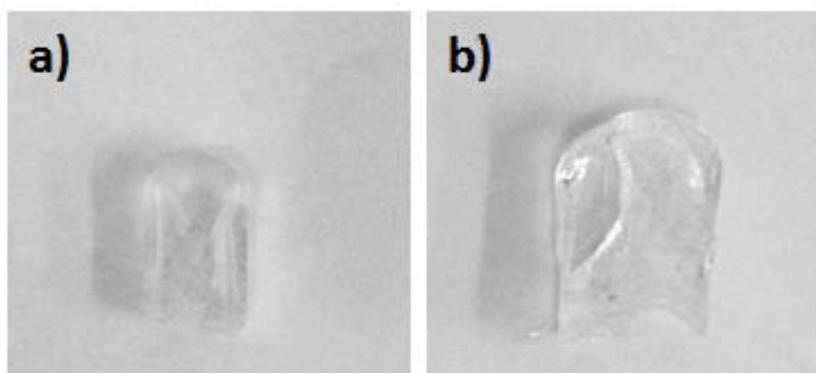


Figure 82 - PVA hydrogels from (a) 5 wt. % and (b) 10 wt. % PVA aqueous solutions.

A range of hydrogels were produced to ascertain practical upper and lower limits of PVA concentration and degree of crosslinking required to produce a stable gel. Stock PVA solutions were synthesised at various concentrations and used for all crosslinking investigations. GA 25% solution was used with HCl employed to control the acidic environment required for activation of GA.

4.3.2 Visual Observations

A large range of hydrogels were produced to evaluate which ratio of crosslinking and PVA concentration would be most suitable to take forward for further development. Gels that were too wet/soft were considered unsuitable as the lack of structure would make incorporation of NPs difficult owing to the lack of mechanical stability. Conversely, gels that were too firm were also considered unsuitable, as homogeneous NP dispersion would be hindered by the densely crosslinked PVA matrix. There would have been a risk of M_xO_y NPs agglomerating if crosslinking were to be conducted too quickly or extensively.

A further consideration was the rate of H_2O loss from the hydrogel. This is an important property and is the mechanism by which a hydrogel material is able to cool a surface to which it is applied. This dehydration must be controllable; too slow and the surface may not be cooled sufficiently, too quick and the gel would need to be rehydrated with unacceptable frequency.

Table 11 – Observations noted about the appearance, strength and speed of formation of hydrogels produced via physical crosslinking in a conventional freezer (298-248-298K). Highlighted in green are the conditions which produced hydrogels with the most desirable properties.

PVA solution concentration (weight %)	Number of freeze/thaw cycles	Properties/observations
2	1	No gel formed
	2	No gel formed
	3	Solution appeared more viscous – no gel formed
	4	Small areas of very thick solution – partial very weak gel formed
	5	Small areas of very thick solution – partial very weak gel formed
4	1	No gel formed
	2	Solution appeared more viscous – no gel formed
	3	Some areas of gelation apparent – non-homogeneous
	4	Very wet gel formed, weak structure
	5	Wet homogeneous gel formed
6	1	No gel formed
	2	Heterogeneous solution/gel formed
	3	Very wet gel formed, weak structure, optically clear
	4	Soft gel formed, very little non-gelled initial solution present
	5	Soft-medium gel formed, weak mechanical properties, slight opaqueness

Table 11 is continued on the next page.

8	1	Solution appeared more viscous – no gel formed
	2	Heterogeneous solution/gel formed
	3	Soft gel formed, very little non-gelled initial solution present
	4	Soft-medium gel formed, weak mechanical properties, slight opaqueness
	5	Medium strength gel formed, malleable and springy to touch
10	1	Solution appeared more viscous – no gel formed
	2	Very wet gel formed, weak structure
	3	Soft gel formed, weak structure
	4	Soft-medium gel formed, weak mechanical properties
	5	Medium strength gel formed, slightly firm to the touch, white in appearance, completely opaque.
15	1	Very viscous liquid, initial signs of gelation
	2	Wet gel formed, weak mechanical properties
	3	Soft-medium gel formed
	4	Medium gel formed, maintains shape when mechanically manipulated
	5	Medium-firm gel formed, signs of brittleness at boundary, opaque
20	1	Very thick viscous aqueous solution, some gelation
	2	Wet gel formed, weak mechanical properties
	3	Soft-medium gel formed, opaque and white
	4	Firm gel formed, signs of brittleness
	5	Very firm gel formed, brittle and not easily manipulated

Table 12 - Observations noted about the appearance, strength and speed of formation of hydrogels produced via physical crosslinking using liquid nitrogen to crash cool the solution (298-77-298K).

PVA solution concentration (weight %)	Number of freeze/thaw cycles	Properties/observations
2	1	No gel formed, no visual difference
	2	No gel formed, no visual difference
	3	Solution appeared more viscous – no gel formed
	4	Solution appeared more viscous – no gel formed
	5	Small areas of very thick solution – partial very weak gel formed

Table 12 is continued on the next page.

4	1	No gel formed
	2	Solution appeared more viscous – no gel formed
	3	Small areas of very thick solution – partial very weak gel formed
	4	Very wet gel formed, weak structure
	5	Wet homogeneous gel formed, very weak, clear appearance
6	1	No gel formed
	2	Areas of gel formed, mostly aqueous solution present
	3	Very wet gel formed, weak structure, optically clear
	4	Soft gel formed, very little non-gelled initial solution present
	5	Soft gel formed, weak mechanical properties, areas of air present in polymer matrix, slight opaqueness
8	1	Solution appeared more viscous – no gel formed
	2	Very wet gel formed, weak structure
	3	Soft gel formed, very little non-gelled initial solution present
	4	Soft-medium gel formed, weak mechanical properties, slight opaqueness, areas of air present
	5	Medium strength gel formed, brittle, areas collapse under pressure, opaque
10	1	Solution appeared more viscous – no gel formed
	2	Soft gel formed, weak structure, spongy
	3	Soft-medium Soft gel formed, weak structure, brittle, opaque
	4	Medium gel formed, weak mechanical properties, brittle
	5	Medium strength gel formed, slightly firm to the touch collapses with firmer pressure, white in appearance
15	1	Very viscous liquid, initial signs of gelation
	2	Soft cloudy gel formed, weak mechanical properties
	3	Medium gel formed, easily torn, air bubbles present
	4	Firm gel formed, some areas very solid, others contain air
	5	Firm gel formed, brittle, opaque, air containing
20	1	Very thick viscous aqueous solution, some gelation
	2	Soft gel formed, weak mechanical properties, white, opaque
	3	Medium-firm gel formed, opaque and white, very brittle
	4	Firm gel formed, brittleness, non-homogeneous
	5	Almost solid gel formed, brittle and not easily manipulated

Table 13 - Observations noted about the appearance, strength and speed of formation of hydrogels produced via chemical crosslinking with GA. Highlighted in green are the conditions which produced hydrogels with the most desirable properties.

PVA solution concentration (weight %)	Volume of GA (ml)	Properties/observations
2	0.1	No visible gel formed
	0.5	Solution appeared more viscous – no gel formed
	1	Wet gel formed, very weak mechanical properties
	2	Weak gel formed, soft to touch
	5	Gel formed quickly, optically clear, weak mechanical properties
	10	Soft gel rapidly formed upon casting; non-homogeneous dispersal apparent
4	0.1	Solution appeared more viscous – no gel formed
	0.5	Wet gel formed – un-crosslinked aqueous PVA present
	1	Gel formed, optically clear, weak mechanical properties
	2	Soft/medium firmness gel formed
	5	Medium firmness gel formed quickly, clear, good mechanical strength
	10	Medium firmness gel formed rapidly, some areas hard indicating a lack of homogeneity
6	0.1	Wet gel formed slowly, very weak
	0.5	Soft gel eventually formed, optically clear, structurally weak
	1	Gel formed, soft to touch, average strength
	2	Medium firmness gel formed quickly, good strength
	5	Firm gel formed rapidly, medium strength, optically clear
	10	Firm gel formed rapidly, very good mechanical properties
8	0.1	Soft gel formed eventually, weak properties, wet to touch
	0.5	Soft gel formed slowly, optically clear
	1	Medium firmness gel formed, good strength
	2	Medium firmness gel formed quickly, optically clear
	5	Firm gel formed, water tightly bound, slight flexibility
	10	Very firm gel formed, some brittleness, optically clear
10	0.1	Weak gel formed slowly, wet to touch
	0.5	Soft/medium firmness gel formed, mechanically weak
	1	Medium firmness gel slowly formed, good strength
	2	Medium/firm gel formed, optically clear, manipulatable
	5	Firm gel formed rapidly, signs of brittleness
	10	Very firm gel formed, brittle, optically clear, not easily manipulated

Table 13 is continued on the next page.

15	0.1	Weak gel formed, wet to touch
	0.5	Soft/medium firmness gel formed, mechanically weak
	1	Medium/strong firmness gel formed, optically clear
	2	Firm gel formed quickly, with potential for manipulation
	5	Firm/hard structure formed; brittleness apparent
	10	Hard, almost solid gel, on board water very tightly bound
20	0.1	Weak gel formed, wet to touch
	0.5	Soft/medium firmness gel formed, mechanically weak
	1	Medium/firm gel formed quickly, good strength, (possible candidate for further use)
	2	Firm gel formed signs of brittleness, optically clear
	5	Very firm gel formed, some brittleness, hard to twist and turn
	10	Hard, almost solid gel formed rapidly, on board water very tightly bound

From the array of samples produced, there were several candidates which showed potential to be taken forward for M_xO_y NP inclusion (highlighted in green). These samples have been selected because of the properties they exhibit. The author is mindful of the potential future applications and commercialisation of these materials and envisions them being applied to the surface of a building. With this in mind samples need to be durable, strong and clear, able to withstand the variety of weather conditions they may experience. It is for these reasons that the samples highlighted are desirable. At this stage it was decided not to pursue the physical crosslinking method using liquid nitrogen. Gels produced via this method were similar to ones produced via the conventional freezer method.

A noticeable difference, however, was the appearance of air pockets/voids in the gels. This was first noticed when mechanical pressure was applied to the gel. The structure would sometimes collapse around the applied area of pressure rather than give a uniform physical resistance. This was thought to be due to air becoming trapped in the gel when it was frozen quickly. When aqueous PVA solution was poured into petri dishes in preparation for freezing, air bubbles would sometimes be present in the solution. Because of the speed of freezing when liquid nitrogen was applied, these bubbles did not dissipate, but instead formed small localised areas of aerogel. Conversely, the slower rate of freezing with a conventional freezer gave enough time for air bubbles to burst/rise to the surface before the solution had completely frozen. For this reason, and the additional health and safety issues surrounding use of liquid nitrogen, combined with greater cost, made this method less desirable. One strong advantage, however, was the increased speed at which hydrogels could be produced.

Hydrogels produced via chemical crosslinking were inherently more controllable, as stoichiometric values could be calculated to give desired levels of crosslinking. However, it was noticed that a lower and upper limit of PVA concentration and volume of GA added. Where concentration of PVA was too low (<4wt.%) hydrogels formed were too soft or weak, with non-crosslinked portions of aqueous PVA present. Where volumes of GA were also low, hydrogels were not formed at all. Alternately, where concentrations of PVA were high (>10wt.%) hydrogels formed were firm and in some cases brittle. This rendered them unsuitable as even dispersion of M_xO_y NPs would be challenging. In cases where PVA concentration and GA volume were high, hydrogels formed rapidly and sometimes unevenly as crosslinking was already occurring before the gel was cast. A reduction in the acidity of the system helped to some degree, but ultimately these gels were too firm to use.

Based on the observations, above 8 – 10wt.% was considered the ideal PVA concentration for both chemical and physically crosslinked hydrogels. GA volumes of 1-2ml were also considered ideal owing to the type of gel produced and the rate formed. The number of freeze-thaw cycles required was 4 or 5 to produce stable gels.

4.3.3 Characterisation of Hydrogels

4.3.3.1 Fourier Transform Infrared Spectroscopy

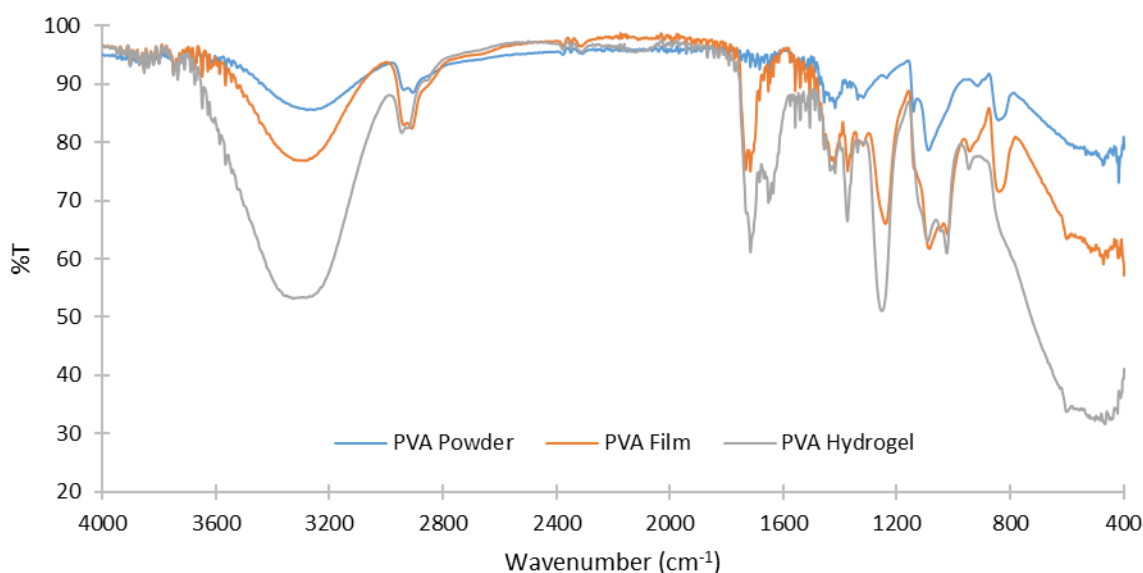


Figure 83 – FTIR-ATR transmission spectra of PVA powder, 8wt.% PVA film and 8wt.% PVA hydrogel.

Fourier transform infrared spectroscopy (FTIR) was used to confirm the identity of the starting materials and the chemical changes undergone when cast as films and hydrogels. This technique was also able to give information about H₂O solvent contained within the PVA-based

hydrogel matrix. A resolution of 2cm^{-1} and 45 repeat scans were selected to obtain accurate and reliable data.

Peaks which have been identified are to be expected for the materials analysed. There is no C=O in PVA powder owing to the high degree of hydrolysis in the starting material.

4.3.3.2 Thermogravimetric Analysis

Thermogravimetric analysis (TGA) was used to confirm the dehydration of H_2O from PVA hydrogel samples and to investigate the temperature at which PVA decomposes. Identical samples of PVA powder (99+% hydrolysed) were run in air and N_2 . Physically crosslinked hydrogel samples produced from 8wt.% PVA aqueous solutions of the same batch of PVA powder were also run in air and N_2 .

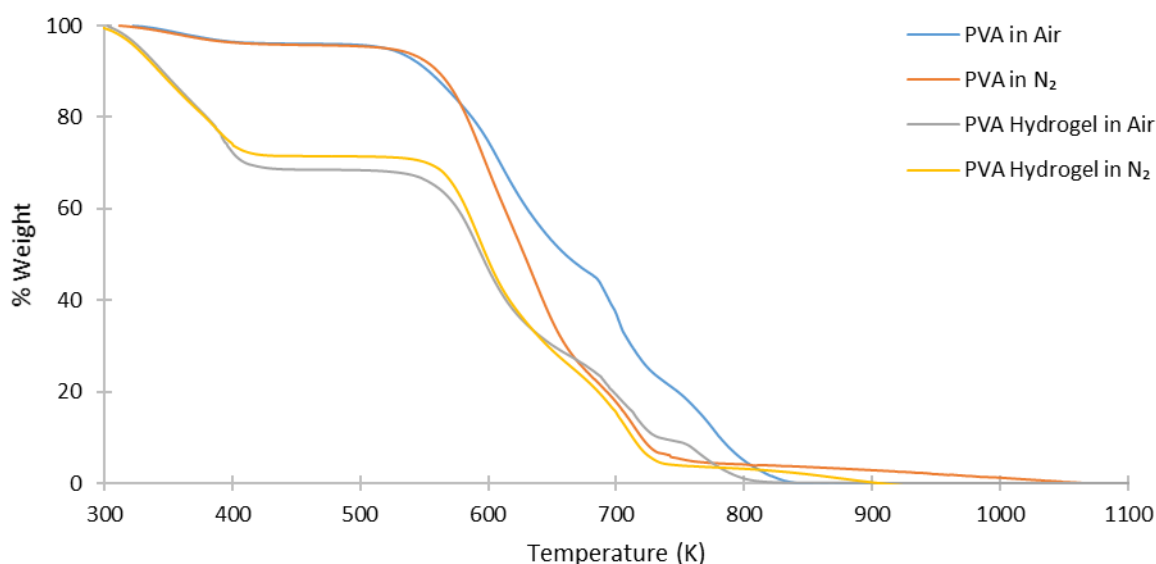


Figure 84 – TGA plot of 99+% hydrolysed PVA powder and physically crosslinked PVA hydrogels in air and N_2 .

Figure 84 shows TGA of PVA powder and a physically crosslinked PVA hydrogel in both air and N_2 . PVA powder shows minimal weight loss (<5%) from 300-580K; this can be attributed to small amounts of H_2O which would have been absorbed by the hydrophilic nature of PVA during storage/pre-processing. A steady weight decrease of 80% can be observed for PVA powder in N_2 between 580-730K at which point a decrease is still observable but at a reduced rate up to the maximum operating temperature of the instrument. The PVA powder in air decreases in weight by >95% between 580-830K. The decrease observed is less smooth than the run in N_2 with an observable “kink” at 695K. This could be the result of chain scission reactions. A constant weight residue for PVA in air is observable from 830K.

The thermal decomposition of PVA hydrogels begins with a clear weight loss of 30% between 300-400K which is the result of dehydration of H₂O from the polymer matrix. No weight is lost between 400-590K. Between 590-730K the hydrogel sample in N₂ loses 70% weight tending to the powdered N₂ PVA weight loss rate. The hydrogel sample in air has a similar observable “kink” to that of the powdered sample at 690K. A weight loss of 75% is observed to 830K after which a constant weight residue is seen.

The thermal degradation of hydrogel samples begins 10-15K later than the powdered sample. This is thought to be due to the entangled polymer chains which were the basis for the hydrogel giving a stronger structure and requiring a greater energy to initiate degradation steps.

4.3.4 Infrared Thermography of PVA Hydrogels

Infrared thermography (IRT) (FLIR is described in 2.1.6) was used to observe the adsorption-cooling effect of a *chemically* crosslinked PVA hydrogel swollen with H₂O (prepared via the method described in 2.3.2), a *physically* crosslinked PVA hydrogel swollen with H₂O (prepared via the method described in 2.3.3.1) and a physically crosslinked PVA hydrogel swollen with H₂O (prepared via the method described in 2.3.3.2).

The purpose of this test was to investigate if the method of crosslinking had an effect on the thermal characteristics of a PVA hydrogel. All samples were prepared from the same batch of 8wt% PVA solution. 50cm³ was measured prior to thermal/chemical treatment for casting as hydrogels. When formed as hydrogels, samples were of similar physical dimensions (90mm diameter, 8mm high, volume = 50.89cm³). Samples were arranged near each other (but not touching) on a cleaned aluminium substrate. IRT images were obtained at 5min intervals over a period of 25hrs. The range was chosen as it enabled a complete daily cycle to be monitored, with atmospheric (and therefore) substrate temperatures likely to be higher during the day and lower at night when the laboratory is unoccupied.

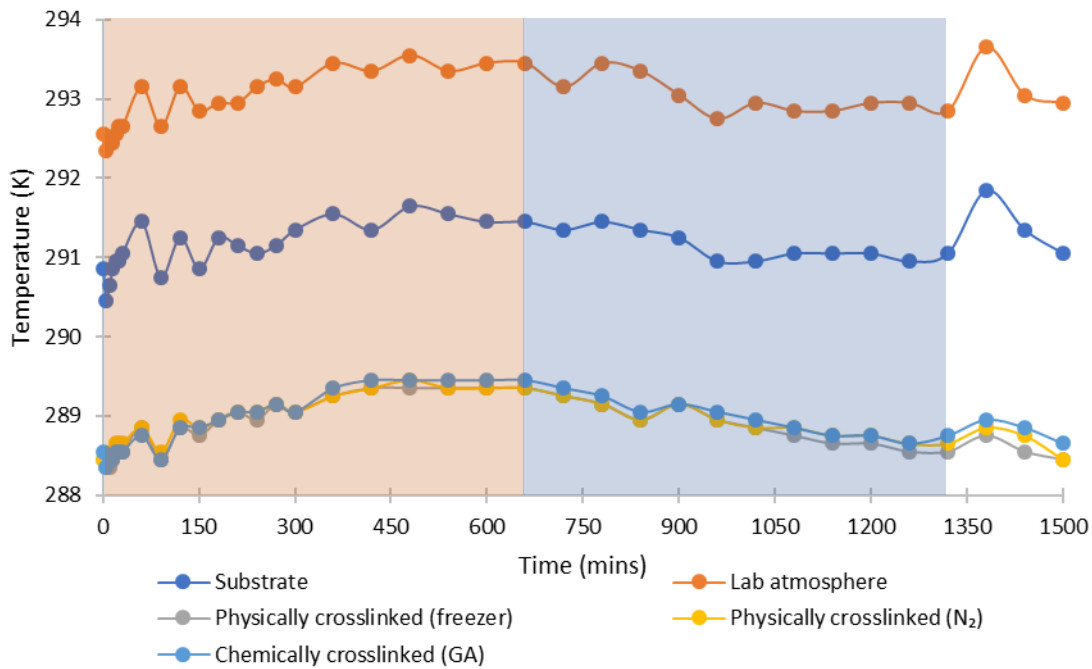


Figure 85 - Temperature variation of a physically crosslinked (freezer method) PVA hydrogel, of a physically crosslinked (N₂) PVA hydrogel and chemically crosslinked (GA) PVA hydrogel compared to local atmospheric and Al uncoated substrate temperature.

Figure 85 shows graphically the temperatures of each hydrogel, the Al substrate temperature and laboratory atmospheric temperature. Firstly, one must consider the atmospheric and Al substrate temperature with respect to time of day. The measurements for this experiment started at 9am (t=0). The temperature of the laboratory atmosphere and Al substrate rose from 290.8K and 292.5K respectively (marked in orange) between t=0 to t=660 (11hrs) to a maximum of 291.7K and 293.6K respectively at 480mins. From t=660 to t=1320 the temperature began to decrease to a minimum of 290.9K at (t=1260) and 292.7K (t=960) (marked in blue) until an increase was once again observed from t=1320 to the end of measurements.

Although slight, these temperature differences indicate the temperature differences between day and night in the laboratory. The higher than expected peaks at 1380mins are a result of the author getting too close to the camera when checking the experiment the following day.

The purpose of this section of work was to determine if the form of crosslinking affects the adsorption-cooling properties of a PVA hydrogel. Figure 86 shows the average temperature difference of each hydrogel compared to the Al substrate. It is apparent that there is no discernible temperature difference between the samples when compared to the substrate. Typically (but not always) the chemically crosslinked hydrogel is <0.1K warmer than the physically crosslinked samples. However, at the start of the experiment (t=0-150mins), the chemically crosslinked sample was indeed cooler than the physically crosslinked samples. The

sample used in this work conforms very closely to what has been previously observed by others (see Figure 89). The chemically crosslinked PVA hydrogel in this work showed a change in temperature (ΔT) of 2.4K compared to 3.6K as recorded by others. It may therefore be concluded that the method of crosslinking has negligible effect on PVA hydrogels, but that confidence can be taken in the performance of the hydrogels prepared.

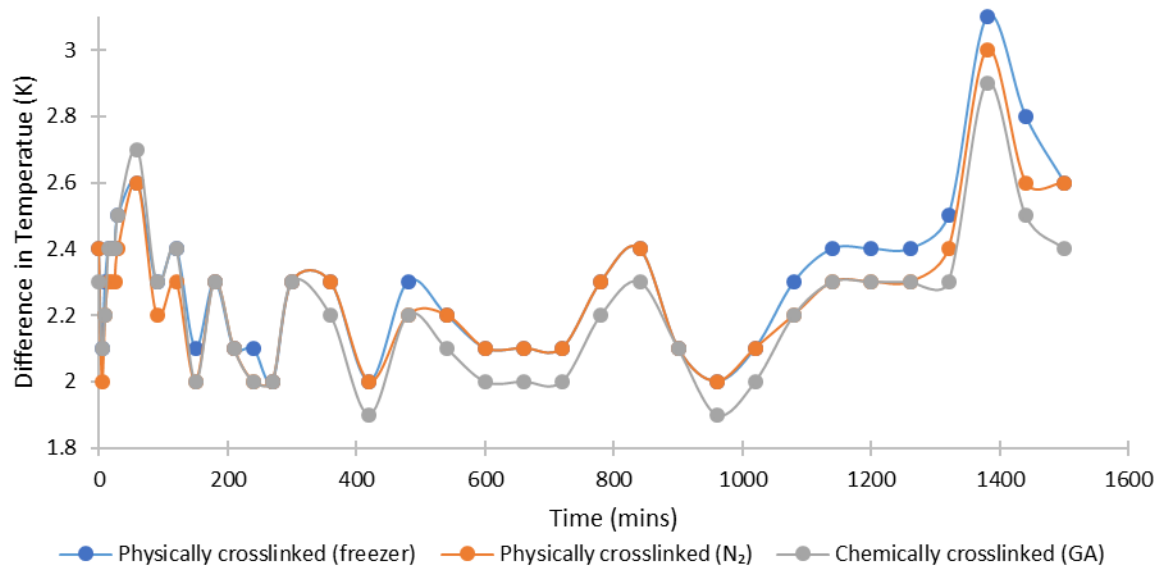


Figure 86 – Average differences in temperature of a physically crosslinked (freezer method), PVA hydrogel, of a physically crosslinked (N₂) and PVA hydrogel and chemically crosslinked (GA) PVA hydrogel compared to Al substrate.

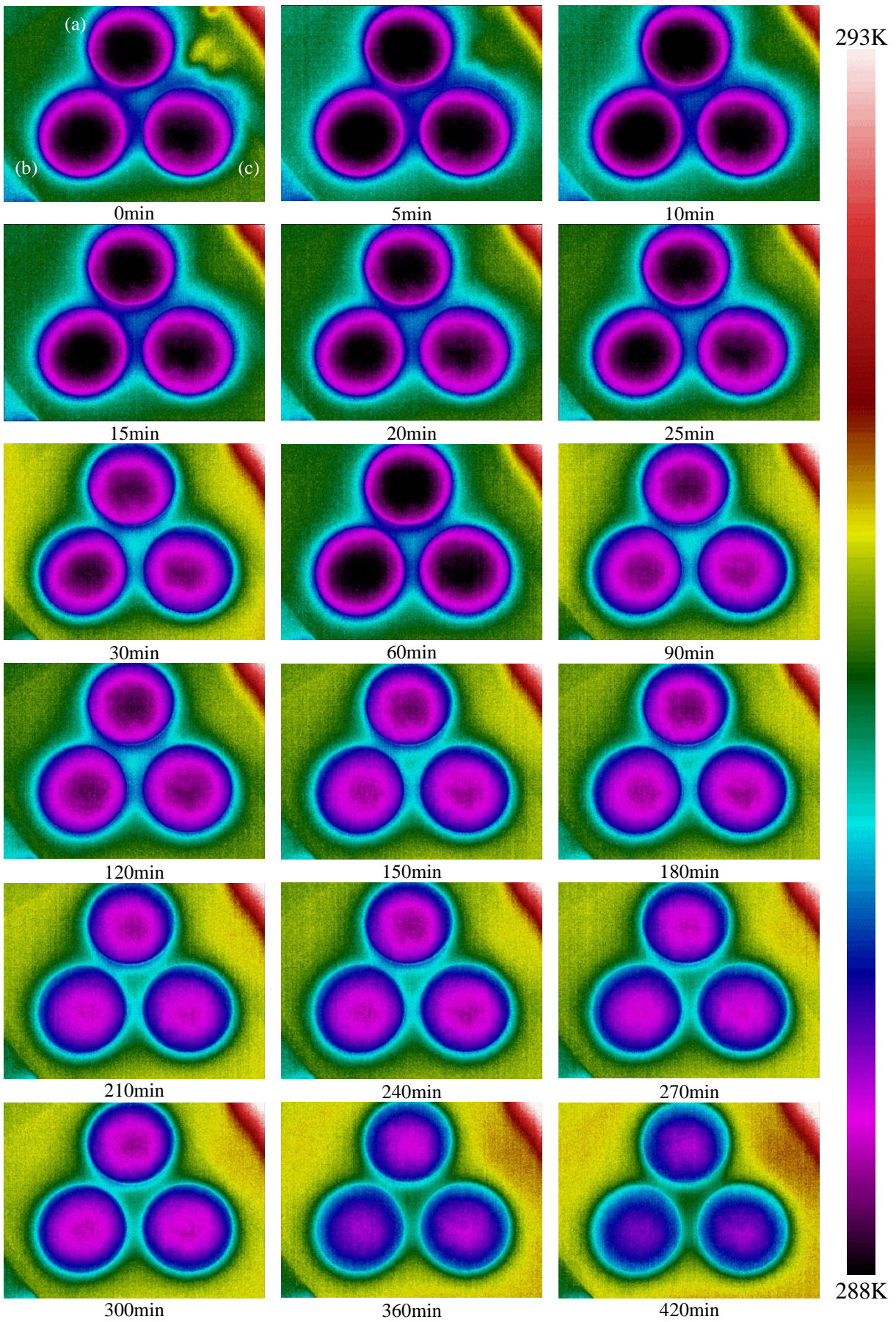


Figure 87- Thermal images of (a) physically crosslinked (freezer method) (b) PVA hydrogel, of a physically crosslinked (N₂) (c) PVA hydrogel and chemically crosslinked (GA) PVA hydrogel (0-420mins).

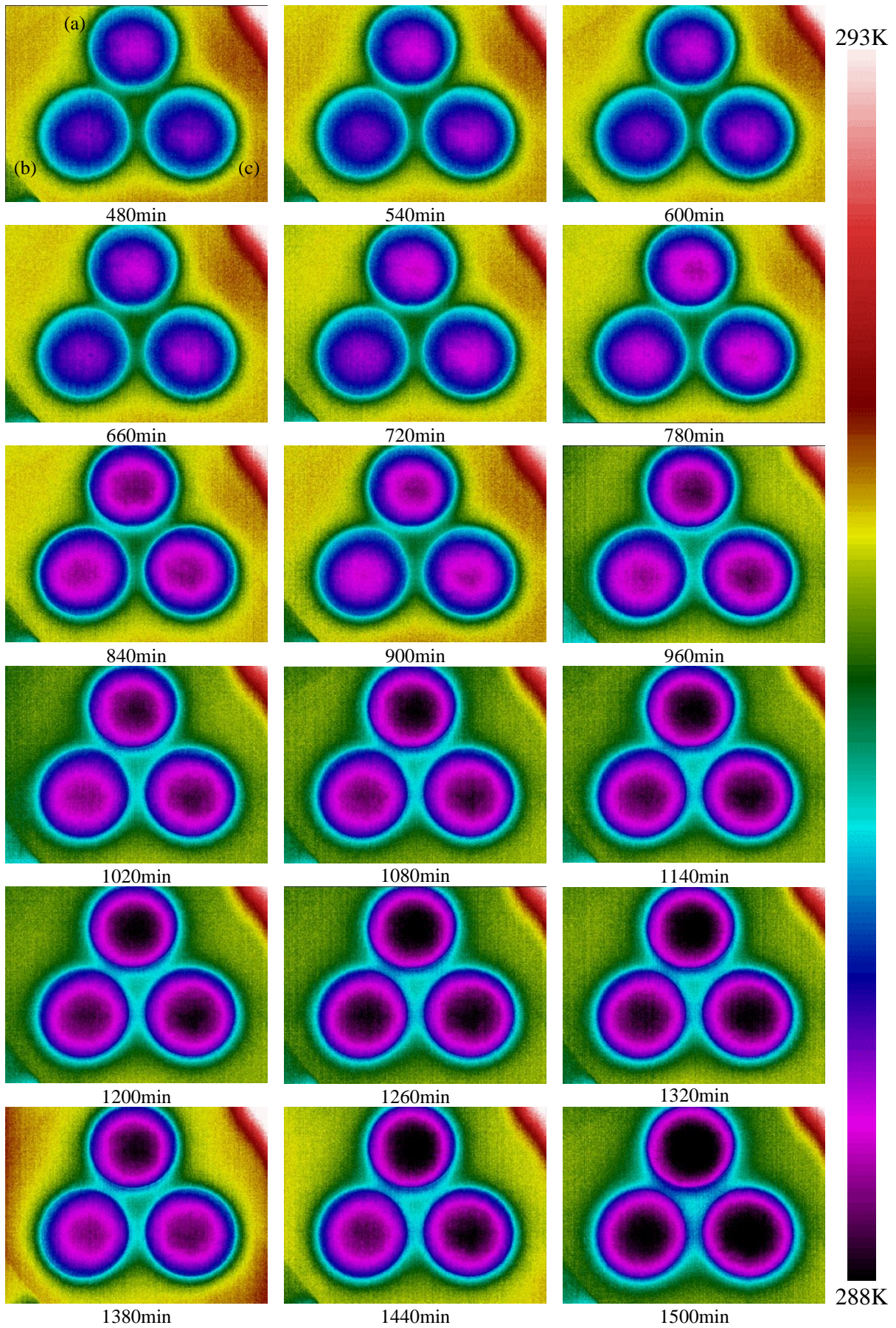


Figure 88 - Thermal images of (a) physically crosslinked (freezer method) (b) PVA hydrogel, of a physically crosslinked (N₂) (c) PVA hydrogel and chemically crosslinked (GA) PVA hydrogel (480-1500mins).

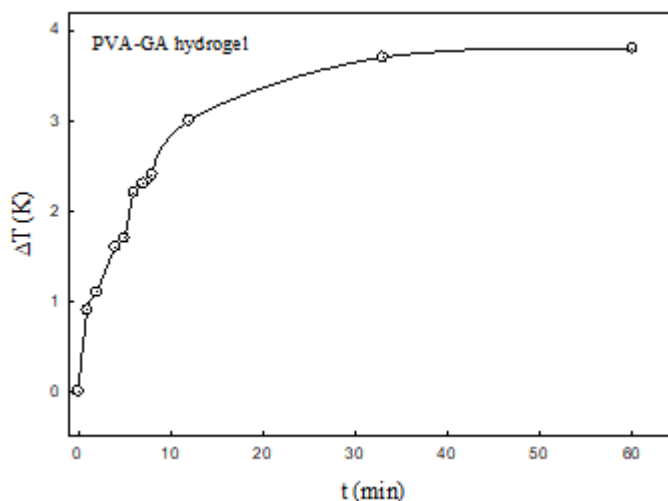


Figure 89 - Temperature between a chemically-crosslinked (GA) PVA hydrogel and its immediate surroundings as a function of time after its preparation. Reproduced from [352].

4.3.5 Viscometry

Viscometry was used to confirm that aqueous PVA solutions were more viscous than H₂O. It was found that the dynamic viscosity of water (2.5cP at 294K) increased significantly on addition of 8wt%PVA (Ave. RMM/kDa = 50,000) to 70.9cP. For a 1%PVA aqueous solution at 298K the surface tension decreases with time to 5000cP from the value for water (7200cP). Hence γ/η decreased on PVA introduction. This was important when considering PVA for use in self-supporting films.

4.3.6 Inclusion of Metal Oxide Nanoparticles in PVA Hydrogels and Films

8wt.% aqueous PVA solution was loaded with 4 and 8wt.% M_xO_y from which self-supporting nanocomposite films were cast. Also produced were physically cross-linked 8wt.% PVA hydrogels loaded with a variety of M_xO_y NPs to investigate the effect this would have on the emissivity (ϵ) of a surface when the sample was applied. The synthesis route for this consisted of producing an 8wt.% aqueous solution of PVA as described in 2.3. From this 50ml was taken for each sample. 4 or 8wt.% of the desired M_xO_y was ground in an agate pestle and mortar with an amount (typically 10ml) of PVA solution to create a PVA/M_xO_y slurry. This step ensured a good level of NP dispersion within the sample. The slurry was then added to the remaining PVA solution and the 50ml sample was then stirred and cast in a petri dish in the case of hydrogels. Four cycles of freeze-thawing (298K to 248K to 298K) were then employed to create the physically-crosslinked sample. For films, the method was similar, but instead circular films were produced using a plastic ring and allowing the film to dry in air. Table 14 lists the samples which were produced for further investigation.

Table 14 - Sample list of PVA hydrogel with amount of MO NP's included and their relevant emissivity's (ϵ)
*Activated Carbon.

M_xO_y	ϵ	wt.% of NP	
		4	8
AC*	0.9 – 1.00	AC	AC
Al ₂ O ₃	~0.2	Al ₂ O ₃	Al ₂ O ₃
SiO ₂	0.55 – 0.62	SiO ₂	SiO ₂
TiO ₂	0.35 – 0.48	TiO ₂	TiO ₂
WO ₃	0.4 – 0.45	WO ₃	WO ₃
ZnO	~0.28	ZnO	ZnO
Au	~0.47	Au	Au

4.3.6.1 Characterisation of PVA- M_xO_y hydrogels

Characterisation of hydrogels loaded with M_xO_y NPs was important to understand how the NPs were dispersed throughout the PVA matrix. The author was ultimately interested in how the NPs affected the image obtained by IRT. By ensuring a good level of dispersion during synthesis, it was hoped that the thermal signal of the sample would be uniform.

4.3.6.2 Scanning Electron Microscopy of PVA/ M_xO_y Slurry Method in Hydrogels

SEM gives a visual indication of the location of NPs within the PVA matrix, able to show if this was disperse or agglomerated. Figure 90 shows SEM micrographs of self-supporting 8wt.%PVA films that contained 4wt.% SiO₂ (a, b) and 4wt.% of AC (c, d). The NPs did not affect the stability of the dried self-supporting PVA films at these low concentrations; however at higher concentrations (8wt.%) the NPs did affect film stability and integrity, with films difficult/unable to be formed.

SEM shows that there is significant agglomeration of inclusive M_xO_y NPs with bulk formations of NPs held together by the polymer network. Therefore, further consideration was given to the method of NP inclusion.

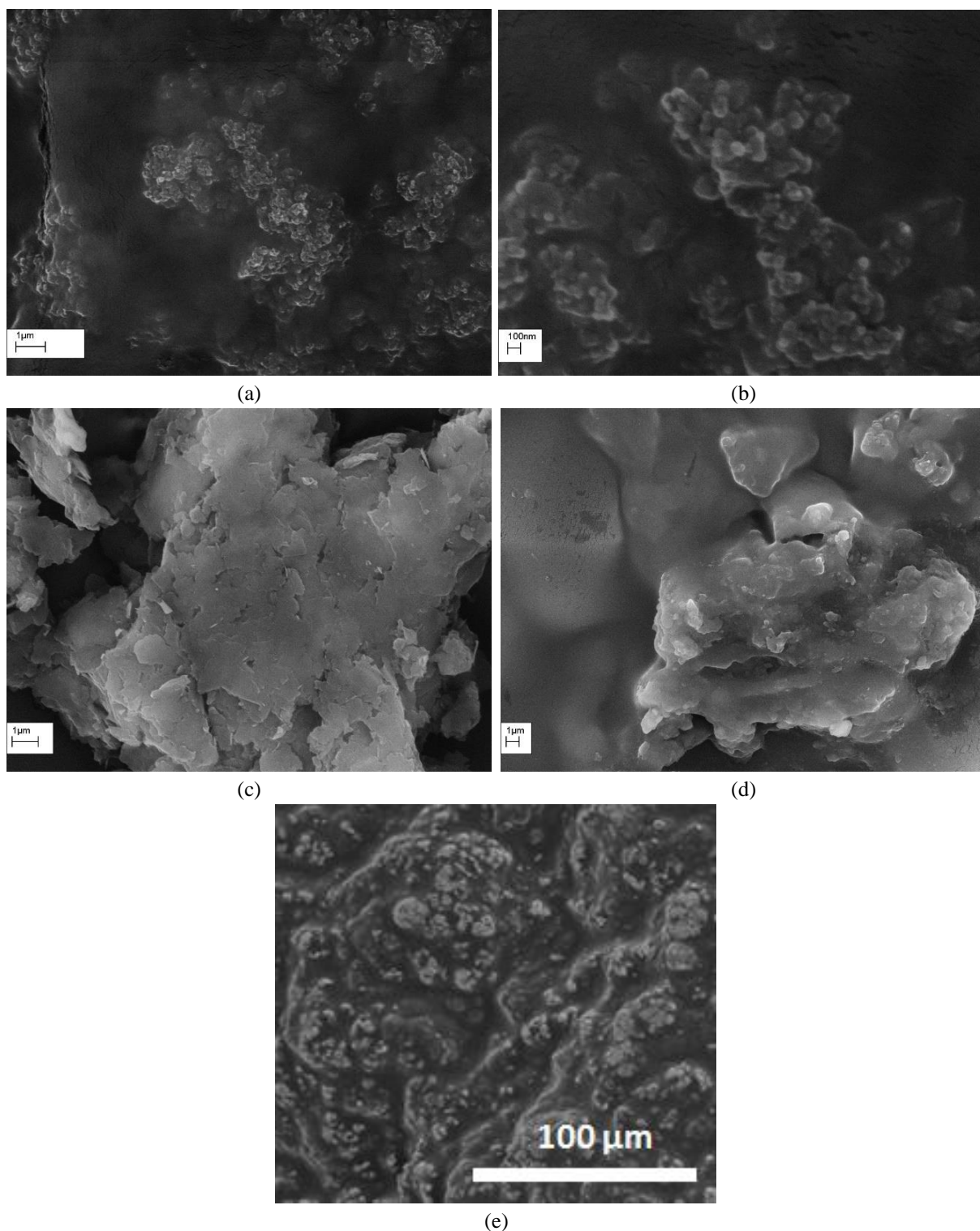


Figure 90 – SEM micrographs of (a, b) 8wt.% PVA+ 4wt.% SiO_2 , (c, d) 8wt.% PVA + 4wt.% AC films and (e) 8wt.% PVA + 4wt.% WO_3 .

4.3.6.3 Energy Dispersive X-ray of PVA/ M_xO_y Slurry Method in Films

SEM-EDX measurements have been performed on a PVA- WO_3 film, obtained by dip-coating a glass slide in a PVA/ M_xO_y slurry produced via the synthesis method described in 2.3.4.2. The elemental maps from EDX show a good distribution of WO_3 throughout the film. This contrasts

with a PVA hydrogel produced from the same slurry. It is considered, that during the physical crosslinking process, WO_3 NPs coalesce owing to the increased time of synthesis and the kinetic movement in the PVA matrix during freeze-thaw cycles. Conversely, a film is a more basic system, able to be cast in a single motion. Once a PVA film is dried (which is a faster process than hydrogel formation) WO_3 NPs are held in position by intermolecular forces originating from polymer chains. It is therefore thought, that providing a good level of mixing occurs immediately prior to dip-coating, a good level of WO_3 NP dispersion can be achieved within a PVA film. Figure 91 shows EDX maps for C, O, W and Au. The Au mapped by EDX originates from gold sputter coating of the sample prior to SEM-EDX analysis.

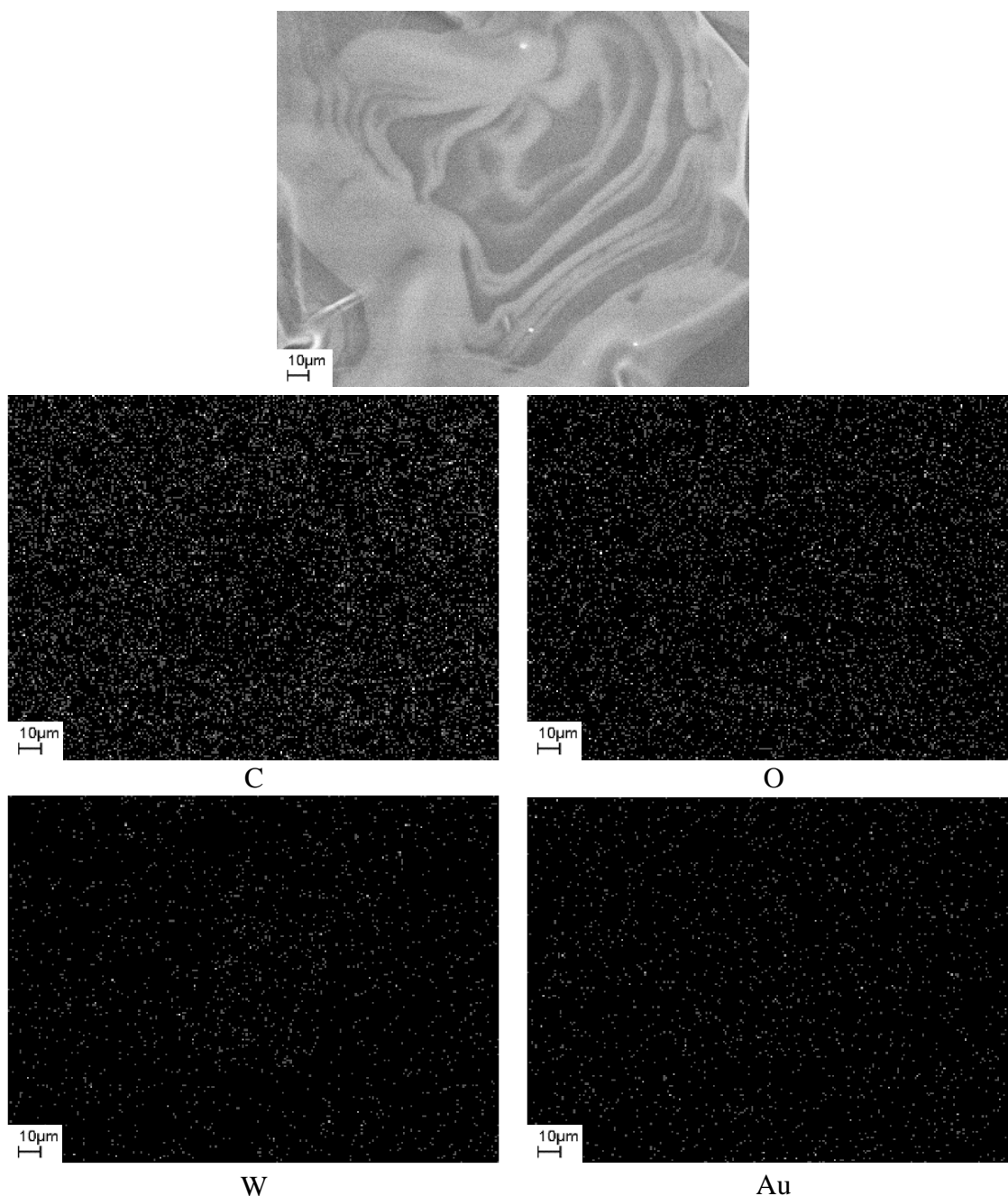


Figure 91 – SEM-EDX of WO_3 in a PVA hydrogel matrix produced via the method described in 2.3.4.3.

4.3.7 Synthesis of Tungsten Trioxide NPs

WO₃ NPs were produced following the method described in 2.3.4.1. SEM revealed an average particle diameter of 40-50nm. This was confirmed by DLS which indicated the average particle size was 48.7nm with a distribution of 15-82nm. It was originally envisioned that NPs produced from this method, would be directly incorporated into PVA hydrogels and films. However the agglomeration apparent in Figure 92 has required investigation into an alternative synthesis route to be conducted.

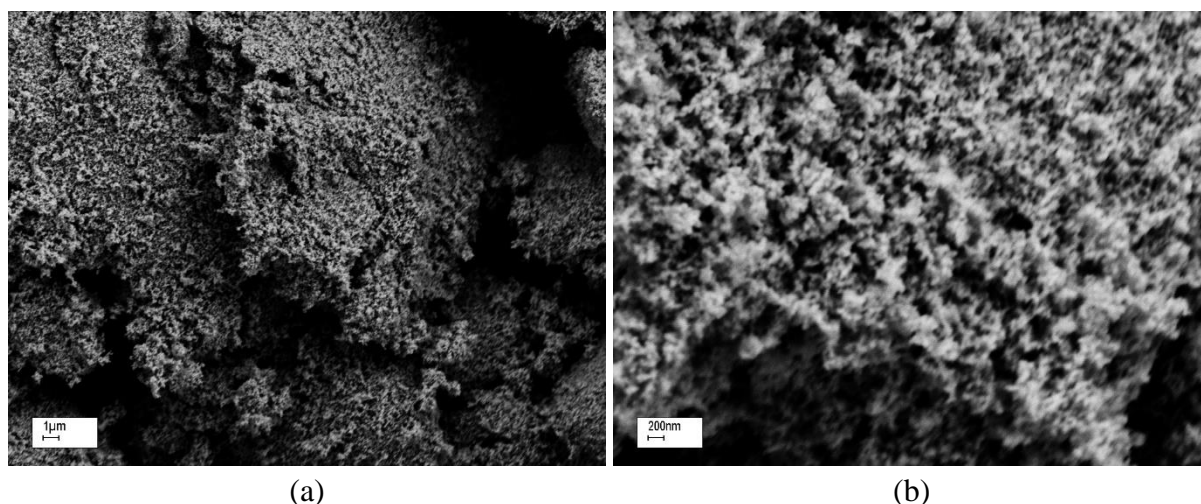


Figure 92 – SEM micrographs of WO₃ NPs synthesised from the method outlined in 2.3.4.1.

4.3.7.1 Thermogravimetric Analysis

Thermogravimetric analysis (TGA) was conducted on the WO₃ NPs produced via the method described in 2.3.4.1. This was undertaken to ensure that the solid obtained was thermally stable. WO₃ NPs were analysed before and after the calcination step (at 773K) as stipulated in the synthesis method. TGA runs were conducted in air with a controlled ramp rate of 10K/min.

Figure 93 shows no weight loss for the sample that had undergone a calcination step. The sample which had not been calcined showed an initial weight loss of 15% between 300-420K attributable to H₂O. A further 5% loss in weight between 420-730K was noted, after which constant weight residues were obtained. TGA has confirmed that the WO₃ NPs produced were thermally stable up to 1200K. The melting point for WO₃ is 1746K, significantly above the temperatures considered here.

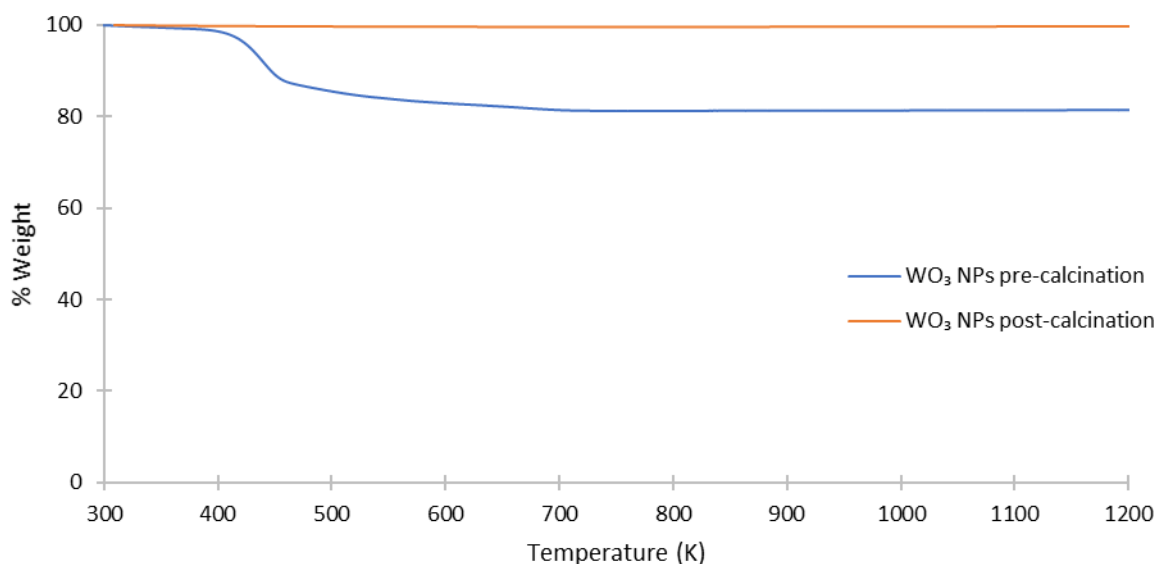


Figure 93 – TGA plot of WO₃ NPs pre- and post- calcination at 773K.

4.3.8 Scanning Electron Microscopy of In-situ PVA Metal Oxide Dispersion Method

The PVA nanocomposite materials produced so far have given different results depending on the method used to cast the precursor. Whilst PVA films may be produced via dip coating with satisfactory NP dispersion (4.3.6.3) the same cannot be said for hydrogels loaded with NPs (4.3.6.2) which show significant areas of NP agglomeration. It is therefore evident that the thickness of a sample (films are thin, hydrogels are thick) has a bearing on the level of NP dispersion throughout the polymer matrix.

PVA hydrogels were produced with inclusive WO₃ NPs via the novel methods described in 2.3.4.3 and 2.3.4.4. SEM-EDX was conducted to investigate the NP dispersion within the polymer matrix.

EDX images in Figure 94 show the extent of WO₃ NP distribution. Homogeneous distribution is evident throughout the area mapped. However the area highlighted by a white arrow shows a reduced concentration of W. If compared to the SEM image this region appears differently perhaps indicating that there are variations in concentration of W. A possible explanation for this difference can be traced back to the synthesis method. As described in 2.3.4.4 it was noted that ensuring the reaction reached an endpoint was problematic owing to the requirement to immerse the gel in a bath of HCl. The timing of this was critical to ensure that NP formation occurred, but that the hydrogel did not dissolve. Therefore, the author believes that the reaction was terminated prematurely and that unreacted Na₂WO₄ may still be present in the polymer matrix. This was not considered at the time and therefore EDX mapping of Na was not conducted. This would be useful to undertake in the future to confirm this theory.

Further SEM-EDX imaging was conducted to evaluate inclusive WO_3 quantitatively (Figure 95). This showed 32.26wt.% of WO_3 which appeared in a monodisperse arrangement.

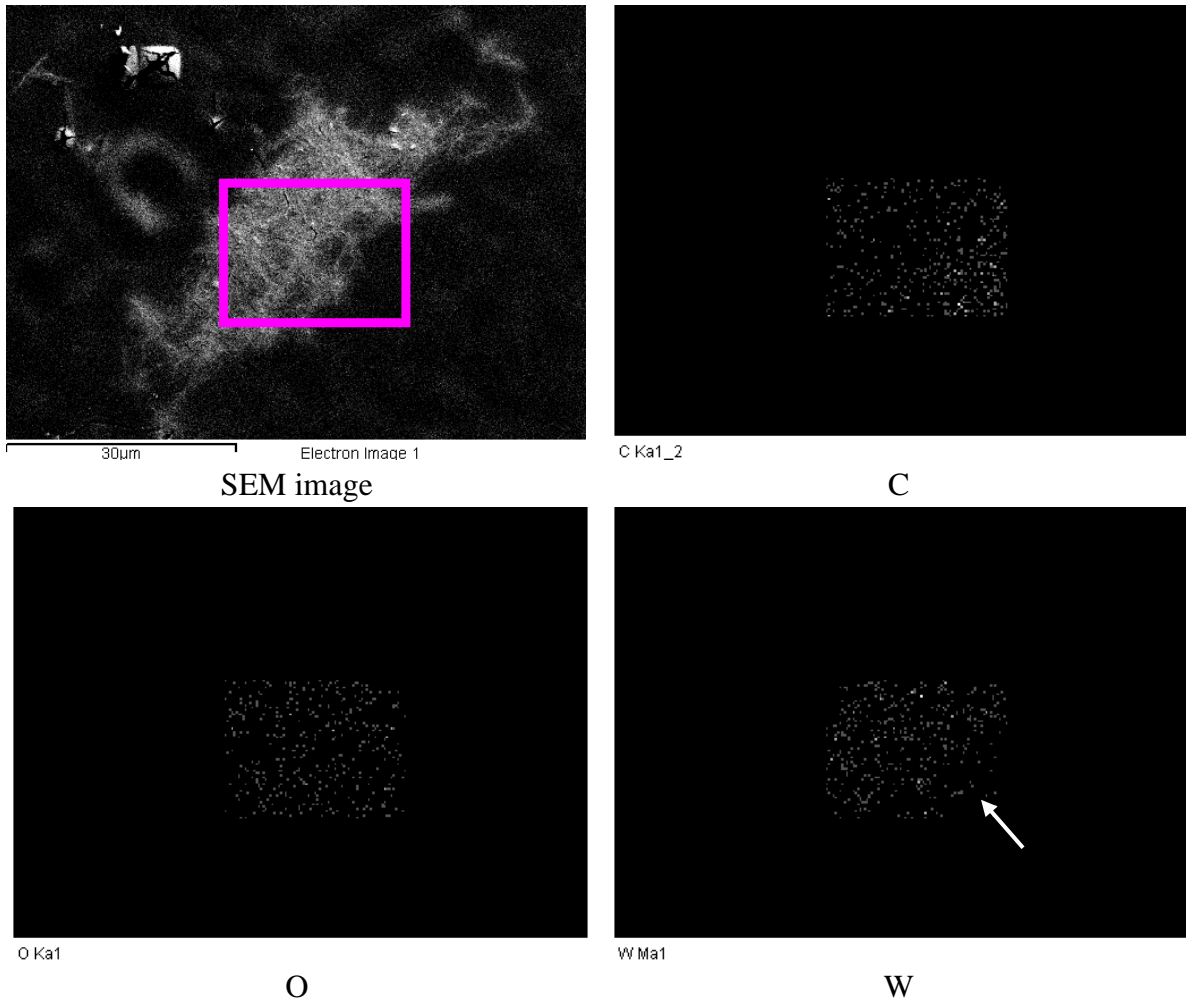
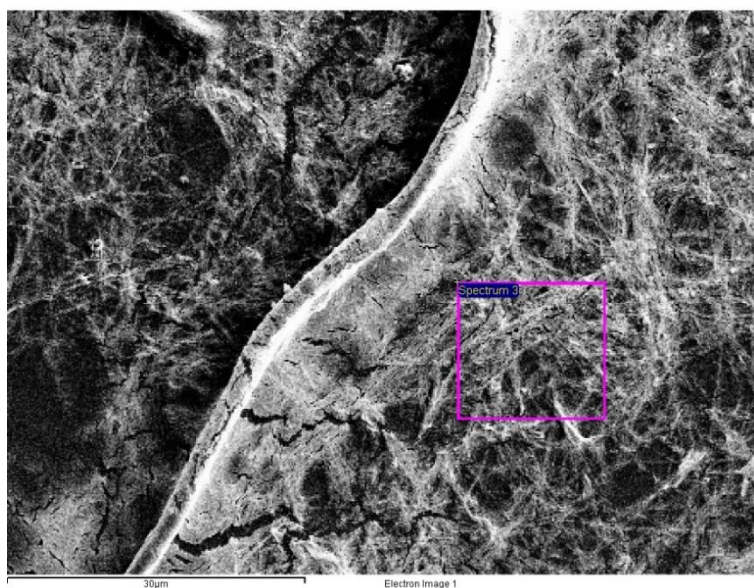


Figure 94 – SEM-EDX micrographs of a dried PVA hydrogel with incorporated WO_3 NPs synthesised via the method described in 2.3.4.4.



Element	Weight%	Atomic%
C K	38.83	61.99
O K	28.91	34.65
W M	32.26	3.36
Totals	100.00	

Figure 95 - SEM-EDX micrograph and generated report of PVA- WO_3 nanocomposite film.

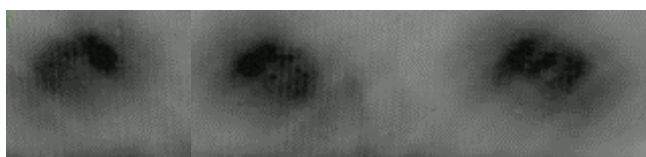
4.3.9 Synthesis of Gold NPs for Inclusion in PVA Hydrogel Matrix

Au NPs were synthesised using the method described by Luo, et al. This method gave monodisperse Au NPs (approximately 2-4nm diameter) for further use in PVA hydrogels [353]. NPs were dispersed in 8wt.% aqueous PVA solution and cast as physically crosslinked hydrogels. A PVA/Au NP film was produced via dip coating a glass slide into the pre-cast solution. The dried film obtained was analysed by SEM-EDX. This presented a problem. Au-sputter coating of the film was not possible as Au was the target atom under investigation. Instead, carbon-sputter coating was considered as an alternative option. However, coating was not as effective as Au and significant charging of the PVA/Au film sample occurred resulting in poor quality micrographs. EDX indicated that Au was present in the sample, but the distribution of particles could not be reliably mapped.

4.3.10 Infrared Thermography of PVA-M_xO_y Hydrogels

“Real-world” IRT was conducted on the most promising PVA-M_xO_y hydrogels (Figure 96). The purpose of this was to investigate how these samples appear from a distance and in an outdoor environment. Physically crosslinked PVA hydrogels produced from 8wt.% aqueous PVA loaded with 4, 8 and 10wt% Au, WO₃ and AC were placed onto a cleaned whiteboard and situated 500m from an IR camera. The atmospheric conditions were:

Temperature – 285K, Humidity – 63%, Wind speed – 12mph



(a) (from L-R) 4wt%, 8wt%, 10wt.% Au NPs in a physically crosslinked PVA hydrogel



(b) (from L-R) 4wt%, 8wt%, 10wt.% WO₃ NPs in a physically crosslinked PVA hydrogel



(c) (from L-R) 4wt%, 8wt%, 10wt.% AC NPs in a physically crosslinked PVA hydrogel

Figure 96 - Thermal images of (a) PVA-Au (b) PVA-WO₃ (c) PVA-AC hydrogels.

Previously, thermal images were taken as a function of time, however, in this instance the author was primarily interested in the appearance of samples compared to the surface to which they were applied.

Hydrogels with on board Au NPs had the greatest contrast to the background surface. Hydrogels with AC showed reasonable contrast and WO_3 NPs were almost indistinguishable from the background. It was also apparent that the concentration of on-board NPs had little effect on the IR properties of the hydrogel. A more telling factor was the species of NPs.

4.4 Hydrogel Electrochromism

Electrochromism in PVA hydrogels is thought to be novel. In this section of work, WO_3 loaded PVA hydrogels prepared using the method in 2.3.4.3 were tested at different voltages, with and without additional salt (Li^+ , Na^+ , K^+ , Ba^{2+}). Additional salts were added during the crosslinking stage of hydrogel synthesis.

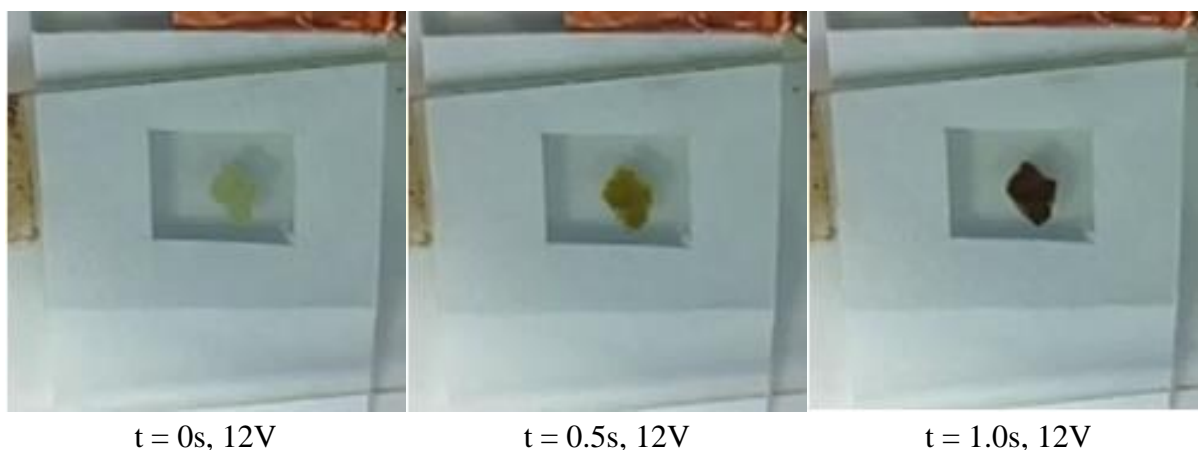


Figure 97 - Optical images of the colour change of a PVA- WO_3 (10 wt. %) hydrogel with no added salt

Figure 97 shows the yellow – dark blue/black colour change of a PVA- WO_3 (10wt.%) hydrogel with no added salt, sandwiched between two glass transparent ITO/FTO electrodes (experimental set-up described in 2.3.4.5) with an applied voltage of 12V. The colour change is essentially instantaneous (<1s), however the voltage was too high in this situation. Lower voltages were used in the range of 1V-12V. It was noted that there was a direct correlation between the voltage and rate of colour change. Low volts resulted in a slow colour change and high volts a quicker change. A possible explanation for this is the higher voltage has a greater motivating effect on dissociated ions in the octahedral structure.

Figure 98 shows the colour change of a lower WO_3 loading of 1wt. %. The colour contrast is still high, even with the hydrogel containing such a very low WO_3 content. This shows that the

oxide particles are subjected to the electron/ion migration even when embedded in a PVA matrix and its guest fluid.

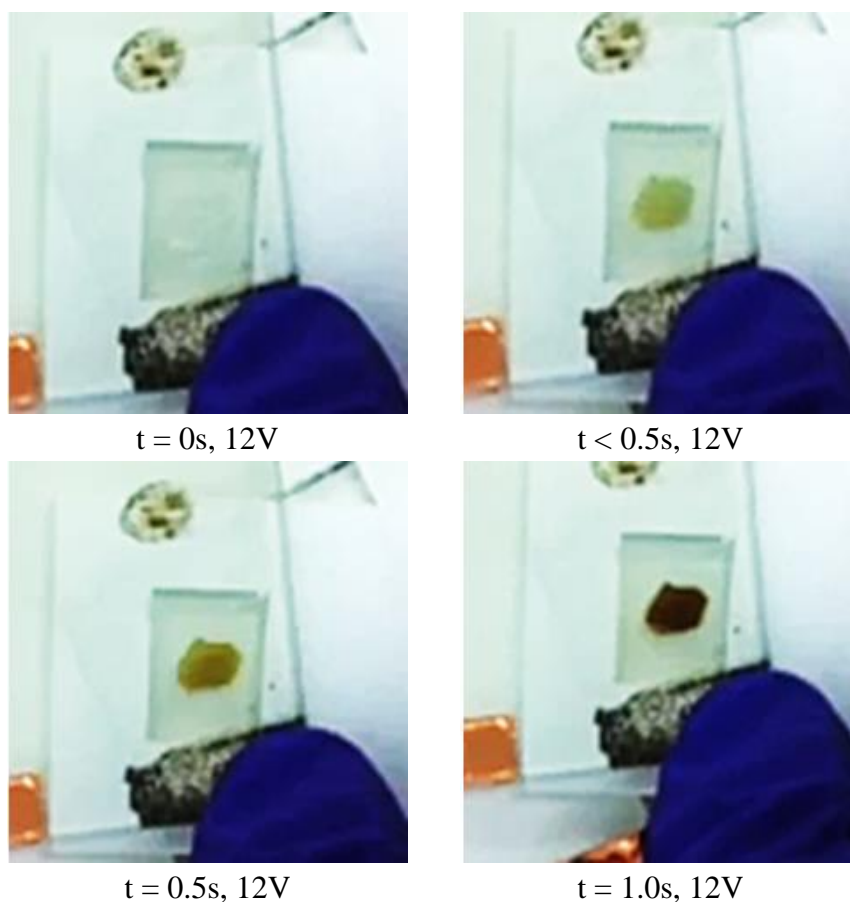


Figure 98 - Optical images of the colour change of a PVA-WO₃ (1 wt.%) hydrogel with no added salt.

Figure 99 shows a series of PVA-WO₃ (5wt. %) hydrogels with perchlorate salts containing cations of varying size present in the porous hydrogel fluid. Here the voltage was ramped slowly from 1 to ~4.5V to discriminate any colour change or speed between the different cation sizes (ion mobility).

It appears that adding salts to the hydrogel increases the intensity of the end colour of the electrochromic gel at a fixed voltage. On the other hand increasing the salt's concentration gives darker shades. The size of the cation affected the mobility (as expected); A_{ii} and B_i appear darker earlier than B_{iii} and C_i and C_{ii}, which have bigger cations. There is little difference in this context between Li⁺ and Na⁺ ions.

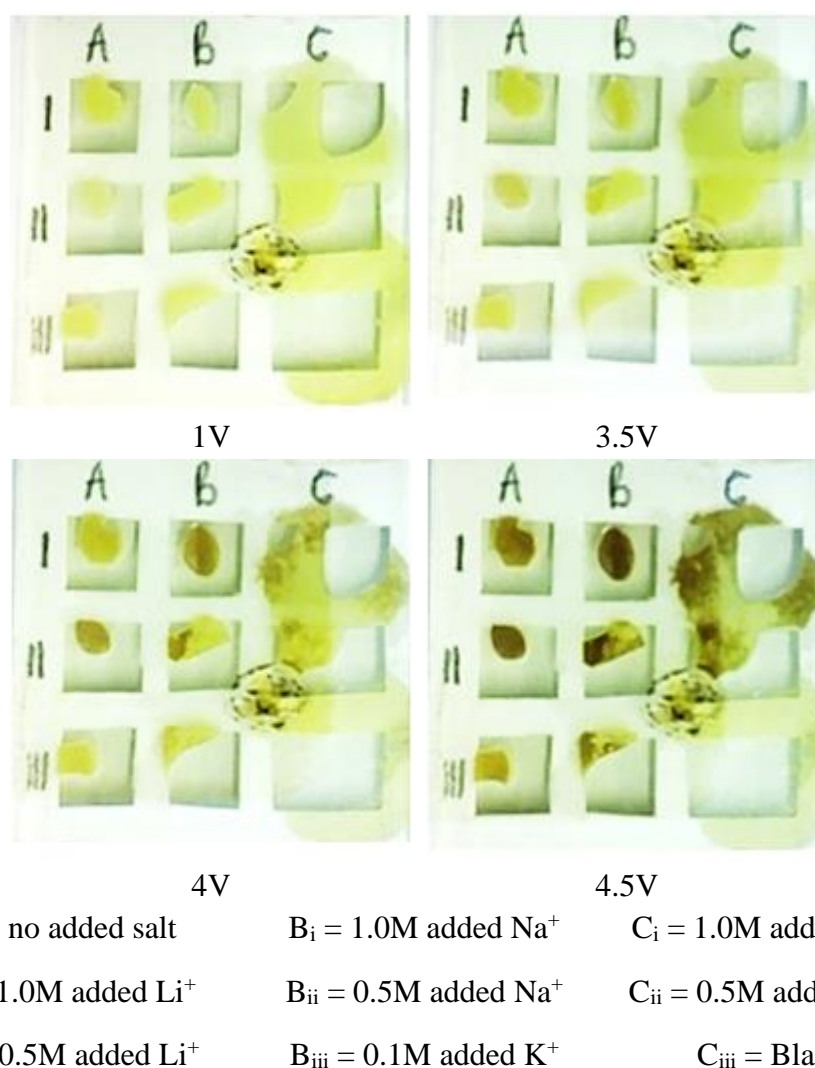


Figure 99 - Optical images of the colour change of PVA- WO_3 (5 wt.%) hydrogels with varying amounts of perchlorate salts and different cations.

4.5 Summary

Work undertaken in this chapter was varied and informative. The thermal adsorption-cooling effect of hydrogels formed by different crosslinking methods has been studied over a 25h period and showed the *method* of crosslinking to have little effect on the thermal properties of the hydrogel. A more critical factor could be the *degree* of crosslinking. Temperature differences between the hydrogels and Al substrate were on average 2.4K lower irrespective of crosslinking method. It is believed that hydrogels from 3D printed PVA is novel and therefore a temperature difference of 2.4K from a 3D printed material is a new achievement. Hydrogels selected for this work were done so on the basis of visual, mechanical and tactile properties. It is likely that the method of crosslinking is largely irrelevant to the adsorption-cooling effect and that the hydrogels used in this work have similar degrees of crosslinking. The amount of

crosslinking ought to be considered further, as this is likely to control the rate of solvent evolution and therefore cooling properties.

A range of MO NPs have been successfully and uniformly dispersed in a PVA hydrogel matrix. Several different methods were trialled to achieve a satisfactory level of dispersion. SEM-EDX has indicated that this has been achieved. Investigation of the thermal characteristics of PVA-MO nanocomposites revealed mixed results. The emissivity values of Au, WO₃ and AC are 0.47, 0.4-0.45 and 0.9-1 respectively. The author therefore believed that the IRT images obtained would reflect this. However, the sample with greatest contrast to the surface it was applied to was PVA-Au. Further investigation is warranted here.

Finally, electrochromism in a PVA hydrogel has been demonstrated with and without additional salts. Colour changes from bleached to coloured (yellow to dark blue) occurred almost instantaneously. The voltage in these initial test was 12V which gave a colour change in <1s, other voltages (1, 3.5, 4 and 4.5V) were used with the colour change observed in 4, 2, 2 and 1.5s respectively. It is therefore likely that the voltage across the material is responsible for the speed of colour change. Further investigation on cycling of colour change (bleached-coloured-bleached) is needed to see if voltage affects the lifespan of the material. Investigations using different salts, revealed an element of tunability in the colours obtained. These results are exciting and are the first step to developing an electrochromic coating which may also be used as a “sweating surface”. It is believed that electrochromism in hydrogels is novel and not only has the author demonstrated this, he has also shown tunability of colour, a significant achievement.

5 3-Dimensional Printed PVA-PLA Materials for Gas/Breathing Sensing Applications

5.1 Introduction

Gas sensors have been around for many years and over time have become more reliable at selectively detecting target analytes. Current common technologies are generally based on carbon, nanofibers, metal oxide nanostructures, metal nanostructures and semiconductor nanostructures. Others utilise photonic crystals, ionic liquids and metal organic frameworks [354, 355].

There is much interest in graphene-based gas sensors because of their superior electronic properties over conventional bulk-based sensors. Faster response times, higher sensitivity and selectivity, lower cost compared to performance are all properties of this type of sensor [356]. Also emerging recently, are a range of electrically conductive 3D printing materials, some of which incorporate graphene. Work on developing 3D printed gas sensors is in its infancy but does exist [357].

5.2 Aims and Objectives

The aim of this part of the author's work is to utilise 3D printing technologies to develop a printable gas sensor able to selectively detect volatile organic compounds (VOCs), carbon dioxide (CO₂), nitrogen dioxide (NO₂) and ammonia (NH₃). By incorporating 3D printing into the process, gas sensors could it was hoped be produced at low cost and in a short space of time. They could it was hoped be produced with varying dimensions appropriate to the intended use/user. Fused deposition modelling (FDM) has been chosen as the most appropriate method of 3D printing, as samples can be printed with a variety of commercially available materials, with a cost and speed of production that are acceptable. A range of asymmetric samples incorporating both single and dual layer asymmetric configurations has been explored. Each layer it was hoped would target different species and might be treated chemically.

An initial specification for a 3D printed gas sensor, is that it should show a response time within 5-10 seconds of a target gas being introduced. Return to baseline levels would ideally be within 30 seconds. Selectivity of species is also important and so an ideal sensor should be able to distinguish between different linear molecules (CO, CO₂, NO₂ & SO₂) and nonlinear (NH₃ VOC's). Sensitivity should also be good with PPB levels of gases detectable; however this is largely dependent on surface area and so there may be a lower and upper limit. The potential

of 3D printed sensors cannot be underestimated, maturation of the technology may even see structural parts to buildings being made using 3D printing, with gas sensing capabilities inbuilt. Furthermore, the almost limitless geometries afforded by 3D printing could enable gas sensors to be hidden as everyday objects, such as vases or ornaments.

5.3 Results

5.3.1 Initial Exploratory Sensor Designs



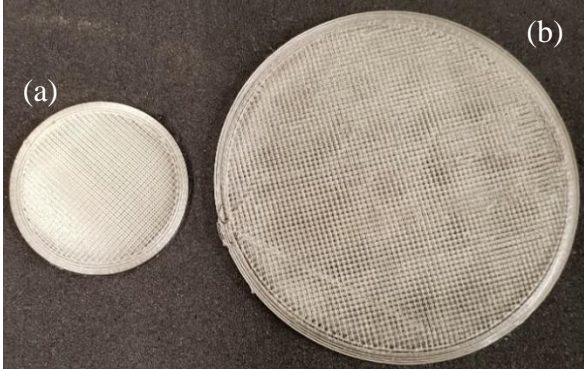
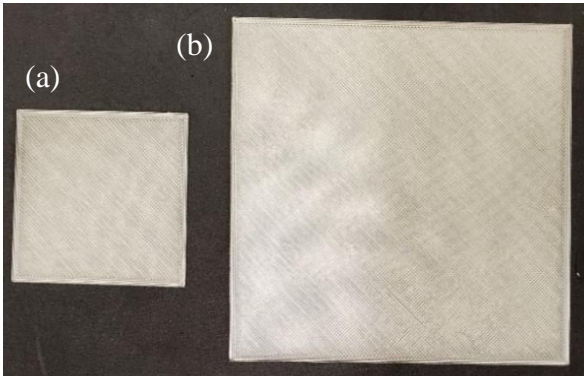
The shape and geometry of the sensor is highly important in terms of the surface area presented to/exposed to the target analytes. Previous studies have found a linear relationship between the surface area of a gas sensor and its sensitivity [358]. This is due to the surface area being proportional to the number of available analyte adsorption sites. Sensors in this project were to be chemically tuneable and therefore had to be adjustable in terms of their aspect ratio and surface area, which would in turn affect their sensitivity. Sensors were also to be durable, stable and also non-toxic and green.

Several simple geometries were initially investigated for PVA only sensors (see Table 15) specifically: thin rectangular cuboid strips (width \neq depth \neq height), cylindrical shaped (radius \neq height) and larger rectangular cuboids (width = depth \neq height). These were designed using Autodesk Fusion 360 and were “sliced” and finalised in Cura. These samples were then subjected to pre-treatment, characterisation and water uptake testing.

The surface texture of these samples is not wholly uniform, with visible ridges of PVA separated with troughs between each strand of deposited material. The setting used on the 3D printer was for normal quality which gave a 150 μ m step changes, i.e. the height of each layer. The controlling factor for the thickness of material strands making up each layer is the diameter of the print nozzle. The nozzle used in the work was 0.4 μ m in diameter. Therefore strands of PVA emerging from the print head (in ideal conditions) should be 0.4 μ m in diameter. One of the limitations of FDM is the surface finish, which will inevitably have some observable layering. This could be accentuated, with noticeable voids between deposited strands if poor fusion has occurred. Possible reasons for this are the temperature and speed settings selected. If filament which has become brittle or chemically changed through absorption of H₂O or contamination, a higher/lower temperature or faster/slower speed of feed to the print head would be required. If this is not done, the result could be strands emerging from the print head with a diameter lower than the nozzle, resulting in gaps between deposited strands.

This layering effect is particularly noticeable on the circular sample of 50mm diameter (b) (see Table 15) which has an appearance similar to a sieve. The diagonal route taken by the print head can be clearly seen. Models are initially printed with an outline which can be seen at the very edge of the samples. This edge is made up of 4 or 5 passes, meaning that the outer boundary is 1.6-2mm thick. Once this boundary layer is complete, the infilling of the model happens, which is where the cross-hatching can be seen. This is the result of the print head route alternating by 90° for each layer, although this is done to maximise the strength of the final model. The circular sample of 50mm diameter (b) is also the thinnest of all initial samples. The combined effect of few layer construction with non-perfect printing conditions has resulted in a model which appears to have voids, although in reality this is unlikely to be the case throughout the entire depth of the model owing to the number of layers.

Table 15 - 3D printed PVA initial designs used here.

Dimensions (mm) [width x depth x height]	3D Printed Model
50 x 5 x 2	
50 x 10 x 2	
Diameter (a): 25 Diameter (b): 50	
50 x 50 x 1 (a) 100 x 100 x 1 (b)	

5.3.1.1 Water Uptake Testing

Once 3D-printed PVA samples had been printed they were dried in a conventional air oven at 353K. After drying over a period of 12h at 353K 3D printed PVA samples were stored in a desiccator with fresh blue indicating silica gel desiccant (impregnated with CoCl_2) to ensure no water was absorbed. Gravimetry was used to monitor how the printed PVA structures absorbed water (DI water) from a humid atmosphere (at defined %RHs).

Some delamination occurred in some multilayer PVA samples (see Figure 100) whereby the individually printed layers of PVA, which would normally have been fused together during printing came apart during the water uptake cycle. This resulted in an uncontrolled much larger surface area being exposed to the humid atmosphere. The layers twisted and buckled with increasing water uptake. Due to this twisting, an exact surface area could not be calculated; however it was noted that the rate of water uptake was greatly increased when compared to the samples which remained as one.

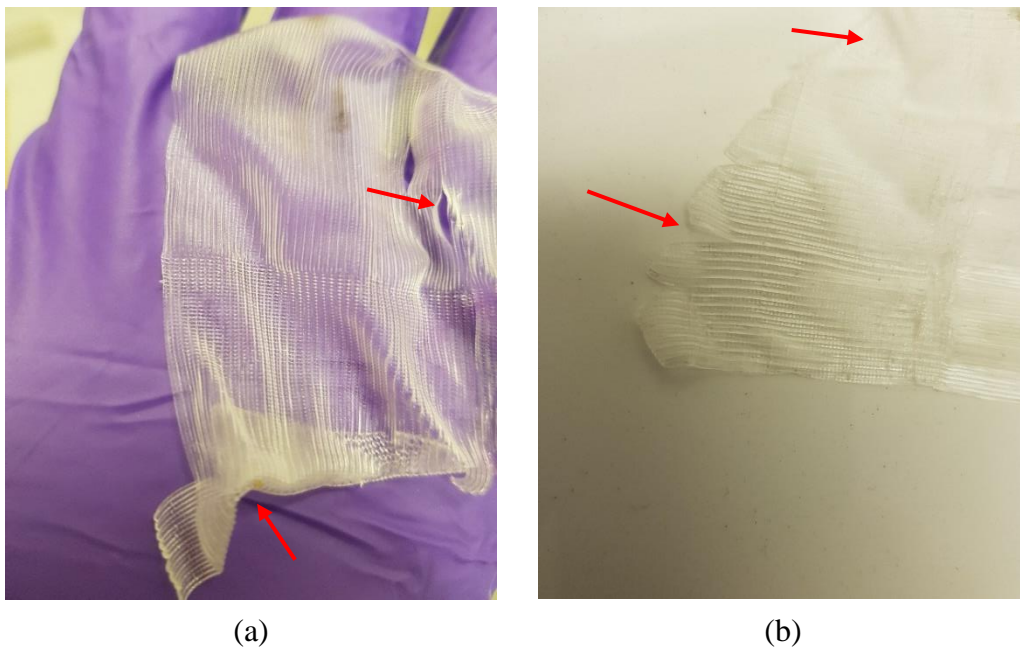


Figure 100 – 3D printed PVA cuboid shapes delaminating into separate layers with increasing water uptake. (a) single layer of printed PVA hydrated with H_2O buckling and twisting evident (b) a different single layer from the same sample of printed PVA hydrated with H_2O showing fused layers coming apart.

Red arrows on Figure 100 indicate where fusion of printed PVA strands has failed due to water uptake. Also highlighted is the curved nature of the edges of each layer that have come apart from the initial boundary layer. Delamination is thought to occur owing to uneven distribution of additional stress on the polymer matrix due to H_2O uptake. Square and rectangular shapes focus mechanical stress at the edges. However, it was noticed that the circular samples did not

show this failure, owing to a more uniform distribution of stress. For this reason it was decided to progress with circular samples in the next phase of study.

Deformation of 3D printed hydrogels should be avoided, and any sign of mechanical failure could affect the sensitivity of the sample. It is already known that surface area is directly proportional to the sensitivity of a gas sensor. Therefore surface area must be accurately calculated in order that sensitivity can be reliably quoted. Other considerations are the longevity of a sensor which may be situated where exposed to a variety of weather conditions. Deformation in this case appears to be a combination of excessive water uptake with poor fusion of 3D printed layers. It is also possible that the rate of water uptake may have an effect on the failure of the sample, i.e. water uptake was too fast.

5.3.1.2 Fourier Transform Infrared

Fourier transform infrared (FTIR) coupled with an ATR diamond crystal accessory was used in transmittance mode to characterise specific chemical groups, particularly to confirm that post-hydration, H₂O was detectable in the PVA matrices. A resolution of 2cm⁻¹ and 45 repeat scans were selected to obtain accurate and reliable data.

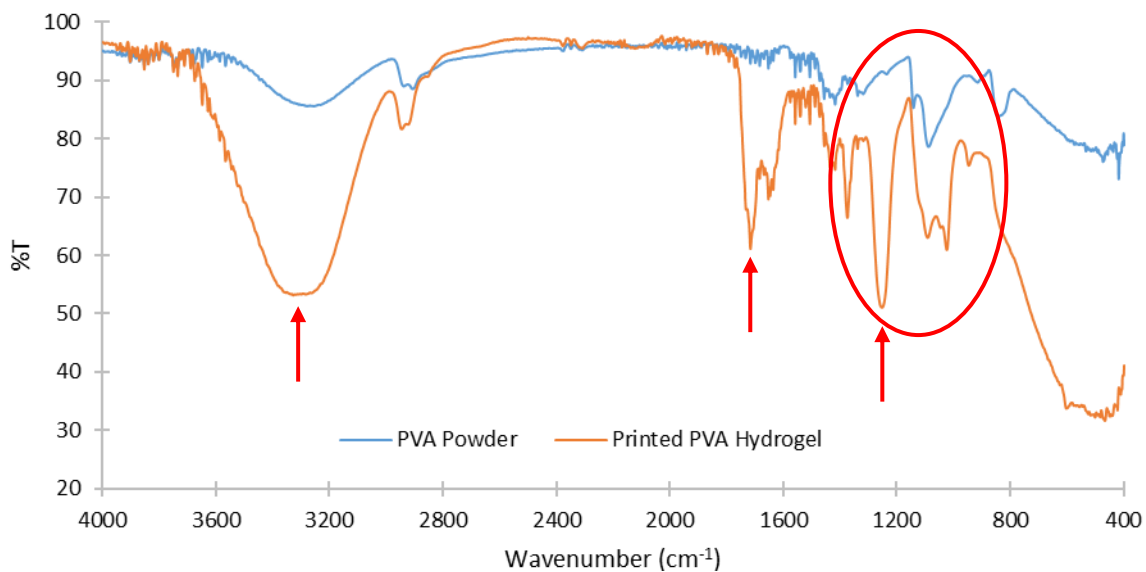


Figure 101 – FTIR-ATR evidence of H₂O uptake in a 3D printed hydrated PVA sample compared to PVA powder.

The observable differences circled in red (Figure 101) occur in the fingerprint region and are the result of the unique pattern associated with different compounds.

From the spectra obtained (see Figure 101) it is evident that H₂O is present within the 3D printed PVA matrix after hydration. This is shown by the increase in % transmittance related to the O-H peak at 3300cm⁻¹ (marked by a red arrow). A small peak at this wavenumber is also

visible in the PVA powder sample; however this is attributable to the O-H group on the polymer chain rather than in H₂O. It is possible that the powder may have absorbed atmospheric water, which would give a peak here too. Regardless, there is clearly a stronger O-H peak in the hydrated 3D printed sample. There is a clear C=O stretching bond in the printed PVA sample at 1716cm⁻¹; ordinarily this would not (and indeed doesn't) show in a fully hydrolysed PVA sample. However, the presence of this peak is indicative of PVA that has not been fully hydrolysed. This is entirely possible, as this sample originated from 3D printer filament, which would not be of as high quality as laboratory grade reagents. The strong C-O peak at 1295cm⁻¹ may also be attributed to incomplete hydrolysis as this does not appear in the powdered PVA sample. A C-O peak would be expected in PVA and does indeed appear for both samples at 1083cm⁻¹ for PVA powder and 1087cm⁻¹ for printed PVA hydrogel.

5.3.1.3 Summary

It was concluded from initial tests that square or rectangular shapes were unsuitable for 3D printed hydrogels owing to the level of delamination that occurs upon swelling with water. Layers of printed PVA material detached from other layers, resulting in the whole structure falling apart. This however was not the case with circular printed designs. These held shape and were able to be swollen with water.

This was thought to be due to the lack of pronounced corners where it was first noticed that layers were separating. In a circular design, the forces of water inclusion on the polymer matrix are evenly spread. It may be possible to swell square and rectangular shapes to a certain point, thus enabling them to maintain shape. However, the author was more interested in exploring the maximum levels of swelling possible, in order that the cooling and gas sensing effects were fully exploited. Therefore, a shape which enabled this to happen was favoured.

Owing to these initial tests, little time was wasted on pursuing geometries which were unsuitable. Going forward, it was decided to explore circular shapes of different sizes and aspect ratios and abandon square or rectangular geometries.

5.3.2 Next Phase Designs

Building on what was learned about the swelling characteristics of different geometrically shaped printed PVA, second phase designs assume a circular disc-like form. Furthermore, dual asymmetric novel composite samples were produced with PVA on one side and PLA/graphene

on the other. This was to enable a printed sensor to have greater scope and tuneability when detecting gaseous species.





	Dimensions (mm) [width x depth x height]		Dimensions (mm) [width x depth x height]
<p><i>Sample 1</i> Top surface of PVA 50 x 50 x 2</p>		<p><i>Sample 1</i> Bottom surface of PLA/G 50 x 50 x 2</p>	
<p><i>Sample 2</i> Edge of PVA 25 x 25 x 2 PLA/G 25 x 25 x 5 composites</p>		<p><i>Sample 3</i> Edge of PVA 50 x 50 x 3 PLA/G 50 x 50 x 0.5 composites</p>	

Figure 102 – Digital photographs of a range of 3D printed asymmetrically layered PVA-PLA/graphene designs.

Disc-like samples were printed in one step, with the initial layer being deposited onto the build plate, followed by the second layer directly on top. The dual extrusion capabilities of the printer enabled this novel and advantageous approach to be taken. Completed layers were geometrically aligned and a short dwell time of the printer when switching materials resulted in good levels of fusion between layers.

The number of individual layers of material which make up a complete asymmetric sample can be calculated using Equation 17:

$$\text{Number of individual layers} = \frac{\text{Thickness of component (mm)}}{\text{Thickness of individual layers (mm)}}$$

Equation 17 – Method to calculate the number of individually printed layers.

Therefore, taking *sample 2* as an example, the PVA layer is 2mm thick and was printed at normal quality (0.15mm layers), so the number of individual layers of PVA can be calculated as $2/0.15 \approx 13$. Obviously a fractional (0.33) layer cannot probably exist, however, the initial layer is printed thicker than subsequent layers to ensure good adhesion to the build plate, which accounts for the extra part-layer.

There is a correlation between the number of printed layers and the mechanical strength of a sample. Also considered is the diameter of the sample. A sample with many layers and small diameter has a greater mechanical strength from point to point than a sample with few layers and large diameter owing to the distribution of force across the surface. As layers are deposited they are fused and so can be considered a single piece of material when dry. However water uptake testing showed that layers can be separated by water causing delamination of layers. It is possible that there is a combination of diameter and number of layers which will not permit delamination, however as alternative shapes have shown to be stable, further investigation into this is unnecessary.

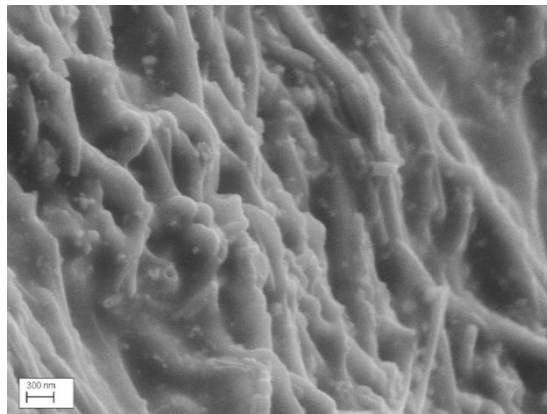
5.3.2.1 Scanning Electron Microscopy

Although hydrophilic PVA and hydrophobic PLA crystallise in separate domains in blends there is inter-polymer inter-domain interfacial hydrogen bonding between -OH groups in PVA and ester groups in PLA [359, 360]. It was thought that this might be explored between layers by μ FTIR, but also by DSC (e.g. does one polymer affect the melting or hydration in the other in the boundary layer). The boundary layer between material layers required SEM analysis to determine the level of fusion obtained during printing. This was considered important information prior to water uptake and sensor testing.

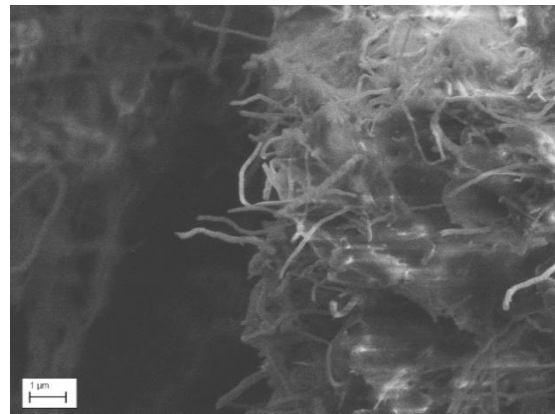
Figure 103 gives images of the unused PVA and PLA/G filaments. PVA showed surface roughness. PLA/G showed fibres emanating from the polymer; these were not expected for G monolayers; it was hoped CNTs were present.

In contrast Figure 104 shows that PVA when printed has a smooth surface, with individual layers hard to distinguish. This may be due to the hydrophilic nature of the material which makes it highly sensitive to moisture. Thus, small amounts of swelling may occur giving a smoothing effect on the surface. Alternatively, the conditions for printing may have been more favourable for PVA, which has produced a consistent and smooth fused sheet. Figure 104 also shows that after printing PLA/G, no layer shows emerging fibres. The 3D printed PLA/graphene shows very clear layers and individual fused lines of material.

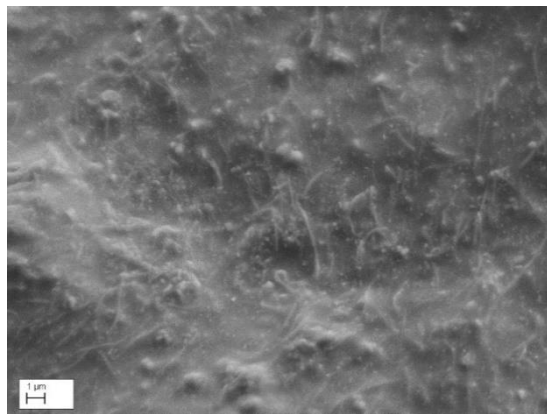
In Figure 104 the interface between PVA and PLA/graphene is seen not to be uniform. It appears different at various points. Figure 104(g) shows the overlapping of the two materials, indicating a strong layer of fusion. However, Figure 104(h) shows a definite gap between layers of approximately $3\mu\text{m}$. This separation has only been observed at the edges of the layers, which suggests an immediate loss in temperature during printing resulting in incomplete fusion of layers. SEM reveals that the PVA and PLA/G layers were $150\mu\text{m}$ thick (as programmed in the software instructions) and that the interlayer region is $3\mu\text{m}$ thick. This was amenable to μFTIR analysis. Internally, the sample would retain heat better than at its extremities which would promote better fusion between layers. As the internal interface is more uniformly fused, an acceptable level of mechanical strength is given.



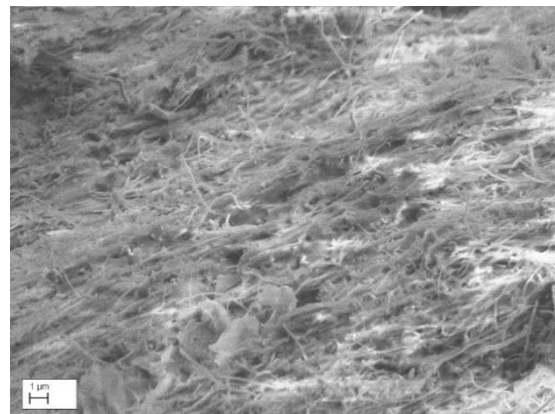
(a) Surface of PLA/graphene filament.



(b) Cross-section of PLA/graphene filament.

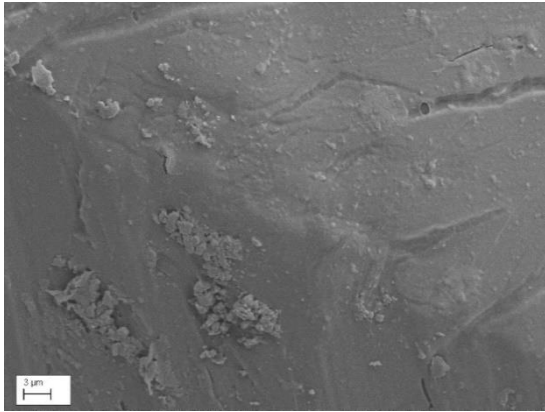


(c) Face of PLA/graphene printed structure.

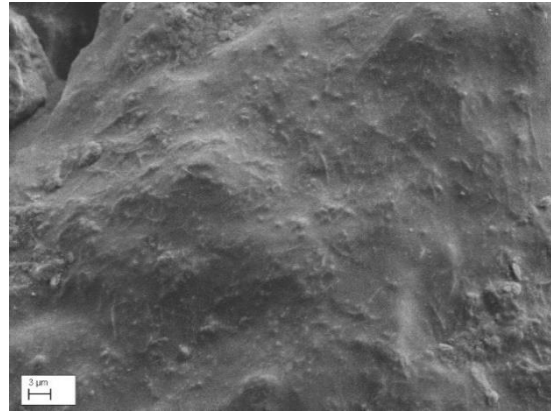


(d) Face of PLA/graphene filament.

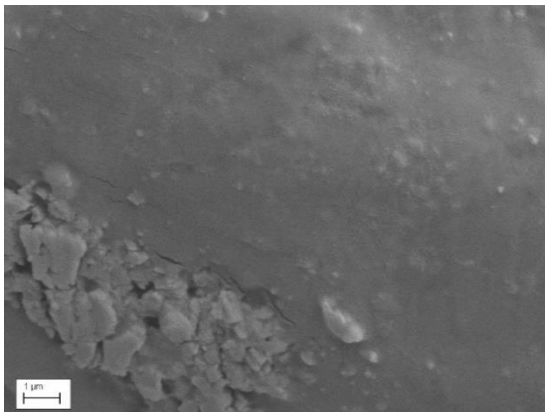
Figure 103 – SEM micrographs of unprocessed PLA/G filament.



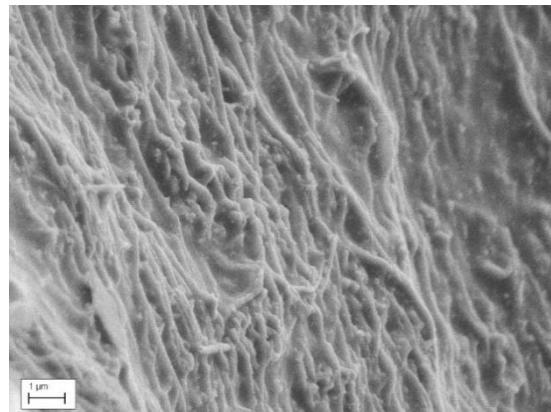
(a) Face of printed PVA.



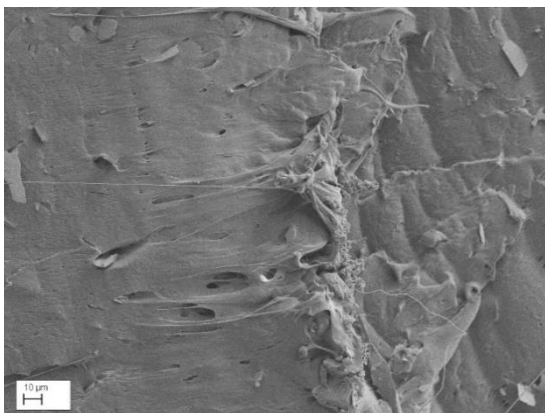
(b) Face of printed PLA/graphene.



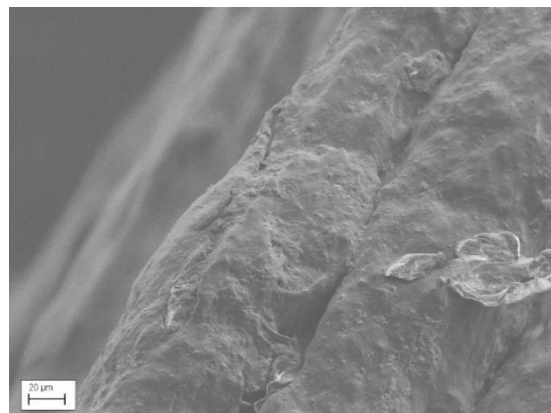
(c) Face of printed PVA.



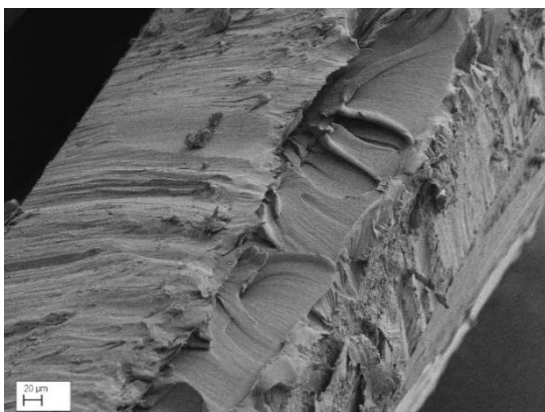
(d) Face of printed PLA/graphene.



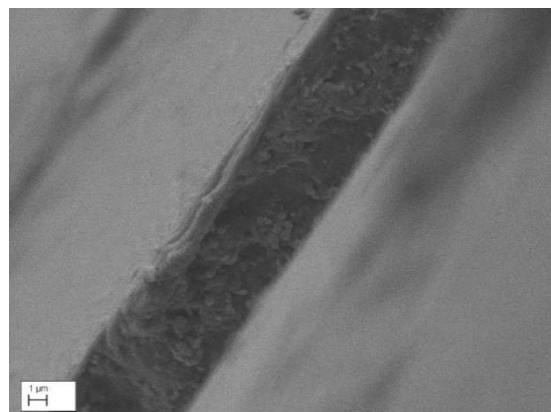
(e) Edge of PVA printed layer.



(f) Edge of PLA/graphene printed layer.



(g) Interface between PVA and PLA/graphene layer.



(h) Interface between PVA and PLA/graphene layer.

Figure 104 – SEM micrographs of faces, edges and interfaces of PVA-PLA/G composites.

Further SEM imagery was obtained on the PLA/graphene filament which appears to show tubular structures protruding from the cross-section of the filament and again on the surface and faces of the printed structure.

These tubular structures have an average diameter of 200-300nm and appear to have a randomised position within the PLA matrix. It is most likely that these structures are in fact MWCNTs, however this would reflect the upper limits of this structure in terms of diameter. Tubes of this diameter would usually be considered nanofibers rather than nanotubes.

5.3.2.2 Fourier Transform Infrared

Fourier transform infrared spectroscopy (FTIR) was used to confirm the identity of the materials pre and post processing. This technique was also able to give information about H₂O solvent(s) contained within the PVA-based hydrogel matrix.

As was found (Figure 105), when the virgin PVA filament was analysed by FTIR it contained peaks which would not be expected to be observed in fully hydrolysed PVA (see Table 32) . These peaks may originate from remnant polyvinyl acetate, a precursor to PVA and may be identified as a C=O stretching mode at 1716cm⁻¹ and a C-O stretch at 1232cm⁻¹ (marked by red arrows). In contrast, the PLA sample, showed all expected peaks, with no unexpected peaks identifiable. It is difficult to identify peaks corresponding to graphene as these tend to be masked by the PLA. It is possible that the region between 1300-1700cm⁻¹ contains bonds attributable to graphene. Raman provided a better and far more reliable method for graphene or CNT identification.

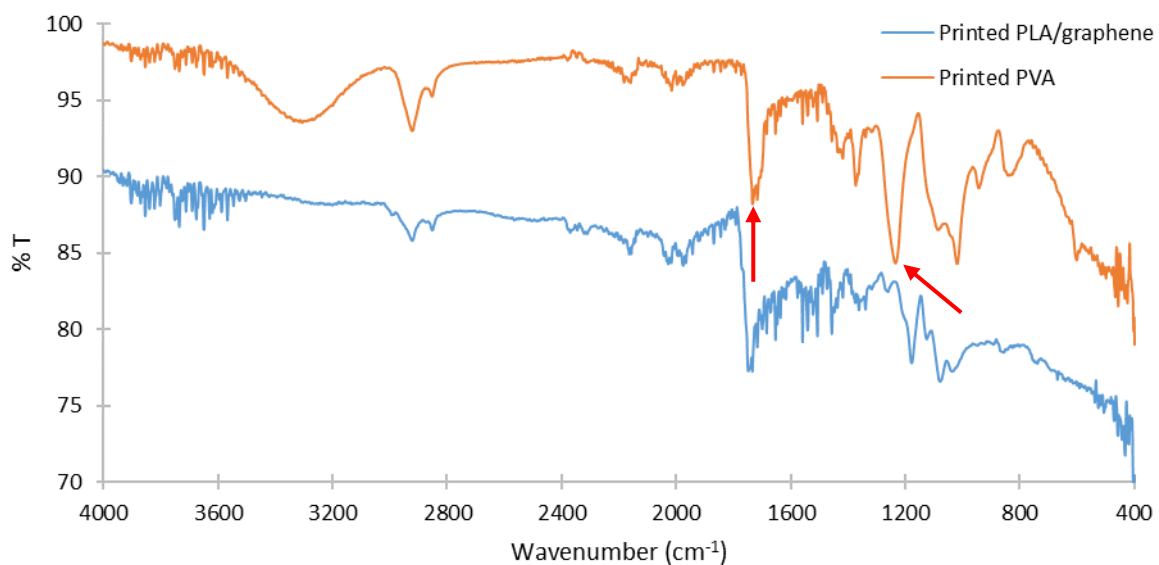


Figure 105 – FTIR-ATR transmission spectra of printed PLA/graphene and PVA.

Analysis of the PVA-PLA/G interface was also conducted; using μ FTIR which is a more appropriate technique as it has a resolution of $100\mu\text{m} \times 100\mu\text{m}$, possibly useful when the edge of PLA/G has a feature $100\mu\text{m}$ wide.

5.3.2.2 Micro Fourier Transform Infrared

μ FTIR was therefore used to investigate the 3D printed PVA-PLA/G interface in asymmetric samples. A dried sample with each layer $500\mu\text{m}$ thick was selected for analysis. The author was primarily interested in the interaction between layers after printing.

Figure 106 shows the PVA-PLA/G interface. The interface ran horizontally across the image, approximately centrally ($\sim 0\mu\text{m}$). A difference in absorbance between $200\text{--}400\mu\text{m}$ and again around $-450\mu\text{m}$ can be seen. This suggests materials of different type. The area in-between ($-400\mu\text{m}\text{--}200\mu\text{m}$) shows an almost uniform absorbance different to the areas above and below, indicative of good chemical mixing.

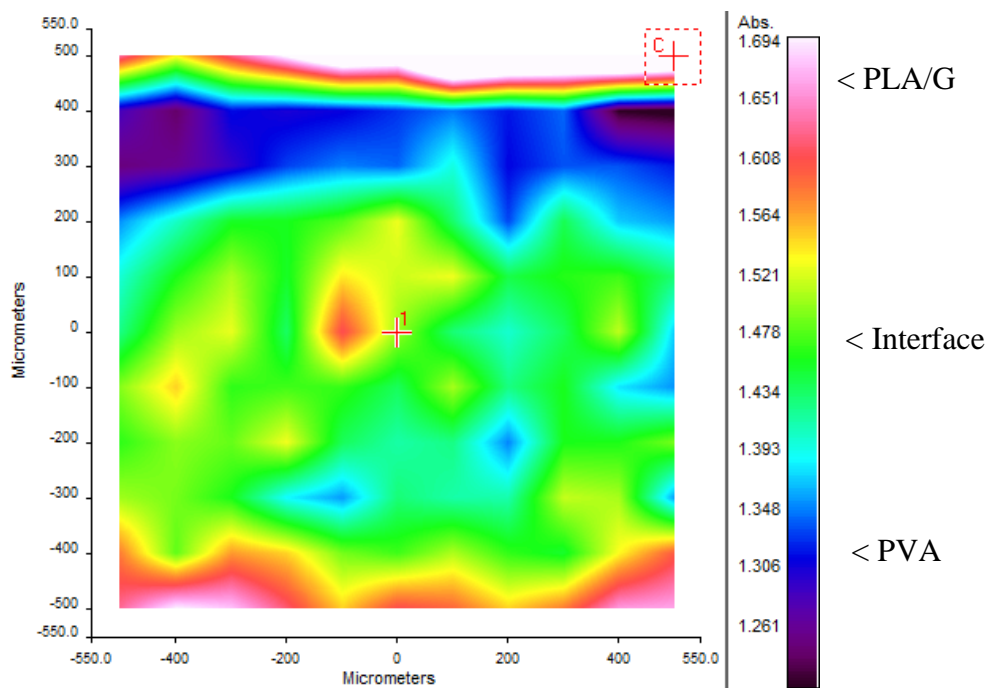


Figure 106 - μ FTIR chemical maps of the interface between PVA-PLA/G.

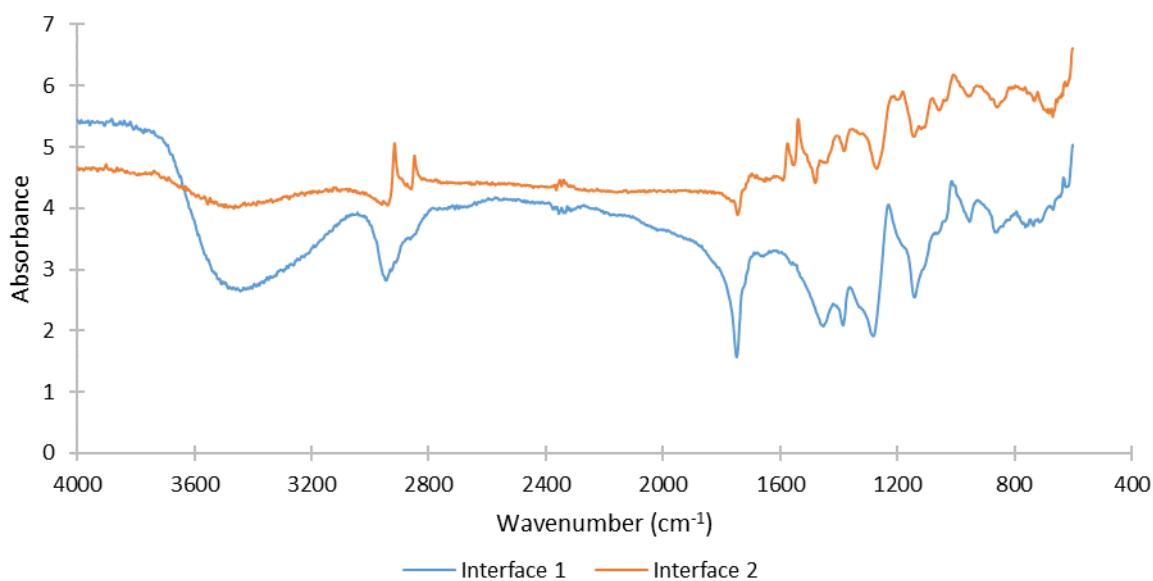


Figure 107 - μ FTIR spectra of the interface between PVA-PLA/G.

Figure 107 shows the spectral differences between two different interfacial regions of the same sample. The main areas of interest are between 2944cm^{-1} and 2844cm^{-1} which correspond to C-H stretches. The different peaks present are thought to be related to C-H stretched occurring in different local environments. This could, perhaps indicate some, but not complete fusion of layers. Also of interest is the peak which appears at 1534cm^{-1} on interface 2, but not interface 1. The author believes this to be a C-H bond which has been distorted.

Overall μ FTIR indicates that there are homogeneous regions between PVA-PLA/G suggesting miscibility. There is also evidence to suggest that at some areas along the interface single phases exist.

5.3.2.3 Raman Spectroscopy

Raman spectroscopy has often been used to confirm the presence of sp^2 and sp^3 carbon. Here it was used to detect graphene within the PLA/G samples. It provides little useful information on PVA: however, the use of Raman spectroscopy in graphene analysis is well documented [361] and as such is a definitive technique in this area.

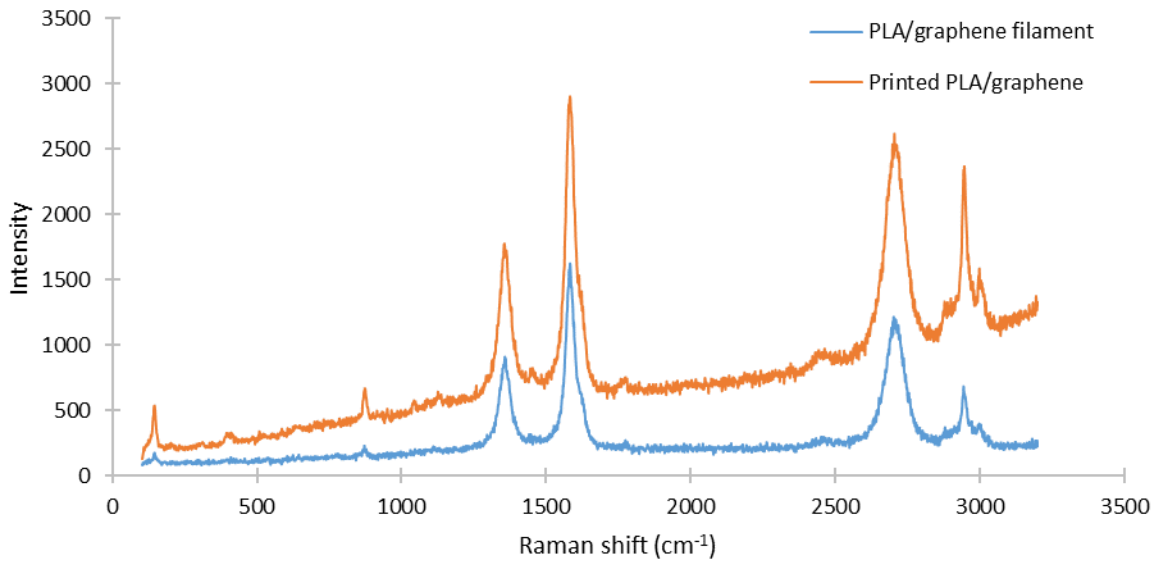


Figure 108 – Raman spectra of PLA/graphene filament and PLA/graphene printed.

Based on the Raman spectra obtained for the PLA/graphene sample, it is clear that this sample does incorporate graphene. Peaks clearly correspond to literature values [361] and appear to be shifted very little (if at all) by the thermal process of 3D printing. Also confirmed by this technique were two bonds expected to be present in a PLA sample.

Table 16 – Peak identification of PLA/graphene filament before and after printing.

Sample	Identification of Peaks					
	G-Band (cm ⁻¹)	G'-Band (cm ⁻¹)	D-Band (cm ⁻¹)	Radial Breathing Modes (cm ⁻¹)	C-O-C	C-CH ₃
Graphene standard	1580	2700	1348	0-300		
PLA/graphene filament	1582	2708	1360	144	877	2945
Printed PLA/graphene	1582	2708	1356	144	872	2947

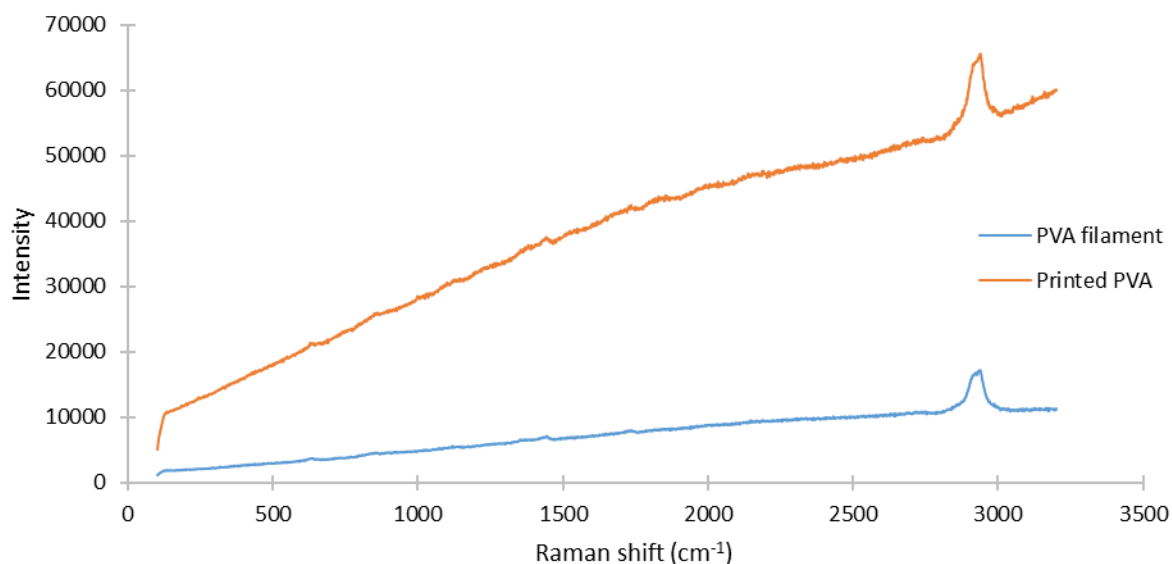


Figure 109 – Raman spectra of PVA filament and PVA printed.

Raman spectroscopy of PVA does not reveal much information; the peak at 2943cm^{-1} for PVA filament and 2943cm^{-1} for printed PVA correspond to C-CH₃. No other identifiable peaks are present.

Table 17 – Peak identification of PVA filament before and after printing

Sample	Identification of Peaks (cm^{-1})
	C-CH ₃
PVA filament	2943
Printed PVA	2943

5.3.2.4 Thermogravimetric Analysis

Thermogravimetric analysis (TGA) was used to confirm the temperature at which PLA/graphene and PVA begin to decompose. Information was also required on differences which may be present between standard bulk analytical grade chemicals and 3D printed materials.

Figure 110 shows TGA analysis of unprocessed PLA/graphene and printed PLA/graphene in both air and N₂. PLA is insoluble in water and therefore dehydration does not occur on heating. However, the printed PLA sample shows a small (10%) loss in weight between 300-620K. This could be attributed to loss of traces of free lactic acid trapped in the layers of PLA. Between 620 and 650K a loss of lactic acid or decomposition with a rapid rate of degradation occurs, with an 80% loss in weight during a 30K temperature change. In some samples a residue of

almost 20% wt. was noted. It would have been useful to analyse this by ^{13}C or ^1H nuclear magnetic resonance (NMR) to give an indication of any organic compounds which may have been formed in the TGA instrument. It would have also been useful to have analysed a PVA-PLA/G sample to investigate if there was a polymer-polymer interaction which may alter the thermal degradation properties of each material.

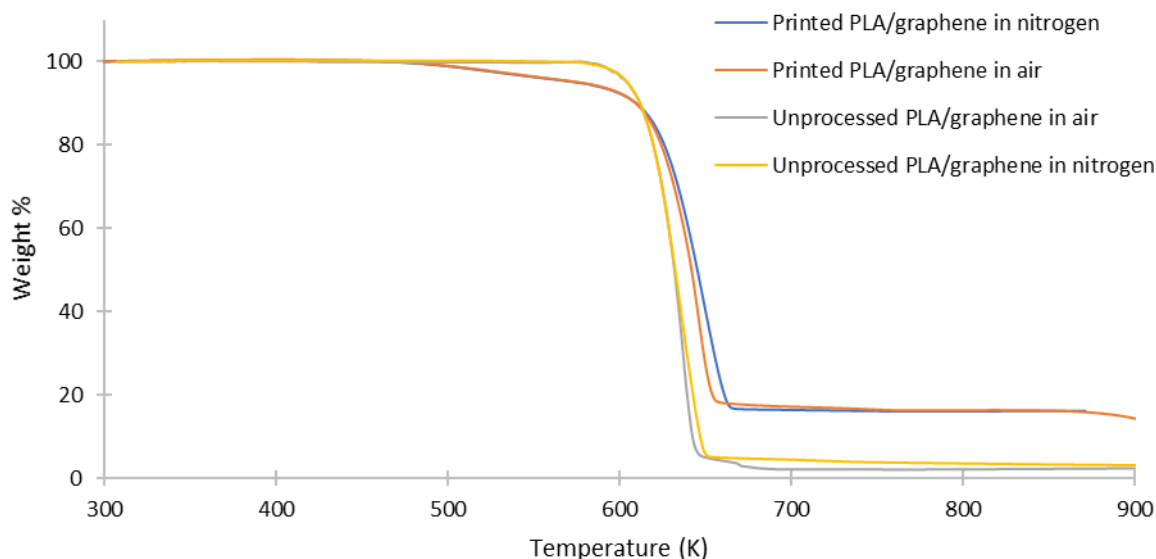


Figure 110 – TGA of printed PLA/graphene and unprocessed PLA/graphene in N_2 and air.

Figure 111 shows equivalent TGA analysis of unprocessed PVA and printed PVA in both air and N_2 . Initial dehydration takes place in the two printed samples between 300-500K with a loss in weight of approximately 10-15%. This is also thought to be due to moisture trapped between printed layers and unprocessed samples did not undergo this initial dehydration.

The degradation process begins at 510K, with the unprocessed sample in N_2 showing a sharp weight loss of 70% before stabilising and giving constant weight residues above 800K it is believed that these are impurities in the filament. Both printed samples and the unprocessed sample in air gave similar degradation to each other from 510K to 700K, after which the unprocessed sample gave a final sharp decrease before meeting the degradation pattern of the printed samples at 790K after which constant weight residues were obtained. Gilman et al. suggest that there are two zones of degradation; firstly at 573-598K and latterly at 673-698K. TGA data obtained in this work partially supports this; however, it is possible that the areas where weight loss is slowed (degradation) are masked by the degradation of impurities in the PVA filament. This is plausible, as unprocessed filament will not have been heated to 490-500K during printing and therefore will not have been subjected to initial chemical changes. The unprocessed filament shows a weight% of approximately 8% even at 800K. The author believes this must be attributable to impurities which were unable to react owing to the absence

of oxygen. It would be wise to repeat this test to understand if these results are reliable. It may also be interesting to include filament which has been heated to 500K, but not printed to see if it is chemically changed and therefore follows the same pattern as printed samples.

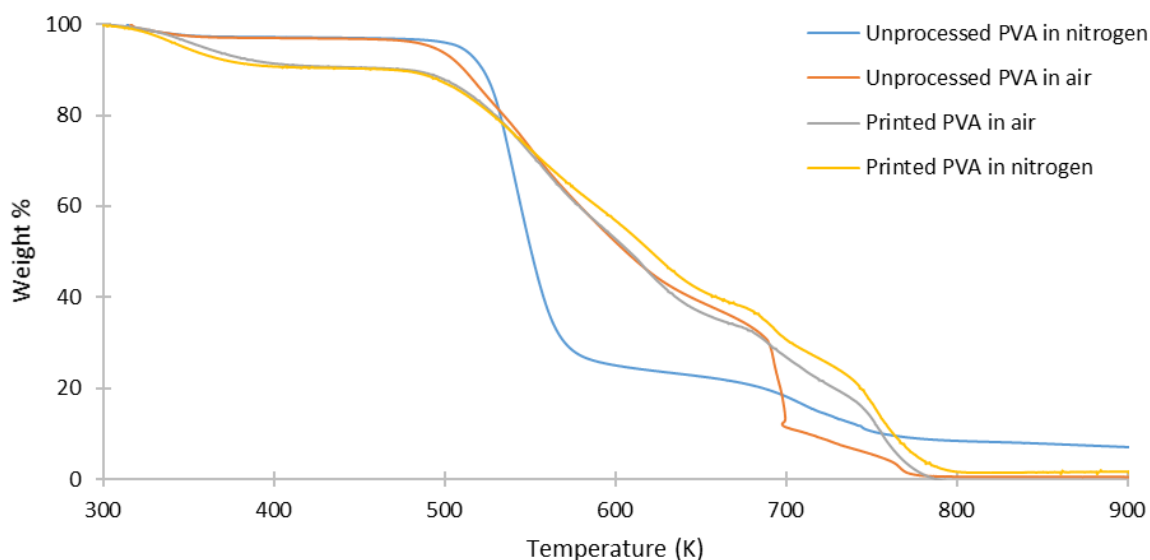


Figure 111 – TGA of printed PVA and unprocessed PVA in N_2 and air.

The exact nature of the various pyrolysis reactions which occur in PVA are complex and have been studied in depth elsewhere [362]. TGA was able to confirm the thermal stability of PVA and PLA which is the level required in this work. In future this ought to be investigated for PVA-PLA/G nanocomposites to reveal levels of interpolymer interaction.

5.3.2.5 Differential Scanning Calorimetry

Differential scanning calorimetry (DSC) was used to investigate phase changes within the PVA matrix to give indications of hydrogel formation and the state of water therein. When cooled below its freezing point water in the hydrogel and on the hydrogel surface will freeze; however the temperature at which this occurs varies. Cryoporosimetry, cryoporometry and thermoporometry approaches have used NMR and DSC analysis of H_2O freezing/melting of guest molecules in constrained hosts to reveal the nature of those hosts. Such melting-freezing is affected by the nature of the hosts in which the H_2O molecules find themselves. This might reveal a host pore size or here a hydrogel chemical matrix [363]. Solid state NMR was not available in the relevant timescale, but DSC was used and was useful.

Hydrogel formation might have been subsequently investigated by TGA of H_2O loss, but here DSC analysis in-situ of on-board H_2O was preferred and is now described. Water held

internally in the polymer hydrogel matrix will remain in liquid form slightly below its normal bulk freezing point in the pure state, owing to the interactions it has with the polymer chain [363]. DSC can sense this freezing process within the hydrogel.

The sample was first cooled to 228K at 10K/min and then heated at 0.5K/min before a second cooling step (0.5K/min) to the original starting temperature. This complete cycle was conducted twice to determine any irreversible changes.

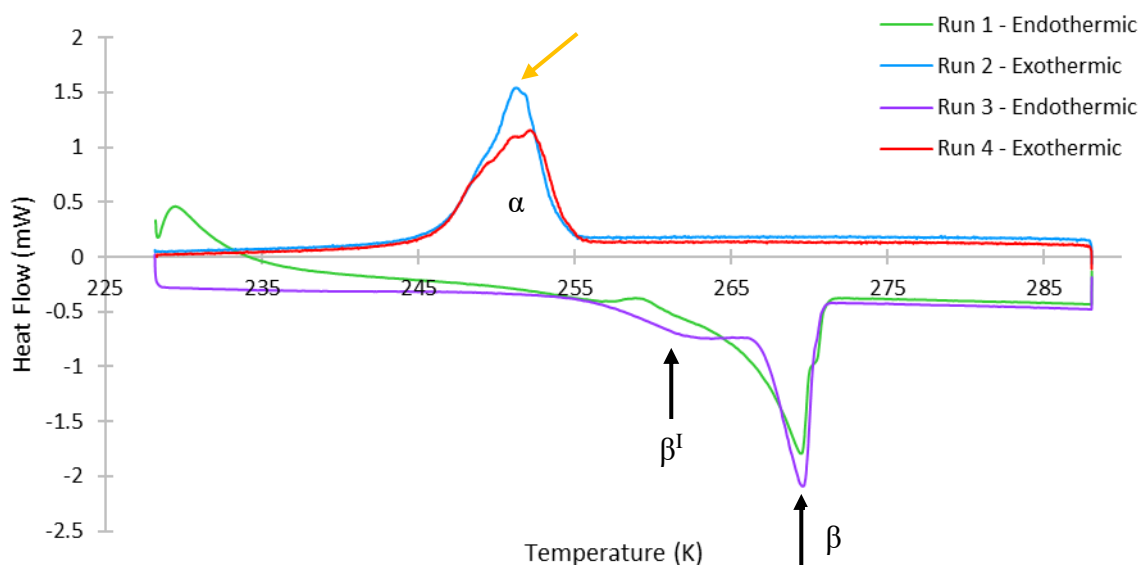


Figure 112 – DSC curve of freezing and thawing of H₂O held in a printed PVA hydrogel.

Figure 112 shows the DSC curve obtained for the freezing-thawing of H₂O in a printed PVA hydrogel. First it should be noted that exothermic freezing and endothermic melting for on-board H₂O are noted in both 1st and 2nd cycles repeatedly. Second, the temperatures of freezing (243-255K) and melting (245-270K) cover significant ranges of temperature, suggesting a range of H₂O environments. None of these processes are occurring at 273.15K expected for bulk pure water, confirming the effect of the hydrophilic PVA polymer host hydrogen-bonding the guest H₂O. Third, the enthalpy of fusion of bulk pure H₂O (333.55kJ/kg at 273.15K and 101.325kPa) is known and the DSC was indium-calibrated. Hence, the integrated areas α and $\beta + \beta^I$ in Figure 112, could be converted to enthalpies of fusion of hydrogel-bound water. By integrating the peaks, it was found that:

Run 1 – 324.1J/g (97.0%), Run 2 – 317.9J/g (95.2%), Run 3 – 304.82J/g (91.3%) and Run 4 – 259.9J/g (77.8%)

The percentage value relates to the closeness of obtained values to that of the enthalpy of fusion of bulk pure H₂O. This shows lower values for the repeat runs, owing to H₂O being irreversibly held in a new state.

This showed a freezing phase change guest of guest water occurs as indicated by the orange arrow and the reverse melting by a black arrow. If there were no major PVA effect it would be expected that two peaks be present, one close to the freezing point of water corresponding to the surface water and a second at a cooler temperature to indicate freezing of the internally bound water. No peak appears at 273K, perhaps indicating no pure or unbound surface water.

The black arrowed melting is indicative of forms of on-board water (internal and surface water). Certainly, the DSC profiles must relate to guest water and not PVA changes [364].

5.3.2.6 PVA Water Uptake Investigations

The level of H₂O uptake and swelling of printed PVA samples was of great importance given that one final application is directly related to the level of hydration from the PVA matrix and the parallel inclusion of a functional agent. The rate and extent of uptake of water vapour by a printed PVA disc was followed at different relative humidity's using the atmospheres above saturated salt solutions as previously (4.3.1.1) and gravimetry.

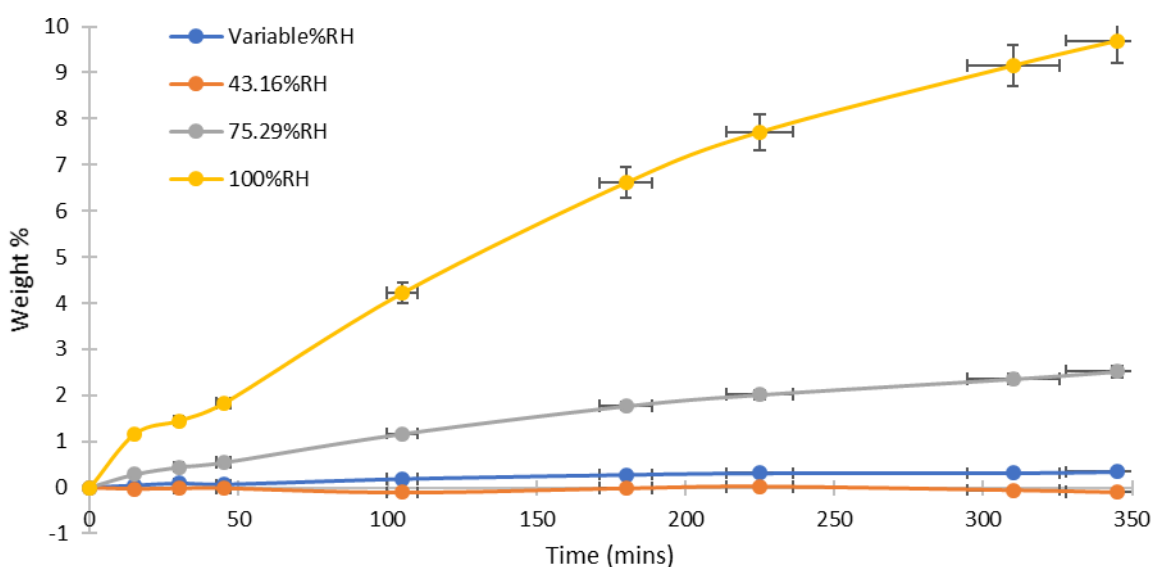


Figure 113 – Weight % increase of printed PVA samples due to H₂O uptake on exposure to different relative humidity's.

The error bars given in Figure 113 are small and show a good degree of certainty about the data. At worst the weight% is $\pm 1\%$. When considering the error of the balance is $\pm 0.1\text{mg}$ and

the actual mass weighed is 0.04499g this error is insignificant. Furthermore repeat tests would increase the reliability of the data.

Table 18 – Mass change and weight % change of printed PVA exposed to various different saturated salt solutions.

Saturated salt solution	% Relative humidity	Weight % change after 350 min
Atmospheric	Variable	0.32
K ₂ CO ₃	43.16 ± 0.39	-0.099
NaCl	75.29 ± 0.12	2.52
H ₂ O	100	9.69

Printed samples of approximately the same weight were dried in an oven at 400K overnight, and their water uptake was measured at 295K as a function of time.

The weight of PVA samples prior to hydration were approximately 1.21g ± 0.1g. Therefore, knowing the density of deionised water is 0.9970 g/mL at 298K the volume of water taken up by the printed PVA may be calculated (using volume = mass / density):

Table 19 – Volume of water taken up by the printed PVA matrix

Saturated salt solution	Dried mass of PVA (g)	Mass change of PVA (g)	Volume of water in PVA matrix (cm ³)
Atmospheric	1.21651	0.00169	0.00170
K ₂ CO ₃	1.21113	-0.00053	-0.00053
NaCl	1.20847	0.01152	0.01155
H ₂ O	1.21729	0.04499	0.04513

This corresponds to a low volume of water taken up by the printed PVA. The 100%RH sample gave a level of swelling of approximately 10wt%. The second most swollen sample has a maximum wt.% increase of 2% indicating that the only viable sample is the one swollen in a 100%RH atmosphere. It is possible that the partial pressure of the saturated salt solutions was noted that no-one has previously made 3D printed hydrogels in this way, and DSC could see the on-board H₂O.

Certainly the water sample felt “gel-like” to touch and was ductile, able to be physically manipulated without any degree of damage occurring or evidence of delamination present. It was encouraging that water was able to be incorporated into the PVA matrix in this manner, maintaining the viability of using this method for inclusion of further or different solvents.

5.3.2.7 Monoethanolamine Inclusion

The possible inclusion of monoethanolamine (MEA) in the samples was important for CO₂ hydrogel-based gas sensing. MEA is well known as an industrial CO₂ gas scrubber [365]. Others have found it could be incorporated into PVA [366]. Here it was found that MEA and ratios of MEA:H₂O could be incorporated into the printed hydrogel matrix by a simple immersive swelling method. The method used was to immerse dried printed PVA disc samples in liquid MEA at 298K for 24hrs. Initially neat MEA was used, however, different ratios of H₂O/MEA were also investigated. When H₂O was included, the printed PVA discs were immersed in the mixtures of H₂O+MEA. An alternative route may be to initially swell the printed PVA discs (as described in 5.2.3.6) before immersing them in neat MEA. The immersive mixture route was favoured, as it was thought this would give a more controlled uptake of H₂O/MEA.

The resultant material was a soft, gel-like material which was slightly yellow/red in appearance. The printed structure remained intact; however individual printed layers could not be distinguished. The structure did not show any signs of delamination and was able to be easily sliced using a scalpel into smaller pieces for gas testing.

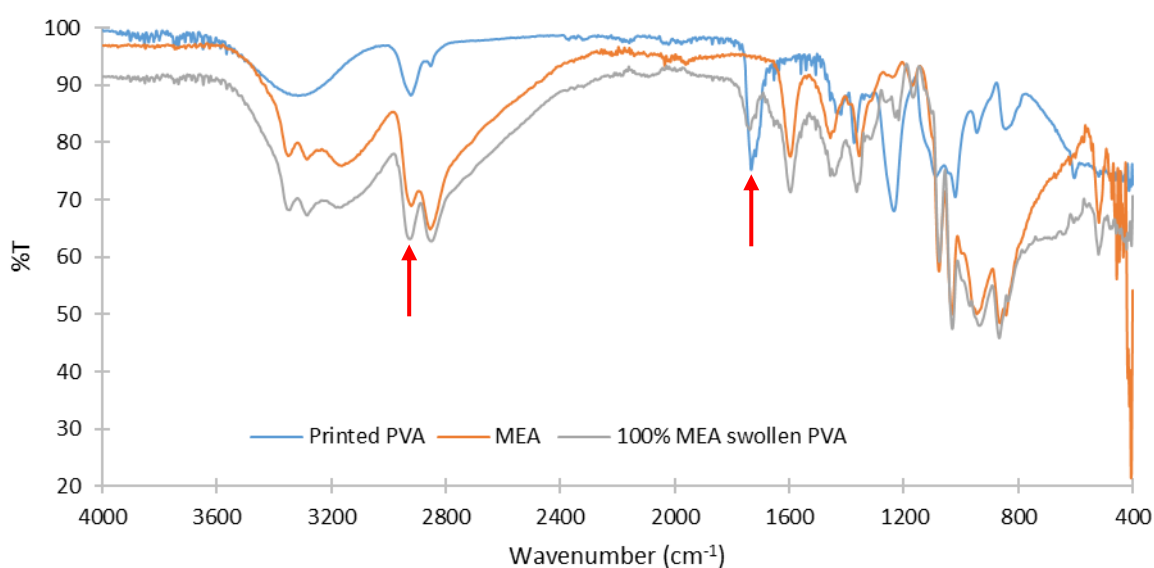


Figure 114 – FTIR-ATR transmission spectra of dried printed PVA, monoethanolamine and printed PVA swollen with MEA.

FTIR investigations indicate that MEA is present within the polymer matrix (see Figure 114). The 100% MEA swollen PVA sample has an FTIR spectra similar to MEA solution in terms of peak positions; however %T values differ. FTIR does not show good correlation between printed PVA and PVA swollen with MEA. It is possible that the PVA is being distorted by the on-board MEA which may inhibit modes of vibration. Of particular interest is the peak indicated by the red arrow. This was identified as C-H stretching (2918cm^{-1} , 88.4%T) in the printed PVA sample and C-H stretching (2920cm^{-1} , 69%T) in the MEA sample. The same peak in the 100% MEA swollen PVA sample is at 2926cm^{-1} , 63.1%T. The author believes that this difference is the result of MEA distorting PVA and thus a different %T intensity and peak position are observed

Also of interest is the peak at 1732cm^{-1} 75.2%T for the printed PVA and 82.3%T for 100% MEA swollen PVA (indicated by a red arrow). This is clearly the same peak and corresponds to C=O. This peak does not appear for MEA. Neither PVA nor MEA has a C=O, however this is thought to originate from un-hydrolysed PVAc, indicating that the PVA filament used in printing was not of very high purity. The %T differs between the two samples, suggesting that they exist in different local environments.

The two peaks highlighted give strong evidence that MEA was successfully incorporated into the PVA polymer network. It would have been useful to undertake DSC to add further evidence to this conclusion.

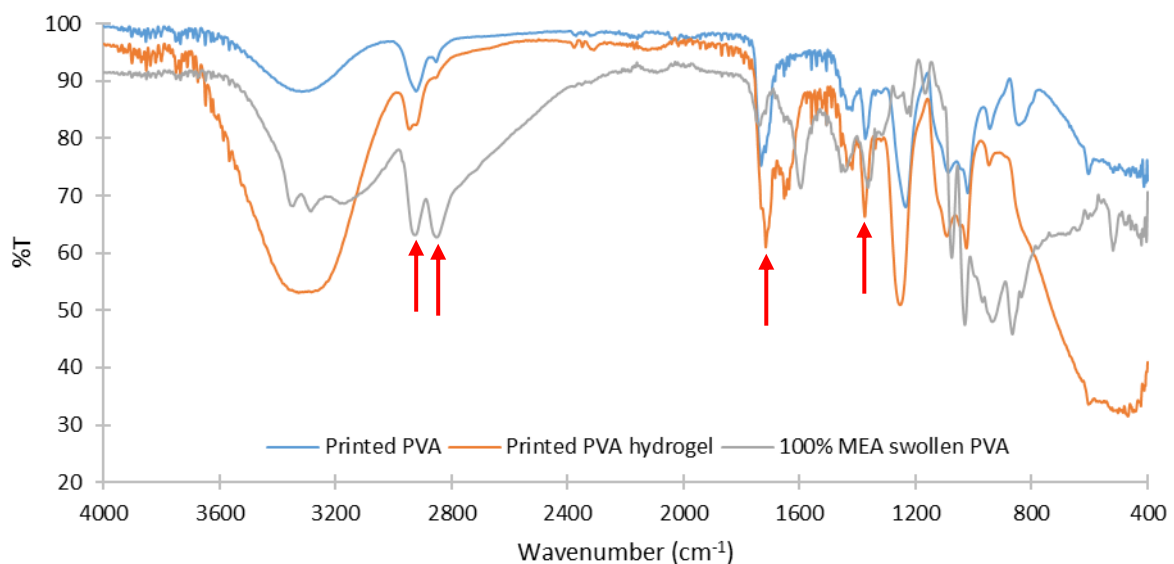


Figure 115 – FTIR-ATR transmission spectra of dried printed PVA, printed PVA swollen with deionised water and printed PVA swollen with MEA.

Figure 115 shows the differences and similarities between printed PVA swollen with H₂O and MEA. It is known from Figure 114 that MEA can be successfully incorporated into the printed PVA matrix. Also known from FTIR (Figure 101) and DSC (Figure 112) is that H₂O can be included in the printed PVA matrix.

Interestingly, when MEA interacts with PVA shifting of peaks and different %T are observed, owing to distortion of PVA by MEA. This is noticeable for the C-H stretch at 2918cm⁻¹, 88.2%T for printed PVA. The same bond is at 2946cm⁻¹, 81.6% for a printed PVA hydrogel (H₂O on-board) and 2926cm⁻¹, 63.2%T for printed PVA swollen with MEA.

Similar distortions occur for a C=O stretch at 1732cm⁻¹, 75.2%T for printed PVA, 1716cm⁻¹, 61.1%T for a printed PVA hydrogel (H₂O swollen) and 1733cm⁻¹, 82.3%T for printed PVA swollen with MEA.

Likewise O-H bending occurs at 1400cm⁻¹, 85.1%T for printed PVA, 1380cm⁻¹, 66.4%T for a printed PVA hydrogel (H₂O swollen) and 1346cm⁻¹, 71.6%T for printed PVA swollen with MEA. This represents a significant shift and highlights the different local environments the on-board solvent is held in.

Also investigated was the effect of altering the H₂O:MEA ratio would have on the PVA polymer matrix. Figure 116 shows a range of PVA:MEA ratios. Of note is the general shift in %T intensity with increasing H₂O content. From 3000cm⁻¹ to 800cm⁻¹ samples with the lowest MEA content (highest H₂O content) have lower %T values. This pattern does not appear to hold in the fingerprint region (between 800cm⁻¹ and 400cm⁻¹) where there is a spectra-structure correlation and a distinct crossover in %T intensities. The author believes that this is due to changing structure of PVA by the guest solvent [367].

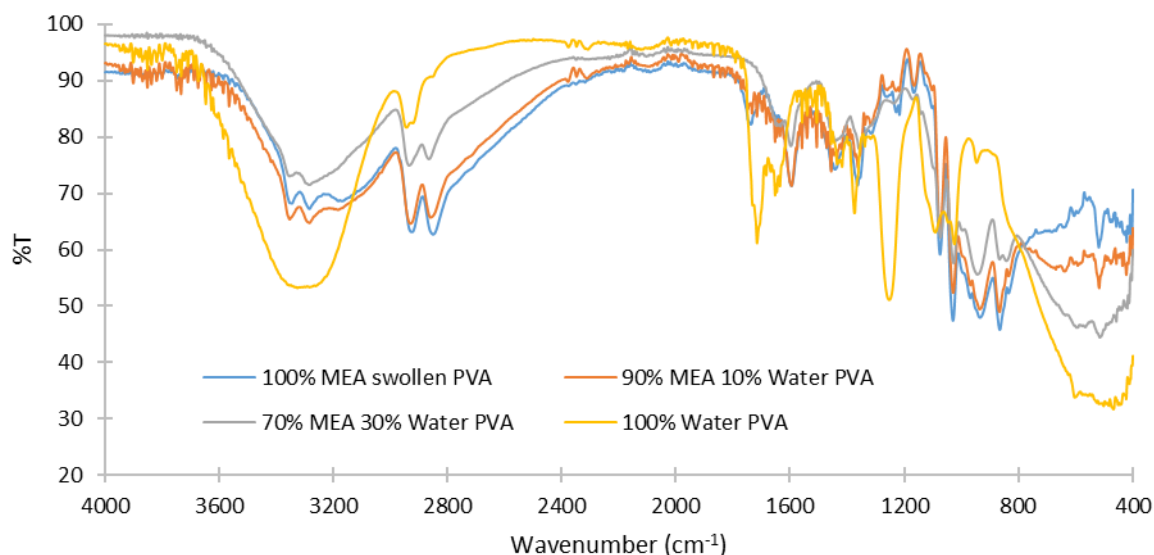


Figure 116 - FTIR-ATR transmission spectra of printed PVA swollen with different ratios of MEA:H₂O.

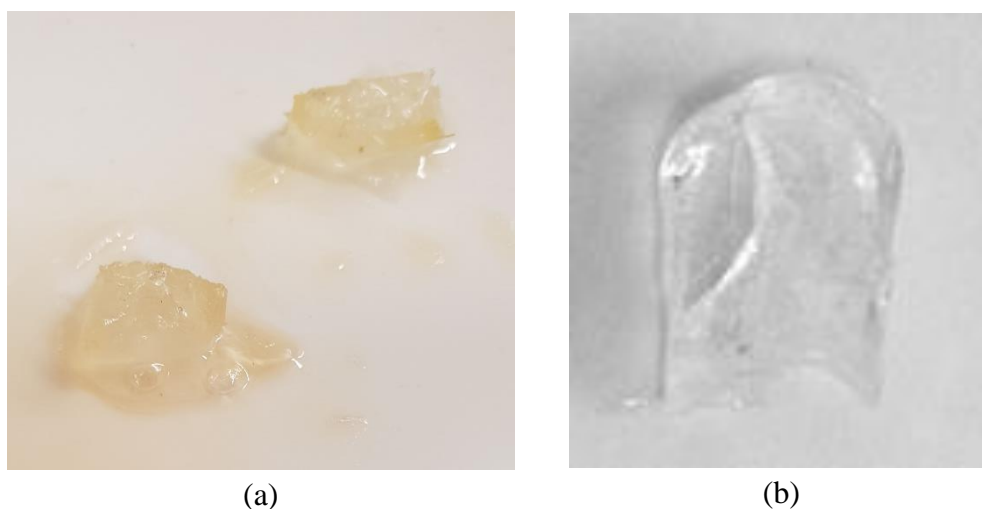


Figure 117 – Images of (a) printed PVA swollen with MEA (b) simple PVA hydrogel swollen with H₂O.

Figure 117 shows the appearance of the two samples tested. The slight yellow tinge apparent in (a) is likely to be the result of oxidation of MEA. MEA is a colourless viscous liquid which oxidises slowly and takes on a slight yellow hue upon doing so. Although the samples were freshly made, they were not photographed immediately. Therefore, the colour difference is likely to be the result of initial oxidation of the on-board MEA. DSC of the on-board MEA might in the future be useful. It is also possible to produce mixtures of H₂O and MEA and follow the same immersive swelling method to obtain a mixed solvent printed PVA hydrogel.

5.3.3 Gas Testing

Gas testing was conducted using a custom designed and built test rig (described in 2.2) incorporating four-point conductivity, residual gas analysis and a commercial gas monitor.

Concentrations of (0.045, 0.089, 0.134, 0.179, 0.223 and 0.268mmol CO₂) were injected into an air carrier gas stream flowing at 250cm³/min. Electronic responses observed via four-point conductivity are attributable to adsorption or desorption of CO₂ from the H₂O and MEA-containing hydrogel samples. An RGA (monitoring at m/z = 16, 18, 28, 30, 32, 44 and 46 in an MCD mode) gave a response to injected samples within 2-3s, returning again to baseline levels within a further 2s. The purpose of the commercial gas sensor was to investigate whether levels of injected gas was sufficient to trigger an alarm response. Gas testing was conducted at room temperature (298K) with the relative humidity of the gas stream kept constant using a saturated solution of NaCl (75.29 ± 0.12%).

Two samples were evaluated: approximately 1g of printed PVA hydrogel swollen with H₂O (approx. surface area = 2.45cm², diameter = 0.6cm, thickness/height = 1cm) and 1g of PVA swollen with MEA (approx. surface area = 2.26cm², diameter = 0.6cm, thickness/height = 0.9cm). The printed PVA hydrogel displayed a conductivity response between 4 and 5s after CO₂ injection. This response was a positive resistance change which reached a maximum after a further 4-6s. Once the maximum was reached an initial decrease in resistance back to pre-exposure levels was observed, although not at the same rate as the increase.

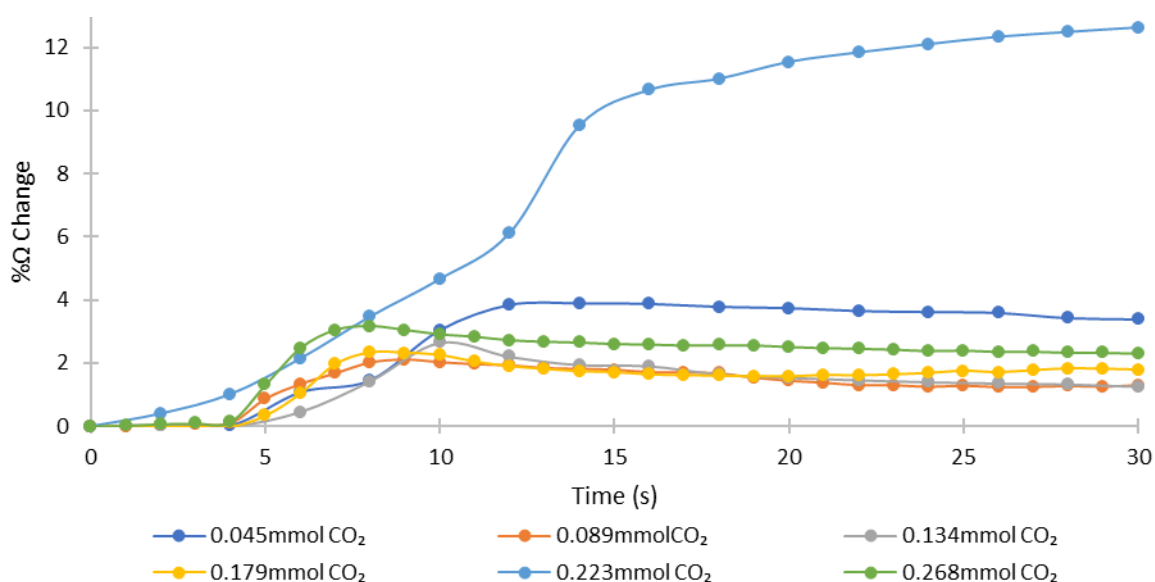


Figure 118 – Response of a printed PVA hydrogel exposed to different volumes of injected CO₂.

An anomaly was discovered with this sample upon the injection of 0.223mmol of CO₂. Unlike other volumes of injected CO₂, the 0.223mmol sample gave an immediate response, quicker even than the RGA. This sample also gave a change in resistance of over 12% which continued

to increase after 30s, contrasting with all other samples which presented a resistance change of between 3 and 4% and begun to return to baseline levels after 10s post injection.

One might at this point consider the nature of this H₂O swollen hydrogel conductivity (the inverse of resistivity) response (e.g. ionic, electronic or ionic-electronic). Here the author believes that the response is largely ionic.

One also ought to consider the flow regime in the sensor/reactor system. The reactor volume (v) is 8.17cm³, the air flow rate (u) is 250cm³/min and so the average molecular residence time (v/u) is 0.033min (2s). The RGA response time was 2.5-3s. The RGA takes a measurement approximately every 0.5s. This combined with error in flow rate (±0.5%) means that the RGA responds as fast as the reactor system will allow, passes through a maximum response and then returns to the baseline equally rapidly. The H₂O-swollen hydrogel sensor responds less rapidly and is then very slow in returning to baseline (see Figure 118).

Another factor possibly having bearing on the response times is the flow pattern of the gas reaching the sample. This may be determined by calculating the Reynolds number, a dimensionless value which indicates is a gas stream is laminar or turbulent, calculated by:

$$Re = \frac{V \times D}{\nu}$$

Equation 18 – Reynolds number (Re) equation, where V is velocity (m/s), D is diameter (m) and ν is kinematic velocity (m²/s).

Undertaking the calculation, a value of ≈ 0.01 is obtained, indicating that the flow is laminar and therefore no/very little mixing of gases occurs. This supports the observed RGA measurements i.e. response to a maxima and a return to baseline within 5s.

Lastly, one ought to consider the prevailing concentration of CO₂ that is seen by the RGA and the H₂O-swollen hydrogel sensor. Dividing the CO₂ RGA response by the N₂ RGA response allows the %CO₂ to be deduced via

$$\%CO_2 = 100 \times \frac{P_{CO_2}}{\left(\frac{100}{79} \times P_{N_2}\right)}$$

$$\frac{79 \times P_{CO_2} (RGA)}{P_{N_2} (RGA)}$$

PVA swollen with MEA gave a different electronic response to the printed PVA hydrogel sample. Both positive and negative changes in resistance were observed ranging between a 3%

positive change and a 6% negative change. Response times also seemed to be randomly spread with apparent changes in resistance observed from 1s (in line with RGA response times) to 12s. Some responses also gave variations, in the case of 0.045mmol CO₂, an initial response was immediate to 1% change, followed by a second change in resistance at 7s, tending to a maximum at 13s before declining again. Owing to the randomised spread of responses and various types, the data obtained from this sample was deemed unreliable.

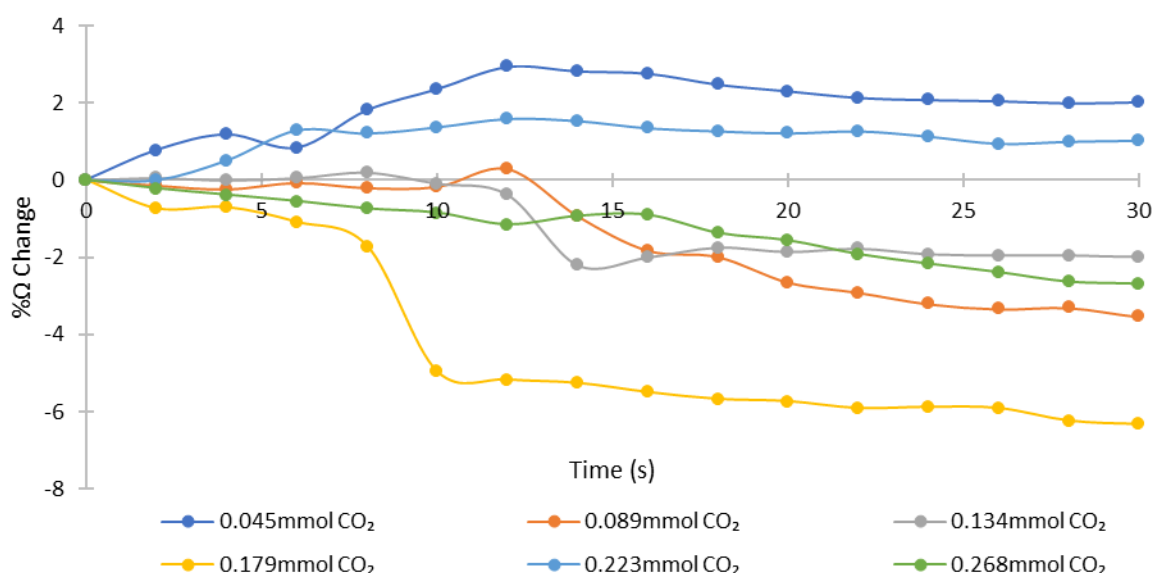


Figure 119 - Response of printed PVA swollen with MEA exposed to different volumes of injected CO₂.

Figure 120 shows the responses measured by the RGA for different concentrations of injected CO₂. The first peak at 238s is indicative of 0.045mmol CO₂, followed by a 0.134mmol injection at 300s. The peak at 351s is 0.223mmol and the final peak at 395s is a 0.268mmol injection. The peaks relate in magnitude to the volume of injected gas.

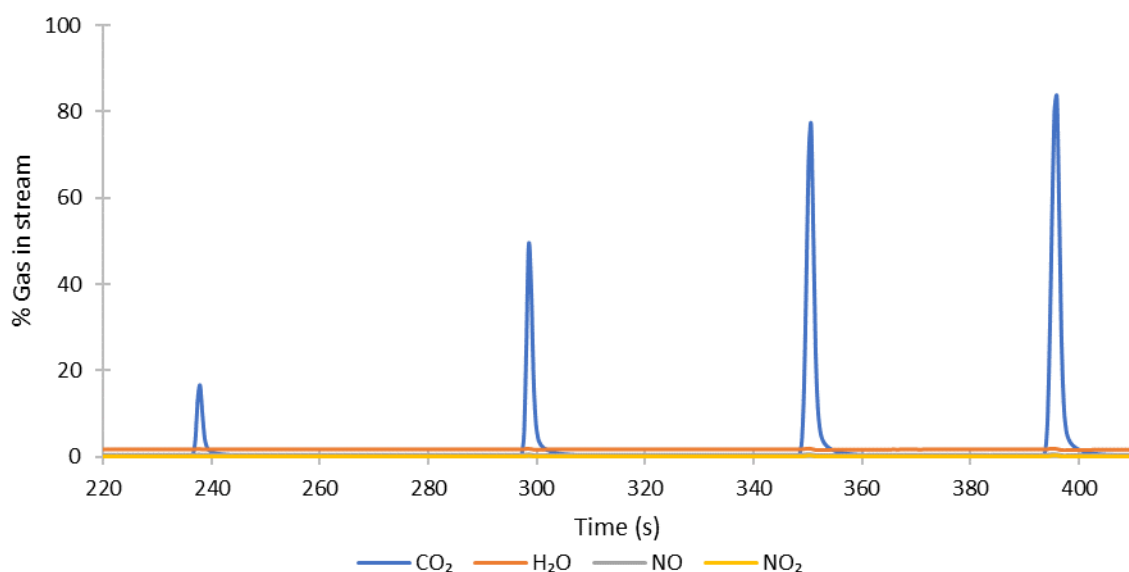


Figure 120 - RGA response to individual pulses of injected CO₂.

RGA responses were within 2.5-3s of gas injection with the RGA situated downstream of the sample cell. The RGA measurements confirm that CO₂ was injected and that it would have passed over the gas sensitive sample on route to the RGA inlet. Individual combination plots of RGA response with sample conductivity response indicates any subtle differences in each sample.

5.3.3.1 Printed PVA Hydrogel Gas Testing

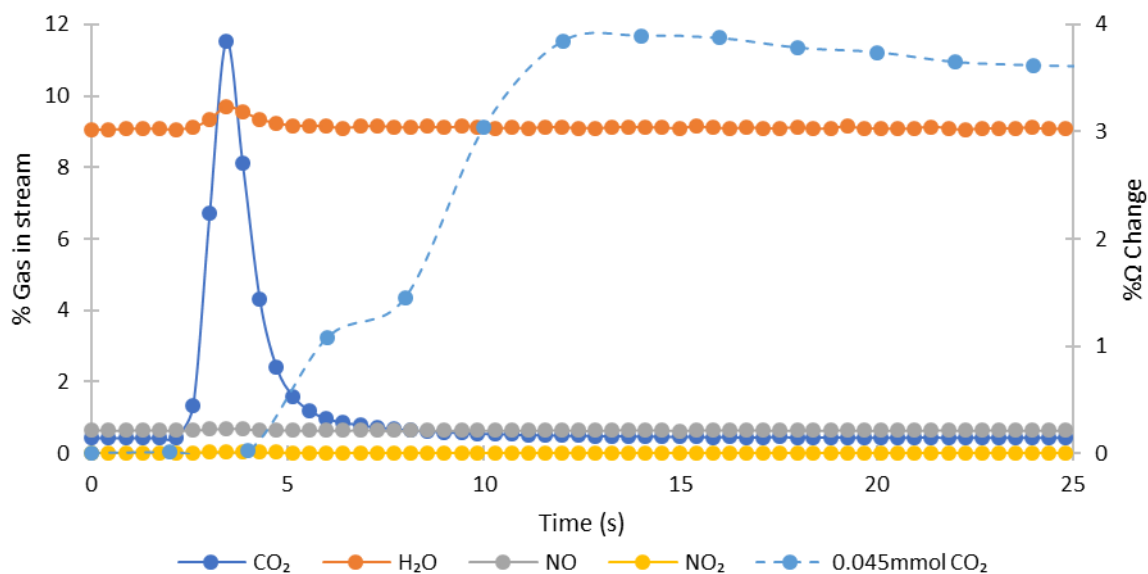


Figure 121 – RGA and printed PVA hydrogel response to 0.045mmol injected CO₂.

The 0.045mmol CO₂ injection for the printed PVA hydrogel is shown in Figure 121. The RGA responds to injected CO₂ within 2.5s. The light blue line representing the %change in resistance of the printed PVA sample, shows an initial response 4s from the point of injection, increasing to a maximum of change of 3.9% Ω 8s later; 12s from the moment of injection. After this maximum, a slow decrease is observed returning towards pre-injection levels.

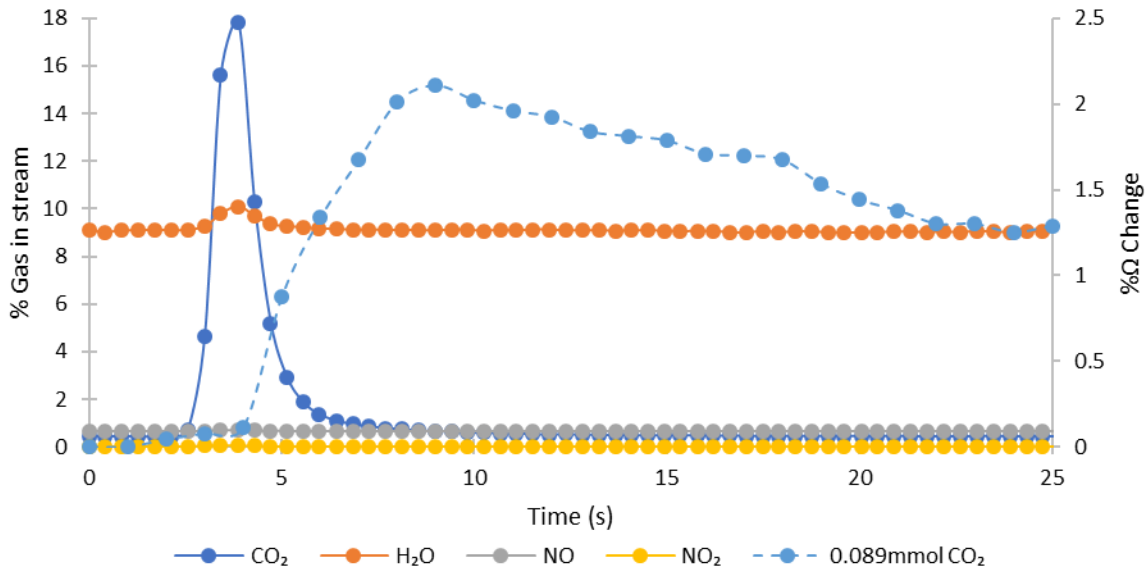


Figure 122 – RGA and printed PVA hydrogel response to 0.089mmol injected CO₂.

Figure 122 shows the RGA and printed PVA hydrogel response for 0.089mmol of injected CO₂. The RGA peak for CO₂ is greater than for 0.045mmol. The printed PVA hydrogel sample indicates an initial response 4s from injection tending to a maximum of 2.1% Ω change, 9s post-injection, 5s after the initial response. A quicker decrease towards baseline levels is evident compared to the 0.045mmol injection.

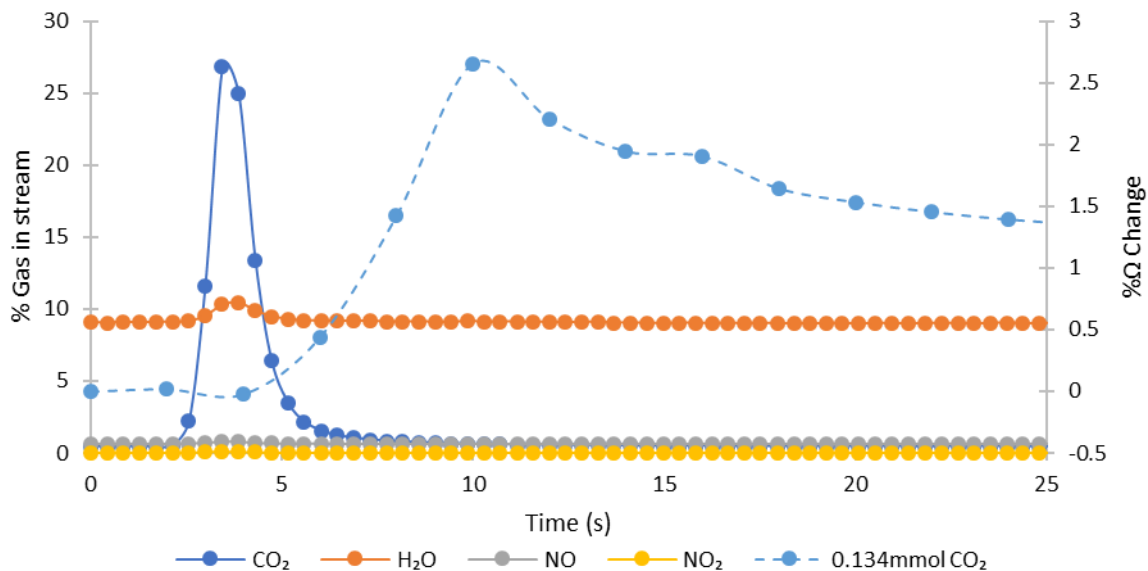


Figure 123 – RGA and printed PVA hydrogel response to 0.134mmol injected CO₂.

0.134mmol CO₂ injection is presented in Figure 123. The preliminary response of the printed PVA hydrogel sample is 4s after injection rising to a maximum of 2.7% Ω change 10s after injection. The return towards baseline decrease is at a similar rate of decrease to the 0.089mmol CO₂ injection. The RGA peak for CO₂ is larger than for 0.045mmol or 0.089mmol.

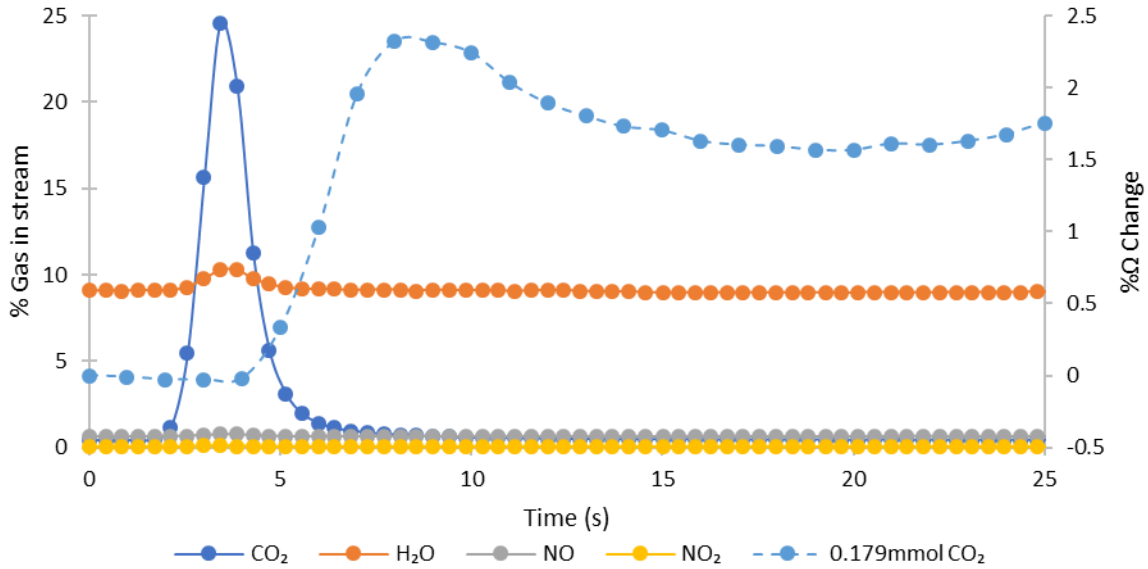


Figure 124 – RGA and printed PVA hydrogel response to 0.179mmol injected CO₂.

A sharp response to 0.179mmol injected CO₂ for the printed PVA hydrogel sample is shown in Figure 124, with the initial increase starting at 4s, and the maximum peak height at 8s. An initial decrease to baseline is not observed until 20s where there is an apparent slight increase again. A maximum % change in resistance is observed at 2.3%. As to be expected the RGA response is within 2.5s with a peak for CO₂. Also of note is the slight increase in H₂O level owing to a difference in the %RH of the CO₂ that was sourced from a metal lecture bottle.

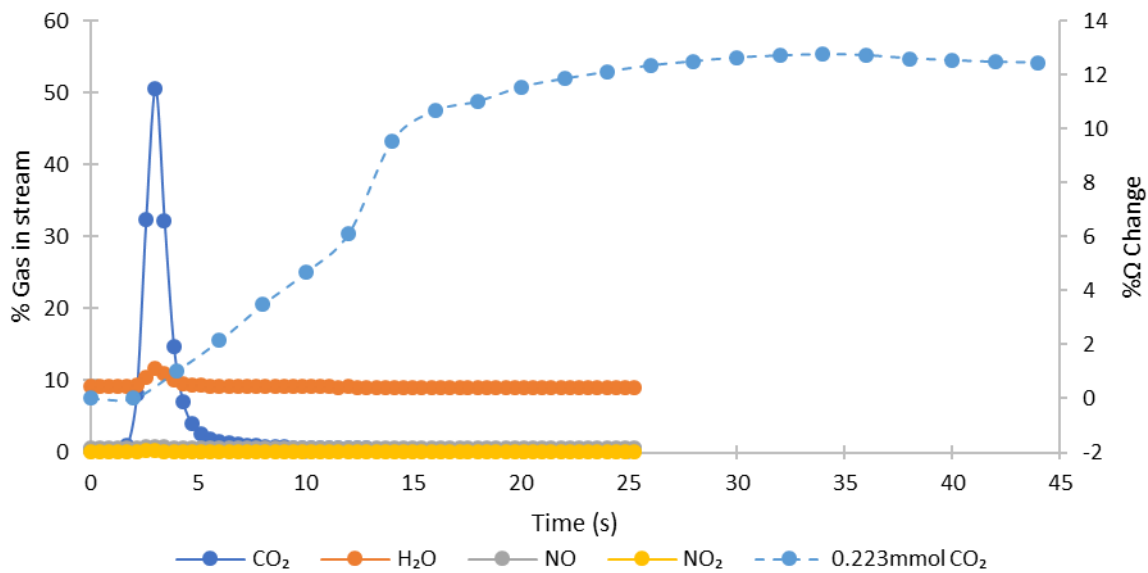


Figure 125 – RGA and printed PVA hydrogel response to 0.223mmol injected CO₂.

The 0.223mmol injection is perhaps the most interesting of all the responses as it presents a response unlike that of all other injection volumes. Shown in Figure 125 the response for the printed PVA hydrogel sample is odd, with an initial response at 2.5s rising to a maximum of 12.7% Ω change 34s after injection. By this stage all other tests had begun a decrease. For this

sample the measurement time was extended allowing for a maximum to be reached and a decrease to be observed.

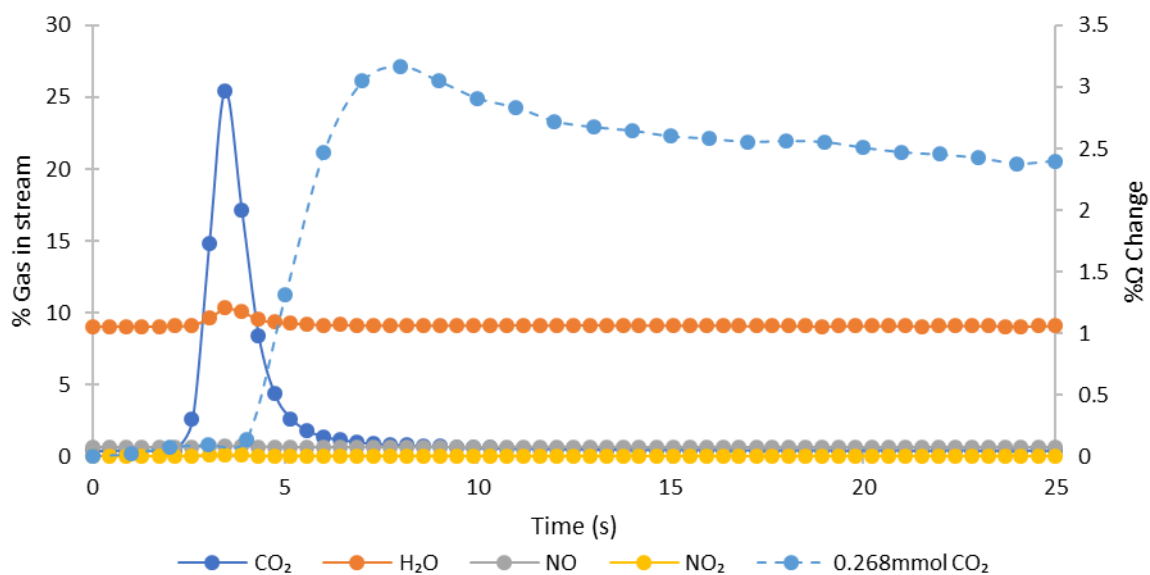


Figure 126 –RGA and printed PVA hydrogel response to 0.268mmol injected CO₂.

The response to 0.268mmol of injected CO₂ shown in Figure 126 was broadly in line with other samples (excluding the 0.223mmol injection). The RGA showed the usual responses at 2.5s from the point of injection. The conductivity response of the printed PVA hydrogel sample occurred after 4s reaching a maximum 8s and showing a definite initial return toward baseline levels.

Overall, some level of confidence can be taken in the observed conductivity changes. Each sample produced an increase in resistance ranging from 2%Ω to over 12%Ω and with responses typically 4-6s from the point of injection when exposed to injected CO₂ compared to a static baseline when exposed to only the air carrier gas.. The main conclusion which can be drawn from this experiment is that the hydrogel is responding electronically to injected gas. What cannot be said without further experimentation is the time taken to return to baseline and if the hydrogel has been chemically changed by the injected gas. Furthermore, it is unclear if these samples are selective as time constrains forbade the testing of different gases.

These conclusions would agree with the theory which suggests that an adsorbed species interrupts the local charge carrier network, thus increasing the observed resistance. Response times were generally 1 or 2s slower than the RGA; a sophisticated and proven analysis technique. When overlaid on the same plots as a function of time, these responses share a strong correlation.

5.3.3.2 Printed PVA Swollen with MEA Gas Testing

As with the standard hydrogel samples, the MEA-based gels underwent the same volumes of CO₂ injection with responses measured in the same manner.

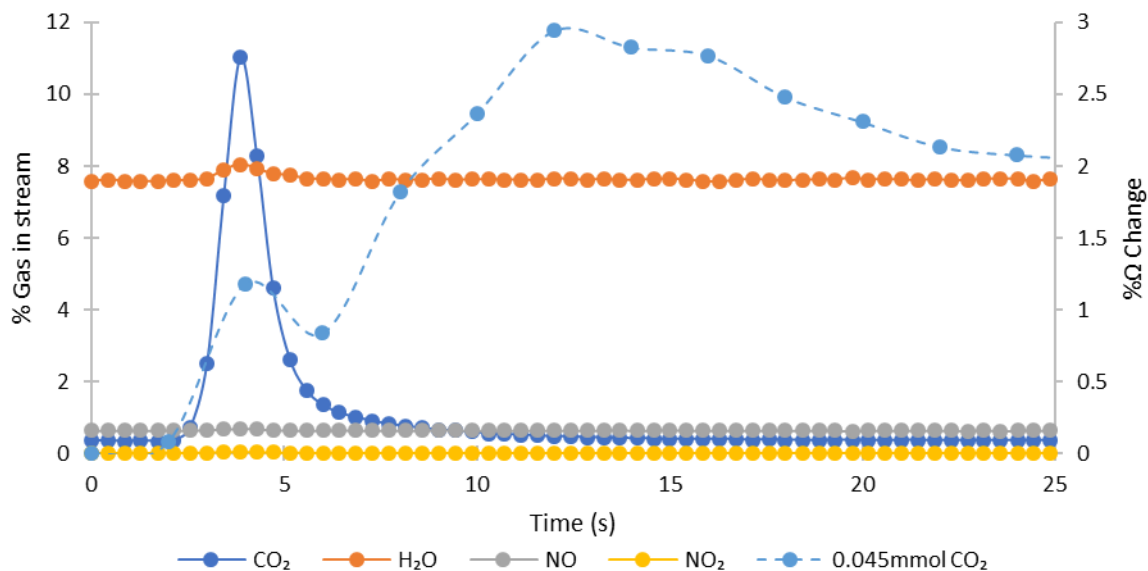


Figure 127 –RGA and printed PVA swollen with MEA response to 0.045mmol injected CO₂.

Figure 127 shows the RGA and PVA-MEA response to 0.045mmol of injected CO₂. As observed in previous studies, the RGA presents an initial response within 2.5s of injection with a clear CO₂ peak. The printed PVA-MEA sample shows a positive change in resistance response within 2s of injection with a slight dip at 6s, followed by a maximum at 12s from injection with a 3% Ω change. A steady decrease can then be seen with an initial return to baseline evident.

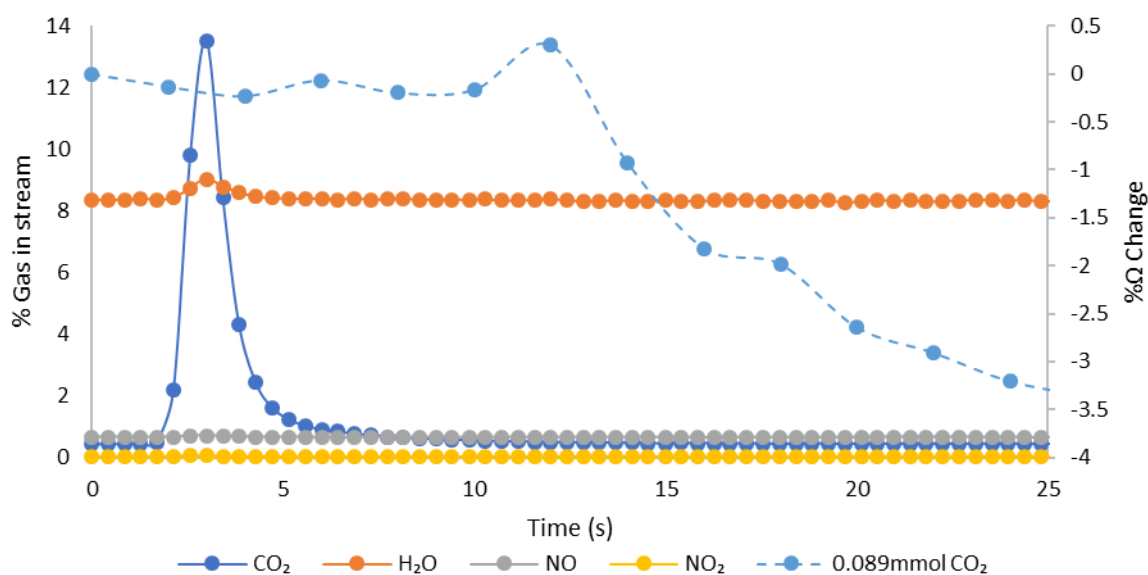


Figure 128 –RGA and printed PVA swollen with MEA response to 0.089mmol injected CO₂.

The response shown in Figure 128 for 0.089mmol of injected CO₂ is different to other runs conducted so far, in the sense that a negative Ω change of 3.3% is observed. The RGA shows the usual response to an injected volume of CO₂, however, the printed PVA-MEA conductivity is very irregular with an almost flat baseline until 12s where a 0.5% increase in resistance is observed followed by a steady decrease. Although not shown graphically, this decrease continued to -6% Ω change at 50 s when measurements were stopped.

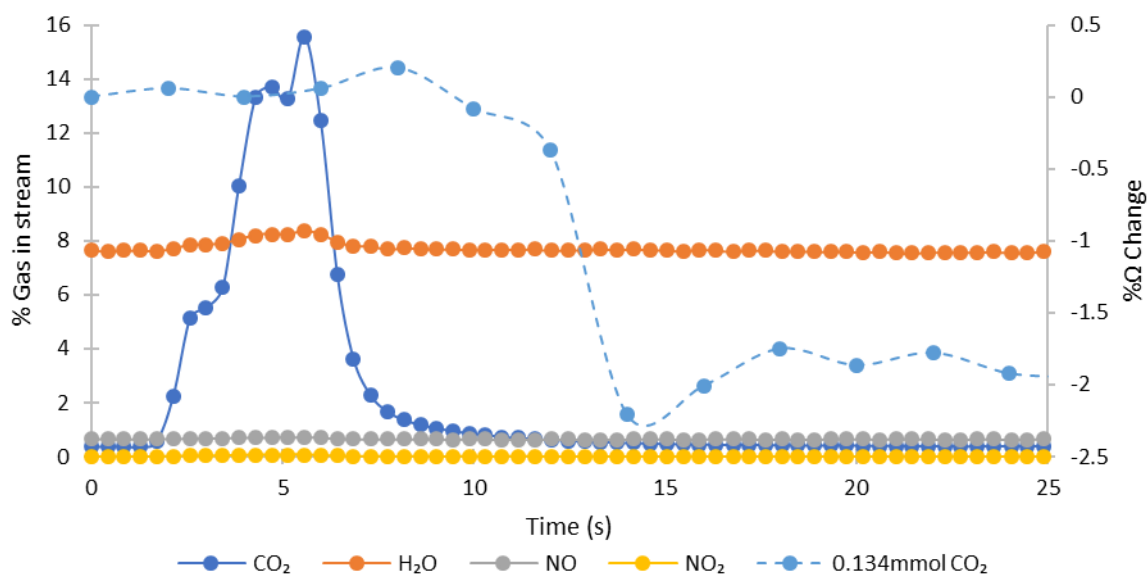


Figure 129 – RGA and printed PVA swollen with MEA response to 0.134mmol injected CO₂.

Unusually, the RGA response for 0.134mmol of injected CO₂ shown in Figure 129 does not show a clear peak, but rather multiple. Equally unusual is the response time of 2s rather than the customary 2.5-3s observed previously. The printed PVA-MEA sample shows a similar initial increase, followed by a decrease similar to that of Figure 128. However, this time a maximum trough level is reached before a steady Ω change of -2% occurs.

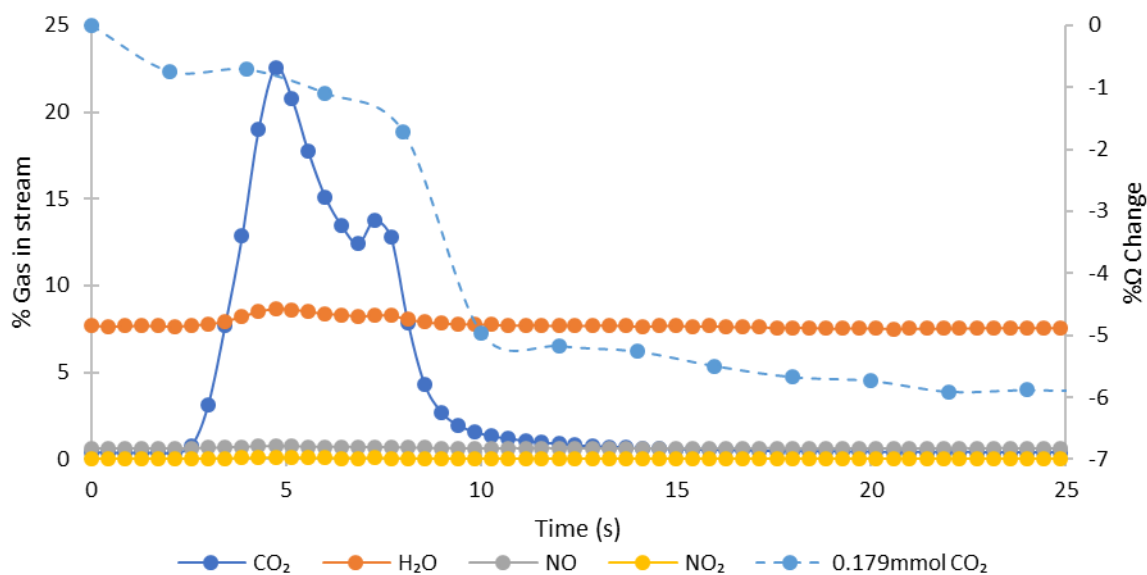


Figure 130 – RGA and printed PVA swollen with MEA response to 0.179mmol injected CO₂.

The combination plot shown in Figure 130 for 0.179mmol of CO₂ follows a similar unusual pattern to the 0.134mmol injection. As in Figure 129 the RGA response for 0.179mmol consists of multiple peaks rather than a single, clear peak as observed in every other injection. The initial RGA response is at 2.5s, tending to a maximum at 5s followed by a return to baseline at 9s. This is peculiar as previously the RGA responds to a species, reaches a maximum and returns to baseline within a 3s window. The response for PVA-MEA reaches a maximum trough level 10s after injection and flatlining at 23s with a -6% Ω change.

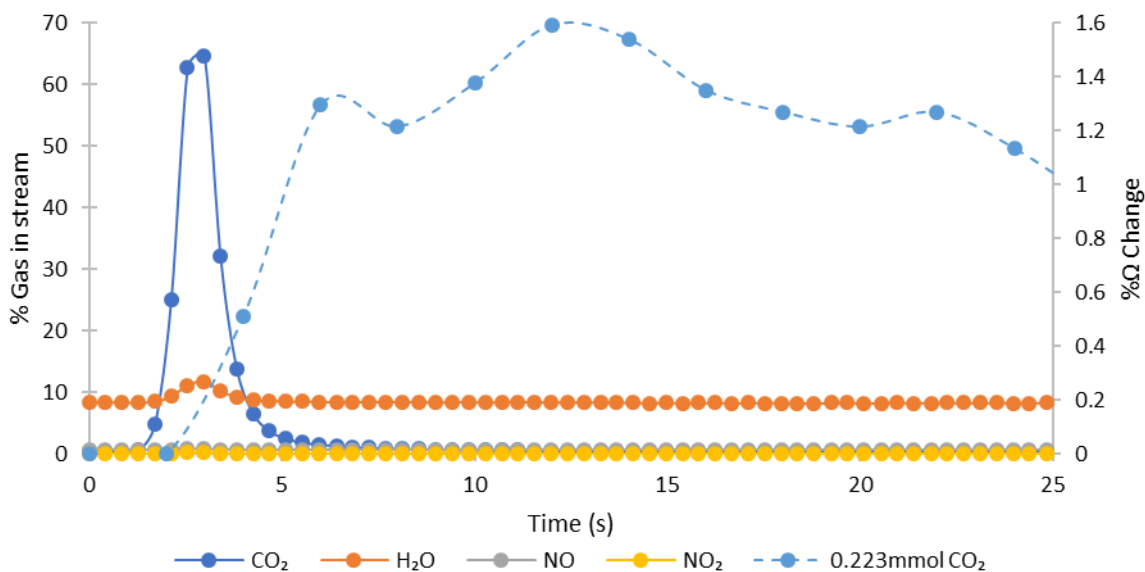


Figure 131 – RGA and printed PVA swollen with MEA response to 0.223mmol injected CO₂.

The printed PVA-MEA response for 0.223mmol of CO₂ in Figure 131 is reminiscent of the printed PVA hydrogel samples and dissimilar to other responses observed for this material. An initial response can be observed 2.5s from the point of injection tending to an initial peak at 6.5s followed by a maximum at 13s, after which an initial decline back to baseline can be seen, with a slight third peak at 22s before a sharper decrease. The RGA peaks for this injection appear as expected with a large CO₂ peak 2s from the point of injection.

The final measurement is 0.268mmol of CO₂ which elicits a standard RGA response as shown in Figure 132. The CO₂ peak observed is the largest seen, indicative of a large volume of injected gas. This correlation between injected concentration and peak size is expected. The printed PVA-MEA response is similar to 0.089, 0.134 and 0.179mmol injections. An initial positive % Ω change can be observed, before a decrease to a maximum trough depth of -1.7% Ω change followed by a steady increase back to pre-exposure levels.

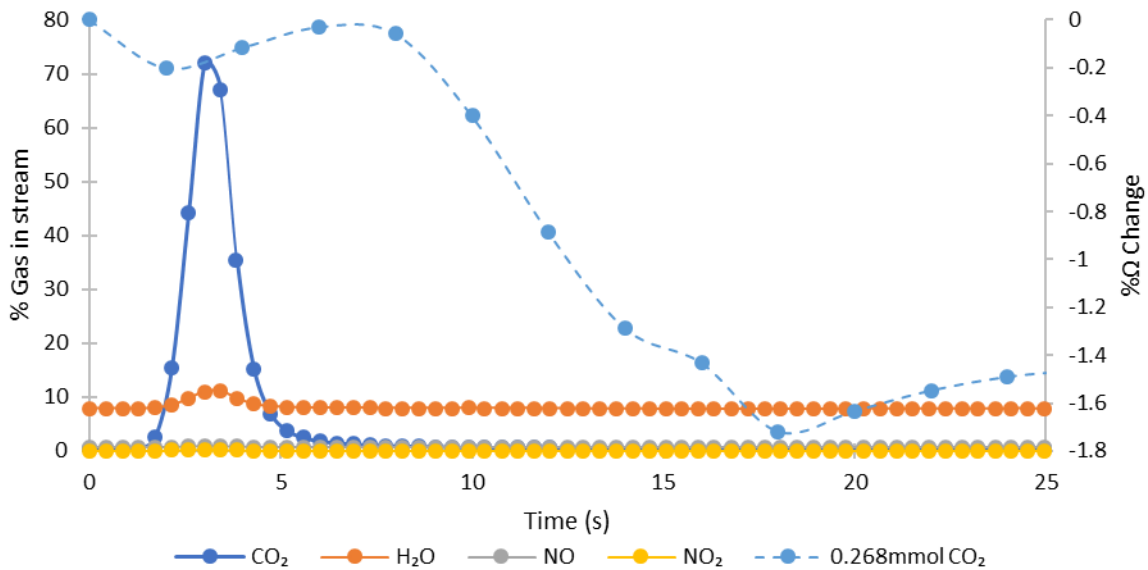


Figure 132 – RGA and printed PVA swollen with MEA response to 0.268mmol injected CO₂.

Overall, the PVA-MEA samples have provided some highly varied data. Out of 6 different concentrations of injected CO₂, 2 gave a positive %Ω changes of approximately 2.5%Ω and 1.5% Ω (0.045 and 0.223mmol) compared to the majority (0.089, 0.134, 0.179 and 0.268mmol) which showed a variety of mostly negative %Ω changes ranging from -2%Ω to -6%Ω. Also of interest were the RGA responses to 0.134 and 0.179mmol injected CO₂ which gave broad, multi-peak plots potentially indicating an issue with the injected gas. It is possible that the injection was conducted quicker, slower or less consistently.

What is clear, is the conductivity responses from the PVA-MEA samples cannot be trusted in the same way as the printed PVA hydrogels which gave more correlated responses. It is unclear why some samples gave negative responses and others gave positive responses. It could be that the sample was not given sufficient time to return to baseline between injected pulses of gas. It may also be the case that chemical changes are occurring within the MEA.

A further consideration is that CO₂ could be being absorbed into MEA solution on the surface of the PVA-MEA gel rather than undergoing a simple adsorption-desorption mechanism. There is literature to support MEA as an industrial gas scrubber. Such absorptions would change the chemical composition of the gel, perhaps leading to irregular conductivity responses.

What is clear about these experiments and those conducted in **5.3.3.1 Printed PVA Hydrogel Gas Testing** is they are inconsistent and show different responses. The author believes that the samples in **5.3.3.1 Printed PVA Hydrogel Gas Testing** respond electronically and the samples in this section are responding as a result of chemical changes to the inclusive MEA.

5.4 Atmospheric Breathing of Adult Males

The breathing experiments carried out in this section were exploratory and were conducted to give the author some view of a typical breathing pattern for adults of different ages. A potential use for 3D printed gas sensors is remote patient monitoring, and so breathing tests are required.

Here 3 adult male subjects of differing ages (24, 28 and 73y.o.) exhaled into a particle analyser and RGA 3 times. UFP, O₂, NO₂, CO₂ and H₂O were measured and a return to baseline was allowed to occur before the next exhalation.

RGA exhalation profiles in Figure 133, Figure 134 & Figure 135 do not show the presence biomarker HCN, however were reasonably consistent with CO₂ concentrations (red) falling during inhalation and rising to 3kPa during exhalation. The minima are above current atmospheric levels previously measured. These were 450ppm (high; 0.045kPa) and 390ppm (low; 0.039kPa) at a suburban site [368].

On the other hand, the background UFP concentrations in Figure 133, Figure 134 & Figure 135 showed agreement with data for an urban atmosphere. In cities, roadside concentrations of UFPs of 30-131/mm³ have been previously detected [369]. Inhalation is when the UFPs are at this background level. Exhalation is when (if there is some UFP retention) a minimum UFP level is seen. CO₂ maxima and UFP minima correlated with exhalation. It is relevant that more than half of the prevailing UFPs were retained by the subject.

RGA CO₂ analysis is useful for breath analysis on exhalation – seeing tidal waves of CO₂. However, a pensioner at risk would not sit comfortably at home with a turbomolecular pump spinning to support an RGA. They could however, feel more comfortable with a soft hydrogel badge on their collar.

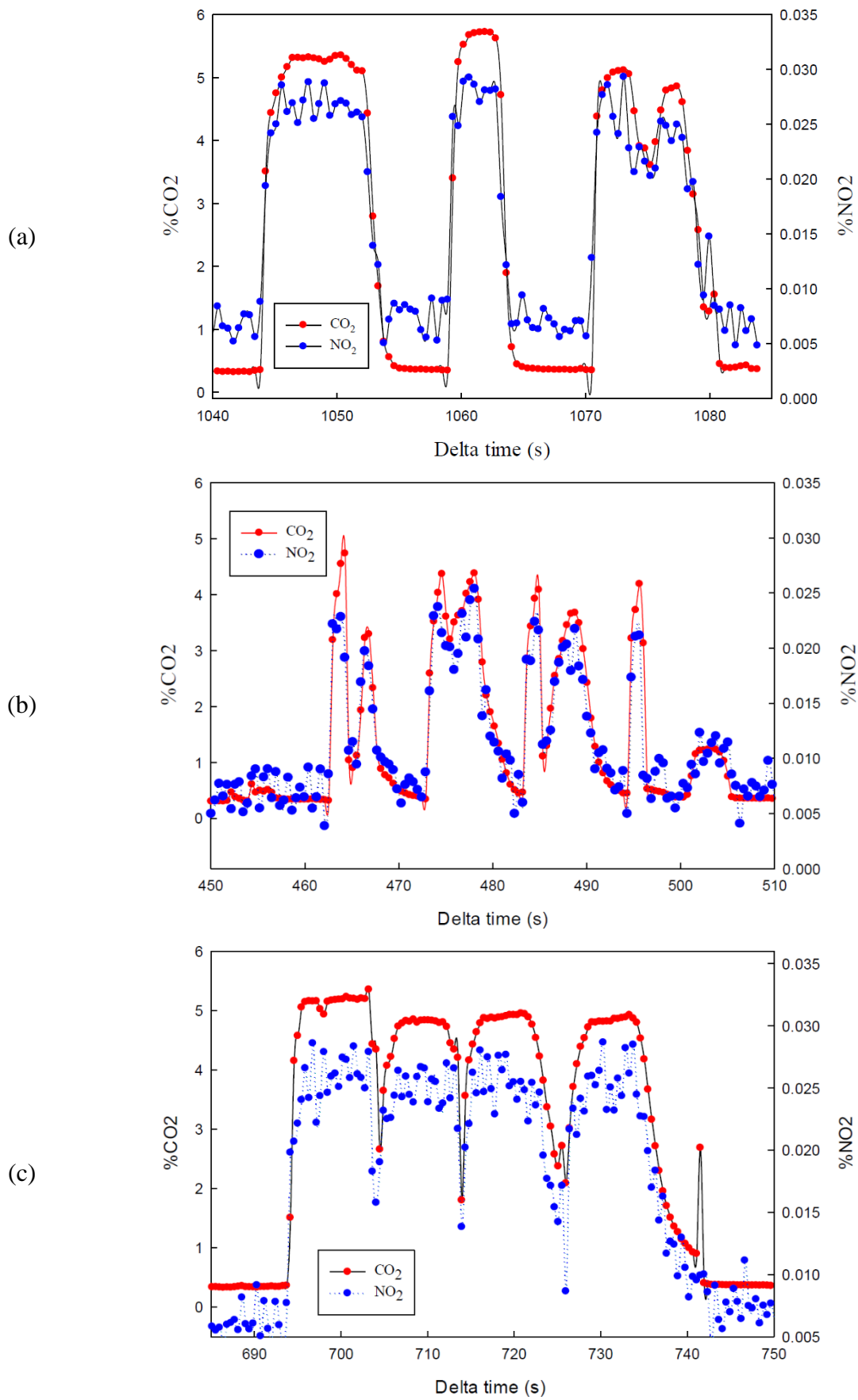


Figure 133 – %CO₂ detected from repeat exhaling from (a) 73yo male (b) 24yo male and (c) 28yo male.

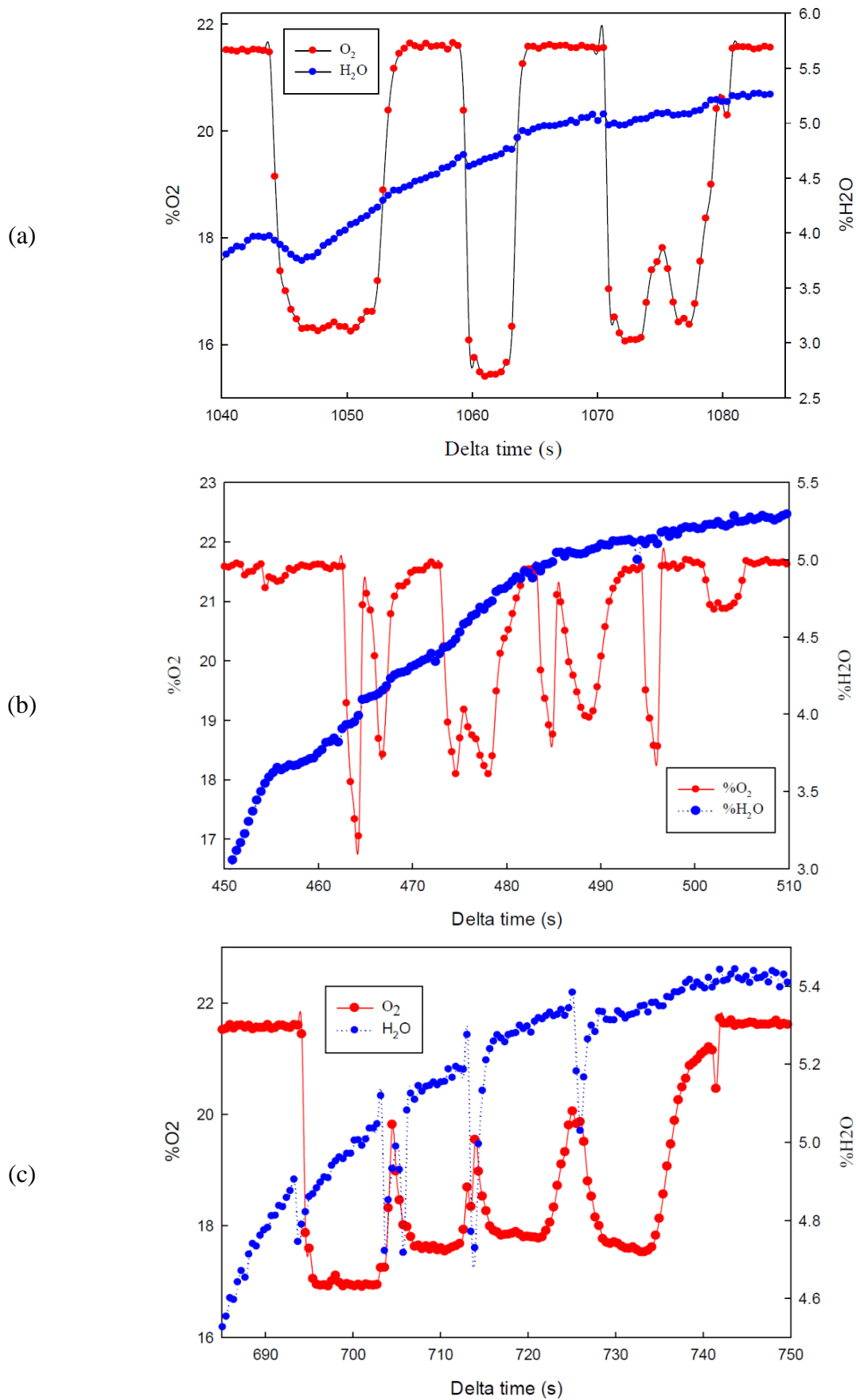


Figure 134 - %O₂ detected from repeat exhaling from (a) 73yo male (b) 24yo male and (c) 28yo male.

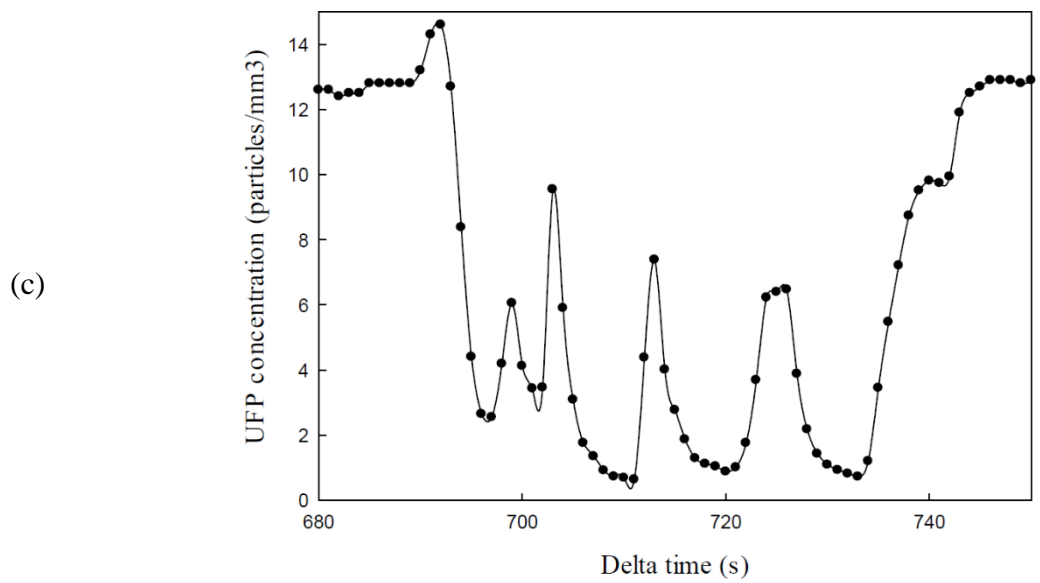
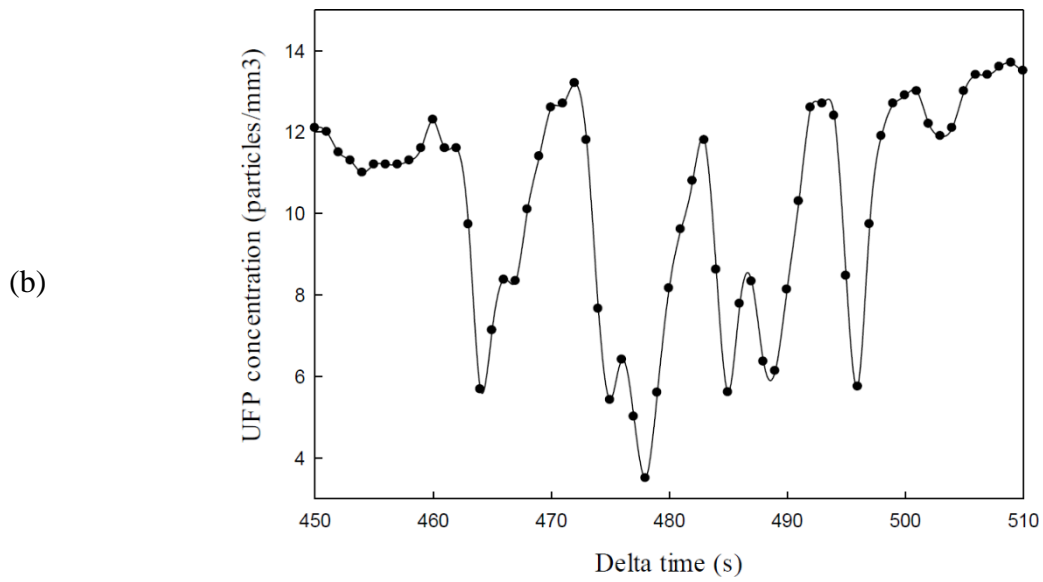
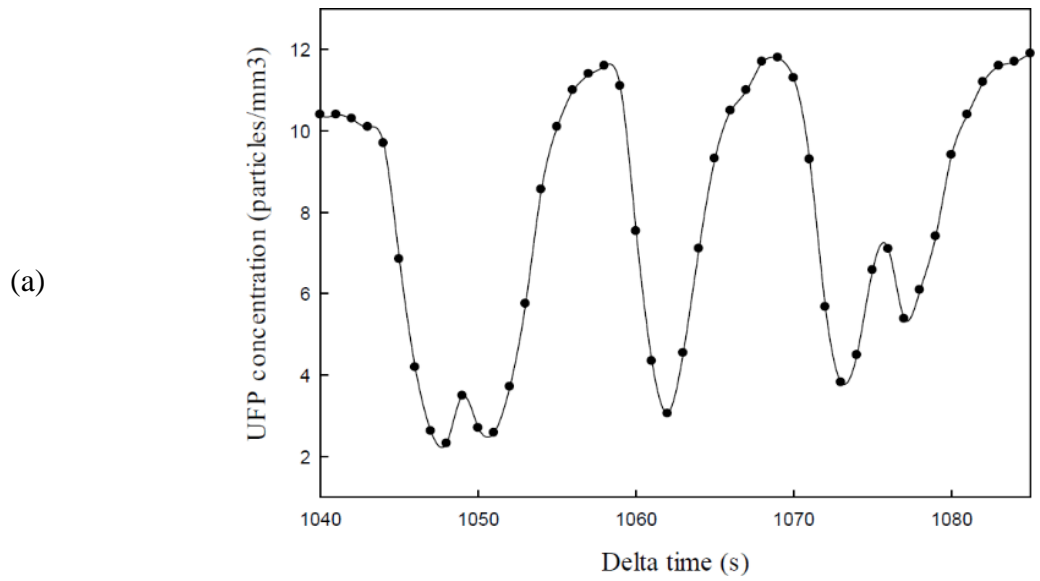


Figure 135 – UFP concentration from repeat exhaling from (a) 73yo male (b) 24yo male and (c) 28yo male.

5.5 Microconductivity

It is apparent in Figure 136 that the simple International Test Solutions (ITS) linear probe sees oil at the surface of water using conductivity analysis. In Figure 136 blue areas are water-rich and red areas are oil-rich. At the start of measurements at zero time the surface is an oil-in-water phase of 10cm depth and below this is a 6-7cm deep layer that is water-in-oil. After travelling across the surface for 3-4h there is a switch to the top 7cm being oil-rich and the 10cm below this being water-rich. After 6h of travelling across the surface the oil is no longer present. Although this is laboratory data, it is possible to see how this could transfer to aircraft/boat-based measurements.

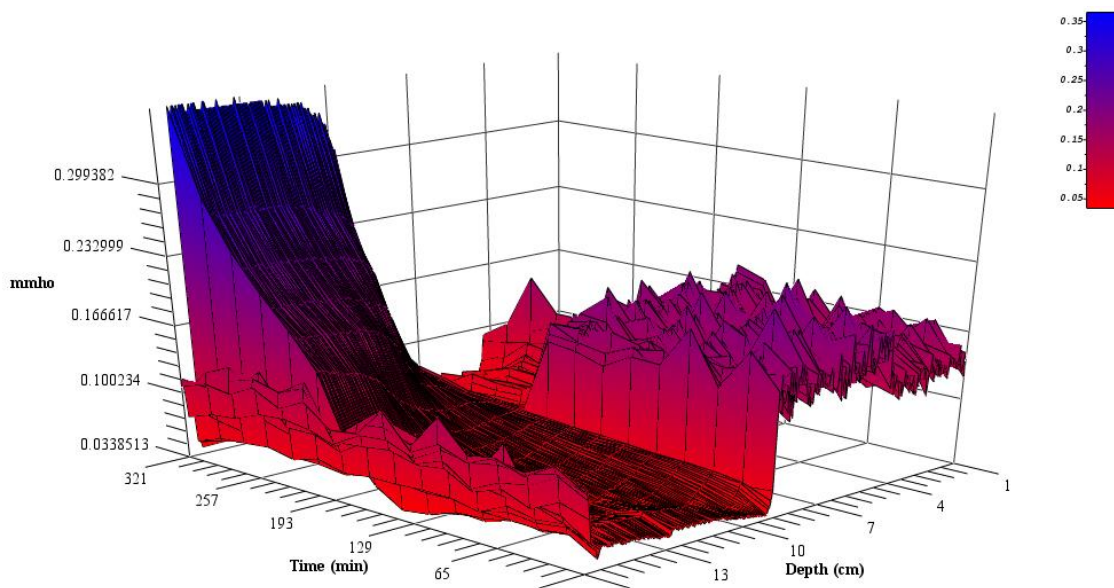


Figure 136 - Preliminary conductivity-time-depth profiles (blue=water and red=oil). The surface is at 0cm depth.

PLA-G results were unreliable and did not differentiate seawater (SW) and deionised water (DW). This is thought to be because of the high resistance ($0.6\Omega\text{cm}^{-1}$) of PLA/G filament. Cu-based micro-conductivity measurements did work and were able to differentiate between SW and DW. It is therefore plausible that this type of sensor would also detect oil in water as this would affect the overall conductivity of the system. The common issue of high resistance possibly caused by low concentration of graphene in the PLA filament, is the most probable cause of this sample failing to detect the change in conductivity of the two systems. This was also an issue in 5.3.3.

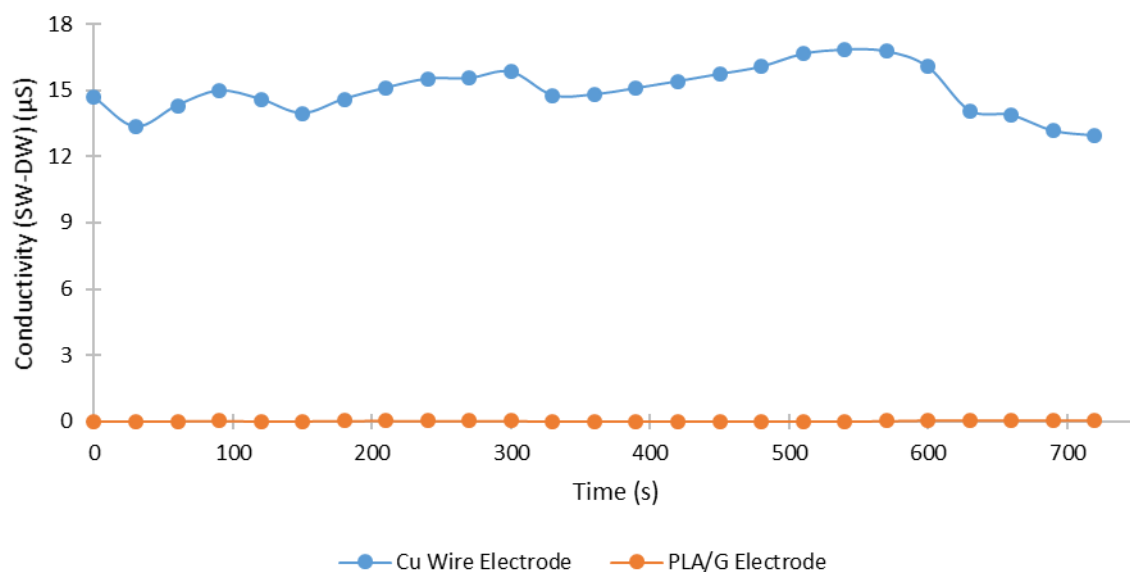


Figure 137 – Plot of seawater (SW) minus deionised water (DW) conductivity (μS) vs time for a Cu wire and PLA/G electrode.

5.6 Summary

In this chapter designs for 3D printed hydrogels have been developed from an initial range of shapes and sizes to fine-tuned geometries with controllable aspect ratios ranging from 100:1 to 5:1. Also developed were dual layer asymmetric samples with PVA and PLA/graphene. Water uptake tests were conducted and show successful inclusion of water as a solvent into the polymer matrix, initially 10wt%. DSC indicates that there is internally bound solvent within these polymer chains. FTIR-ATR also indicates where solvent has been included in a polymer matrix as well as giving clues to the level of hydrolysis of the PVA starting material. FTIR-ATR has also allowed inclusion of MEA in printed PVA to be investigated with differing ratios of H₂O:MEA (100:1, 70:30, 30:70). Indications are that MEA and H₂O can be included via a simple immersive method. Further work would see DSC evaluate on-board MEA. Also of interest would be the level at which H₂O may be included in the PVA matrix via immersion before a solution was formed. It could be that MEA:H₂O mixtures are only effective to a certain point. SEM has given visual clues to the interaction between materials and to the nature of fusion between printed layers. It has also given clues towards the form graphene is in when included in PLA filament/printed. Raman spectroscopy confirms the presence of graphene in PLA unequivocally. μFTIR has given clues to the type of interaction which exists between PVA-PLA/G. The author believes that this interaction is mostly miscible and that layers are strongly bonded. TGA provided information regarding the thermal stability of materials used and how the thermal cycle of 3D printing may have affected this.

Gas testing has shown that printed PVA hydrogels with on-board H₂O give a typical electronic response of 1-2%Ω to different concentrations of injected CO₂. However, a response of 12%Ω was recorded for a single sample. Responses were typically within 4s of injection compared to an RGA response of 1.5s. PVA swollen with MEA gave a less certain responses with both positive (2%Ω) and negative -6%Ω being recorded. This range of samples therefore requires further investigation.

Overall, it appears that printed PVA when converted into a water-based hydrogel or combined with a second material forms a responsive gas sensor and is also successful as a passive cooling method.

6 Cooling Performance of 3D Printed Hydrogels and Composites

6.1 Introduction

With 40% of all global energy use directed at heating and lighting of residential and industrial buildings [370], the potential for reduction through building retrofit technologies is vast. So called “sweating surfaces” are one such way to achieve a reduction in temperature, thus negating dependence on high power consuming air-conditioning units. A “sweating surface” is a material designed to release a solvent (e.g. H₂O) at a controlled rate, thus reducing the temperature of the substrate by removing heat from it. This type of evaporation is so called as it mimics the natural sweating undertaken by humans and other mammals in order to lower the core temperature of their bodies.

There is interest in hydrogel-based coatings for development of sweating surfaces owing to their ability to hold large amounts of guest solvent and be produced with high mechanical strength [371].

Utilising the ever-improving capabilities of 3D printing, it was hoped that PVA may be printed prior to being exposed to a controlled %RH atmosphere to facilitate H₂O uptake into the polymer matrix. The adsorption-desorption properties of the on-board H₂O may then be investigated in a thermal sense to understand how this may affect the temperature of the surface to which it is applied.

Advantages of this method over traditional casting from aqueous PVA solution followed by crosslinking, is the speed of production (no requirement to undertake multiple freeze-thaw cycles) and the lack of potentially harmful chemical crosslinker in acidic conditions. Thus, it was envisioned that hydrogels of this form may be produced in non-laboratory settings, to dimensions required by the user.

6.2 Aims and Objectives

The aim of this part of the work is to investigate the adsorption-cooling properties of 3D printed hydrogels with on-board H₂O and MEA. Although it is unlikely that an MEA based hydrogel would be useable in a commercial way, it gives a useful comparison as MEA has successfully been included in printed PVA previously (see chapter 4).

Comparisons can also be drawn with conventionally prepared PVA hydrogels, synthesised using physical and chemical crosslinking from aqueous solutions of PVA. The author is

interested to see if there is a significant performance difference between a conventionally prepared hydrogel and one produced via 3D printing.

6.3 Results

6.3.1 3D Printed Hydrogel Preparation

As discovered from previous investigations (see **5.3.1**), the most efficient and durable shape for a 3D printed hydrogel is circular. Therefore, a range of circular discs of PVA were printed before being exposed to a humid atmosphere (at defined %RH).

The time printed PVA discs were exposed to the humid atmosphere set at 12, 24 and 48hrs. This was based on the information obtained during previous water uptake investigations (see **5.3.2.6**). With investigations already conducted on the nature of water uptake, it was not considered necessary to repeat these as the PVA discs were printed with the same batch of material, under identical conditions and were of identical sizes.

6.3.2 Infrared Thermography of 3D Printed Samples

Infrared thermography (FLIR is described in **2.1.6**) was used to observe the adsorption-cooling effect of a printed PVA hydrogel swollen with H₂O, printed PVA swollen with MEA and a dual layer printed PLA/graphene-PVA hydrogel composite swollen with H₂O. This was of interest as the samples could be considered dual-purpose if cooling and gas sensing properties were both favourable. Obviously a sample that releases MEA (443K) to the atmosphere is not a very green adsorptive cooling coating. Previously, work on hydrogel cooling has been described by [372].

Samples were prepared in advance and stored in a fridge at 276K in their swollen state containing maximum amounts of H₂O. When ready to use samples were cut to similar physical dimensions and weighed, each sample being approximately 4g. These were then arranged on a cleaned sheet of aluminium. The thermal camera looked vertically onto the sample tray with a focal distance of 0.7m (minimum focal distance of the camera is 0.5m). Images were obtained at 20s intervals, with minimum, maximum and area temperatures obtained. The temperature of the laboratory (302-304K) and Al substrate (302-313K) was also measured periodically as a reference. On one hand the elevated temperatures would have contributed to faster loss of H₂O or MEA, resulting in accentuated cooling. Conversely, the higher temperatures are exactly the

conditions the materials would be expected to perform in, assuming they were to be used as a “sweating surface”.

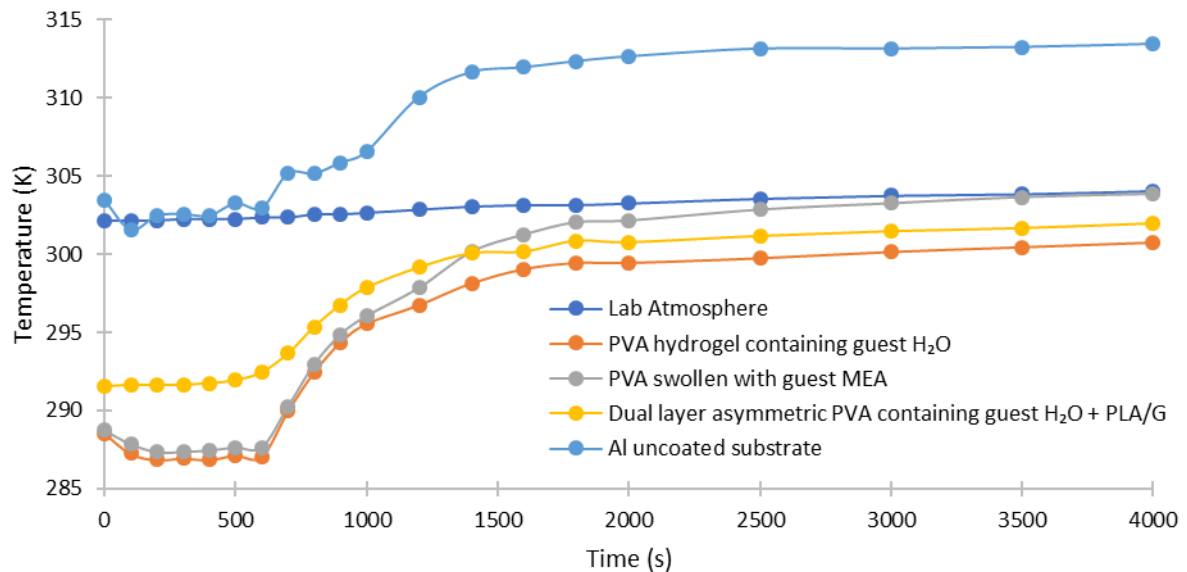


Figure 138 – Temperature variation of a printed PVA hydrogel H₂O-swollen, PVA swollen with MEA and dual layered asymmetric PVA hydrogel-PLA/graphene compared to local atmospheric and Al uncoated substrate temperature.

Figure 138 gives the average temperatures of each sample with respect to the atmospheric temperature and uncoated Al substrate in the lab. Initially the temperature difference between sample and Al substrate was 14.9K for the printed PVA hydrogel reaching the largest difference of 16.1K, 500s from the start of measurements. The initial difference in temperature was 14.7K for PVA swollen with MEA, with the largest difference at 500s which reached 15.6K. The dual layer printed PVA hydrogel-PLA/G composite initially performed differently, with the greatest difference in temperature being 12K at time 2500s.

The typical errors originating from this form of measurement can be divided into two types. Firstly the largest accuracy error originates from the instrumentation, particularly the IR camera (± 2 K). Because of this it is possible that the difference between two individual measurements could be as much as 4K. This is important to consider when comparing data sets and drawing conclusions. Other types of errors are a result of experimental design such as other lab users inadvertently standing too close to the camera. Other errors could become apparent during data processing, with area and spot measurements not being taken at the absolute coolest point, or selection of areas being inconsistent. Because of this range of errors, it could be argued that the overall accuracy of these results is in the region of ± 2 -3K and are therefore each sample shows an average cooling effect identical to one another.

Each sample followed a similar, mostly flat initial cooling rate to 600s where all samples began to increase in temperature causing the temperature difference to the atmospheric temperature decreased steadily. Interestingly, the temperature difference between samples and the Al substrate remained reasonably constant. This decrease continued to 1800s where each sample began to show signs of reaching a plateau. Although initially appearing cooler the PVA-MEA sample crossed over with the dual layer sample at 1400s, indicative of different rates of warming and potentially solvent evaporation. After 2000s, each sample remained on course to maintain a temperature difference. From 2000-4000s the temperature difference between the Al substrate and printed PVA hydrogel was on average 13K, for PVA swollen with MEA the average difference was 10K and for the dual layered sample was on average 11.8K.

Between 2000-4000s the difference in temperature between the atmosphere and printed PVA hydrogel with guest H₂O went from 3.8K to 3.3K, for PVA swollen with MEA, the change was 1.1K to 0.2K and for the dual layered sample it was 2.5K to 2.1K. This is interesting; by 4000s the printed hydrogel and asymmetric sample were still slightly cooler than the atmosphere, but significantly cooler than the Al substrate. Clearly, the cooling performance of these materials had not been exhausted by 4000s and measurements over a longer period should be considered in order to find an equilibrium point.

Also of interest was the temperature distribution across each sample. Observing significant areas cooler or warmer than others gave an indication of the solvent distribution throughout the sample.

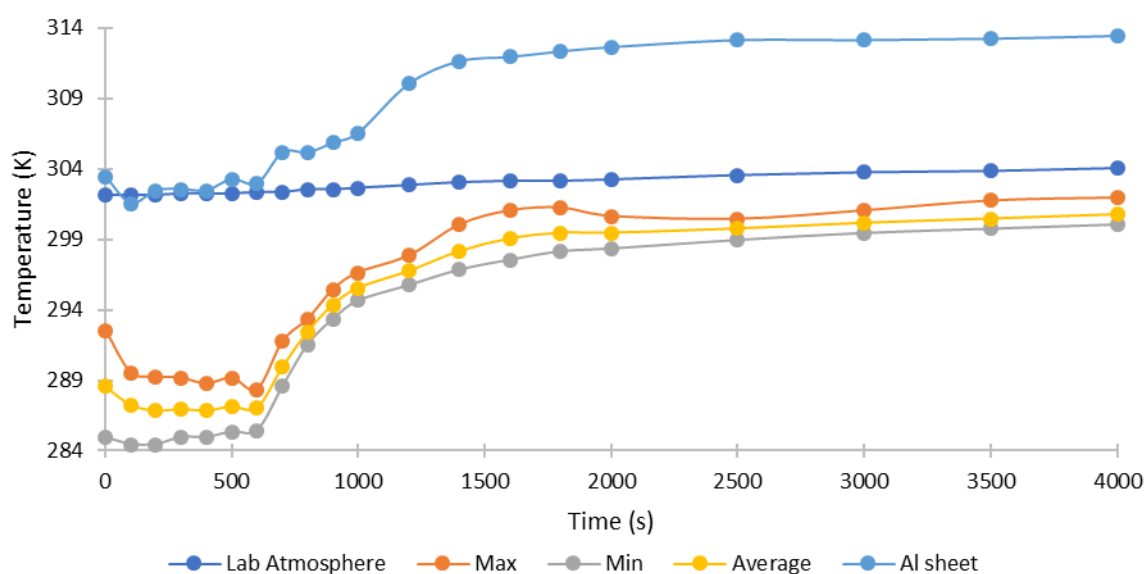


Figure 139 – Temperature variation of printed PVA hydrogel swollen with H₂O compared to atmospheric and Al uncoated substrate temperature.

Figure 139 shows the maximum, minimum and average temperatures recorded in the printed PVA hydrogel sample. The absolute minimum temperature recorded was between 100 – 200s and was 284.4K compared to a substrate temperature of 302.4K and an atmospheric temperature of 302.2K, a difference of 18K and 17.8K respectively. By 4000s, the average temperature was 12.7K lower than the Al substrate and 3.7K cooler than the atmospheric temperature. This indicates that a complete cycle of solvent desorption had not finished.

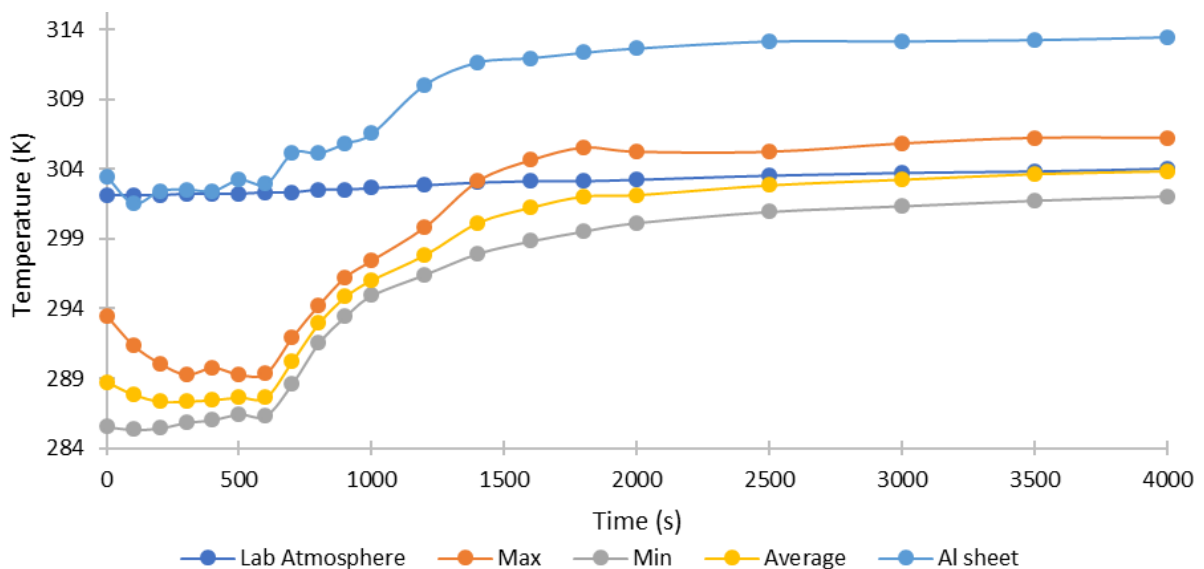


Figure 140 – Temperature variation of printed PVA swollen with MEA compared to atmospheric and Al uncoated substrate temperature.

Printed PVA swollen with MEA is the most disappointing sample in terms of cooling performance. Although initially following a similar temperature profile to the water swollen samples, this was the only sample to equal the atmospheric temperature after 4000s. However, by 4000s, the temperature difference between the sample and Al substrate was still 9.6K. The apparent initial decrease in temperature from the starting point is thought to be due to a variation in the accuracy of the area selected for temperature measurements.

The temperature profiles for a dual layer asymmetric sample are shown in Figure 141. This sample, like the single layered PVA hydrogel performed well throughout the measurement period with all recorded temperatures being below that of the Al substrate and atmosphere. Of note are the variations in the maximum temperature. This may be attributable to the location of the sample. Images presented in Figure 142 indicate a heat source close to this sample. As with other samples the temperature profile of the sample closely resembles that of the Al substrate. Towards the end of measurements the difference between Al substrate temperature and sample temperature begins to narrow. However, the cooling performance of the dual-layered sample is by no means exhausted by the time measurements were stopped.

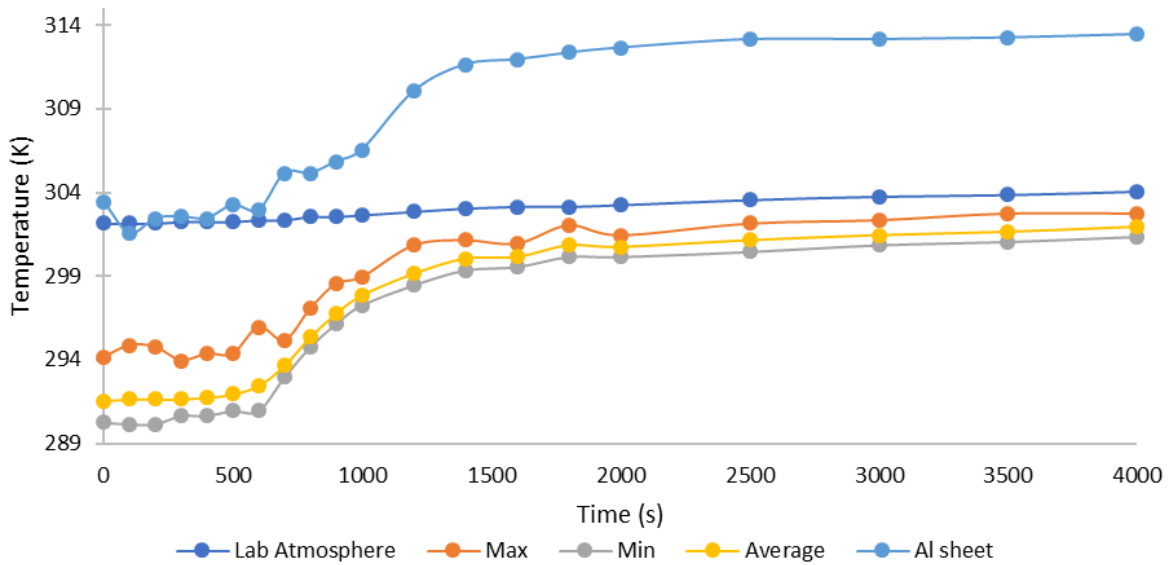


Figure 141 – Temperature variation of a dual asymmetric printed PVA hydrogel-PLA/G (non-swollen) compared to atmospheric and Al uncoated substrate temperature.

Images show three identifiable circles of identical size with temperatures cooler than the surrounding area. As time progresses the circles, while still apparent, begin to merge into a larger area, cooler than the surrounding area. This is thought to be the cooling effect of the samples on the aluminium tray they are positioned on. Aluminium is highly thermally conductive and therefore easily subject to variations in heat. Consideration ought to be given to the positioning of samples as the close proximity to one another on a thermally conductive surface, may mask the true performance of each sample. In future work, samples should be positioned independently.

As time progresses further, a rectangular item can be made out in the top right of the images; this item is the hottest measured area on the Al substrate reaching in excess of 313K compared to an atmospheric temperature of 303K. Whilst care was taken to place the sample tray away from all known sources of heat, it is possible that the power transformer for the camera was not initially considered as a potential heat source. This was located underneath the camera tripod and as time progressed it is thought that the transformer increased in temperature thus creating a heating effect below the Al uncoated substrate on which the samples were positioned.

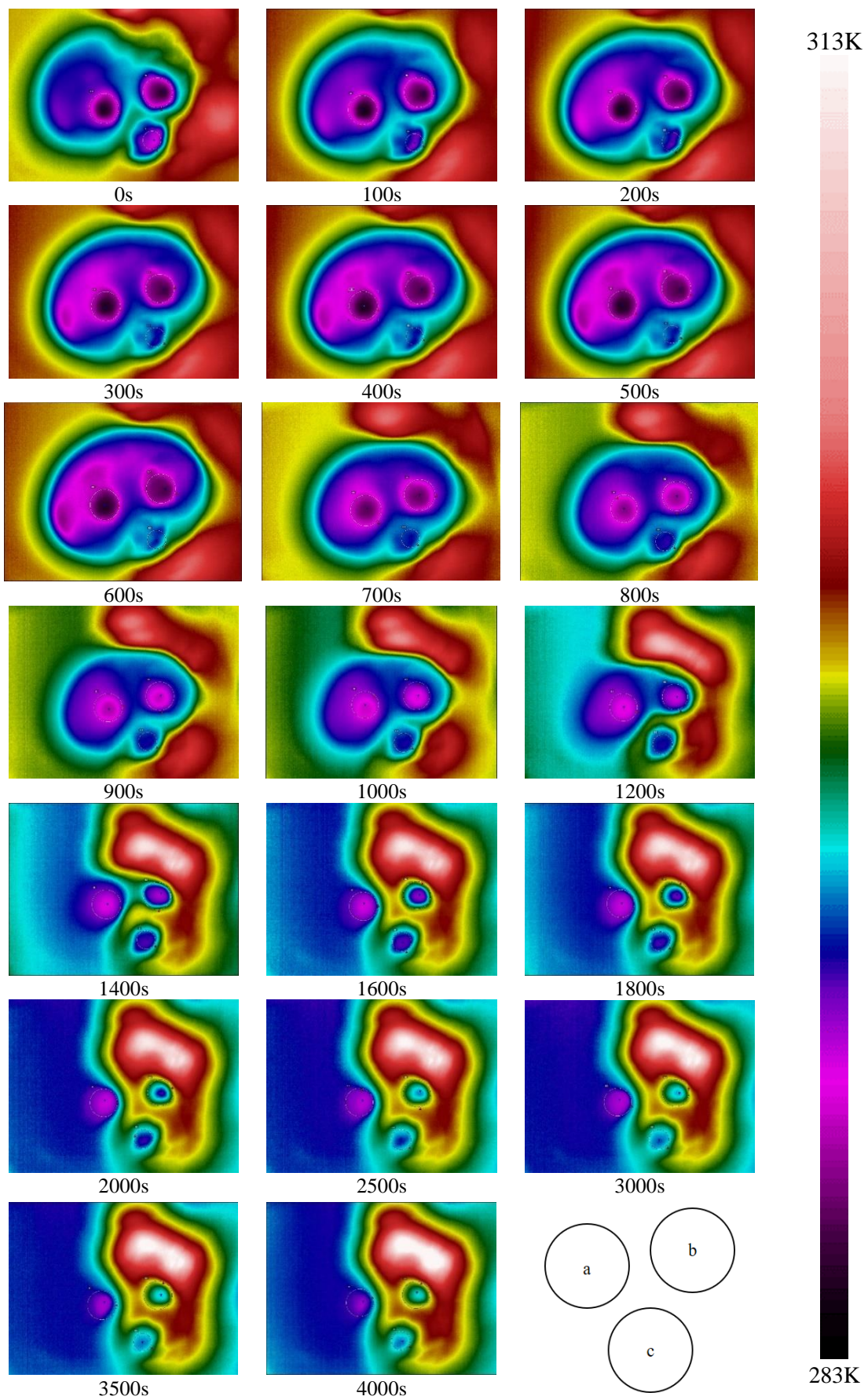


Figure 142 – Thermal images of (a) printed PVA hydrogel (b) printed PVA swollen with MEA (c) dual asymmetric layers printed PVA hydrogel and PLA/graphene.

As was graphically evident the printed PVA hydrogel was the sample with greatest temperature difference followed by the dual layer asymmetric sample, with both remaining cooler than the atmospheric temperature after 4000s. Finally the printed PVA swollen with MEA whilst initially appearing cool, had aligned with the atmospheric temperature by 4000s. The difference in temperature of water swollen samples was thought to be due to the volume of solvent retention. Whilst starting weights were the same, the dual layered sample contained no solvent in the PLA layer as this is hydrophobic. Therefore, the single-layered sample was able to contain a larger volume of inclusive water.

6.3.3 Infrared Thermography of Conventionally Prepared PVA Hydrogel

A physically crosslinked PVA hydrogel was synthesised in the conventional manner as described in **2.3.3.1**. It should be noted immediately that a hydrogel produced via this method would be significantly larger and thus, contain a greater quantity of on-board H₂O than a hydrogel produced via 3D printing. However, the purpose of this test was to evaluate the adsorption-cooling properties of a conventional hydrogel compared to a 3D printed one. Therefore longevity of the sample at this stage was not considered overly important.

Figure 143 shows the various temperatures recorded by the IR camera. Figure 144 shows an obvious circle where the hydrogel is situated. Using the circular area function on the IR camera maximum, minimum and average temperatures can be obtained directly. There are noticeable fluctuations in the temperature of Al substrate from 0-2500s. Interestingly, the hydrogel sample does not fluctuate also, but instead remains fairly constant. The fluctuations are thought to be caused by other researchers working in the laboratory. Owing to the high thermal conductivity and high reflectivity of aluminium, a human body passing or being near to the experimental set-up near or at the point of measurement, would be sufficient to cause a fluctuation in temperature. On first glance, these fluctuations caused by a third party could be considered frustrating. However, it has provided evidence to support the thermal stability of the hydrogel and that it is not affected by small fluctuations in surface temperature.

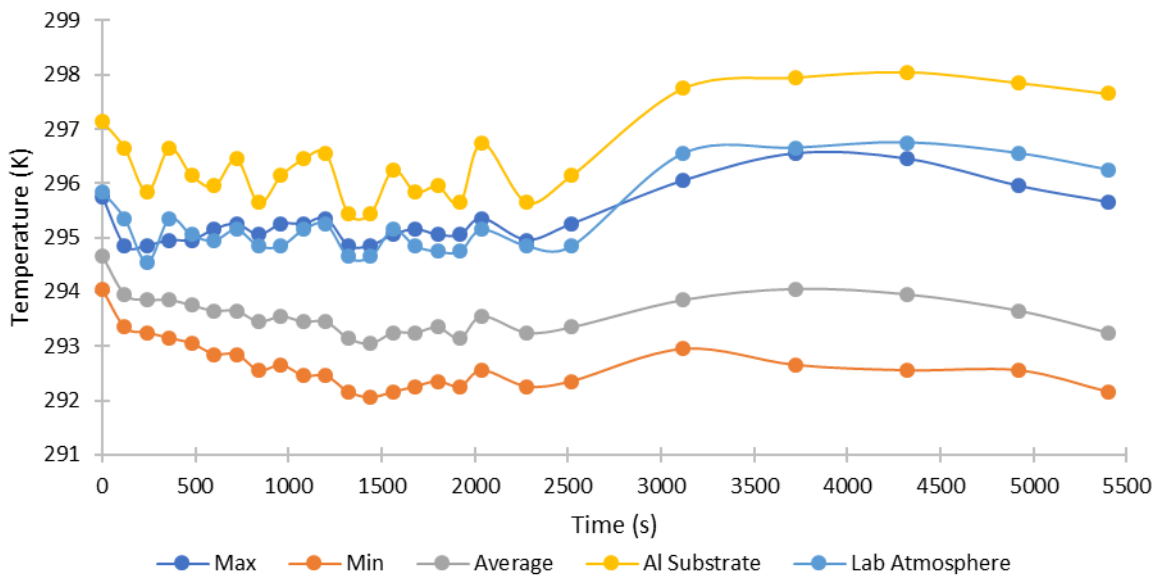


Figure 143 - Temperature variation of a conventionally produced PVA hydrogel compared to atmospheric and Al uncoated substrate temperature.

Figure 144 shows thermal images taken of the PVA hydrogel with guest H₂O over a period of 90mins (5400s). There appears to be very little change on temperature of the hydrogel. Interestingly, the hydrogel surface appears to be getting cooler despite an obvious increase in the temperature of the surrounding area.

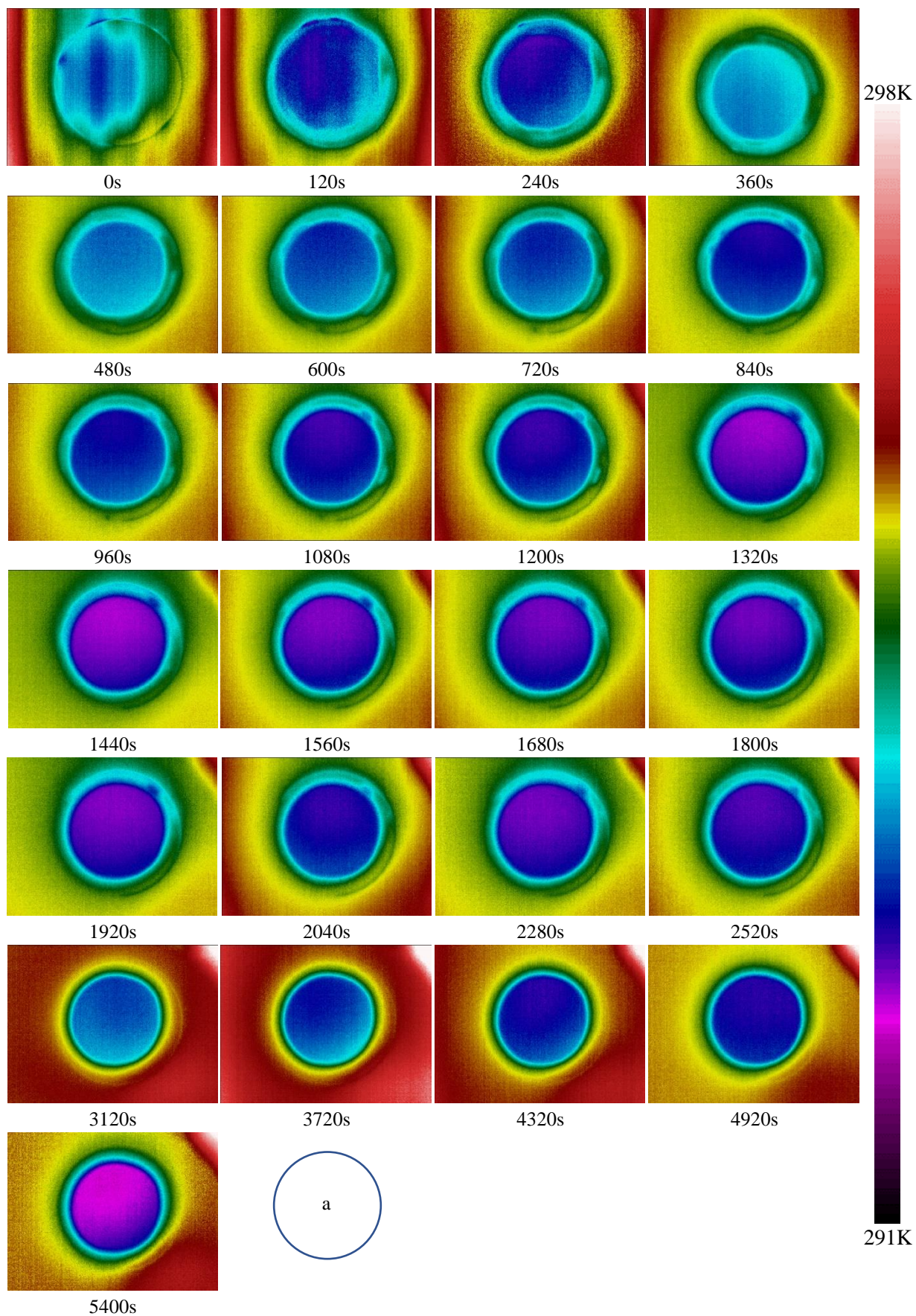


Figure 144 – Thermal images of (a) conventionally prepared physically crosslinked PVA hydrogel with on-board H_2O .

6.4 Summary

Thermography was successful, with both conventionally prepared hydrogels and 3D printed hydrogels (with different guest solvents) cooling the surface of an Al substrate convincingly. The temperature difference between the Al substrate and the samples was initially averaged at 15.5K (t=0s). Halfway through the run (2000s) the average temperature differences were 12.4K for all samples and by the end of the analysis (t=4000s) the temperature difference for all samples was on average 11K less than the Al substrate. It is clear that IRT was not carried out over a long enough time period and that no sample reached a temperature equilibrium with the substrate. Owing to this oversight, it is difficult to make direct comparisons between the performance of a conventionally prepared hydrogel and a 3D printed one.

However, it should be noted that there was a larger temperature difference between 3D printed samples and the Al substrate than for the conventionally prepared hydrogel. Typically 3D printed samples were 1.2K cooler than conventionally prepared samples. It is possible that this temperature difference would have been identical were the samples measured in identical conditions. As previously mentioned in **6.3.2 Infrared Thermography of 3D Printed Samples** the errors associated with the equipment and methods are between $\pm 2-3$ K, therefore a temperature difference between samples cannot be reliably quoted as significantly different.

There is clear potential for further work here. On-board solvent volumes, size of samples, conditions and temperature equilibrium point are all variables which could be further explored. Indeed it is possible that those who died of heat stress in SAS trials in South Wales might not have done so with hydrogel coated wearables.

7 Conclusions

7.1 Achievement of Aims

The aims as set-out in section 1.6 were varied, but strongly linked and were based upon the authors understanding of the current state of gas sensing and active/passive building cooling technologies. It was noticed that there was crossover of materials between these two areas which sparked the idea to combine technologies.

A range of PVA hydrogels have been produced and fully characterised incorporating both chemical and physical crosslinking. Functional M_xO_y NPs have been incorporated into the hydrogel matrix via different methods with characterisation and electrochromic properties examined. In-situ hydrolysis of PVAc to PVA was not successfully achieved, however understanding of organic solvent drying rates and characteristics was. Finally, a range of gas sensor substrates were successfully produced via 3D printing, with hydrogels formed from these substrates and gas sensing achieved.

Table 20 - Summary table of aims/objectives and the amount (as a %) the author believes has been achieved.

Aim/Objective	% Achieved
To develop methods for inclusion of M_xO_y nanoparticles within a PVA electrochromic hydrogel matrix for emissivity tuning of an industrial-type aluminum surface. Additionally, to explore PVA/PVAc hydrogels/thin films incorporating various organic solvents to assess drying rates.	80%
To synthesize and explore PVA hydrogels for their absorption/desorption properties of water cooling for the purpose of passive cooling devices.	75%
To develop 3D printed substrates, both single layer and asymmetrically layered with PVA/PLA-G, which may be chemically treated/processed in order to enhance their gas sensing characteristics.	90%
Fully characterize the above materials/structures using an array of analytical techniques.	95%

7.2 PVA- M_xO_y Nanocomposite Films and Hydrogels

A range of nanocomposite PVA films and hydrogels were synthesised using a carefully selected range of M_xO_y NPs, with a view to developing coatings which may be applied to a

surface and be detectable using an infrared camera. Hydrogels of differing PVA concentration and degrees of crosslinking were produced via *chemical* crosslinking using the crosslinker GA and via *physical* crosslinking using (i) a conventional freezer and (ii) liquid nitrogen. Simple visual and mechanical observations were used to select hydrogels with the most appropriate properties.

Characterisation by FTIR confirmed the presence of PVA and TGA plots revealed H₂O evaporation from the hydrogel followed by the expected decomposition profile. IRT was used to investigate if the type of crosslinking had an effect of the adsorption-cooling characteristics of simple PVA hydrogels swollen with H₂O. When identical weight/size samples were compared under identical atmospheric conditions over a period of 25h, it was found that all samples were consistently cooler (average 2.6K) than the substrate to which they were applied. Therefore, it is not believed that the type of crosslinking has a significant effect on solvent evaporation and therefore, thermal characteristics of PVA hydrogels.

Investigation into the emissive tuneability of PVA hydrogels by inclusive nanomaterials was considered. NPs including WO₃, AC, SiO₂, TiO₂, Al₂O₃, ZnO and Au were incorporated into the PVA polymer matrix at concentrations of 4, 8 and 10wt.% via a simple “slurry” method and by a more complex “in-situ” synthesis. The latter method enabled NPs to be produced within the polymer during (*chemical*) or after (*physical*) crosslinking. SEM-EDX showed a homogeneous dispersion of NPs within PVA films and (dried) hydrogels when the “in-situ” method was used. DLS was used to estimate the average particle size of NPs synthesised by the author (WO₃ and Au) and revealed WO₃ to have an average particle size of 48.7nm and Au to be 3nm.

“Real world” IRT was conducted outdoors with a distance of 500m from a range of PVA-M_xO_y nanocomposites and concentrations. This revealed noticeable differences between samples compared to the background surface to which they were applied. The samples with the greatest contrast were AC, WO₃ and Au. This test revealed that when considering the emissive tuneability of a hydrogel, the species of M_xO_y NP is more important than the concentration.

Building on this, consideration was given to PVA films and how application to a surface could be made to ensure (a) quick drying time of solvent and (b) good dispersion of the PVA-M_xO_y. It was envisioned that the material would be delivered via a mechanical spray or aerosol method and that solvent evolution would be key. The evaporation characteristics of a range of organic solvents including MF, MA, EA, DCM and MEK were investigated by IRT. These

investigations revealed MF to evaporate quickest, which, when considered with a boiling point figure of 306K (the lowest investigated) was a logical outcome. It was already known that PVA is insoluble in many organic solvents and therefore an alternative method of inclusion was investigated.

PVAc readily dissolves in the organic solvents selected and therefore controlled base hydrolysis of PVAc in solvent using a range of catalysts was studied (NaCl, MgCl₂ and Mg(NO₃)₂). NH₄OH was also used to neutralise CH₃COOH which is produced during hydrolysis of PVA. FTIR spectra were taken at intervals of 21, 88, 114 and 133h to track new bond formation and give an indication of hydrolysis progress. By 133h it was apparent that the hydrolysis reaction had not been initiated or was progressing at a very slow rate. The Mg(NO₃)₂ catalysed sample gave a tantalising glimpse that a new -OH bond was beginning to form, but this was of a too low %T to be reliably identified. It must be recommended that hydrolysis when performed in this way does not yield PVA.

7.3 Electrochromic Hydrogels

PVA-WO₃ nanocomposite hydrogels were produced using the “in-situ” synthesis method in **2.3.4.3**. Concentrations of 1, 5 and 10wt.% of WO₃ NPs were homogeneously dispersed in 8 and 10wt.% aqueous PVA before being cast as hydrogels. Small quantities (typically 0.5g) of PVA-WO₃ hydrogel were sandwiched between ITO/FTO glass and a voltage between 1-12v applied. Instantaneous colour changes (<1s) from yellow to dark blue were observed. When the voltage was reversed the hydrogel returned to its bleached (yellow) state.

Investigations were evolved further with incorporation of various salts (Li⁺, Na⁺, K⁺, Ba²⁺) at concentrations of 0.5-1M into the PVA solution prior to casting. Upon testing, the inclusive salts showed an ability to control the colour change by increasing or decreasing the intensity of colour observed. The voltage applied also impacted on the colour change observed; increasing voltage led to more intense colour changes at quicker switching speeds. From the observations it is clear that electrochromism in hydrogels is successful and that tuneability of colour intensity and speed of switching can be achieved.

The commercial possibilities of electrochromic hydrogels are wide-ranging. The author originally envisaged hydrogels would be applied to the interior, exterior and or roof of a building, enabling it to act as a passive cooling device (sweating surface). The inclusion of an electrochromic material could enable colour matching for aesthetic reasons and/or to absorb/reflect solar and IR radiation thus acting as a two stage cooling device.

Other uses of these materials could be in low power advertising. Current LCD screens are power hungry, whereas electrochromic devices only require a small voltage and current (1-12v) to drive a colour change. If sufficient colours were available, pictures and text could be worked into a 3D design, printed and displayed. As the polymer substrate is non-toxic and biodegradable, there would be few issues in the general public accessing them.

Finally uses may be found in the military or search and rescue sector. It is possible that sprayable hydrogels could be stored in a suitable vessel for use in an emergency and when deployed may be visible only in the IR spectrum. Search and rescue teams or forces equipped with IRT may be able to spot a target at night which is marked out with fast evaporating hydrogels or even gel microspheres loaded with metal oxides.

7.4 3D Printed Gas Sensors

FDM has been used to create PVA and asymmetric PVA-PLA/G discs for use in gas sensing and “cool coatings”. Initial investigations into sample geometry and swelling characteristics were informative and showed shapes with pronounced corners (square or rectangular) to be unsuitable for solvent uptake, with structural failure occurring. Circular shapes were found to be the most amenable to H₂O-swelling and were subsequently taken forward.

PLA with incorporated graphene obtained from a supplier was characterised before and after printing by Raman spectroscopy. This confirmed the presence of graphene in the filament and printed sample. SEM was then used to evaluate the form of graphene incorporated in the filament. It was concluded that graphene was most likely in MWCNT form as SEM showed cylindrical structures of approximately 250-300nm diameter emanating from within the PLA/G filament.

Printed PVA samples were subjected to H₂O uptake testing via gravimetry using a range of saturated salt solutions of known %RHs. This was done to control the rate of H₂O uptake by the printed samples. It was discovered that samples exposed to low %RH's showed negligible mass increase, indicative of H₂O not being incorporated into the PVA polymer matrix. The sample exposed to 100%RH showed a weight increase of almost 10%. This sample was further analysed by DSC which confirmed the presence of on-board H₂O.

Asymmetrically layered PVA-PLA/G samples were produced, and the boundary layer investigated by μ FTIR and SEM. This confirmed some small non-fused areas between layers, but more significantly, large areas of good chemical mixing and fusion. Confidence could then

be taken going forward that separation of layers would not occur once the PVA layer had been swollen with solvent.

Inclusion of MEA and ratios of MEA/PVA into the PVA layer was achieved using an immersive swelling method. FTIR confirmed the presence of MEA in the PVA layer. This was considered important for gas sensing. A 3D printed PVA hydrogel and a printed PVA disc swollen with MEA underwent gas testing. Various concentrations (0.045, 0.089, 0.134, 0.179, 0.223 and 0.268mmol) of CO₂ were injected into an air carrier gas stream flowing at 250mL/min. The printed PVA hydrogel (H₂O) gave electronic responses to all injected concentrations indicated by an increase in % Ω . Response times were typically 4s from the point of injection, with an initial return to pre-injection baseline levels observed. This was comparable with the response of an RGA which was 2.5s from the point of injection returning to baseline levels 6s after injection. The electronic responses ($\Delta\% \Omega$) for the MEA inclusive sample were less clear with both negative and positive $\Delta\% \Omega$ observed and seemingly random electronic responses. It may therefore be concluded that printed PVA converted to a hydrogel forms a responsive gas sensor, but that PVA with on-board MEA does not.

Printed PVA swollen with H₂O and MEA was also investigated for adsorption-cooling characteristics which may be compared to PVA hydrogels produced in the conventional manner. Samples of approximately 4g in weight were tested over a period of 4000s. Maximum temperature differences at t=4000s of printed samples compared to an Al substrate were observed at 13K (H₂O swollen), 10K (MEA swollen) and 11.8K (H₂O – asymmetric sample). It can therefore be concluded that printed PVA hydrogel samples when applied to a surface, are equally, if not more effective than conventionally prepared hydrogels at reducing the surface temperature.

7.5 Future Work

It is clear that avenues exist for future work associated with the research presented in this thesis. The interconnected nature of the materials investigated, enables wide-ranging applications of similar base materials to be realised. The aims of this work set out in section 1.6, have been successfully achieved on a small scale.

Areas which would benefit wider-ranging investigation are the degree of crosslinking in PVA-M_xO_y hydrogels and how this may affect the adsorption-cooling properties of the material. The work conducted by the author suggests that the method of crosslinking does not play a

significant role in the thermal characteristics of the hydrogel. However, fine tuning of the cooling properties of this type of hydrogel (difference in temperature vs length of time before regeneration is required) ought to be considered. Also of interest here would be investigation into the long-term stability of a M_xO_y hydrogel/film coating once applied to a surface. It is evident that when investigated by IRT, hydrogels were not fully dehydrated. It would be curious to understand how the coating behaves once fully dehydrated i.e. what happens to the M_xO_y – do they remain bound but unchanged in structure and morphology in their dispersed positions in the hydrogel host; this may require HRTEM. At the same do the guest NPs modify the host – this may require in-situ real-time solution and magic-angle NMR.

Gas testing is an area which also warrants further work. PVA swollen with MEA gave conflicting responses to injected CO_2 . It would be interesting to explore this further. However the most exciting possibility for future study is the concentration of graphene/CNTs in a 3D printed polymer matrix. When used in this work, the PLA/G was unresponsive to injected CO_2 which would appear to conflict with expected characteristics. The author believes that the concentration of CNTs in the PLA as supplied was not sufficient to enable ionic conductivity throughout the sample to occur, thus gas sensing was not achieved. Further work might consider investigating synthesis “in-house” rather than relying on a 3rd party supplier. This way the researcher would be able to produce 3D printer filament with the properties they desire. Linked to this is the possibility of using a paste extruder to print novel polymer blends.

Electrochromism in hydrogels is novel and fascinating and as such, many possibilities for further work exist. Incorporation of different electrochromic M_xO_y materials (V_2O_5 , MoO_3 , NiO) or even organic electrochromics (poly(3,4-ethylene-dioxythiophene) (PEDOT), polypyrrole (PPy), polythiophene and polyaniline (PANI)) ought to be considered, the latter may form interesting arrangements with common 3D printing materials, able to be paste extruded, providing yet another link between areas in this work.

Despite clear possibilities for further work, this work has been novel in many areas.

In a broader context one should be able to see bio-hydrogels developed from PVA-gelatine and even biomimetic hydrogel jellyfish sensing the state of corals in the ocean and oil-pollution that might harm them or CO_2 causing a rise in ocean acidity that might damage. The author expects more exciting development. For the moment he is proud of what he has achieved.

8 Appendix Items

8.1 FTIR Peak identification tables

Table 21 - FTIR-ATR peak identifications of methyl formate with 5, 8 and 10wt.% of dissolved PVAc.

Sample	Bond	Wavenumber (cm ⁻¹)	%T	Compound
Methyl Formate (MF)	C-H stretch	2970	84.0	MF
MF + 5%PVAc	C-H stretch	2970	84.1	MF
MF + 8%PVAc	C-H stretch	2970	85.3	MF
MF + 10%PVAc	C-H stretch	2954	90.2	MF/PVAc
Methyl Formate (MF)	C=O stretch	1718	9.2	MF
MF + 5%PVAc	C=O stretch	1718	9.3	MF
MF + 8%PVAc	C=O stretch	1718	9.4	MF
MF + 10%PVAc	C=O stretch	1720	27.8	MF
Methyl Formate (MF)	C-H bending	1435	70.7	MF
MF + 5%PVAc	C-H bending	1435	70.9	MF
MF + 8%PVAc	C-H bending	1435	71.8	MF
MF + 10%PVAc	C-H bending	1435	76.7	MF
Methyl Formate (MF)	C-H bending	1365	64.5	MF
MF + 5%PVAc	C-H bending	1365	63.5	MF
MF + 8%PVAc	C-H bending	1373	64.8	MF/PVAc
MF + 10%PVAc	C-H bending	1373	62.1	MF/PVAc
Methyl Formate (MF)	C-O stretch	1203	21.0	MF
MF + 5%PVAc	C-O stretch	1203	20.8	MF
MF + 8%PVAc	C-O stretch	1205	21.4	MF
MF + 10%PVAc	C-O stretch	1205	29.0	MF
Methyl Formate (MF)	C-O stretch	1151	19.1	MF
MF + 5%PVAc	C-O stretch	1151	19.5	MF
MF + 8%PVAc	C-O stretch	1151	20.0	MF
MF + 10%PVAc	C-O stretch	1155	37.8	MF
Methyl Formate (MF)	C-O stretch	1029	85.6	MF
MF + 5%PVAc	C-O stretch	1028	84.7	MF
MF + 8%PVAc	C-O stretch	1028	83.8	MF
MF + 10%PVAc	C-O stretch	1022	59.8	PVAc
Methyl Formate (MF)	C-H bending	908	54.2	MF
MF + 5%PVAc	C-H bending	908	54.3	MF
MF + 8%PVAc	C-H bending	908	55.1	MF
MF + 10%PVAc	C-H bending	908	66.3	MF
Methyl Formate (MF)	C-H bending	767	69.8	MF
MF + 5%PVAc	C-H bending	767	70.9	MF

MF + 8%PVAc	C-H bending	767	70.9	MF
MF + 10%PVAc	C-H bending	767	78.1	MF
MF + 10%PVAc	C-H bending	605	81.9	PVAc

Table 22 - FTIR-ATR peak identifications of dichloromethane with 5, 8 and 10wt.% of dissolved PVAc.

Sample	Bond	Wavenumber (cm ⁻¹)	%T	Compound
DCM	C-H stretch	3055	96.7	DCM
DCM + 5%PVAc	C-H stretch	3055	95.2	DCM
DCM + 8%PVAc	C-H stretch	3055	95.4	DCM
DCM + 10%PVAc	C-H stretch	3055	95.0	DCM
DCM	C-H bending	1734	89.9	DCM
DCM + 5%PVAc	C=O stretch	1734	69.4	PVAc
DCM + 8%PVAc	C=O stretch	1735	65.3	PVAc
DCM + 10%PVAc	C=O stretch	1735	62.6	PVAc
DCM	C-H bending	1373	93.9	DCM
DCM + 5%PVAc	C-H bending	1373	84.3	DCM
DCM + 8%PVAc	C-H bending	1373	82.9	DCM
DCM + 10%PVAc	C-H bending	1373	81.1	DCM
DCM		1263	46.4	
DCM + 5%PVAc	C-O stretching	1263	49.3	PVAc
DCM + 8%PVAc	C-O stretching	1263	47.9	PVAc
DCM + 10%PVAc	C-O stretching	1263	48.3	PVAc
DCM + 5% PVAc	C-O stretch	1022	92.0	PVAc
DCM + 8%PVAc	C-O stretch	1022	86.9	PVAc
DCM + 10%PVAc	C-O stretch	1022	85.6	PVAc
DCM	C-Cl	731	10.3	DCM
DCM + 5%PVAc	C-Cl	731	11.9	DCM
DCM + 8%PVAc	C-Cl	731	11.3	DCM
DCM + 10%PVAc	C-Cl	731	12.9	DCM

Table 23 - FTIR-ATR peak identifications of methyl acetate with 5, 8 and 10wt.% of dissolved PVAc.

Sample	Bond	Wavenumber (cm ⁻¹)	%T	Compound
MA	C-H stretch	2955	91.1	MA
MA + 5%PVAc	C-H stretch	2957	90.5	MA
MA + 8%PVAc	C-H stretch	2955	91.6	MA
MA + 10%PVAc	C-H stretch	2955	91.1	MA
MA	C=O stretch	1740	17.8	MA
MA + 5%PVAc	C=O stretch	1740	23.4	MA
MA + 8%PVAc	C=O stretch	1740	17.2	MA

MA + 10%PVAc	C=O stretch	1740	17.1	MA
MA	C-H bending	1437	64.1	MA
MA + 5%PVAc	C-H bending	1437	64.0	MA
MA + 8%PVAc	C-H bending	1437	64.3	MA
MA + 10%PVAc	C-H bending	1437	64.1	MA
MA	C-H bending	1369	53.5	MA
MA + 5%PVAc	C-H bending	1369	53.7	MA
MA + 8%PVAc	C-H bending	1369	52.4	MA
MA + 10%PVAc	C-H bending	1369	52.2	MA
MA	C-O stretch	1236	12.8	MA
MA + 5%PVAc	C-O stretch	1236	14.7	MA
MA + 8%PVAc	C-O stretch	1236	12.2	MA
MA + 10%PVAc	C-O stretch	1236	12.2	MA
MA	C-O stretch	1043	37.0	MA
MA + 5%PVAc	C-O stretch	1043	38.3	MA
MA + 8%PVAc	C-O stretch	1043	36.9	MA
MA + 10%PVAc	C-O stretch	1043	36.8	MA
MA	C-H bending	843	54.2	MA
MA + 5%PVAc	C-H bending	843	57.4	MA
MA + 8%PVAc	C-H bending	843	54.5	MA
MA + 10%PVAc	C-H bending	843	54.4	MA
MA	C-H bending	640	74.7	MA
MA + 5%PVAc	C-H bending	640	73.1	MA
MA + 8%PVAc	C-H bending	640	74.9	MA
MA + 10%PVAc	C-H bending	640	74.2	MA

Table 24- FTIR-ATR peak identifications of ethyl acetate with 5, 8 and 10wt.% of dissolved PVAc.

Sample	Bond	Wavenumber (cm ⁻¹)	%T	Compound
EA	C-H stretch	2983	87.3	EA
EA + 5%PVAc	C-H stretch	2983	87.5	EA
EA + 8%PVAc	C-H stretch	2983	86.9	EA
EA + 10%PVAc	C-H stretch	2983	86.9	EA
EA	C=O stretch	1736	19.4	EA
EA + 5%PVAc	C=O stretch	1736	20.9	EA
EA + 8%PVAc	C=O stretch	1736	19.1	EA
EA + 10%PVAc	C=O stretch	1736	18.3	EA
EA	C-H bending	1446	86.3	EA
EA + 5%PVAc	C-H bending	1446	85.4	EA
EA + 8%PVAc	C-H bending	1446	85.9	EA

EA + 10%PVAc	C-H bending	1446	85.5	EA
EA	C-H bending	1371	51.9	EA
EA + 5%PVAc	C-H bending	1371	51.9	EA
EA + 8%PVAc	C-H bending	1371	50.7	EA
EA + 10%PVAc	C-H bending	1371	49.8	EA
EA	C-O stretch	1232	15.6	EA
EA + 5%PVAc	C-O stretch	1232	15.7	EA
EA + 8%PVAc	C-O stretch	1232	15.3	EA
EA + 10%PVAc	C-O stretch	1232	14.7	EA
EA	C-O stretch	1043	27.6	EA
EA + 5%PVAc	C-O stretch	1043	28.6	EA
EA + 8%PVAc	C-O stretch	1043	28.4	EA
EA + 10%PVAc	C-O stretch	1043	28.1	EA
EA	C-H bending	847	82.5	EA
EA + 5%PVAc	C-H bending	847	81.2	EA
EA + 8%PVAc	C-H bending	847	83.2	EA
EA + 10%PVAc	C-H bending	847	83.1	EA
EA	C-H bending	634	81.0	EA
EA + 5%PVAc	C-H bending	634	81.1	EA
EA + 8%PVAc	C-H bending	634	80.5	EA
EA + 10%PVAc	C-H bending	634	80.1	EA
EA	C-H bending	607	78.1	EA
EA + 5%PVAc	C-H bending	607	77.0	EA
EA + 8%PVAc	C-H bending	607	76.6	EA
EA + 10%PVAc	C-H bending	607	76.0	EA

Table 25 - FTIR-ATR peak identifications of methyl ethyl ketone with 5, 8 and 10wt.% of dissolved PVAc.

Sample	Bond	Wavenumber (cm ⁻¹)	%T	Compound
MEK	C-H stretch	2978	86.6	MEK
MEK + 5%PVAc	C-H stretch	2978	85.7	MEK
MEK + 8%PVAc	C-H stretch	2978	86.8	MEK
MEK + 10%PVAc	C-H stretch	2978	86.2	MEK
MEK	C=O stretch	1713	36.1	MEK
MEK + 5%PVAc	C=O stretch	1713	35.5	MEK
MEK + 8%PVAc	C=O stretch	1713	35.7	MEK
MEK + 10%PVAc	C=O stretch	1713	35.5	MEK
MEK	C-H bending	1458	83.0	MEK
MEK + 5%PVAc	C-H bending	1458	81.8	MEK
MEK + 8%PVAc	C-H bending	1458	83.2	MEK

MEK + 10%PVAc	C-H bending	1458	82.0	MEK
MEK	C-H bending	1417	79.5	MEK
MEK + 5%PVAc	C-H bending	1417	78.5	MEK
MEK + 8%PVAc	C-H bending	1417	79.5	MEK
MEK + 10%PVAc	C-H bending	1417	78.9	MEK
MEK	C-H bending	1364	61.0	MEK
MEK + 5%PVAc	C-H bending	1364	59.7	MEK
MEK + 8%PVAc	C-H bending	1364	60.1	MEK
MEK + 10%PVAc	C-H bending	1364	59.8	MEK
MEK	C-CO-C bend	1171	60.8	MEK
MEK + 5%PVAc	C-CO-C bend	1171	60.4	MEK
MEK + 8%PVAc	C-CO-C bend	1171	60.7	MEK
MEK + 10%PVAc	C-CO-C bend	1171	60.1	MEK
MEK	C-H bending	943	86.8	MEK
MEK + 5%PVAc	C-H bending	943	85.1	MEK
MEK + 8%PVAc	C-H bending	945	85.1	MEK
MEK + 10%PVAc	C-H bending	945	84.3	MEK
MEK	C-H bending	736	84.3	MEK
MEK + 5%PVAc	C-H bending	736	85.6	MEK
MEK	C-H bending	586	87.0	MEK
MEK + 5%PVAc	C-H bending	586	86.6	MEK
MEK + 8%PVAc	C-H bending	590	86.3	MEK
MEK + 10%PVAc	C-H bending	590	84.8	MEK

Table 26 - FTIR-ATR peak identifications of PVA and catalysed (NaCl) hydrolysis products of PVAc.

Sample	Bond	Wavenumber (cm ⁻¹)	%T
PVA	O-H stretch	3275	66.0
PVA	C-H stretch	2906	75.8
88hrs	C=O stretch	1728	87.7
114hrs	C=O stretch	1726	90.7
133hrs	C=O stretch	1730	87.4
PVA	O-H bending	1419	71.7
88hrs	C-H bending	1369	92.3
114hrs	C-H bending	1369	93.8
133hrs	C-H bending	1373	90.5
PVA	O-H bending	1323	73.9
88hrs	C-O stretching	1226	85.8
114hrs	C-O stretching	1226	89.0
133hrs	C-O stretching	1226	85.7

PVA	C-O stretching	1087	50.9
88hrs	C-O stretching	1018	89.0
114hrs	C-O stretching	1018	90.9
133hrs	C-O stretching	1018	87.0
PVA	C-H bending	846	63.9

Table 27 - FTIR-ATR peak identifications of PVA and catalysed ($MgCl_2$) hydrolysis products of PVAc.

Sample	Bond	Wavenumber (cm^{-1})	%T
PVA	O-H stretch	3275	66.0
PVA	C-H stretch	2906	75.8
88hrs	C=O stretch	1730	90.7
114hrs	C=O stretch	1724	91.7
133hrs	C=O stretch	1734	89.9
PVA	O-H bending	1419	71.7
88hrs	C-H bending	1369	93.7
114hrs	C-H bending	1369	94.3
133hrs	C-H bending	1369	93.9
PVA	O-H bending	1323	73.9
88hrs	C-O stretching	1224	89.1
114hrs	C-O stretching	1222	90.6
133hrs	C-O stretching	1224	91.4
PVA	C-O stretching	1087	50.9
88hrs	C-O stretching	1018	91.0
114hrs	C-O stretching	1016	92.0
133hrs	C-O stretching	1018	91.4
PVA	C-H bending	846	63.9

Table 28 - FTIR-ATR peak identifications of PVA and catalysed $Mg(NO_3)_2$ hydrolysis products of PVAc.

Sample	Bond	Wavenumber (cm^{-1})	%T
PVA	O-H stretch	3275	66.0
PVA	C-H stretch	2906	75.8
88hrs	C=O stretch	1734	87.5
114hrs	C=O stretch	1728	75.5
133hrs	C=O stretch	1730	83.7
PVA	O-H bending	1419	71.7
88hrs	C-H bending	1369	92.6
114hrs	C-H bending	1369	85.0
133hrs	C-H bending	1369	89.8
PVA	O-H bending	1323	73.9

88hrs	C-O stretching	1226	86.8
114hrs	C-O stretching	1226	72.7
133hrs	C-O stretching	1226	81.4
PVA	C-O stretching	1087	50.9
88hrs	C-O stretching	1018	89.5
114hrs	C-O stretching	1016	79.4
133hrs	C-O stretching	1018	85.4
PVA	C-H bending	846	63.9
88hrs	C-H bending	603	93.6
114hrs	C-H bending	603	88.0
133hrs	C-H bending	603	91.5

Table 29 – FTIR-ATR peak identifications of PVA powder 99+% hydrolysed.

Bond	Wavenumber (cm ⁻¹)	%T
O-H stretching	3263	85.7
C-H stretching	2889	88.7
C-O stretching	1082	79.1
C-C stretching	830	78.4

Table 30 – FTIR-ATR peak identifications of PVA film cast from 8wt.% aqueous PVA solution.

Bond	Wavenumber (cm ⁻¹)	%T
O-H stretching	3384	76.7
C-H stretching	2918	82.9
C=O stretching	1716	75.0
O-H bending	1373	74.9
C-O stretching	1240	65.9
C-O stretching	1085	61.7
C-H bending	450-600	59.1

Table 31 – FTIR-ATR peak identifications of a physically crosslinked hydrogel cast from 8wt.% aqueous PVA solution.

Bond	Wavenumber (cm ⁻¹)	%T
O-H stretching	3300	55.3
C-H stretching	2919	81.9
C=O stretching	1716	61.1
O-H bending	1375	66.4
C-O stretching	1248	51.3
C-O stretching	1024	60.9
C-H bending	450-600	31.5

Table 32 – Identification of peaks in FTIR spectra of PVA power.

Bond	Wavenumber (cm ⁻¹)	%T
O-H stretching	3300	85.2
C-H stretching	2920	88.4
C-O stretching	1083	78.4
C-C stretching	830	83.2

Table 33 – Identification of peaks in FTIR spectra of printed PVA hydrogel.

Bond	Wavenumber (cm ⁻¹)	%T
O-H stretching	3300	53.2
C-H stretching	2930	81.9
C=O stretching	1716	60.9
O-H bending	1380	66.4
C-O stretching	1295	51.3
C-O stretching	1087	60.7
C-H bending	450-600	31.6

Table 34 – FTIR-ATR peak identifications for printed PLA/graphene.

Bond	Wavenumber (cm ⁻¹)	%T
C-H stretching	2918	85.9
C-H stretching	2848	86.7
C=O stretching	1734	77.2
C-O stretching	1174	78.0
C-O stretching	1074	76.5

Table 35 – FTIR-ATR peak identifications for printed PVA.

Bond	Wavenumber (cm ⁻¹)	%T
O-H stretching	3300	93.6
C-H stretching	2930	92.9
C=O stretching	1716	88.4
O-H bending	1371	89.6
C-O stretching	1232	84.3
C-O stretching	1018	84.2
C-C stretching	830	90.1

Table 36 - FTIR-ATR peak identifications for printed PVA.

Bond	Wavenumber (cm ⁻¹)	%T
O-H stretching	3315	88.1
C-H stretching	2918	88.4
C=O stretching	1732	75.2
O-H	1417	84.1
C-O	1232	68.0
C-O	1049	70.1

Table 37 - FTIR-ATR peak identifications for monoethanolamine.

Bond	Wavenumber (cm ⁻¹)	%T
N-H stretching	3392	76.9
N-H stretching	3282	77.2
C-H stretching	2920	69.0
C-H stretching	2839	66.8
N-H bending	1575	77.4
C-H bending	1456	80.8
O-H bending	1354	77.7
C-N stretching	1041	50.0
C-O stretching	952	50.1
C-O stretching	858	49.8

Table 38 - FTIR-ATR peak identifications for printed PVA swollen with monoethanolamine.

Bond	Wavenumber (cm ⁻¹)	%T
N-H stretching	3392	68.4
N-H stretching	3282	67.3
C-H stretching	2926	63.1
C-H stretching	2845	62.9
C=O stretching	1733	82.3
N-H bending	1593	71.5
C-H bending	1440	74.3
O-H bending	1361	71.7
C-N stretching	1041	47.4
C-O stretching	952	48.2
C-O stretching	858	45.7

Table 39 - FTIR-ATR peak identifications for printed PVA.

Bond	Wavenumber (cm ⁻¹)	%T
O-H stretching	3315	88.1
C-H stretching	2918	88.2
C=O stretching	1732	75.2

O-H bending	1400	85.1
C-O stretching	1232	68.1
C-O stretching	1049	70.8

Table 40 - FTIR-ATR peak identifications for printed PVA swollen with water.

Bond	Wavenumber (cm ⁻¹)	%T
O-H stretching	3300	53.1
C-H stretching	2945	81.6
C=O stretching	1716	61.1
O-H bending	1380	66.4
C-O stretching	1295	51.0
C-O stretching	1024	60.9
C-H bending	450-600	30.3

Table 41 - FTIR-ATR peak identifications for printed PVA swollen with monoethanolamine.

Bond	Wavenumber (cm ⁻¹)	%T
N-H stretching	3392	77.1
N-H stretching	3282	67.2
C-H stretching	2926	63.2
C-H stretching	2839	62.7
C=O stretching	1733	82.3
N-H bending	1575	71.3
C-H bending	1482	74.2
O-H bending	1346	71.6
C-N stretching	1041	47.4
C-O stretching	952	47.9
C-O stretching	858	45.7

Table 42 - FTIR-ATR peak identifications for printed PVA swollen in neat MEA.

Bond	Wavenumber (cm ⁻¹)	%T
N-H stretching	3392	77.1
N-H stretching	3282	67.2
C-H stretching	2895	63.2
C-H stretching	2839	62.7
C=O stretching	1735	84.0
N-H bending	1575	71.3
C-H bending	1482	74.2
O-H bending	1346	71.6
C-N stretching	1041	47.4
C-O stretching	952	47.9

C-O stretching	858	45.7
----------------	-----	------

Table 43- FTIR-ATR peak identifications for printed PVA swollen with 90% MEA 10% H₂O.

Bond	Wavenumber (cm ⁻¹)	%T
N-H stretching	3392	71.6
N-H stretching	3282	64.8
C-H stretching	2895	65.7
C-H stretching	2839	66.1
C=O stretching	1735	85.8
N-H bending	1575	71.6
C-H bending	1482	76.6
O-H bending	1346	75.9
C-N stretching	1041	52.4
C-O stretching	952	49.5
C-O stretching	858	49.0

Table 44 - FTIR-ATR peak identifications for printed PVA swollen with 70% MEA 30% H₂O.

Bond	Wavenumber (cm ⁻¹)	%T
N-H stretching	3392	77.1
N-H stretching	3282	67.2
C-H stretching	2895	63.2
C-H stretching	2839	62.7
C=O stretching	1735	84.0
N-H bending	1575	71.3
C-H bending	1482	74.2
O-H bending	1346	71.6
C-N stretching	1041	47.4
C-O stretching	952	47.9
C-O stretching	858	45.7

Table 45- FTIR-ATR peak identifications for printed PVA swollen in 100% H₂O.

Bond	Wavenumber (cm ⁻¹)	%T
O-H stretching	3300	53.1
C-H stretching	2930	81.6
C=O stretching	1716	61.1
O-H	1380	66.4
C-O	1295	51.0
C-O	1024	60.9
C-H bending	450-600	30.3

8.2 List of Conferences Attended

2013 XVIIth International Sol-Gel Conference, Madrid, Spain.

- Poster presentation (accepted abstract below)

Sol-gel Electrochromic Coatings

Sam Rust

Nanomaterials Laboratory, Wolfson Centre for Materials Processing, Brunel University, Uxbridge, Middx, UB8 3PH

In electrochromic films the host cathode can be oxide TO_n (WO_3 , MoO_3 or TiO_2), the inserted ion can be H^+ or Li^+ (or cations of Na, K, Rb, Cs, Cu, Ag, Zn, etc) and the anode can be NiO_2 , IrO_2 or RhO_2 . At the TO_n cathode a solid non-stoichiometric bronze M_xTO_n is formed by intercalation of an electron and a cation insertion into the host lattice. Oxide hydrogen bronzes (e.g. H_xWO_3) have been in use as reversible electrode materials, electrochromic devices, heterogeneous catalysts, electro-catalysts (for fuel cells or water lysis) and hydrogen storage devices. We have worked on these bronzes previously [1].

We show here that sol-gel $WO_3/C \leftrightarrow X_xWO_3/C$, $MoO_3 \leftrightarrow X_xMoO_3/C$ and $WO_3-MoO_3 \leftrightarrow X_xWO_3-X_xMoO_3/C$ electrochromic coatings can be prepared and have exceptional response times. Their properties are compared with those of unsupported oxides \leftrightarrow bronzes. The potential of these coatings in nanofuel cells are considered.

[1] M.S.W.Vong Solid State Ionics 32-3,91- 96,(1989); 26,180,(1988); S.A.Lawrence Proc.Roy.Soc. 411A,95-121,(1987); S.Stevenson J.Chem.Soc.Farad.Trans. I 83,2175-2191,(1987); G.C.Bond Mater.Res.Bull. 19, 701-704,(1984)

2013 Brunel Graduate School and Specialist Research Institutes Research Conference, Uxbridge Campus.

- Poster presentation

2014 Brunel University Research Student Conference, Uxbridge Campus.

- Poster presentation – placed in the top 10 entries

2014 Materials Research Exchange: UK Advanced Materials Research Showcase, Coventry.

2014 Joliot-Curie Conference – Royal Society of Chemistry, Edinburgh.

- Poster presentation

2017 HiPerNano17, Knowledge Transfer Network, London.

2017 46th Intelligent Sensing Program – Sensing the Air Quality and Emissions, Birmingham.

8.3 List of Presentations Given

2013 Wolfson Centre for Materials Processing – Seminar

- Presentation title – A History of Electrochromic Materials

2014 Wolfson Centre for Materials Processing – Seminar

- Presentation title – Infrared Stealth Coatings

2014 Brunel University Graduate School – Researcher Development Series

- Life as a “lab based” PhD Student

8.3 Miscellaneous Honours

2014 Chair of interviewing panel of PGR students for the role of “Institute Director”.

Invited by the Vice Provost (Research) to chair a panel of PGR students to interview senior academic candidates for the “Institute Director” role as part of the University TxP development programme.

2015 Attended a dinner meeting with the Vice Provost (Education) to discuss PGR students’ views on TxP and how the University could better support research students. One of 10 PGR students selected.

8.4 Teaching

2013 & 2014 Lab demonstrator for “Communications, Projects and Electronic Engineering” module for the College of Engineering, Design and Physical Sciences.

9 References

- [1] Baklanov, A., Molina, L. T., & Gauss, M. (2016). Megacities, air quality and climate. *Atmospheric Environment*, 126, 235–249.
- [2] Huang, J., Liu, Q., & Guo, X. (2018). Short-term effects of particulate air pollution on human health. In *Reference Module in Earth Systems and Environmental Sciences*. Elsevier, USA
- [3] Tsui, H.-C., Chen, C.-H., Wu, Y.-H., Chiang, H.-C., Chen, B.-Y., & Guo, Y. L. (2018). Lifetime exposure to particulate air pollutants is negatively associated with lung function in non-asthmatic children. *Environmental Pollution*, 236, 953–961.
- [4] Brilli, F., Fares, S., Ghirardo, A., de Visser, P., Calatayud, V., Muñoz, A., Annesi-Maesano, I., Sebastiani, F., Alivernini, A., Varriale, V. and Menghini, F. (2018). Plants for Sustainable Improvement of Indoor Air Quality. *Trends in Plant Science*, 23(6), pp.507-512.
- [5] Apte, K., & Salvi, S. (2016). Household air pollution and its effects on health. *F1000 Research*, 5, Faculty rev-2593.
- [6] Brugha, R., Edmondson, C., & Davies, J. C. (2018). Outdoor air pollution and cystic fibrosis. *Paediatric Respiratory Reviews*. *In press, corrected proof*.
- [7] Liu, C., Yin, P., Chen, R., Meng, X., Wang, L., Niu, Y., Lin, Z., Liu, Y., Liu, J., Qi, J., You, J., Kan, H. and Zhou, M. (2018). Ambient carbon monoxide and cardiovascular mortality: a nationwide time-series analysis in 272 cities in China. *The Lancet Planetary Health*, 2(1), 12-18.
- [8] Wang, L., Liu, C., Meng, X., Niu, Y., Lin, Z., Liu, Y., Liu, J., Qi, J., You, J., Tse, L., Chen, J., Zhou, M., Chen, R., Yin, P. and Kan, H. (2018). Associations between short-term exposure to ambient sulfur dioxide and increased cause-specific mortality in 272 Chinese cities. *Environment International*, 117, pp.33-39.
- [9] Collart, P., Dubourg, D., Levêque, A., Sierra, N. B., & Coppieters, Y. (2018). Short-term effects of nitrogen dioxide on hospital admissions for cardiovascular disease in Wallonia, Belgium. *International Journal of Cardiology*, 255, 231–236.
- [10] Zhang, Z., Yan, X., Gao, F., Thai, P., Wang, H., Chen, D., Zhou, L., Gong, D., Li, Q., Morawska, L. and Wang, B. (2018). Emission and health risk assessment of volatile organic compounds in various processes of a petroleum refinery in the Pearl River Delta, China. *Environmental Pollution*, 238, pp.452-461.

- [11] Hsu, C., Chiang, H., Shie, R., Ku, C., Lin, T., Chen, M., Chen, N. and Chen, Y. (2018). Ambient VOCs in residential areas near a large-scale petrochemical complex: Spatiotemporal variation, source apportionment and health risk. *Environmental Pollution*, 240, pp.95-104.
- [12] Du, W., Chen, Y., Shen, G., Wang, W., Zhuo, S., Huang, Y., Pan, X. and Tao, S. (2018). Winter air pollution by and inhalation exposure to nitrated and oxygenated PAHs in rural Shanxi, north China. *Atmospheric Environment*, 187, pp.210-217.
- [13] Martins, N. R., & Carrilho da Graça, G. (2018). Impact of PM_{2.5} in indoor urban environments: A review. *Sustainable Cities and Society*, 42, 259–275.
- [14] Jan, R., Roy, R., Yadav, S., & Satsangi, P. G. (2017). Exposure assessment of children to particulate matter and gaseous species in school environments of Pune, India. *Building and Environment*, 111, 207–217.
- [15] Gaffin, J., Hauptman, M., Petty, C., Sheehan, W., Lai, P., Wolfson, J., Gold, D., Coull, B., Koutrakis, P. and Phipatanakul, W. (2018). Nitrogen dioxide exposure in school classrooms of inner-city children with asthma. *Journal of Allergy and Clinical Immunology*, 141(6), 2249-2255.
- [16] Kim, D., Chen, Z., Zhou, L.-F., & Huang, S.-X. (2018). Air pollutants and early origins of respiratory diseases. *Chronic Diseases and Translational Medicine*, 4(2), 75–94.
- [17] Chin, W.-S., Chang, Y.-K., Huang, L.-F., Tsui, H.-C., Hsu, C.-C., & Guo, Y.-L. L. (2018). Effects of long-term exposure to CO and PM 2.5 on microalbuminuria in type 2 diabetes. *International Journal of Hygiene and Environmental Health*, 221(4), 602–608.
- [18] Xiao, Q., Chen, H., Strickland, M., Kan, H., Chang, H., Klein, M., Yang, C., Meng, X. and Liu, Y. (2018). Associations between birth outcomes and maternal PM 2.5 exposure in Shanghai: A comparison of three exposure assessment approaches. *Environment International*, 117, 226-236.
- [19] Salinas-Rodríguez, A., Fernández-Niño, J. A., Manrique-Espinoza, B., Moreno-Banda, G. L., Sosa-Ortiz, A. L., Qian, Z. (Min), & Lin, H. (2018). Exposure to ambient PM_{2.5} concentrations and cognitive function among older Mexican adults. *Environment International*, 117, 1–9.
- [20] Gonzalez-Casanova, I., Stein, A., Barraza-Villarreal, A., Feregrino, R., DiGirolamo, A., Hernandez-Cadena, L., Rivera, J., Romieu, I. and Ramakrishnan, U. (2018). Prenatal exposure to environmental pollutants and child development trajectories through 7 years. *International Journal of Hygiene and Environmental Health*, 221(4), 616-622.

- [21] Delpont, B., Mariet, A. S., Blanc, C., Bejot, Y., Giroud, M., & Reis, J. (2018). Environmental Air Pollution: An Emerging Risk Factor for Stroke. In *Encyclopedia of Cardiovascular Research and Medicine* (pp. 231–237). Elsevier. UK.
- [22] Huang, J., Pan, X., Guo, X., & Li, G. (2018). Impacts of air pollution wave on years of life lost: A crucial way to communicate the health risks of air pollution to the public. *Environment International*, 113, 42–49.
- [23] World Health Organisation. Burden of disease from Ambient Air Pollution for 2012. Geneva, Switzerland: World Health Organisation, Public Health, Social and Environmental Determinants of Health Department; 2014.
- [24] Shi, S. (2018). Contributions of indoor and outdoor sources to airborne polycyclic aromatic hydrocarbons indoors. *Building and Environment*, 131, 154–162.
- [25] Azuma, K., Uchiyama, I., Uchiyama, S., & Kunugita, N. (2016). Assessment of inhalation exposure to indoor air pollutants: Screening for health risks of multiple pollutants in Japanese dwellings. *Environmental Research*, 145, 39–49.
- [26] Rösch, C., Kohajda, T., Röder, S., Bergen, M. von, & Schlink, U. (2014). Relationship between sources and patterns of VOCs in indoor air. *Atmospheric Pollution Research*, 5(1), 129–137.
- [27] Thevenet, F., Debono, O., Rizk, M., Caron, F., Verrielle, M., & Locoge, N. (2018). VOC uptakes on gypsum boards: Sorption performances and impact on indoor air quality. *Building and Environment*, 137, 138–146.
- [28] Shin, S. H., & Jo, W. K. (2012). Volatile organic compound concentrations, emission rates, and source apportionment in newly-built apartments at pre-occupancy stage. *Chemosphere*, 89(5), 569–578.
- [29] Andrade, A., & Dominski, F. H. (2018). Indoor air quality of environments used for physical exercise and sports practice: Systematic review. *Journal of Environmental Management*, 206, 577–586.
- [30] Perera, F. (2017). Pollution from Fossil-Fuel Combustion is the Leading Environmental Threat to Global Pediatric Health and Equity: Solutions Exist. *International Journal of Environmental Research and Public Health*, 15(1), 16.
- [31] Franchini, M., & Mannucci, P. M. (2018). Mitigation of air pollution by greenness: A narrative review. *European Journal of Internal Medicine*, 55, 1-5.
- [32] Tuckett, R. (2018). Greenhouse Gases. In *Reference Module in Chemistry, Molecular Sciences and Chemical Engineering*. Elsevier, London.

- [33] The Lancet Planetary Health. (2018). Can the Paris Agreement save us from a climate catastrophe? *The Lancet Planetary Health*, 2(4), e140.
- [34] Gromke, C., & Ruck, B. (2012). Pollutant Concentrations in Street Canyons of Different Aspect Ratio with Avenues of Trees for Various Wind Directions. *Boundary-Layer Meteorology*, 144(1), 41–64.
- [35] Mendes, A., & Teixeira, J. P. (2014). Sick Building Syndrome. In *Encyclopedia of Toxicology* (pp. 256–260). Elsevier. Portugal.
- [36] Jansz, J. (2017). Sick Building Syndrome. In *International Encyclopedia of Public Health* (pp. 502–505). Elsevier. Amsterdam
- [37] Nelson, M., & Wolverton, B. C. (2011). Plants + soil/wetland microbes: Food crop systems that also clean air and water. *Advances in Space Research*, 47(4), 582–590.
- [38] Gladyszewska-Fiedoruk, K. (2011). Concentrations of carbon dioxide in a car. *Transportation Research Part D: Transport and Environment*, 16(2), 166–171.
- [39] Jung, H. S., Grady, M. L., Victoroff, T., & Miller, A. L. (2017). Simultaneously reducing CO₂ and particulate exposures via fractional recirculation of vehicle cabin air. *Atmospheric Environment*, 160, 77–88.
- [40] Scott, J. L., Kraemer, D. G., & Keller, R. J. (2009). Occupational hazards of carbon dioxide exposure. *Journal of Chemical Health and Safety*, 16(2), 18–22.
- [41] Spiru, P., & Simona, P. L. (2017). A review on interactions between energy performance of the buildings, outdoor air pollution and the indoor air quality. *Energy Procedia*, 128, 179–186.
- [42] Mauderly, J. L., & Samet, J. M. (2009). Is There Evidence for Synergy Among Air Pollutants in Causing Health Effects? *Environmental Health Perspectives*, 117(1), 1–6
- [43] Air quality guidelines for particulate matter, ozone, nitrogen dioxide and sulfur dioxide, Global update 2005, Summary of risk assessment. World Health Organization. Occupational and Environmental Health Team. Geneva.
- [44] Kolavennu, S., & Gonía, P. (2016). Wireless gas sensors for industrial life safety. In *Industrial Wireless Sensor Networks* (pp. 155–166). Elsevier.
- [45] Borgia, E. (2014). The Internet of Things vision: Key features, applications and open issues. *Computer Communications*, 54, 1–31
- [46] Kassal, P., Steinberg, M. D., & Steinberg, I. M. (2018). Wireless chemical sensors and biosensors: A review. *Sensors and Actuators B: Chemical*, 266, 228–245

- [47] Lorwongtragool, P., Sowade, E., Watthanawisuth, N., Baumann, R., & Kerdcharoen, T. (2014). A Novel Wearable Electronic Nose for Healthcare Based on Flexible Printed Chemical Sensor Array. *Sensors*, 14(10), 19700–19712.
- [48] Campaniço, H., Hollmuller, P., & Soares, P. M. M. (2014). Assessing energy savings in cooling demand of buildings using passive cooling systems based on ventilation. *Applied Energy*, 134, 426–438
- [49] Üрге-Vorsatz, D., Cabeza, L. F., Serrano, S., Barreneche, C., & Petrichenko, K. (2015). Heating and cooling energy trends and drivers in buildings. *Renewable and Sustainable Energy Reviews*, 41, 85–98
- [50] Benito, A., & Alonso, G. (2018). Energy and air transport. In *Energy Efficiency in Air Transportation* (pp. 5–20). Elsevier. UK.
- [51] Mathiesen, B., Lund, H., Connolly, D., Wenzel, H., Østergaard, P., Möller, B., Nielsen, S., Ridjan, I., Karnøe, P., Sperling, K. and Hvelplund, F. (2015). Smart Energy Systems for coherent 100% renewable energy and transport solutions. *Applied Energy*, 145, pp.139-154.
- [52] Pikridas, M., Vrekoussis, M., Sciare, J., Kleanthous, S., Vasiliadou, E., Kizas, C., Savvides, C. and Mihalopoulos, N. (2018). Spatial and temporal (short and long-term) variability of submicron, fine and sub-10 μm particulate matter (PM_1 , $\text{PM}_{2.5}$, PM_{10}) in Cyprus. *Atmospheric Environment*, 191, pp.79-93.
- [53] Dey, A. (2018). Semiconductor metal oxide gas sensors: A review. *Materials Science and Engineering: B*, 229, 206–217.
- [54] Liu, X., Cheng, S., Liu, H., Hu, S., Zhang, D., & Ning, H. (2012). A Survey on Gas Sensing Technology. *Sensors*, 12(7), 9635–9665.
- [55] Patil, S. J., Patil, A. V., Dighavkar, C. G., Thakare, K. S., Borase, R. Y., Nandre, S. J., ... Ahire, R. R. (2015). Semiconductor metal oxide compounds based gas sensors: A literature review. *Frontiers of Materials Science*, 9(1), 14–37.
- [56] Simões, F. R., & Xavier, M. G. (2017). Electrochemical Sensors. In *Nanoscience and its Applications* (pp. 155–178). Elsevier. USA.
- [57] Szulczyński, B., & Gębicki, J. (2017). Currently Commercially Available Chemical Sensors Employed for Detection of Volatile Organic Compounds in Outdoor and Indoor Air. *Environments*, 4(1), 21

- [58] Pang, X., Shaw, M. D., Gillot, S., & Lewis, A. C. (2018). The impacts of water vapour and co-pollutants on the performance of electrochemical gas sensors used for air quality monitoring. *Sensors and Actuators B: Chemical*, 266, 674–684.
- [59] Zhao, D., Brown, A., Wang, T., Yoshizawa, S., Sfeir, C., & Heineman, W. R. (2018). In vivo quantification of hydrogen gas concentration in bone marrow surrounding magnesium fracture fixation hardware using an electrochemical hydrogen gas sensor. *Acta Biomaterialia*, 73, 559–566.
- [60] Su, S., Chen, S., & Fan, C. (2018). Recent advances in two-dimensional nanomaterials-based electrochemical sensors for environmental analysis. *Green Energy & Environment*, 3(2), 97–106.
- [61] Altai, M. M., Rounaghi, G. H., & Deiminiat, B. (2018). Fabrication of a new electrochemical sensor based on Au Pt bimetallic nanoparticles decorated multi-walled carbon nanotubes for determination of diclofenac. *Microchemical Journal*.
- [62] Zhang, X., Wang, K.-P., Zhang, L.-N., Zhang, Y.-C., & Shen, L. (2018). Phosphorus-doped graphene-based electrochemical sensor for sensitive detection of acetaminophen. *Analytica Chimica Acta*, 1036, 26-32.
- [63] Mao, Y., Bao, Y., Han, D.-X., & Zhao, B. (2018). Research Progress on Nitrite Electrochemical Sensor. *Chinese Journal of Analytical Chemistry*, 46(2), 147–155.
- [64] Delfos, R., Rops, C. M., Kockx, J. P., & Nieuwstadt, F. T. M. (2001). Measurement of the re-coalescence flux into the rear of a Taylor bubble. *Physics of Fluids*, 13(5), 1141–1150.
- [65] Daynes, H. A., (1933) Gas analysis by measurement of thermal conductivity, pp. 1-10, Cambridge University Press, London
- [66] Struk, D., Shirke, A., Mahdaviifar, A., Hesketh, P. J., & Stetter, J. R. (2018). Investigating time-resolved response of micro thermal conductivity sensor under various modes of operation. *Sensors and Actuators B: Chemical*, 254, 771–777.
- [67] Sorge, S., & Pechstein, T. (1997). Fully integrated thermal conductivity sensor for gas chromatography without dead volume. *Sensors and Actuators A: Physical*, 63(3), 191–195.
- [68] Hübner, T., Boon-Brett, L., Palmisano, V., & Bader, M. A. (2014). Developments in gas sensor technology for hydrogen safety. *International Journal of Hydrogen Energy*, 39(35), 20474–20483.

- [69] Udina, S., Carmona, M., Carles, G., Santander, J., Fonseca, L., & Marco, S. (2008). A micromachined thermoelectric sensor for natural gas analysis: Thermal model and experimental results. *Sensors and Actuators B: Chemical*, 134(2), 551–558.
- [70] Simon, I., & Arndt, M. (2002). Thermal and gas-sensing properties of a micromachined thermal conductivity sensor for the detection of hydrogen in automotive applications. *Sensors and Actuators A: Physical*, 97–98, 104–108.
- [71] Morris, A. S., & Langari, R. (2016). Variable Conversion. In *Measurement and Instrumentation* (pp. 177–217). Elsevier. London, UK.
- [72] Castro, H. F., Correia, V., Pereira, N., Costab, P., Oliveiraa, J., & Lanceros-Méndez, S. (2018). Printed Wheatstone bridge with embedded polymer based piezoresistive sensors for strain sensing applications. *Additive Manufacturing*, 20, 119–125.
- [73] Meena, K. V., Mathew, R., Leelavathi, J., & Ravi Sankar, A. (2017). Performance comparison of a single element piezoresistor with a half-active Wheatstone bridge for miniaturized pressure sensors. *Measurement*, 111, 340–350.
- [74] Talić, A., Čerimović, S., Beigelbeck, R., Kohl, F., Jachimowicz, A., & Keplinger, F. (2009). Novel thermal flow sensors based on a Wheatstone bridge read-out. *Procedia Chemistry*, 1(1), 136–139.
- [75] Sun, L., Qiu, F., & Quan, B. (2000). Investigation of a new catalytic combustion-type CH₄ gas sensor with low power consumption. *Sensors and Actuators B: Chemical*, 66(1–3), 289–292
- [76] Sasahara, T., Kido, A., Ishihara, H., Sunayama, T., & Egashira, M. (2005). Highly sensitive detection of volatile organic compounds by an adsorption/combustion-type sensor based on mesoporous silica. *Sensors and Actuators B: Chemical*, 108(1–2), 478–483.
- [77] Ozawa, T., Ishiguro, Y., Toyoda, K., Nishimura, M., Sasahara, T., & Doi, T. (2005). Detection of decomposed compounds from an early stage fire by an adsorption/combustion-type sensor. *Sensors and Actuators B: Chemical*, 108(1–2), 473–477.

- [78] Debeda, H., Dulau, L., Dondon, P., Menil, F., Lucat, C., & Massok, P. (1997). Development of a reliable methane detector. *Sensors and Actuators B: Chemical*, 44(1–3), 248–256.
- [79] Dinh, T.-V., Choi, I.-Y., Son, Y.-S., & Kim, J.-C. (2016). A review on non-dispersive infrared gas sensors: Improvement of sensor detection limit and interference correction. *Sensors and Actuators B: Chemical*, 231, 529–538.
- [80] Kosse, P., Kleeberg, T., Lübken, M., Matschullat, J., & Wichern, M. (2018). Quantifying direct carbon dioxide emissions from wastewater treatment units by nondispersive infrared sensor (NDIR) – A pilot study. *Science of the Total Environment*, 633, 140–144.
- [81] Fleming, L., Gibson, D., Song, S., Li, C., & Reid, S. (2018). Reducing N₂O induced cross-talk in a NDIR CO₂ gas sensor for breath analysis using multilayer thin film optical interference coatings. *Surface and Coatings Technology*, 336, 9–16.
- [82] Vincent, T. A., & Gardner, J. W. (2016). A low cost MEMS based NDIR system for the monitoring of carbon dioxide in breath analysis at ppm levels. *Sensors and Actuators B: Chemical*, 236, 954–964.
- [83] Kim, J., Lee, K., & Yi, S. (2016). NDIR ethanol gas sensor with two elliptical optical structures. *Procedia Engineering*, 168, 359–362.
- [84] Sklorz, A., & Lang, W. (2011). Strategies for passive sensitivity improvement of NDIR ethylene gas detectors. *Procedia Engineering*, 25, 1153–1156.
- [85] Nakamura, H. (2003). Development of hydrocarbon analyser using heated-NDIR method and its application to on-board mass emission measurement system. *JSAE Review*, 24(2), 127–133.
- [86] Tan, Q., Tang, L., Yang, M., Xue, C., Zhang, W., Liu, J., & Xiong, J. (2015). Three-gas detection system with IR optical sensor based on NDIR technology. *Optics and Lasers in Engineering*, 74, 103–108.
- [87] Yamazoe, N. (2005). Toward innovations of gas sensor technology. *Sensors and Actuators B: Chemical*, 108(1–2), 2–14.
- [88] Riegel, J. (2002). Exhaust gas sensors for automotive emission control. *Solid State Ionics*, 152–153, 783–800.

- [89] Moos, R., Sahner, K., Fleischer, M., Guth, U., Barsan, N., & Weimar, U. (2009). Solid state gas sensor research in Germany – a Status Report. *Sensors*, 9(6), 4323–4365
- [90] Shimizu, Y., Nakano, H., Takase, S., & Song, J.-H. (2018). Solid electrolyte impedancemetric NO_x sensor attached with zeolite receptor. *Sensors and Actuators B: Chemical*, 264, 177–183.
- [91] Adhi, P. M., Okubo, N., Komatsu, A., Kondo, M., & Takahashi, M. (2017). Electrochemical impedance analysis on solid electrolyte oxygen sensor with gas and liquid reference electrodes for liquid LBE. *Energy Procedia*, 131, 420–427.
- [92] Gao, X., Liu, T., Yu, J., & Li, L. (2017). Limiting current oxygen sensor based on La_{0.8}Sr_{0.2}Ga_{0.8}Mg_{0.2}O_{3-δ} as both dense diffusion barrier and solid electrolyte. *Ceramics International*, 43(8), 6329–6332.
- [93] Wang, L., Gao, C., Dai, L., Zhou, H., Li, Y., Meng, W., He, Z. and Kumar, R. (2018). Improvement of Al³⁺ ion conductivity by F doping of (Al_{0.2}Zr_{0.8})_{4/3}NbP₃O₁₂ solid electrolyte for mixed potential NH₃ sensors. *Ceramics International*, 44(8), 8983-8991.
- [94] Zhang, J., Zhang, C., Xia, J., Li, Q., Jiang, D., & Zheng, X. (2017). Mixed-potential NH₃ sensor based on Ce_{0.8}Gd_{0.2}O_{1.9} solid electrolyte. *Sensors and Actuators B: Chemical*, 249, 76–82.
- [95] Vonau, C., Zosel, J., Paramasivam, M., Ahlborn, K., Gerlach, F., Vashook, V., & Guth, U. (2012). Polymer based materials for solid electrolyte sensors. *Solid State Ionics*, 225, 337–341.
- [96] Leonova, L., Shmygleva, L., Ukshe, A., Levchenko, A., Chub, A., & Dobrovolsky, Y. (2016). Solid-state hydrogen sensors based on calixarene—12-phosphatotungstic acid composite electrolytes. *Sensors and Actuators B: Chemical*, 230, 470–476.
- [97] Schelter, M., Zosel, J., Oelßner, W., Guth, U., & Mertig, M. (2013). A solid electrolyte sensor for trace gas analysis. *Sensors and Actuators B: Chemical*, 187, 209–214.
- [98] Barsan, N., Koziej, D., & Weimar, U. (2007). Metal oxide-based gas sensor research: How to? *Sensors and Actuators B: Chemical*, 121(1), 18–35.
- [99] Seiyama, T., Kato, A., Fujiishi, K., & Nagatani, M. (1962). A new detector for gaseous components using semi conductive thin films. *Analytical Chemistry*, 34(11), 1502–1503.

- [100] Huang, X.-J., & Choi, Y.-K. (2007). Chemical sensors based on nanostructured materials. *Sensors and Actuators B: Chemical*, 122(2), 659–671
- [101] Kolmakov, A., Zhang, Y., Cheng, G., & Moskovits, M. (2003). Detection of CO and O₂ using tin oxide nanowire sensors. *Advanced Materials*, 15(12), 997–1000.
- [102] Galstyan, V., Comini, E., Baratto, C., Faglia, G., & Sberveglieri, G. (2015). Nanostructured ZnO chemical gas sensors. *Ceramics International*, 41(10), 14239–14244.
- [103] Urasinska-Wojcik, B., Vincent, T. A., Chowdhury, M. F., & Gardner, J. W. (2017). Ultrasensitive WO₃ gas sensors for NO₂ detection in air and low oxygen environment. *Sensors and Actuators B: Chemical*, 239, 1051–1059.
- [104] Mardare, D., Cornei, N., Mita, C., Florea, D., Stancu, A., Tiron, V., Manole, A. and Adomnitei, C. (2016). Low temperature TiO₂ based gas sensors for CO₂. *Ceramics International*, 42(6), 7353-7359.
- [105] Nakate, U., Lee, G., Ahmad, R., Patil, P., Bhopate, D., Hahn, Y., Yu, Y. and Suh, E. (2018). Hydrothermal synthesis of p-type nanocrystalline NiO nanoplates for high response and low concentration hydrogen gas sensor application. *Ceramics International*, 44(13), 15721-15729.
- [106] Hou, L., Zhang, C., Li, L., Du, C., Li, X., Kang, X.-F., & Chen, W. (2018). CO gas sensors based on p-type CuO nanotubes and CuO nanocubes: Morphology and surface structure effects on the sensing performance. *Talanta*, 188, 41–49.
- [107] Yoon, J.-W., Kim, H.-J., Jeong, H.-M., & Lee, J.-H. (2014). Gas sensing characteristics of p-type Cr₂O₃ and Co₃O₄ nanofibers depending on inter-particle connectivity. *Sensors and Actuators B: Chemical*, 202, 263–271.
- [108] Quang, P. L., Cuong, N. D., Hoa, T. T., Long, H. T., Hung, C. M., Le, D. T. T., & Hieu, N. V. (2018). Simple post-synthesis of mesoporous p-type Co₃O₄ nanochains for enhanced H₂S gas sensing performance. *Sensors and Actuators B: Chemical*, 270, 158–166.
- [109] Kim, H.-J., & Lee, J.-H. (2014). Highly sensitive and selective gas sensors using p-type oxide semiconductors: Overview. *Sensors and Actuators B: Chemical*, 192, 607–627.
- [110] Hübner, M., Simion, C. E., Tomescu-Stănoiu, A., Pokhrel, S., Bârsan, N., & Weimar, U. (2011). Influence of humidity on CO sensing with p-type CuO thick film gas sensors. *Sensors and Actuators B: Chemical*, 153(2), 347–353.

- [111] Krippner, P., Wetzko, M., Szasz, P., Andres, B., & Bauer, T. (2007). MEMS based paramagnetic oxygen measurement. In *Transducers 2007 - 2007 International Solid-State Sensors, Actuators and Microsystems Conference*. IEEE. 2393-2396.
- [112] Vonderschmidt, S., & Müller, J. (2013). A fluidic bridge-based MEMS paramagnetic oxygen sensor. *Sensors and Actuators B: Chemical*, 188, 22–30
- [113] Ko, F., & Mu, J. (2010). A novel micro paramagnetic oxygen sensor based on an anisotropic magneto resistance-device. In *2010 IEEE Sensors*. IEEE.
- [114] Soutar, A., Watt, M., W. Cherrie, J., & Seaton, A. (1999). Comparison between a personal PM₁₀ sampling head and the tapered element oscillating microbalance (TEOM) system. *Atmospheric Environment*, 33(27), 4373–4377.
- [115] AQEG (2005) *Particulate Matter in the UK*. Defra, London.
- [116] Zhang, R., Liu, X., Zhou, T., Wang, L., & Zhang, T. (2018). Carbon materials-functionalized tin dioxide nanoparticles toward robust, high-performance nitrogen dioxide gas sensor. *Journal of Colloid and Interface Science*, 524, 76–83.
- [117] Woo H-S, Na CW, Lee J-H. 2016, Design of Highly Selective Gas Sensors via Physicochemical Modification of Oxide Nanowires: Overview. *Sensors*. 16(9), 1531.
- [118] Chen, X., Huang, Z., Li, J., Wu, C., Wang, Z., & Cui, Y. (2018). Methane gas sensing behavior of lithium ion doped carbon nanotubes sensor. *Vacuum*, 154, 120–128.
- [119] Kim, W., Choi, M., & Yong, K. (2015). Generation of oxygen vacancies in ZnO nanorods/films and their effects on gas sensing properties. *Sensors and Actuators B: Chemical*, 209, 989–996.
- [120] Mane, A. A., & Moholkar, A. V. (2017). Orthorhombic MoO₃ nanobelts based NO₂ gas sensor. *Applied Surface Science*, 405, 427–440
- [121] Liu, D., Tang, Z., & Zhang, Z. (2018). Nanoplates-assembled SnS₂ nanoflowers for ultrasensitive ppb-level NO₂ detection. *Sensors and Actuators B: Chemical*, 273, 473–479
- [122] Al-Ruqeishi, M. S., & Mohiuddin, T. (2015). Growth of Single-sided ZnO nanocombs/ML graphene Heterostructures. *Arabian Journal of Chemistry*.
- [123] Song, Z., Xu, S., Liu, J., Hu, Z., Gao, N., Zhang, J., Yi, F., Zhang, G., Jiang, S. and Liu, H. (2018). Enhanced catalytic activity of SnO₂ quantum dot films employing atomic

- ligand-exchange strategy for fast response H₂S gas sensors. *Sensors and Actuators B: Chemical*, 271, 147-156.
- [124] Zhang, H., & Yi, J. (2018). Enhanced ethanol gas sensing performance of ZnO nanoflowers decorated with LaMnO₃ perovskite nanoparticles. *Materials Letters*, 216, 196–198.
- [125] Fan, X., Elgammal, K., Smith, A. D., Östling, M., Delin, A., Lemme, M. C., & Niklaus, F. (2018). Humidity and CO₂ gas sensing properties of double-layer graphene. *Carbon*, 127, 576–587.
- [126] Flowers, P. F., Reyes, C., Ye, S., Kim, M. J., & Wiley, B. J. (2017). 3D printing electronic components and circuits with conductive thermoplastic filament. *Additive Manufacturing*, 18, 156–163.
- [127] Sharifzadeh, M., Lubiano-Walochik, H., & Shah, N. (2017). Integrated renewable electricity generation considering uncertainties: The UK roadmap to 50% power generation from wind and solar energies. *Renewable and Sustainable Energy Reviews*, 72, 385–398
- [128] Kvellheim, A. K. (2017). The power of buildings in climate change mitigation: The case of Norway. *Energy Policy*, 110, 653–661.
- [129] Ma, Z., Cooper, P., Daly, D., & Ledo, L. (2012). Existing building retrofits: Methodology and state-of-the-art. *Energy and Buildings*, 55, 889–902.
- [130] Pittaluga, M. (2015). Electrochromic glazing and walls for reducing building cooling needs. In *Eco-Efficient Materials for Mitigating Building Cooling Needs* (pp. 473–497). Elsevier, Cambridge, UK.
- [131] Granqvist, C. G. (2014). Electrochromics for smart windows: Oxide-based thin films and devices. *Thin Solid Films*, 564, 1–38.
- [132] Choi, Y., Sim, D. M., Hur, Y. H., Han, H. J., & Jung, Y. S. (2018). Synthesis of colloidal VO₂ nanoparticles for thermochromic applications. *Solar Energy Materials and Solar Cells*, 176, 266–272
- [133] Wu, L. Y. L., Zhao, Q., Huang, H., & Lim, R. J. (2017). Sol-gel based photochromic coating for solar responsive smart window. *Surface and Coatings Technology*, 320, 601–607.

- [134] Casini, M. (2018). Active dynamic windows for buildings: A review. *Renewable Energy*, 119, 923–934.
- [135] Gao, Y., Dong, J., Isabella, O., Santbergen, R., Tan, H., Zeman, M., & Zhang, G. (2018). A photovoltaic window with sun-tracking shading elements towards maximum power generation and non-glare daylighting. *Applied Energy*, 228, 1454–1472.
- [136] Khandelwal, H., Schenning, A. P. H. J., & Debije, M. G. (2017). Infrared Regulating Smart Window Based on Organic Materials. *Advanced Energy Materials*, 7(14), 1-18.
- [137] Ataalla, M., Afify, A. S., Hassan, M., Abdallah, M., Milanova, M., Aboul-Enein, H. Y., & Mohamed, A. (2018). Tungsten-based glasses for photochromic, electrochromic, gas sensors, and related applications: A review. *Journal of Non-Crystalline Solids*, 491, 43–54.
- [138] Varghese Hansen, R., Yang, J., & Zheng, L. (2018). Flexible electrochromic materials based on CNT/PDA hybrids. *Advances in Colloid and Interface Science*, 258, 21–35.
- [139] Granqvist, C. G. (1995) *Handbook of Inorganic Electrochromic Materials*. Elsevier, Amsterdam, The Netherlands.
- [140] Lawrence, S. A., Stevenson, S., Mavadia, K., & Sermon, P. A. (1987). Solid-State Properties of Some Polycrystalline Alkali-Metal Tungsten Bronzes. *Proceedings of the Royal Society A: Mathematical, Physical and Engineering Sciences*, 411(1840), 95–121
- [141] Larsson, S. (2017). Quantum Chemistry and Superconductors. In *Advances in Quantum Chemistry* (pp. 209–226). Elsevier.
- [142] Vong, M., Stevenson, S., & Sermon, P. (1989). Copper tungsten bronzes: Novel preparative routes and reactivity. *Solid State Ionics*, 32–33, 91–96.
- [143] Jittiarporn, P., Badilescu, S., Al Sawafta, M. N., Sikong, L., & Truong, V.-V. (2017). Electrochromic properties of sol–gel prepared hybrid transition metal oxides – A short review. *Journal of Science: Advanced Materials and Devices*, 2(3), 286–300.
- [144] Kharade, R. R., Patil, K. R., Patil, P. S., & Bhosale, P. N. (2012). Novel microwave assisted sol–gel synthesis (MW-SGS) and electrochromic performance of petal like h-WO₃ thin films. *Materials Research Bulletin*, 47(7), 1787–1793.

- [145] Ding, J.-R., & Kim, K.-S. (2016). Rapid growth of vertically aligned tungsten oxide nanostructures by flame vapour deposition process. *Chemical Engineering Journal*, 300, 47–53
- [146] Xiao, F., Miao, Q., Wei, S., Liang, W., Fan, X., Pan, K., & Xu, L. (2018). Hydrothermal synthesis of nanoplates assembled hierarchical h-WO₃ microspheres and phase evolution in preparing cubic Zr(Y)O₂-doped tungsten powders. *Advanced Powder Technology*, 29(11), 2633-2643.
- [147] Hirano, T., Nakakura, S., Rinaldi, F. G., Tanabe, E., Wang, W.-N., & Ogi, T. (2018). Synthesis of highly crystalline hexagonal caesium tungsten bronze nanoparticles by flame-assisted spray pyrolysis. *Advanced Powder Technology*, 29(10), 2512–2520.
- [148] More, A. J., Patil, R. S., Dalavi, D. S., Mali, S. S., Hong, C. K., Gang, M. G., Kim., J. H., Patil, P. S. (2014). Electrodeposition of nano-granular tungsten oxide thin films for smart window application. *Materials Letters*, 134, 298–301.
- [149] Garcia, I. T. S., Corrêa, D. S., de Moura, D. S., Pazinato, J. C. O., Pereira, M. B., & da Costa, N. B. D. (2015). Multifaceted tungsten oxide films grown by thermal evaporation. *Surface and Coatings Technology*, 283, 177–183
- [150] Rakibuddin, M., & Kim, H. (2018). Synthesis and characterization of facile industrially scalable and cost effective WO₃ micro–nanostructures for electrochromic devices and photocatalyst. *Ceramics International*, 44(14), 16615–16623.
- [151] Pehlivan, İ. B., Marsal, R., Pehlivan, E., Runnerstrom, E. L., Milliron, D. J., Granqvist, C. G., & Niklasson, G. A. (2014). Electrochromic devices with polymer electrolytes functionalized by SiO₂ and In₂O₃:Sn nanoparticles: Rapid coloring/bleaching dynamics and strong near-infrared absorption. *Solar Energy Materials and Solar Cells*, 126, 241–247.
- [152] Zhou, A., Liu, X., Dou, Y., Guan, S., Han, J., & Wei, M. (2016). The fabrication of oriented organic–inorganic ultrathin films with enhanced electrochromic properties. *Journal of Materials Chemistry C*, 4(35), 8284–8290.
- [153] Liu, W., Zhang, X., Liu, J., Ma, X., Zeng, J., Liu, P., & Xu, T. (2017). Electrochromic properties of organic-inorganic composite materials. *Journal of Alloys and Compounds*, 718, 379–385.

- [154] Yue, Y., Li, H., Li, K., Wang, J., Wang, H., Zhang, Q., Yaogang, L., Chen, P. (2017). High-performance complementary electrochromic device based on $\text{WO}_3 \cdot 0.33\text{H}_2\text{O}$ /PEDOT and Prussian blue electrodes. *Journal of Physics and Chemistry of Solids*, 110, 284–289.
- [155] Dulgerbaki, C., Maslakci, N. N., Komur, A. I., & Oksuz, A. U. (2018). Electrochromic strategy for tungsten oxide/polypyrrole hybrid nanofiber materials. *European Polymer Journal*, 107, 173–180
- [156] Gadgil, B., Damlin, P., Ääritalo, T., & Kvarnström, C. (2014). Electrosynthesis of viologen cross-linked polythiophene in ionic liquid and its electrochromic properties. *Electrochimica Acta*, 133, 268–274.
- [157] Zhou, K., Wang, H., Jiu, J., Liu, J., Yan, H., & Sukanuma, K. (2018). Polyaniline films with modified nanostructure for bifunctional flexible multicolor electrochromic and supercapacitor applications. *Chemical Engineering Journal*, 345, 290–299.
- [158] da Silva, A. J. C., Ribeiro Nogueira, F. A., Tonholo, J., & Ribeiro, A. S. (2011). Dual-type electrochromic device based on polypyrrole and polythiophene derivatives. *Solar Energy Materials and Solar Cells*, 95(8), 2255–2259.
- [159] Chotsuwan, C., Asawapirom, U., Shimo, Y., Akiyama, H., Ngamaroonchote, A., Jiemsakul, T., & Jiramitmongkon, K. (2017). Investigation of the electrochromic properties of tri-block polyaniline-polythiophene-polyaniline under visible light. *Synthetic Metals*, 226, 80–88.
- [160] Van Bemmelen, J. M. (1897). Die Absorption. Das Wasser in den Kolloïden, besonders in dem Gel der Kieselsäure. *Zeitschrift Für Anorganische Chemie*, 13(1), 233–356.
- [161] Bemmelen, J. M., (1907) Der Hydrogel und das kristallinische Hydrat des Kupferoxydes. *Zeitschrift für Chemie und Industrie der Kolloide*, 1(7), 213–214
- [162] Wichterle, O., & Lím, D. (1960). Hydrophilic gels for biological use. *Nature*, 185(4706), 117–118.
- [163] Warson, H. (2000). *Modern Superabsorbent Polymer Technology*, Edited by F L Buchholz and A T Graham, Wiley-VCH, New York, 1998, *Polymer International*. 49. 1548-1548.

- [164] Mahinroosta, M., Jomeh Farsangi, Z., Allahverdi, A., & Shakoori, Z. (2018). Hydrogels as intelligent materials: A brief review of synthesis, properties and applications. *Materials Today Chemistry*, 8, 42–55.
- [165] Yegappan, R., Selvaprithiviraj, V., Amirthalingam, S., & Jayakumar, R. (2018). Carrageenan based hydrogels for drug delivery, tissue engineering and wound healing. *Carbohydrate Polymers*, 198, 385–400.
- [166] Fu, X., Hosta-Rigau, L., Chandrawati, R., & Cui, J. (2018). Multi-Stimuli-Responsive Polymer Particles, Films, and Hydrogels for Drug Delivery. *Chem*. 4(9), 2084-2107.
- [167] Rao, K. M., Kumar, A., & Han, S. S. (2018). Polysaccharide-based magnetically responsive polyelectrolyte hydrogels for tissue engineering applications. *Journal of Materials Science & Technology*, 34(8), 1371–1377.
- [168] Yang, J.-A., Yeom, J., Hwang, B. W., Hoffman, A. S., & Hahn, S. K. (2014). In situ-forming injectable hydrogels for regenerative medicine. *Progress in Polymer Science*, 39(12), 1973–1986.
- [169] Koehler, J., Brandl, F. P., & Goepferich, A. M. (2018). Hydrogel wound dressings for bioactive treatment of acute and chronic wounds. *European Polymer Journal*, 100, 1–11.
- [170] Wang, K., & Han, Z. (2017). Injectable hydrogels for ophthalmic applications. *Journal of Controlled Release*, 268, 212–224.
- [171] Deng, K., Bellmann, C., Fu, Y., Rohn, M., Guenther, M., & Gerlach, G. (2018). Miniaturized force-compensated hydrogel-based pH sensors. *Sensors and Actuators B: Chemical*, 255, 3495–3504.
- [172] Yetisen, A., Butt, H., Volpatti, L., Pavlichenko, I., Humar, M., Kwok, S., Koo, H., Kim, K., Naydenova, I., Khademhosseini, A., Hahn, S. and Yun, S. (2016). Photonic hydrogel sensors. *Biotechnology Advances*, 34(3), 250-271.
- [173] Nam, J., Jung, I.-B., Kim, B., Lee, S.-M., Kim, S.-E., Lee, K.-N., & Shin, D.-S. (2018). A colorimetric hydrogel biosensor for rapid detection of nitrite ions. *Sensors and Actuators B: Chemical*, 270, 112–118.
- [174] Arregui, F. J., Ciaurriz, Z., Oneca, M., & Matías, I. R. (2003). An experimental study about hydrogels for the fabrication of optical fibre humidity sensors. *Sensors and Actuators B: Chemical*, 96(1–2), 165–172

- [175] Cui, S., Ahn, C., Wingert, M. C., Leung, D., Cai, S., & Chen, R. (2016). Bio-inspired effective and regenerable building cooling using tough hydrogels. *Applied Energy*, 168, 332–339.
- [176] Rotzetter, A. C. C., Schumacher, C. M., Bubenhofer, S. B., Grass, R. N., Gerber, L. C., Zeltner, M., & Stark, W. J. (2012). Thermoresponsive polymer induced sweating surfaces as an efficient way to passively cool buildings. *Advanced Materials*, 24(39), 5352–5356.
- [177] Mohammadzadeh Pakdel, P., & Peighambaroust, S. J. (2018). A review on acrylic based hydrogels and their applications in wastewater treatment. *Journal of Environmental Management*, 217, 123–143
- [178] Thombare, N., Mishra, S., Siddiqui, M. Z., Jha, U., Singh, D., & Mahajan, G. R. (2018). Design and development of guar gum based novel, superabsorbent and moisture retaining hydrogels for agricultural applications. *Carbohydrate Polymers*, 185, 169–178.
- [179] Wang, J., & Wei, J. (2016). Hydrogel brushes grafted from stainless steel via surface-initiated atom transfer radical polymerization for marine antifouling. *Applied Surface Science*, 382, 202–216.
- [180] Giannouli, P., & Morris, E. R. (2003). Cryogelation of xanthan. *Food Hydrocolloids*, 17(4), 495–501.
- [181] Yuan, N., Xu, L., Xu, B., Zhao, J., & Rong, J. (2018). Chitosan derivative-based self-healable hydrogels with enhanced mechanical properties by high-density dynamic ionic interactions. *Carbohydrate Polymers*, 193, 259–267.
- [182] Popa, N., Novac, O., Profire, L., Lupusoru, C. E., & Popa, M. I. (2009). Hydrogels based on chitosan–xanthan for controlled release of theophylline. *Journal of Materials Science: Materials in Medicine*, 21(4), 1241–1248.
- [183] Basu, A., Kunduru, K. R., Doppalapudi, S., Domb, A. J., & Khan, W. (2016). Poly(lactic acid) based hydrogels. *Advanced Drug Delivery Reviews*, 107, 192–205.
- [184] Mansur, H. S., Sadahira, C. M., Souza, A. N., & Mansur, A. A. P. (2008). FTIR spectroscopy characterization of poly (vinyl alcohol) hydrogel with different hydrolysis degree and chemically crosslinked with glutaraldehyde. *Materials Science and Engineering: C*, 28(4), 539–548.

- [185] Rice, J. E. (2014). Functional Groups. In *Organic Chemistry Concepts and Applications for Medicinal Chemistry* (pp. 51–65). Elsevier. USA.
- [186] Rudin, A., & Choi, P. (2013). Free-Radical Polymerization. In *The Elements of Polymer Science & Engineering* (pp. 341–389). Elsevier. London, UK.
- [187] Raia, N. R., Partlow, B. P., McGill, M., Kimmerling, E. P., Ghezzi, C. E., & Kaplan, D. L. (2017). Enzymatically crosslinked silk-hyaluronic acid hydrogels. *Biomaterials*, 131, 58–67.
- [188] Hennink, W. E., & van Nostrum, C. F. (2012). Novel crosslinking methods to design hydrogels. *Advanced Drug Delivery Reviews*, 64, 223–236.
- [189] Li, H., Tan, C., & Li, L. (2018). Review of 3D printable hydrogels and constructs. *Materials & Design. Accepted Manuscript*, 1-67.
- [190] Roopavath, U. K., & Kalaskar, D. M. (2017). Introduction to 3D printing in medicine. In *3D Printing in Medicine* (pp. 1–20)
- [191] Economidou, S. N., Lamprou, D. A., & Douroumis, D. (2018). 3D printing applications for transdermal drug delivery. *International Journal of Pharmaceutics*. 544(2), 415-424
- [192] Lin, H.-H., Lonic, D., & Lo, L.-J. (2018). 3D printing in orthognathic surgery – A literature review. *Journal of the Formosan Medical Association*. 117(7), 547-558
- [193] Farooqi, K. M., Saeed, O., Zaidi, A., Sanz, J., Nielsen, J. C., Hsu, D. T., & Jorde, U. P. (2016). 3D Printing to Guide Ventricular Assist Device Placement in Adults with Congenital Heart Disease and Heart Failure. *JACC: Heart Failure*, 4(4), 301–311.
- [194] Malik, H. H., Darwood, A. R. J., Shaunak, S., Kulatilake, P., El-Hilly, A. A., Mulki, O., & Baskaradas, A. (2015). Three-dimensional printing in surgery: a review of current surgical applications. *Journal of Surgical Research*, 199(2), 512–522.
- [195] Obregon, F., Vaquette, C., Ivanovski, S., Hutmacher, D. W., & Bertassoni, L. E. (2015). Three-Dimensional Bioprinting for Regenerative Dentistry and Craniofacial Tissue Engineering. *Journal of Dental Research*, 94, 143–152
- [196] Project focuses on automotive 3D printing. (2017). *Metal Powder Report*, 72(6), 441–442.

- [197] Murr, L. E. (2016). Frontiers of 3D Printing/Additive Manufacturing: from Human Organs to Aircraft Fabrication. *Journal of Materials Science & Technology*, 32(10), 987–995
- [198] Dunham, S., Mosadegh, B., Romito, E. A., & Zgaren, M. (2018). Applications of 3D Printing. In *3D Printing Applications in Cardiovascular Medicine* (pp. 61–78). Elsevier. London, UK.
- [199] Kalsoom, U., Nesterenko, P. N., & Paull, B. (2018). Current and future impact of 3D printing on the separation sciences. *TrAC Trends in Analytical Chemistry*, 105, 492–502
- [200] Lee, J.-Y., An, J., & Chua, C. K. (2017). Fundamentals and applications of 3D printing for novel materials. *Applied Materials Today*, 7, 120–133.
- [201] Gu, B. K., Choi, D. J., Park, S. J., Kim, M. S., Kang, C. M., & Kim, C.-H. (2016). 3-dimensional bioprinting for tissue engineering applications. *Biomaterials Research*, 20(1), 12.
- [202] Klein, R. (2011). *Laser Welding of Plastics*. Wiley-VCH Verlag GmbH & Co. KGaA. Germany.
- [203] Masood, S. H. (2014). Introduction to Advances in Additive Manufacturing and Tooling. In *Comprehensive Materials Processing* (pp. 1–2). Elsevier, London, UK.
- [204] Adel, M., Abdelaal, O., Gad, A., Nasr, A. B., & Khalil, A. (2018). Polishing of fused deposition modeling products by hot air jet: Evaluation of surface roughness. *Journal of Materials Processing Technology*, 251, 73–82.
- [205] Awad, A., Trenfield, S. J., Gaisford, S., & Basit, A. W. (2018). 3D printed medicines: A new branch of digital healthcare. *International Journal of Pharmaceutics*, 548(1), 586–596.
- [206] Chohan, J. S., Singh, R., Boparai, K. S., Penna, R., & Fraternali, F. (2017). Dimensional accuracy analysis of coupled fused deposition modelling and vapour smoothing operations for biomedical applications. *Composites Part B: Engineering*, 117, 138–14
- [207] Mohamed, O. A., Masood, S. H., & Bhowmik, J. L. (2015). Optimization of fused deposition modelling process parameters: a review of current research and future prospects. *Advances in Manufacturing*, 3(1), 42–53.

- [208] Marro, A., Bandukwala, T., & Mak, W. (2016). Three-dimensional printing and medical imaging: A review of the methods and applications. *Current Problems in Diagnostic Radiology*, 45(1), 2–9.
- [209] Dou, R., Wang, T., Guo, Y., & Derby, B. (2011). Ink-Jet printing of zirconia: coffee staining and line stability. *Journal of the American Ceramic Society*, 94(11), 3787–3792.
- [210] Mitsouras, D., Liacouras, P., Imanzadeh, A., Giannopoulos, A., Cai, T., Kumamaru, K., George, E., Wake, N., Caterson, E., Pomahac, B., Ho, V., Grant, G. and Rybicki, F. (2015). Medical 3D printing for the radiologist. *RadioGraphics*, 35(7), 1965-1988.
- [211] Upadhyay, M., Sivarupan, T., & El Mansori, M. (2017). 3D printing for rapid sand casting—A review. *Journal of Manufacturing Processes*, 29, 211–220.
- [212] Do, T., Shin, C. S., Stetsko, D., VanConant, G., Vartanian, A., Pei, S., & Kwon, P. (2015). Improving structural integrity with boron-based additives for 3D printed 420 stainless steel. *Procedia Manufacturing*, 1, 263–272.
- [213] Kunchala, P., & Kappagantula, K. (2018). 3D printing high density ceramics using binder jetting with nanoparticle densifiers. *Materials & Design*, 155, 443–450.
- [214] Salmi, M. (2016). Possibilities of preoperative medical models made by 3D printing or additive manufacturing. *Journal of Medical Engineering*, 2016, 1–6
- [215] Koike, R., Ashida, R., Yamazaki, K., Kakinuma, Y., Aoyama, T., Oda, Y., Kuriya, T., Fujishima, M. (2016). Graphical Evaluation Method for Void Distribution in Direct Energy Deposition. *Procedia Manufacturing*, 6, 105–112.
- [216] Gibson, I., Rosen, D., & Stucker, B. (2015). *Additive Manufacturing Technologies*. Springer New York.
- [217] Salmi, M., Partanen, J., Tuomi, J., Chekurov, S., Björkstrand, R., Huutilainen, E., Kukko, K., Kretschmar, N., Akmal, J., Jalava, K., Koivisto, S., Vartiainen, M., Metsä-Kortelainen, S., Puukko, P., Jussila, A., Riipinen, T., Reijonen, J., Tanner, H., Mikkola, M. (2018). *Digital Spare Parts*. VTT Technical Research Centre of Finland.
- [218] Thompson, A., Maskery, I., & Leach, R. K. (2016). X-ray computed tomography for additive manufacturing: a review. *Measurement Science and Technology*, 27(7), 72001.

- [219] Cronskär, M., 2011, The use of additive manufacturing in the custom design of orthopedic implants, Dept. of Technology and Sustainable Development, Mid Sweden University, Kopieringen.
- [220] Semini, C., Goldsmith, J., Manfredi, D., Calignano, F., Ambrosio, E. P., Pakkanen, J., & Caldwell, D. G. (2015). Additive manufacturing for agile legged robots with hydraulic actuation. In 2015 International Conference on Advanced Robotics (ICAR). IEEE. Istanbul, 123-129
- [221] Hafkamp, T., van Baars, G., de Jager, B., & Etman, P. (2018). A feasibility study on process monitoring and control in vat photopolymerization of ceramics. *Mechatronics. In Press, Corrected Proof.*
- [222] Lohfeld, S., Barron, V., & McHugh, P. E. (2005). Biomodels of bone: A review. *Annals of Biomedical Engineering*, 33(10), 1295–1311.
- [223] Mekonnen, B. G., Bright, G., & Walker, A. (2016). A study on state-of-the-art technology of laminated object manufacturing (LOM). In *Lecture Notes in Mechanical Engineering* (pp. 207–216). Springer India.
- [224] Ben Halima, N. (2016). Poly(vinyl alcohol): Review of its promising applications and insights into biodegradation. *RSC Advances*, 6(46), 39823–39832.
- [225] Kabir, M. L., Kim, H. J., Lee, C. J., & Choi, S.-J. (2018). Highly proton conductive poly(vinyl acetate)/Nafion® composite membrane for proton exchange membrane fuel cell application. *Journal of Nanoscience and Nanotechnology*, 18(9), 6536–6540.
- [226] Norazlina, H., & Kamal, Y. (2015). Graphene modifications in polylactic acid nanocomposites: a review. *Polymer Bulletin*, 72(4), 931–961
- [227] Gupta, B., Revagade, N., & Hilborn, J. (2007). Poly(lactic acid) fiber: An overview. *Progress in Polymer Science*, 32(4), 455–482
- [228] Novoselov, K. S. (2004). Electric field effect in atomically thin carbon films. *Science*, 306(5696), 666–669
- [229] Martín, A., & Escarpa, A. (2014). Graphene: The cutting-edge interaction between chemistry and electrochemistry. *TrAC Trends in Analytical Chemistry*, 56, 13–26

- [230] Gumfekar, S. P. (2018). Graphene-based materials for clean energy applications. In *Nanomaterials for Green Energy* (pp. 351–383). Elsevier. Amsterdam, Netherlands.
- [231] Schedin, F., Geim, A. K., Morozov, S. V., Hill, E. W., Blake, P., Katsnelson, M. I., & Novoselov, K. S. (2007). Detection of individual gas molecules adsorbed on graphene. *Nature Materials*, 6(9), 652–655
- [232] Yang, T., Zhao, X., He, Y., & Zhu, H. (2018). Graphene-based sensors. In *Graphene* (pp. 157–174). Elsevier.
- [233] Zhang, D., Chi, B., Li, B., Gao, Z., Du, Y., Guo, J., & Wei, J. (2016). Fabrication of highly conductive graphene flexible circuits by 3D printing. *Synthetic Metals*, 217, 79–86.
- [234] Gnanasekaran, K., Heijmans, T., van Bennekom, S., Woldhuis, H., Wijnia, S., de With, G., & Friedrich, H. (2017). 3D printing of CNT- and graphene-based conductive polymer nanocomposites by fused deposition modelling. *Applied Materials Today*, 9, 21–28
- [235] Qiu, H., & Yang, J. (2017). Structure and properties of carbon nanotubes. In *Industrial Applications of Carbon Nanotubes* (pp. 47–69). Elsevier. Amsterdam, Netherlands.
- [236] Hermanson, G. T. (2013). Buckyballs, Fullerenes, and Carbon Nanotubes. In *Bioconjugate Techniques* (pp. 741–755). Elsevier. London, UK.
- [237] Liu, P., Hu, D. C. M., Tran, T. Q., Jewell, D., & Duong, H. M. (2016). Electrical property enhancement of carbon nanotube fibres from post treatments. *Colloids and Surfaces A: Physicochemical and Engineering Aspects*, 509, 384–389
- [238] Lukes, J. R., & Zhong, H. (2007). Thermal conductivity of individual single-wall carbon nanotubes. *Journal of Heat Transfer*, 129(6), 705
- [239] Li, T., Tang, Z., Huang, Z., & Yu, J. (2017). A comparison between the mechanical and thermal properties of single-walled carbon nanotubes and boron nitride nanotubes. *Physica E: Low-Dimensional Systems and Nanostructures*, 85, 137–142.
- [240] Jeong, H., Lee, D., Choi, H., Lee, D., Kim, J., Lee, J., Lee, W., Kim, S. and Choi, S. (2010). Flexible room-temperature NO₂ gas sensors based on carbon nanotubes/reduced graphene hybrid films. *Applied Physics Letters*, 96(21), 213105

- [241] Andre, R. S., Sanfelice, R. C., Pavinatto, A., Mattoso, L. H. C., & Correa, D. S. (2018). Hybrid nanomaterials designed for volatile organic compounds sensors: A review. *Materials & Design*, 156, 154–166.
- [242] Hasani, A., Le, Q. V., Nguyen, T. P., Choi, K. S., Sohn, W., Jang, H. W., & Kim, S. Y. (2018). A thorough study on electrochromic properties of metal doped tungsten trioxide film prepared by a facile solution process. *Electrochimica Acta*, 283, 1195–1202
- [243] Patil, V. B., Adhyapak, P. V., Patil, P. S., Suryavanshi, S. S., & Mulla, I. S. (2015). Hydrothermally synthesized tungsten trioxide nanorods as NO₂ gas sensors. *Ceramics International*, 41(3), 3845–3852.
- [244] Zhao, W., Wang, Z., Shen, X., Li, J., Xu, C., & Gan, Z. (2012). Hydrogen generation via photoelectrocatalytic water splitting using a tungsten trioxide catalyst under visible light irradiation. *International Journal of Hydrogen Energy*, 37(1), 908–915.
- [245] Najafi-Ashtiani, H., Gholipour, S., & Rahdar, A. (2018). Surface plasmon resonance effect for a new structure of Ag/WO₃ nanorod-shell nanocomposites and application in smart window. *Journal of Molecular Structure*, 1169, 25–30.
- [246] Wei, S., Zhao, G., Du, W., & Tian, Q. (2016). Synthesis and excellent acetone sensing properties of porous WO₃ nanofibers. *Vacuum*, 124, 32–39.
- [247] Bamwenda, G. R., & Arakawa, H. (2001). The visible light induced photocatalytic activity of tungsten trioxide powders. *Applied Catalysis A: General*, 210(1–2), 181–191
- [248] Zou, Y. S., Zhang, Y. C., Lou, D., Wang, H. P., Gu, L., Dong, Y. H., Song, X. F., Zeng, H. B. (2014). Structural and optical properties of WO₃ films deposited by pulsed laser deposition. *Journal of Alloys and Compounds*, 583, 465–470.
- [249] Makarov, V. O., & Trontelj, M. (2000). Effect of Al₂O₃ on the microstructure and electrical properties of WO₃ -based varistor ceramics. *Journal of the European Ceramic Society*, 20(6), 747–749.
- [250] Soliman, H. M. A., Kashyout, A. B., El Nouby, M. S., & Abosehly, A. M. (2010). Preparation and characterizations of tungsten oxide electrochromic nanomaterials. *Journal of Materials Science: Materials in Electronics*, 21(12), 1313–1321.

- [251] Giardina, M., Olesik, S. & Phillips, S., (2003). Application of low-temperature glassy carbon-coated macrofibers for solid-phase microextraction analysis of simulated breath volatiles. *Anal.Chem.* 75, 1604
- [252] Montuschi, P., Kharitonov, S.A., Ciabattini, G. & Barnes, P.J. (2003). Exhaled leukotrienes and prostaglandins in COPD *Thorax* 58, 585-588
- [253] Taucher, J., Hansel, A., Jordan, A., Fall, R., Futrell, J. and Lindinger, W. (1997). Detection of isoprene in expired air from human subjects using proton-transfer-reaction mass spectrometry. *Rapid Communications in Mass Spectrometry*, 11(11), 1230-1234.
- [254] Deng, C.H., Zhang, J., Yu, X.F., Zhang, W. & Zhang, X.M. (2004). Determination of acetone in human breath by gas chromatography-mass spectrometry and solid-phase microextraction with on-fiber derivatization. *J.Chromatog.* 810B, 269-275
- [255] Phillips, M., M.Sabas, M. & Greenberg, J. (1993). Increased pentane and carbon disulfide in the breath of patients with schizophrenia. *J.Clin.Pathology* 46, 861
- [256] Morselli-Labate, A.M., Fantini, L. & Pezzilli, R. (2007). Hydrogen sulfide, nitric oxide and a molecular mass 66 u substance in the exhaled breath of chronic pancreatitis patients. *Pancreat.* 7, 497-504
- [257] Smith, D. & Spanel, P. (2017) on the importance of accurate quantification of individual volatile metabolites in exhaled breath. *J.Breath Res.* 11, 047106
- [258] Steeghs, M.M.L., Cristescu, S.M., Munnik, P., Zanen, P. & Harren, F (2007). An off-line breath sampling and analysis method suitable for large screening studies. *J.M. Physiol. Measurement* 28, 503-514
- [259] Mirnaghi, F. S., Soucy, N., Hollebhone, B. P. & Brown C. E. (2018). Rapid fingerprinting of spilled petroleum products using fluorescence spectroscopy coupled with parallel factor and principal component analysis. *Chemosphere* 208, 185-195
- [260] Creton, B. & Mougin, P., (2016). Equivalent alkane carbon number of live crude oil: A predictive model based on thermodynamics. *Oil Gas Sci. Technol.- Rev. IFP Energ. Nouv.* 71, AR 62
- [261] Queste, S. Salager, J. L., Strey, R. and Aubry, J. M., (2007). The EACN scale for oil classification revisited thanks to fish diagrams. *J. Coll. Interf. Sci.* 312, 98-107

- [262] Bruckberger, M. C., Bastow, T. P., Morgan, M. J., Gleeson, D., Banning, N., Davis, G., & Puzon, G. J. (2018). Biodegradability of polar compounds formed from weathered diesel. *Biodegradation*, 29(5), 443–461.
- [263] Leshuk, T., Peru, K. M., Livera, D. D., Tripp, A., Bardo, P., Headley, J. V., and Gu, F. (2018). Petroleomic analysis of the treatment of naphthenic organics in oil sands process-affected water with buoyant photocatalysts. *Water Res.* 141, 297-306
- [264] Dogra, Y., Scarlett, A. G., Rowe, D., Galloway, T. S., & Rowland, S. J., (2018). Predicted and measured acute toxicity and developmental abnormalities in zebrafish embryos produced by exposure to individual aromatic acids. *Chemosphere* 205, 98-107
- [265] Doptis, L. E., Jenkins, L. R., & Young, R. (1978). Evaluation of comparative toxicity and shipboard hazards of selected petroleum and oil-shale derived fuels. *In Situ* 2, 354-354
- [266] Hansen, B. H., Sorensen, L., Carvalho, P. A., Meier, S., Booth, A. M., Altin, D., Farkas J., & Nordtug, T. (2018). Adhesion of mechanically and chemically dispersed crude oil droplets to eggs of Atlantic cod (*Gadus morhua*) and haddock (*Melanogrammus aeglefinus*). *Sci.Tot.EnvIRON.* 640, 138-143
- [267] Tatem, H. E., Cox, B. A., & Anderson, J. W. (1978). Toxicity of oils and petroleum hydrocarbons to estuarine crustaceans. *Estur.Coast.Mar.Sci.* 6, 365-373
- [268] Pereira, T. M., Mercon, J., Passos, L. S., Coppo, G. C., Lopes, T. O. M., Cabral, D. S., Scherer, R. & Chippari-Gomes, A. R. (2018). Effects of the water-soluble fraction of diesel oil (WSD) on the fertilization and development of a sea urchin (*Echinometra lucunter*). *Ecotoxicol.EnvIRON.Safety.* 162, 59-62
- [269] Li, X. S., Ding, G. H., Xiong, Y. J., Ma, X. R., Fan, Y. M., & Xiong, D. Q. (2018). Toxicity of Water-Accommodated Fractions (WAF), Chemically enhanced WAF (CEWAF) of Oman crude oil and dispersant to early-life stages of Zebrafish (*Danio rerio*). *Bull.EnvIRON.Contam.Toxicol.* 101, 314-319
- [270] Al-Fanharawi, A. A., Rabee, A. M., & Al-Mamoori, A. M. J. (2018). Biochemical and molecular alterations in freshwater mollusks as biomarkers for petroleum product, domestic heating oil. *Ecotoxicol.EnvIRON.Safety* 158, 69-77

- [271] Xie, W. J., Li, R., Li, X. P., Liu, P., Yang, H. J., Wu, T., & Zhang, Y. P. (2018). Different responses to soil petroleum contamination in monocultured and mixed plant systems. *Ecotoxicol. Environ. Safety* 161, 763-768
- [272] Couillard, C. M. & Leighton, F. A. (1993). Invitro red-blood-cell assay for oxidant toxicity of petroleum oil. *Environ. Toxicol. Chem.* 12, 839-845
- [273] Leighton, F. A. (1990). The systemic toxicity of Prudhoe Bay crude and other petroleum oils to CD-1 mice. *Archiv. Environ. Contam. Toxicol.* 19, 257-262
- [274] Gomer, C. J. & Smith, D. M. (1980). Acute skin photo-toxicity in hairless mice following exposure to crude shale oil or natural petroleum oil. *Toxicol.* 18, 75-85
- [275] Yang, Z. Y., Shah, K., Crevier, C., Laforest, S., Lambert, P., Hollebhone, B. P., Yang, C., Brown, C. E., Landriault, M. & Goldthorp, M. (2018). Occurrence, source and ecological assessment of petroleum related hydrocarbons in intertidal marine sediments of the Bay of Fundy, New Brunswick, Canada *Mar. Pollut. Bull.* 133, 799-807
- [276] Marzooghi, S., Finch, B. E., Stubblefield W. A. & Di Toro D. M. (2018). Predicting phototoxicity of alkylated PAHs, mixtures of PAHs, and water accommodated fractions (WAF) of neat and weathered petroleum with the phototoxic target lipid model. *Environ. Toxicol. Chem.* 37, 2165-2174
- [277] Siron, R., Giusti, G., Berland, B., Moralesloo, R. & Pelletier, E. (1991). Water-soluble petroleum compounds – Chemical aspects and effects on the growth of microalgae. *Sci. Tot. Environ.* 104, 211-227
- [278] Camarillo, M. K. & Stringfellow, W. T. (2018). Biological treatment of oil and gas produced water: a review and meta-analysis. *Clean Technol. Environ. Pol.* 20, 1127-1146
- [279] Truax, D., Britto, R. and Sherrard, J. (1995). Bench-scale studies of reactor-based treatment of fuel-contaminated soils. *Waste Management*, 15(5-6), 351-357.
- [280] Odermatt, J. and Menatti, J. (1996). Methodology for using contaminated soil leachability testing to determine soil cleanup levels at contaminated petroleum underground storage tank (UST) sites. *Journal of Soil Contamination*, 5(2), 157-169.
- [281] Castro, C., O'Shea, S., Wang, W. and Bartnicki, E. (1996). Biodehalogenation: Oxidative and Hydrolytic Pathways in the Transformations of Acetonitrile,

Chloroacetonitrile, Chloroacetic Acid, and Chloroacetamide by *Methylosporium trichosporium* OB-3b. *Environmental Science & Technology*, 30(4), 1180-1184.

- [282] Li, D. and Lundegard, P. (1996). Evaluation of Subsurface Oxygen Sensors for Remediation Monitoring. *Groundwater Monitoring & Remediation*, 16(1), 106-111.
- [283] Li, K. Y., Zhang, Y., & Xu, T. (1995). Bioremediation of oil-contaminated soil — A rate model. *Waste Management*, 15(5–6), 335–338.
- [284] Møller, J., Winther, P., Lund, B., Kirkebjerg, K., & Westermann, P. (1996). Bioventing of diesel oil-contaminated soil: Comparison of degradation rates in soil based on actual oil concentration and on respirometric data. *Journal of Industrial Microbiology*, 16(2), 110–116.
- [285] Gladden, L. F. (1996). Structure-transport relationships in porous media. *Magnetic Resonance Imaging*, 14(7–8), 719–726
- [286] Gulyas, H., Von-bismark, R. & Hemmerling, L. (1995). Treatment of industrial wastewaters with ozone/hydrogen peroxide. *Water Sci. Technol.* 32, 127
- [287] Van kemenade, I., Anderson, W. A., Scharer, J. M & Moo-young, M. (1996) Chemical pre-oxidation for enhancing bioremediation of contaminated soils *Proc. Safety Environ. Protection* 74,(2), 125
- [288] Chua C. K., Leong K. F., Lim C. S. (2003) *Rapid prototyping: principles and applications*, World Scientific Publishing, Singapore
- [289] Yakovlev, A., Trunova, E., Grevey, D., Pilloz, M., & Smurov, I. (2005). Laser-assisted direct manufacturing of functionally graded 3D objects. *Surface and Coatings Technology*, 190(1), 15–24
- [290] Alimardani, M., Toyserkani, E., & Huissoon, J. P. (2007). Three-dimensional numerical approach for geometrical prediction of multilayer laser solid freeform fabrication process. *Journal of Laser Applications*, 19(1), 14–25.
- [291] Wang, X., Jiang, M., Zhou, Z., Gou, J., & Hui, D. (2017). 3D printing of polymer matrix composites: A review and prospective. *Composites Part B: Engineering*, 110, 442–458

- [292] Luo, Y., Li, Y., Qin, X., & Wa, Q. (2018). 3D printing of concentrated alginate/gelatin scaffolds with homogeneous nano apatite coating for bone tissue engineering. *Materials & Design*, 146, 12–19.
- [293] Hu, Z., Chen, F., Xu, J., Nian, Q., Lin, D., Chen, C., Zhu, X., Chen, Y. and Zhang, M. (2018). 3D printing graphene-aluminium nanocomposites. *Journal of Alloys and Compounds*, 746, pp.269-276.
- [294] Sánchez, M. S., & Rossell, G. T. (2017). Graphene reinforced nanocomposites for 3D printing applications. In *Proceedings of the 3rd World Congress on Mechanical, Chemical, and Material Engineering*. Avestia Publishing.
- [295] Prashantha, K., & Roger, F. (2016). Multifunctional properties of 3D printed poly(lactic acid)/graphene nanocomposites by fused deposition modelling. *Journal of Macromolecular Science, Part A*, 54(1), 24–29.
- [296] Redwood, B., Schöffner, F., Garret, B., 2017, *The 3D Printing Handbook*, Coers & Roest Netherlands
- [297] Egerton, R. F. (2005). *Physical principles of electron microscopy*. Springer USA
- [298] Simon, A. H. (2018). Sputter processing. In *Handbook of Thin Film Deposition* (pp. 195–230). Elsevier. Oxford, UK.
- [299] Bell, D. C., & Erdman, N. (Eds.). (2012). *Low Voltage Electron Microscopy*. John Wiley & Sons, Ltd. USA
- [300] Armstrong, G., & Kailas, L. (2017). Hyphenated analytical techniques for materials characterisation. *European Journal of Physics*, 38(5), 53001
- [301] Schwander, S., Haussmann, T., Hagelstein, G., Solé, A., Cabeza, L. F., Diarce, G., Hohenauer, W., Lager, D., Ristic, A., Rathgeber, C., Hennemann, P., Mehling, H., Peñalosa, C. & Lázaro, A. (2015). Standardization of PCM Characterization via DSC. *13th International Conference on Energy Storage* (2015). 1-9
- [302] Tao, J. (2013). FTIR and Raman studies of structure and bonding in mineral and organic–mineral composites. In *Research Methods in Biomineralization Science* (pp. 533–556). Elsevier. San Diego, USA.

- [303] Lewandowska, R., & Liu, J. (2016). Raman microscopy: Analysis of nanomaterials. In Reference Module in Materials Science and Materials Engineering. Elsevier.
- [304] Nanda, S. S., Kim, M. J., Yeom, K. S., An, S. S. A., Ju, H., & Yi, D. K. (2016). Raman spectrum of graphene with its versatile future perspectives. *TrAC Trends in Analytical Chemistry*, 80, 125–131
- [305] Zhao, W., Tan, P. H., Liu, J., & Ferrari, A. C. (2011). Intercalation of few-layer graphite flakes with FeCl₃: Raman determination of Fermi level, layer by layer decoupling, and stability. *Journal of the American Chemical Society*, 133(15), 5941–5946
- [306] Kalbac, M., Reina-Cecco, A., Farhat, H., Kong, J., Kavan, L., & Dresselhaus, M. S. (2010). The influence of strong electron and hole doping on the Raman intensity of chemical vapour-deposition Graphene. *ACS Nano*, 4(10), 6055–6063.
- [307] Casiraghi, C., Pisana, S., Novoselov, K. S., Geim, A. K., & Ferrari, A. C. (2007). Raman fingerprint of charged impurities in graphene. *Applied Physics Letters*, 91(23), 233108.
- [308] Kumar, C. V., & Pattammattel, A. (2017). Characterization techniques for graphene. In *Introduction to Graphene* (pp. 45–74). Elsevier. Amsterdam Netherlands.
- [309] Ferrari, A. C., & Basko, D. M. (2013). Raman spectroscopy as a versatile tool for studying the properties of graphene. *Nature Nanotechnology*, 8(4), 235–246.
- [310] Subramanian, A., & Rodriguez-Saona, L. (2009). Fourier transform infrared (FTIR) spectroscopy. In *Infrared Spectroscopy for Food Quality Analysis and Control* (pp. 145–178). Elsevier USA
- [311] Du, C., & Zhou, J. (2009). Evaluation of soil fertility using infrared spectroscopy – a review. In *Climate Change, Intercropping, Pest Control and Beneficial Microorganisms* (pp. 453–483). Springer Netherlands
- [312] Hang, N. T., Zhang, S., Noh, J.-S., & Yang, W. (2018). Study on the optimization of graphene sensors using Ag-nanostructures decoration. *Thin Solid Films*. 660, 631-636
- [313] Zhang, R., & Zhu, H. (2018). Potential applications and perspectives. In *Graphene* (pp. 233–249). Elsevier. UK

- [314] Xiao, Z., Kong, L., Ruan, S., Li, X., Yu, S., Li, X., Jiang, Y., Yao, Z., Ye, S., Wang, C., Zhang, T., Zhou, K. and Li, S. (2018). Recent development in nanocarbon materials for gas sensor applications. *Sensors and Actuators B: Chemical*, 274, 235-267.
- [315] Nag, A., Mitra, A., & Mukhopadhyay, S. C. (2018). Graphene and its sensor-based applications: A review. *Sensors and Actuators A: Physical*, 270, 177–194.
- [316] Lee, J. M., Moon, J. Y., Kim, T. H., Lee, S. W., Ahrberg, C. D., & Chung, B. G. (2018). Conductive hydrogel/nanowire micropattern-based sensor for neural stem cell differentiation. *Sensors and Actuators B: Chemical*, 258, 1042–1050.
- [317] You, J.-O., & Auguste, D. T. (2010). Conductive, physiologically responsive hydrogels. *Langmuir*, 26(7), 4607–4612
- [318] Geometric Factors in Four Point Resistivity Measurement, H. Topsøe, (1966)
- [319] Drenik, A., Alegre, D., Brezinsek, S., Castro, A., Kruezi, U., Meisl, G., Mozetic, M., Oberkofler, M., Panjan, M., Primc, G., Resnik, M., Rohde, V., Seibt, M., Tabarés, F. and Zaplotnik, R. (2017). Detection of ammonia by residual gas analysis in AUG and JET. *Fusion Engineering and Design*, 124, 239-243.
- [320] Abdel-Samad, S., Abdel-Bary, M., & Kilian, K. (2005). Residual gas analysis in the TOF vacuum system. *Vacuum*, 78(1), 83–89.
- [321] Delsol, R., Chapelon, L., Chaabouni, H., Broussous, L., Schellenberger, M., Ostrovski, A., & Normandon, P. (2007). Integrated monitoring of ULK dielectrics out-gassing and measurement of pore sealing efficiency by residual gas analysis technique. *Microelectronic Engineering*, 84(11), 2719–2722.
- [322] P. Hofmann. *Lecture Notes on Surface Science*. Aarhus University, 2005.
- [323] Mellon, F. A. (2003). *Mass Spectrometry Principles and Instrumentation*. In *Encyclopedia of Food Sciences and Nutrition* (pp. 3739–3749)
- [324] Faull, K., Dooley, A., Halgand, F., Shoemaker, L., Norris, A., Ryan, C., Laganowsky, A., Johnson, J. and Katz, J. (2008). Chapter 1 an introduction to the basic principles and concepts of mass spectrometry. *Comprehensive Analytical Chemistry*, 1-46.
- [325] Gross, J. H. (2017). *Instrumentation in mass spectrometry* (pp. 151–292). Springer International Publishing.

- [326] Hou, J., Ci, H., Wang, P., Wang, C., Lv, B., Miao, L., & You, G. (2018). Nanoparticle tracking analysis versus dynamic light scattering: Case study on the effect of Ca^{2+} and alginate on the aggregation of cerium oxide nanoparticles. *Journal of Hazardous Materials*, 360, 319-328.
- [327] Turley, R. S., Benavides, R., Hernández-Viezcas, J. Á., & Gardea-Torresdey, J. L. (2018). Insights on ligand interactions with titanium dioxide nanoparticles via dynamic light scattering and electrophoretic light scattering. *Microchemical Journal*, 139, 333–338
- [328] Langevin, D., Lozano, O., Salvati, A., Kestens, V., Monopoli, M., Raspaud, E., Mariot, S., Salonen, A., Thomas, S., Driessen, M., Haase, A., Nelissen, I., Smisdom, N., Pompa, P., Maiorano, G., Pundes, V., Puchowicz, D., Stępnik, M., Suárez, G., Riediker, M., Benetti, F., Mičetić, I., Venturini, M., Kreyling, W., van der Zande, M., Bouwmeester, H., Milani, S., Rädler, J., Mülhopt, S., Lynch, I. and Dawson, K. (2018). Inter-laboratory comparison of nanoparticle size measurements using dynamic light scattering and differential centrifugal sedimentation. *NanoImpact*, 10, 97-107.
- [329] Allahbakhsh, A., & Bahramian, A. R. (2018). Self-assembly of graphene quantum dots into hydrogels and cryogels: Dynamic light scattering, UV–Vis spectroscopy and structural investigations. *Journal of Molecular Liquids*, 265, 172–180
- [330] Bhattacharjee, S. (2016). DLS and zeta potential – What they are and what they are not? *Journal of Controlled Release*, 235, 337–351
- [331] Glatter, O. (2018). Dynamic light scattering (DLS). In *Scattering Methods and their Application in Colloid and Interface Science* (pp. 223–263). Elsevier Amsterdam Netherlands
- [332] Sakho, E. H. M., Allahyari, E., Oluwafemi, O. S., Thomas, S., & Kalarikkal, N. (2017). Dynamic light scattering (DLS). In *Thermal and Rheological Measurement Techniques for Nanomaterials Characterization* (pp. 37–49). Elsevier. Amsterdam Netherlands
- [333] Leng, X., Luo, D., Xu, Z., & Wang, F. (2018). Modified graphene oxide/Nafion composite humidity sensor and its linear response to the relative humidity. *Sensors and Actuators B: Chemical*, 257, 372–381.

- [334] Ding, X., Chen, X., Chen, X., Zhao, X., & Li, N. (2018). A QCM humidity sensor based on fullerene/graphene oxide nanocomposites with high quality factor. *Sensors and Actuators B: Chemical*, 266, 534–542.
- [335] Škipina, B., Luyt, A. S., Csóka, L., Djoković, V., & Dudić, D. (2018). Generation of photo charge in poly(ethyleneimine)-TiO₂ -anthocyanin modified papers conditioned at different humidity's. *Dyes and Pigments*, 149, 51–58.
- [336] Greenspan, L. (1977). Humidity fixed points of binary saturated aqueous solutions, *Journal of Research of the National Bureau of Standards – A. Physics and Chemistry*, 81A, 89-96.
- [337] Basiuk, E. V., Anis, A., Bandyopadhyay, S., Alvarez-Zauco, E., Chan, S. L. I., & Basiuk, V. A. (2009). Poly(vinyl alcohol)/CNT composites: An effect of cross-linking with glutaraldehyde. *Superlattices and Microstructures*, 46(1–2), 379–383.
- [338] Bonakdar, S., Emami, S. H., Shokrgozar, M. A., Farhadi, A., Ahmadi, S. A. H., & Amanzadeh, A. (2010). Preparation and characterization of polyvinyl alcohol hydrogels crosslinked by biodegradable polyurethane for tissue engineering of cartilage. *Materials Science and Engineering: C*, 30(4), 636–643.
- [339] Shi, J., Hu, G., Sun, Y., Geng, M., Wu, J., Liu, Y., Ge, M., Tao, J., Cao, M. and Dai, N. (2011). WO₃ nanocrystals: Synthesis and application in highly sensitive detection of acetone. *Sensors and Actuators B: Chemical*, 156(2), 820-824.
- [340] Khani, A. H., Rashidi, A. M., & Kashi, G. (2017). Synthesis of tungsten nanoparticles by reverse micelle method. *Journal of Molecular Liquids*, 241, 897–903
- [341] Saini, D., Hopkins, G., Chen, C., Seay, S., Click, E., Lee, S., Hartings, J. and Frothingham, R. (2011). Sampling port for real-time analysis of bioaerosol in whole body exposure system for animal aerosol model development. *Journal of Pharmacological and Toxicological Methods*, 63(2), 143-149.
- [342] Delavari, S., Amin, N. A. S., & Ghaedi, M. (2016). Photocatalytic conversion and kinetic study of CO₂ and CH₄ over nitrogen-doped titania nanotube arrays. *Journal of Cleaner Production*, 111, 143–154

- [343] Matson, U., Ekberg, L. E., and Afshari, A. (2004). Measurement of ultrafine particles: A comparison of two handheld condensation particle counters. *Aerosol Sci. Technol.* 38, 487–495
- [344] Shi, T. M., Simons, S. J. R., Dickin, F. J., & Williams, R. A. (1993). Electrical sensing of dispersion behaviour. *Colloids and Surfaces A: Physicochemical and Engineering Aspects*, 77(1), 9–27.
- [345] Ramirez, A., Daily, W., LaBrecque, D., Owen, E., & Chesnut, D. (1993). Monitoring an underground steam injection process using electrical resistance tomography. *Water Resources Research*, 29(1), 73–87
- [346] Dickin, F. & Wang, M. Electrical resistance tomography for process applications (1996). *Meas. Sci. Technol.* 7, 247
- [347] Daily, W., & Ramirez, A. (1995). Environmental process tomography in the United States. *The Chemical Engineering Journal and the Biochemical Engineering Journal*, 56(3), 159–165.
- [348] Lee, Q. F., & Bennington, C. P. J. (2010). Liquor flow in a model kraft batch digester. *Chemical Engineering Journal*, 158(1), 51–60.
- [349] Kowalski, A., Davidson, J., Flanagan, M., & York, T. (2010). Electrical resistance tomography for characterisation of physical stability in liquid compositions. *Chemical Engineering Journal*, 158(1), 69–77.
- [350] Baker, M. I., Walsh, S. P., Schwartz, Z., & Boyan, B. D. (2012). A review of polyvinyl alcohol and its uses in cartilage and orthopedic applications. *Journal of Biomedical Materials Research Part B: Applied Biomaterials*, 100B(5), 1451–1457.
- [351] Bhattacharya, A., & Ray, P. (2004). Studies on surface tension of poly(vinyl alcohol): Effect of concentration, temperature, and addition of chaotropic agents. *Journal of Applied Polymer Science*, 93(1), 122–130.
- [352] Masuda, M. Chapter 12 in Finch, C. A. 'Polyvinyl Alcohol Developments' J.Wiley Chichester (1992)
- [353] Luo, J., Chu, W., Sall, S., & Petit, C. (2013). Facile synthesis of monodispersed Au nanoparticles-coated on Stöber silica. *Colloids and Surfaces A: Physicochemical and Engineering Aspects*, 425, 83–91.

- [354] Dey, A. (2018). Semiconductor metal oxide gas sensors: A review. *Materials Science and Engineering: B*, 229, 206–217.
- [355] Korotcenkov, G. (2013). *Handbook of gas sensor materials. Integrated Analytical Systems*. Springer New York.
- [356] Seekaew, Y., Lokavee, S., Phokharatkul, D., Wisitsoraat, A., Kerdcharoen, T., & Wongchoosuk, C. (2014). Low-cost and flexible printed graphene–PEDOT:PSS gas sensor for ammonia detection. *Organic Electronics*, 15(11), 2971–2981.
- [357] Bogue, R. (2016). 3D printing: an emerging technology for sensor fabrication. *Sensor Review*, 36(4), 333–338.
- [358] Gómez-Pozos, H., González-Vidal, J., Torres, G., Olvera, M., & Castañeda, L. (2013). Physical characterization and effect of effective surface area on the sensing properties of tin dioxide thin solid films in a propane atmosphere. *Sensors*, 14(1), 403–415
- [359] Restrepo, I., Medina, C., Meruane, V., Akbari-Fakhrabadi, A., Flores, P., & Rodríguez-Llamazares, S. (2018). The effect of molecular weight and hydrolysis degree of poly(vinyl alcohol)(PVA) on the thermal and mechanical properties of poly(lactic acid)/PVA blends. *Polímeros*, 28(2), 169–177.
- [360] Yeh, J.-T., Yang, M.-C., Wu, C.-J., Wu, X., & Wu, C.-S. (2008). Study on the crystallization kinetic and characterization of poly(lactic acid) and poly(vinyl alcohol) blends. *Polymer-Plastics Technology and Engineering*, 47(12), 1289–1296.
- [361] Malard, L. M., Pimenta, M. A., Dresselhaus, G., & Dresselhaus, M. S. (2009). Raman spectroscopy in graphene. *Physics Reports*, 473(5–6), 51–87.
- [362] Gilman, J. W., VanderHart, D. L., & Kashiwagi, T. (1995). Thermal decomposition chemistry of poly(vinyl alcohol). In *ACS Symposium Series* (pp. 161–185). American Chemical Society.
- [363] Pescosolido, L., Feruglio, L., Farra, R., Fiorentino, S., Colombo, I., Coviello, T., Matricardi, P., Hennink, W., Vermonden, T. and Grassi, M. (2012). Mesh size distribution determination of interpenetrating polymer network hydrogels. *Soft Matter*, 8(29), 7708.
- [364] Gun'ko, V., Savina, I., & Mikhalovsky, S. (2017). Properties of water bound in hydrogels. *Gels*, 3(4), 37.

- [365] Koller, M., Wappel, D., Trofaier, N., & Gronald, G. (2011). Test results of CO₂ spray scrubbing with monoethanolamine. *Energy Procedia*, 4, 1777–1782.
- [366] Taniguchi, I., Kinugasa, K., Toyoda, M., & Minezaki, K. (2017). Effect of amine structure on CO₂ capture by polymeric membranes. *Science and Technology of Advanced Materials*, 18(1), 950–958.
- [367] Chalmers, J.M. (2004). Artifacts and common errors in using vibrational spectroscopy techniques mid-infrared spectroscopy: Anomalies, Artifacts and Common Errors. John Wiley & Sons, Ltd. USA
- [368] Esteki, K., Prakash, N., Li, Y.L., Mu, C. & Du, K. (2017). Seasonal variation of CO₂ vertical Distribution in the atmospheric boundary layer and impact of meteorological parameters. *J. Environ. Res.* 11, 707-721
- [369] Kumar, P., Morawska, L., Birmili, W., Paasonen, P., Hu, M., Kulmala, M., Harrison, R., Norford, L. and Britter, R. (2014). Ultrafine particles in cities. *Environment International*, 66, 1-10.
- [370] Vanaga, R., Blumberga, A., Freimanis, R., Mols, T., & Blumberga, D. (2018). Solar facade module for nearly zero energy building. *Energy*, 157, 1025–1034.
- [371] Gong, J. P., Katsuyama, Y., Kurokawa, T., & Osada, Y. (2003). Double-network hydrogels with extremely high mechanical strength. *Advanced Materials*, 15(14), 1155–1158.
- [372] Nandakumar, D. K., Ravi, S. K., Zhang, Y., Guo, N., Zhang, C., & Tan, S. C. (2018). A super hygroscopic hydrogel for harnessing ambient humidity for energy conservation and harvesting. *Energy & Environmental Science*, 11(8), 2179–2187.